11-7-2017

Numerical Evaluation of the Lateral Behavior of Vertical and Battered Pile Group Foundations Using 3-D Finite Element Modeling

Ahmad Souri
Louisiana State University and Agricultural and Mechanical College, lsuasouri@gmail.com

NUMERICAL EVALUATION OF THE LATERAL BEHAVIOR OF VERTICAL AND BATTERED PILE GROUP FOUNDATIONS USING 3-D FINITE ELEMENT MODELING

A Dissertation

Submitted to the Graduate Faculty of the
Louisiana State University and
Agricultural and Mechanical College
in partial fulfillment of the
requirements for the degree of
Doctor of Philosophy

in

The Department of Civil and Environmental Engineering

by
Ahmad Souri
B.S., University of Jordan, 2007
M.S., Ohio University, 2012
December 2017

Acknowledgments

My greatest thanks and appreciation goes to my advisor Dr. Murad Abu-Farsakh for his continuous support, guidance, and suggestions throughout my entire studies. Dr. Murad's work ethic and limitless passion for conducting research and contributing to the body of knowledge in geotechnical engineering is the main driving force for completing this work. His inspirations and insights helped me overcome many hurdles I encountered in my Ph.D. studies and will have an ever-lasting impact in my future endeavors.

I would like to express appreciation for my co-advisor Dr. George Voyiadjis for his support, guidance, and invaluable courses in the areas of mechanics of materials and numerical modeling. I am also thankful for Dr. Ayman Okiel and Dr. Charles Berryman for agreeing to serve on my dissertation committee. A special gratitude goes out to LSU and LTRC for providing the funding and support for my studies.

I am grateful to my friends and colleagues at LTRC for the stimulating discussions, for the sleepless nights we were working together before deadlines, and for all the fun we have had in the last five years: Allam Ardah, Firouz Rosti, Qiming Chen, Milad Saghebfar, Md. Nafiul Haque.

Last but not least, I am grateful to my wife for her endless and kind support especially in difficult moments, and to my parents and siblings for their constant support and encouragement.

TABLE OF CONTENTS

Acknowledgments ii

Abstract v

Chapter 1. Introduction 1
1.1 Problem statement 3
1.2 Objectives 3
1.3 Research scope 4
1.4 Outline 4

Chapter 2. Literature Review 5
2.1 Static lateral behavior of single piles 5
2.2 Static lateral behavior of pile groups 15
2.3 Dynamic lateral behavior of single piles 21
2.4 Dynamic lateral behavior of pile groups 25

Chapter 3. Methodology 28
3.1 Finite element modeling 28
3.2 Material constitutive models 33

Chapter 4. Simulation of the Static Load Test at M19 Pier Foundation 44
4.1 Introduction 44
4.2 Description of the lateral load test of M19 pier foundation 44
4.3 Finite element model description 45
4.4 Results and discussion 48
4.5 Conclusions 57

Chapter 5. The Effect of Pile Group Configuration on the Static Lateral Behavior of Pile Groups 59
5.1 Introduction 59
5.2 Static lateral load test on M19 pier foundation 60
5.3 Finite element model description 61
5.4 Material Constitutive and interface models 63
5.5 Results 64

Chapter 6. Parametric Study for the Effect of Pile Spacing and Clay Soil Type on the Lateral Behavior of Pile Groups 77
6.1 Introduction 77
6.2 FE models 77
6.3 Results 80

Chapter 7. The Dynamic Lateral Behavior of Pile Groups Subjected to Barge Impact 95
7.1 Introduction and background 95
7.2 Additional considerations for dynamic FE simulations 97
7.3 FE models for the barge impact problem 103

7.4 Results 116

Chapter 8. Summary, Conclusions, and Recommendations 144
8.1 Summary 144
8.2 Conclusions 145
8.3 Recommendations for future work 148

References 149

Appendix A. Permissions 158

Appendix B. Soil Resistance Profiles Used in the Parametric Study 159

Vita 168

Abstract

The design of pile foundations to resist lateral loads is essential in offshore structures and bridge foundations. The lateral behavior of piles has been studied in the past by experimental investigations coupled with analytical and numerical methods. The problem is complex due to the nonlinearities from soil behavior, gap formation, and pile-soil-pile interaction in pile groups (or the group effect). In this work, the finite element (FE) modeling was used to study the lateral behavior of pile groups. The FE method is robust and allows incorporating the necessary aspects for studying the behavior of pile groups. The nonlinear material behavior was incorporated using nonlinear constitutive models. The pile-soil interface was modeled using the zero-thickness surface-surface interaction, which provided the capability for modeling the gap behind the piles, and the transfer of interface normal and frictional stresses. The group interaction was facilitated thru the interaction of stress fields around the piles, and by the continuity of the FE mesh.

The lateral behavior of three pile group (PG) configurations (vertical, battered, mixed) with a similar number of piles were evaluated under static and dynamic loading. In the static analysis, the case study of the M19 pier foundation field test was used to verify the FE models. A parametric investigation for the effect of pile spacing and clay soil type was performed. The results showed that the lateral stiffness of the battered and mixed PGs was significantly higher than the vertical PG (+120%, +50%, respectively). The lateral load was found unevenly distributed among the piles in all PGs, and the exterior piles carried 1.5-2% higher load than the interior piles. The influence of the group effect vanished at pile spacings greater than 5D (D is pile width). Also, the influence of pile spacing was more prominent along the load direction. In the dynamic analysis, the PGs behavior was evaluated in barge impact simulations. The results showed that the battered and mixed PGs had similar and large lateral stiffness, which resulted in limited pile cap displacement and large deformation in the barge bow. The weak lateral stiffness of the vertical PG allowed the development of significantly larger impact force and pile cap displacement compared to the battered and mixed PG.

Chapter 1. Introduction

Piles are one type of deep foundations that are designed to resist vertical loads. Their long, beam-like shape allows transfer of vertical loads to the soil thru side friction and tip bearing. Piles are usually used in group form with a pile cap (i.e. concrete thick slab) on top which supports the superstructure elements above ground. Some of the purposes of using pile foundations are (Poulos and Davis 1980) (1) carry the superstructure elements and transfer vertical and lateral loads to the soil, (2) resist uplift or overturning for mats below water table, (3) control settlements for mats and spread footing over compressible soils, (4) support offshore structures by transmitting loads thru water to underlying soil. Depending on the soil type, piles are installed either by driving (hammering) or by pre-boring (augured or drilled).

The design of piles is mainly based on vertical load capacity. However, design for lateral resistance has become necessary especially for cases where considerable lateral loads are present as in offshore structures, bridge abutments, and foundations near slopes. The lateral capacity of single piles and pile groups has been well investigated by field experiments, centrifuge (lab tests), analytical methods, and numerical methods (e.g. Matlock and Reese 1960; Reese et al. 1975; Reese and Welch 1975; Brown et al. 1988; McVay et al. 1996; Trochanis et al. 1991; Ashour et al. 1998; Yang and Jeremić 2002). The beam on elastic foundation theory (Hetényi 1946) provides a simplified analogy for the problem of pile-soil system subjected to lateral loads. The system is idealized (in 2-D space) as a long beam (pile) supported by a series of independent elastic springs (soil) (Figure 1.1). In order to solve the problem, assumptions are needed for springs stiffness. For example, Winkler (1867) assumed constant linear spring stiffness, while others assumed nonlinear spring stiffness after experiments proving the latter case (e.g. Matlock and Reese 1960). The nonlinear soil spring stiffness is referred to as '*p-y* curve', which relates the soil reaction to pile deflection at certain depth.

The assumption regarding the soil model allows solving the problem either analytically or by using numerical methods. The analytical solution is based on solving the beam differential equation for the pile-soil system using appropriate boundary conditions. The numerical approach is used in the case of nonlinear spring stiffness of soil which requires iterative procedure. Solutions using the two mentioned approaches are available for the single pile case. For pile groups, single pile solutions can be extended by adjusting the soil spring stiffness to account for the effect of nearby piles, which is called the group effect. The influence of the group effect can be explained by the overlapping of stress zones from the nearby piles when the group is subjected to lateral load. The group effect apparently reduces soil stiffness compared to the isolated single pile case.

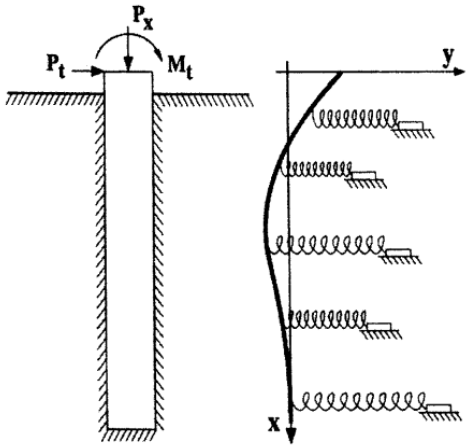

Figure 1.1. Spring idealization of soil in the laterally loaded pile problem

Numerically, the group effect is accounted for using reduction factors called '*p*-multipliers' applied to the soil spring stiffness. The reduction factors for pile groups are deduced by comparing the soil resistance in case of a pile in a group to the soil resistance in the isolated single pile case. Those factors are empirical and have recommended values based on previous experiments.

Recently, the finite element (FE) method became one of the powerful methods for solving complex problems especially with the huge leap in the computational power and speed of computers. Experimental studies for pile groups are expensive and can be limited, and the FE method provides practical, affordable, and reliable alternative to the experimental approach. It has the capability to study and analyze problems in 1, 2, or 3-D space. The use of the FE method for the pile-soil problem allows modeling of several aspects of nonlinearity in the problem such as pile and soil material nonlinearity, multilayered soil, pile-soil gapping, interface friction, and pile group effect. Furthermore, the use of 3-D pile group models allows studying non-uniform pile group spacing. When experimental results are limited, an FE model can be used to extract more results after being verified using the available results from the experiment. However, the FE method requires understanding of the problem mechanics and strong knowledge in numerical modeling.

The lateral behavior of pile groups can be well studied using the FE method. While the experimental approach is reliable, it can be limited and expensive for large-scale problems. The analytical approach is limited by assumptions and the size of the problem. The established numerical approaches based on *p-y* curves are reliable and well tested. However, these methods have semi-empirical nature, and the soil springs work in 1-D space only.

1.1 Problem statement

The lateral behavior of pile groups is a 3-D problem and incorporates several sources of nonlinearity. The FE method provides a feasible alternative to field experiments to study the aspects of the problem. Experimental investigations for pile groups are costly and difficult. Some researchers opted to use small-scale pile models in centrifuge device to reduce the costs, which also has its own challenges and limitations. One of the challenges in full-scale testing, in addition to cost, is in the amount of instrumentation to obtain measurements of piles deflection, inclination, axial force, and bending moment. Additionally, there is no direct method for measuring the soil resistance, which is one of the main outcomes needed in studying the lateral behavior of piles. The differences between vertical and battered pile groups are yet to be addressed under static and dynamic loads, and in practice, the soil resistance models are assumed similar for both. The FE method allows modeling 3-D problems, studying different cases, and incorporating several nonlinearity sources. The output from FE analysis provides the necessary variables such as pile deflection and inclination, stresses and strains, axial force, shear force, and bending moment.

1.2 Objectives

The objectives of the study are

1. Conduct literature review for the lateral behavior of piles and pile groups.
2. Develop and verify the Fortran code for the Anisotropic Modified Camclay constitutive model in Abaqus UMAT.
3. Develop and verify the FE model for the static load test conducted on M19 pier foundation.
4. Study the aspects of the lateral behavior of battered pile group of M19 pier foundation.
5. Develop FE models for vertical and mixed pile groups based on the M19 FE model, and study their lateral behavior in comparison to the battered pile group.
6. Conduct a parametric study to investigate the influence of pile spacing and soil type on the lateral behavior of pile groups.
7. Develop charts for the *p*-multipliers for the three pile group types as function of pile spacing and soil type.
8. Develop the FE model for the statnamic test of pile TP7 to verify the response of the soil model under dynamic loading.
9. Develop the FE model for the Jumbo Hopper barge for the barge-pile group collision study.
10. Develop FE models for the vertical, battered, mixed pile groups and the Jumbo Hopper barge for the barge-pile group impact study.
11. Study the aspects of the lateral behavior of pile groups subjected to barge impact.

1.3 Research scope

This study is focused on using the 3-D FE method to study the lateral behavior of pile groups under static and barge impact loads. The FE models are developed in Abaqus software package and utilize the library of constitutive models for simulating the nonlinear material behavior. Additionally, the Anisotropic Modified Camclay model is implemented thru the UMAT subroutine and used to simulate the nonlinear clay soil behavior. The pile groups studied are made of prestressed concrete and their design is based on the case study of M19 pier foundation. There are three pile group configurations in the study: vertical, battered and mixed, in which the pile's inclination in the battered and mixed pile groups is fixed at 1H:6V. The pile groups in the parametric study have 4x4 piles arrangement because (1) it allows modeling half of the geometry, (2) the influence of the group effect for the interior piles is similar for pile groups greater than 4x4. In the static analysis, the results discuss the influence of the group effect on the lateral resistance in terms of load-displacement response (i.e. lateral capacity), distribution of the lateral load per pile, axial reaction in the piles, bending moment profiles, soil resistance profiles, *p-y* curves, and *p*-multipliers. For the barge impact study, the barge design is based on the Jumbo Hopper barge specs, which is the most common barge type in US waterways. The barge impact is studied at three different barge speeds. The lateral behavior of the vertical, battered, and mixed pile groups subjected to barge impact is investigated in terms of load-displacement response, barge crush depth, distribution of the lateral load per pile, axial reaction in the piles, and bending moment at the pile cap elevation.

1.4 Outline

The dissertation contents are: Chapter 2 presents literature review for the previous work on single piles and pile groups. Chapter 3 presents the study methods and techniques used in the FE modeling and a comprehensive review of the constitutive models. Chapter 4 presents FE simulation for the case study of static load test on M19 pier foundation. Chapter 5 presents the comparison of three pile group configurations based on the M19 case study. Chapter 6 presents the parametric study for the effect of pile spacing and clay soil type on the behavior of pile groups. Chapter 7 presents the study of the lateral behavior of pile groups subjected to barge impact.

Chapter 2. Literature Review

2.1 Static lateral behavior of single piles

The lateral behavior of pile foundations is an interaction problem between the pile and the surrounding soil. This is usually faced in offshore platforms as well as bridge foundations crossing waterways. The lateral forces acting on the foundation is resisted by the rigidity of the piles and the soil surrounding it. The problem can be visualized as a deflecting beam (pile) resting on continuous support along its length (soil). The interaction between the pile and the soil is interdependent and nonlinear at large deflections. The lateral pile deflection depends on the soil reaction, which is also a function of the pile deflection.

Several methods are established for analysis of the lateral behavior of piles. For single pile, the main approaches are: Winkler approach, the *p-y* curve method, elastic solutions, the finite element method. In the following sections, each approach is briefly reviewed.

2.1.1 Winkler model

The differential equation (Eq.1) governing the pile-soil system was first introduced by Hetenyi (1946). The solution starts by assuming a beam resting on elastic foundation (Winkler foundation) subjected to horizontal forces and axial forces (Figure 2.1).

$$\frac{d^2M}{dx^2} + P_x\frac{d^2y}{dx^2} - \frac{dV_v}{dx} = 0 \qquad \text{Eq.1}$$

Furthermore, the differential of the bending moment function is related to the pile deflection as

$$\frac{d^2M}{dx^2} = E_pI_p\frac{d^4y}{dx^4}$$
$$\frac{dV_v}{dx} = p \qquad \text{Eq.2}$$

The variation in shear force is equal to the soil resistance (*p)* which is assumed as a distributed load. Winkler hypothesis assumes that the soil reaction is a function of the pile deflection (y) as

$$p = E_{py} * y \qquad \text{Eq.3}$$

Where E_{py} is the soil modulus (Force/Length/Length). In literature, the soil modulus is estimated from the modulus of subgrade reaction and the pile size D (diameter, width) as

$$E_{py} = k_h * D \qquad \text{Eq.4}$$

The value of the subgrade reaction modulus k_h is a function of depth. Palmer and Thomson (1948) suggested a nonlinear (exponential) relation for k_h over depth assuming

a maximum value at pile tip. Terzaghi (1955) suggested constant value for k_h over depth, and that the vertical and horizontal soil modulus of reaction are the same. He estimated the value of k_h using the subgrade modulus from plate load test. Matlock and Reese (1960) suggested that k_h for the soil is linearly varying with depth for granular and normally consolidated (NC) soils. Gill and Demars (1970) suggested other variations for k_h with depth such as step function, hyperbolic function, and exponential function.

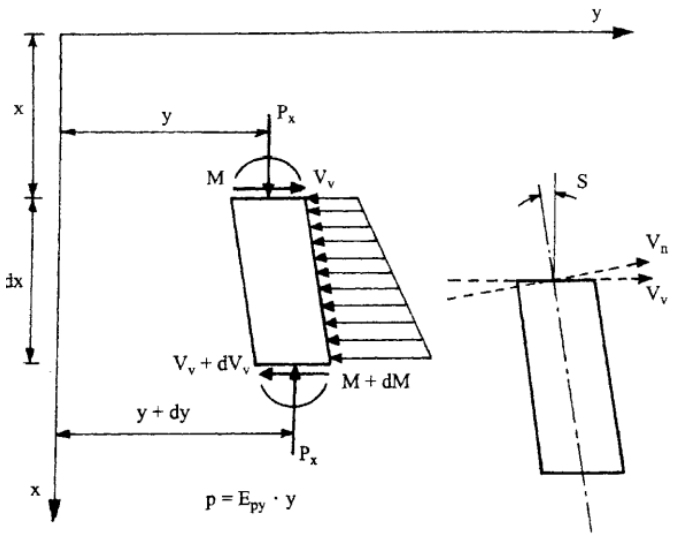

Figure 2.1: Analysis of beam resting on elastic foundation (Hetényi 1946)

The final form of the beam equation is obtained by substituting the previous equations (2, 3, 4) into equation (1)

$$E_p I_p \frac{d^4y}{dx^4} + P_x \frac{d^2y}{dx^2} - p(x) + W = 0 \qquad \text{Eq.5}$$

Where W is the load on the upper portion of the pile.

A general solution to the differential equation is achieved by assuming (1) no axial loading, (2) $E_p I_p$ constant, (3) constant soil modulus E_{py}

$$y = e^{\beta x}(\xi_1 \cos \beta x + \xi_2 \sin \beta x) + e^{-\beta x}(\xi_3 \cos \beta x - \xi_4 \sin \beta x) \qquad \text{Eq.6}$$

Where $\xi_{1,2,3,4}$ are solution constants, β is given as $\beta = \sqrt[4]{\frac{E_{py}}{4E_p I_p}}$.

Solutions for several pile cases can be achieved by introducing boundary conditions to equation (6). For example, for long piles, the first term in equation (6) vanishes and the solution for pile's deflection, slope, bending moment, shear, and soil reaction is obtained (Eq.7) (Reese et al. 2006).

$$y = \frac{2P_t\beta}{\alpha}\, C_1 + \frac{M_t}{2E_pI_p\beta^2} B_1$$

$$S = \frac{2P_t\beta^2}{\alpha} A_1 - \frac{M_t}{E_pI_p\beta}\, C_1$$

$$M = \frac{P_t}{\beta} D_1 + M_t A_1$$

$$V = P_t B_1 - 2M_t\beta D_1$$

$$p = -2P_t\beta C_1 - 2M_t\beta^2 B_1$$

Eq.7

Where A,B,C,D are constants obtained from solution tables found in the reference.

Another solution for the governing differential equation is found by assuming no axial load, and a linear variation of soil modulus with depth (Eq. 8). The method utilizes non-dimensional parameters (A_x, B_x) which can be obtained from charts. The method is useful but requires several trails to achieve convergence. The differential equation for the pile-soil system can also be solved using the finite difference method and computer.

$$y = A_y \frac{P_t T^3}{E_pI_p} + B_y \frac{M_t T^2}{E_pI_p}$$

$$S = A_s \frac{P_t T^2}{E_pI_p} + B_s \frac{M_t T}{E_pI_p}$$

$$M = A_m P_t T + B_m M_t$$

$$V = A_v P_t + B_v \frac{M_t}{T}$$

Eq.8

$$T = \sqrt[5]{\frac{E_pI_p}{k_{py}}}$$

$$Z_{max} = \frac{L}{T}$$

2.1.2 *p-y* curve method

Soil stresses surrounding the pile in the loaded and unloaded cases are shown in Figure 2.2. For the unloaded case, the stresses are the same around the pile; however, when the pile is deflected under lateral load, the stress distribution becomes uneven. The pile deflection increases the soil resistance at pile front (in movement direction) and decreases

it at the back of the pile. Integration of the stresses around the pile yields net reaction force from the soil at certain depth.

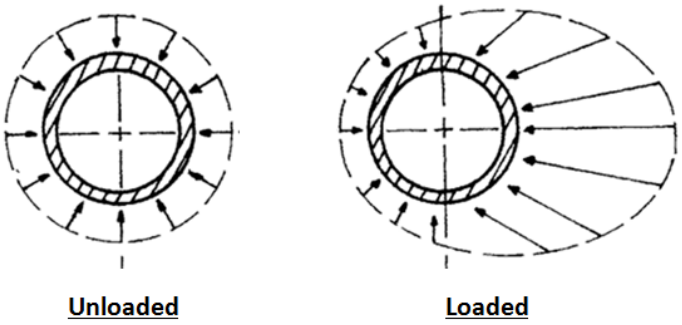

Figure 2.2: Distribution of soil stresses around the pile

A *p-y* curve is a representation of soil resistance that gives the magnitude of soil reaction force at a certain depth as a function of soil deflection due to lateral pile deflection. The terminology came after the use of plots of soil resistance force (*p*) as a function of the lateral deflection (y), see Figure 2.3.

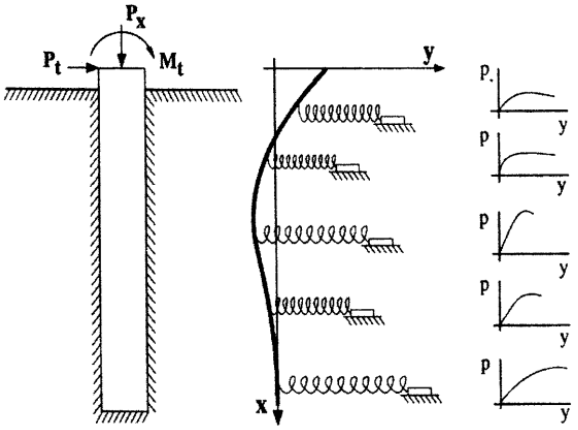

Figure 2.3. Illustration of the *p-y* curve concept

The *p-y* curve is initially straight and has a final flat portion at the ultimate resisting force. The initial portion is related to the initial soil modulus in the stress-strain curve. While the ultimate resistance p_{ult} is related to the soil strength in bearing mode. The *p-y* curve is affected by the type of loading: static, sustained (long-term), and cyclic loading. For NC clays, the soil resistance decreases under sustained loading due to consolidation. Under cyclic loading, degradation in the soil resistance may occur and should be accounted for prior to the use of *p-y* curves from the static case, especially for cohesive soils.

In the differential equation of pile-soil system, the *p-y* curve is used to determine the soil reaction (*p*). The differential equation for the system is solved using finite difference or finite element techniques with the appropriate boundary conditions. The boundary

conditions of the system depend on the type of loading (e.g. lateral force, moment loading), rotation at top of pile (fixed head, partially restrained, free head), and shear force at pile toe (whether its zero or certain value). Implementation of the *p-y* curves is found in software packages such as FB-MultiPier, LPILE, and COM624P.

Construction of p-y curves

Experimentally, the *p-y* curves can be obtained using strain gage (SG) data in instrumented piles (e.g. Matlock and Ripperger 1956). SG measurements are used to calculate the bending moment at points over the pile length. Bending moment as function of pile's length is found by a polynomial fit. By integrating the bending moment function, one can obtain the pile deflection (y) as a function of depth. Furthermore, the soil reaction (*p*) can be obtained by differentiating (twice) the bending moment function. Finally, using the *p* and y values at selected depths, a family of *p-y* curves is constructed. Reese and Cox (1969) presented a slightly different approach; they used the experimental data to obtain values for deflection, slope, bending moment, and shear force. Then they used the non-dimensional method by Matlock and Reese (1960) to solve for E_{py} as a function of depth. Also, a number of methods were proposed to construct *p-y* curves from in-situ tests, such as dilatometer (Robertson et al. 1989), cone penetrometer (Robertson et al. 1984), and pressuremeter (Ruesta and Townsend 1997).

p-y curves for clay

p-y curves for clays can have different shapes depending on the clay type (stiff, soft). The earliest method to obtain *p-y* curves for clays was proposed by McClelland and Focht (1956). This method was based on experimental studies and utilized the stress-strain data from triaxial tests for samples confined at the overburden pressure. The soil resistance was estimated using the maximum normal stress (in the stress-strain curve), and the corresponding soil deflection was estimated using the strain at corresponding stress level.

Later, Matlock (1970) proposed a method to obtain *p-y* curves for soft clays in presence of water. The *p-y* curve in this method is divided into three parts: initial straight portion, nonlinear portion, and final flat portion resembling the ultimate resistance p_u. This method requires soil properties such as undrained shear strength S_u and the strain at one half of maximum principal stress difference. The initial slope in the *p-y* curve can be determined from experiments or using suggested values. The nonlinear portion is constructed using Eq.9

$$\frac{p}{p_u} = 0.5\left(\frac{y}{y_{50}}\right)^{1/3} \qquad \text{Eq.9}$$

Where maximum value for *p* is reached at $y = 8y_{50}$, y_{50} is estimated as $y_{50} = 2.5\varepsilon_{50}b$, and p_u is the smallest value from Eq.10

$$p_u = \left[3 + \frac{\gamma'}{c} + \frac{J}{b} z\right] cb \qquad \text{Eq.10}$$

$$p_u = 9cb$$

The method also proposed modifications to the *p-y* curve for cyclic loading case to account for the loss in soil resistance. Figure 2.4 shows *p-y* curves for both cases of loading.

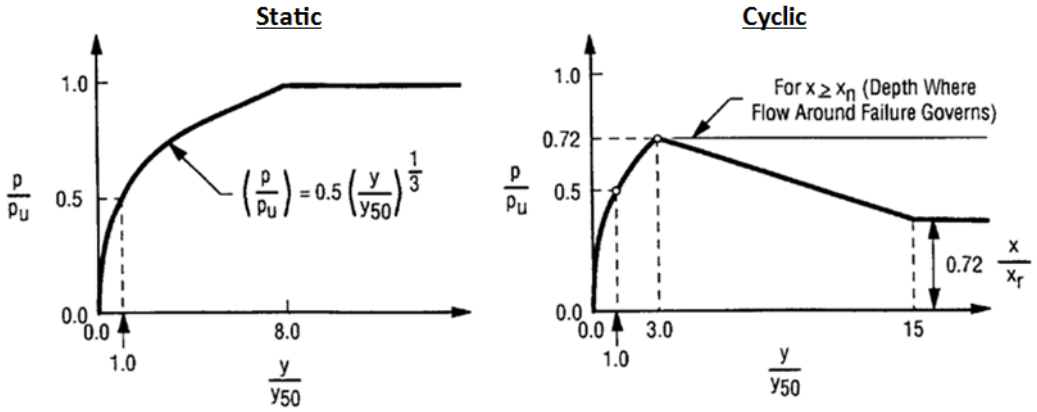

Figure 2.4. Characteristic *p-y* curves for static and cyclic loading for soft clay in water (Matlock 1970)

In a similar way, methods for construction of *p-y* curves for the cases of stiff clay in presence of water (Reese et al. 1975), and stiff clay with no water was proposed (Welch and Reese 1972; Reese and Welch 1975).

p-y curves for sands

The difference between sands and clay soil is that sands do not exhibit softening behavior at large deformations or under cyclic loading. Reese et al. (1974) proposed a procedure to construct *p-y* curves for sands. The strength of sand is estimated using the friction angle ϕ which can be determined in-situ or from triaxial tests. The *p-y* curve for sands is composed of 4 parts: initial sloping part, parabolic part, straight part, and final flat part at the ultimate soil resistance, see Figure 2.5. The slope of the initial part K_{py} is determined experimentally or from recommended values as in Reese et al. (2006). The parabolic part is determined using Eq. 11

$$p = \bar{C} y^{1/n} \ , \ \bar{C} = \frac{p_m}{y_m^{1/n}} \qquad \text{Eq.11}$$

Where p_m and y_m are defined next.

The straight part coming after the parabolic part is the line connecting between the two points with p values of

$$p_u = A_s p_s \quad \text{or} \quad p_u = A_c p_s$$
$$p_m = B_s p_s \quad \text{or} \quad p_m = B_c p_s \qquad \text{Eq.12}$$

Where A, B are non-dimensional constants accounts for the variation in the ultimate soil resistance with depth. The constants are determined from charts created for static load (lower case 's') and cyclic load cases (lower case 'c').

Finally, the flat part is determined by the ultimate soil resistance p_u given as the smaller of

$$p_s = \gamma z \left[\frac{K_0 \tan\phi \tan\beta}{\tan(\beta-\phi)\cos\alpha} + \frac{\tan\beta}{\tan(\beta-\phi)}(b + z\tan\beta\tan\alpha) + K_0 z \tan\beta(\tan\phi \sin\beta - \tan\alpha) - K_A b \right] \qquad \text{Eq.13}$$

$$p_s = K_A b\gamma z(\tan^8\beta - 1) + K_0 b\gamma z \tan\phi \tan^4\beta$$

Where γ is soil unit weight, z is the depth for *p-y* curve, ϕ is soil friction angle, $\beta = 45 + \frac{\phi}{2}$, b is pile size, α is defined as $\alpha = \frac{\phi}{2}$ for loose sand and $\alpha = \phi$ for dense sand, K_0, K_A are the at-rest and active coefficient of lateral earth pressure, respectively.

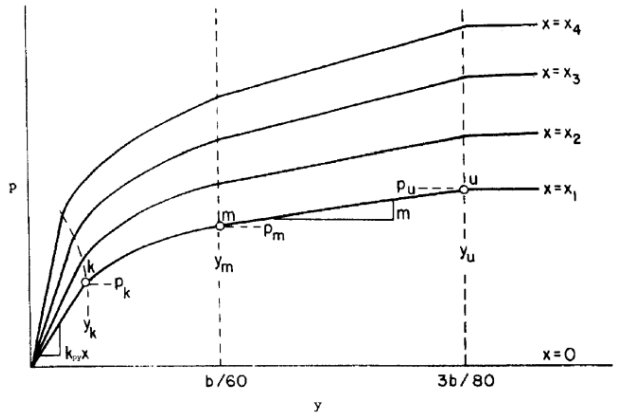

Figure 2.5. Construction of *p-y* curves for sand (Reese et al. 1974)

Comments on the p-y curve method

The advantage of the *p-y* curve approach over Winkler approach is that the nonlinearity of soil is incorporated. However, the *p-y* curve method has disadvantages such as (1) there is no coupling between adjacent *p-y* curves (i.e. the continuous nature of soil is omitted), (2) construction of *p-y* curve requires in-situ testing and (3) it has semi-empirical nature.

2.1.3 Elastic continuum solutions

Poulos (1980) obtained a solution for laterally loaded piles under static load treating the soil as an elastic continuum. The pile is assumed as thin rectangular vertical strip with

constant flexibility. Soil displacements were estimated using Mindlin's solution for horizontal displacement of a point within a semi-infinite mass caused by horizontal point load. The solution assumptions were (1) homogeneous, isotropic, elastic soil, (2) the soil pressure at any point does not exceed the ultimate pressure, (3) the shear stress at pile sides is neglected, (4) soil-pile separation is not considered. The solution starts with the following system of equations

$$\{y\} = \frac{D}{E_s}.[I].\{p\} \qquad \text{Eq.14}$$

Where $\{y\}$ is the column vector of soil displacements, D is pile diameter, E_s is soil modulus, $[I]$ is matrix of factors from Mindlin's solution, and $\{p\}$ is the column vector of horizontal load between soil and pile.

The previous equations are substituted in the beam differential equation. Then, the system of equations is solved using the finite difference technique. Poulos indicated that higher soil reactions that exceed the ultimate soil resistance developed near the top due to the elastic assumption. In that case, he suggested using iterations in the solution to ensure that the maximum soil reaction possible at any point don't exceed the ultimate resistance.

Later, Sun (1994) used the modified Vlasov model by Vallahban and Das (1991) for analysis of beams on elastic foundations and presented a numerical solution for laterally loaded piles. The soil in this model is considered homogeneous elastic continuum. The solution approach used variational calculus principles to obtain the differential equation for the pile-soil system. Soil displacements were assumed a function of radial distance from the pile. Sun compared his solution to the elastic solution by Poulos (1980), and showed an agreement between the two solutions with a slight difference. Sun's solution is powerful; however, it requires determination of several factors and moderate computational effort and is limited to single layered soils. Later, Basu et al. (2009) extended Sun's solution for single soil profile to multi-layer soil profile. They also improved Sun's solution by assuming different soil displacement fields in radial and angular directions.

In a similar approach to Sun (1994), Guo and Lee (2001) developed a closed form solution for laterally loaded piles in homogeneous elastic soil medium. Their approach differed from Sun's in the simplified stress field which ignored higher order stress components. Guo and Lee indicated that their solution excelled Sun's solution in its modeling accuracy for cases with Poisson's ratio greater than 0.3.

2.1.4 Strain wedge model

Developed by Norris (1986), the strain wedge (SW) model assumes that the pile is resisted by a 3-D passive soil wedge in front of it. The side friction on the sides is considered in this

model as part of the total lateral resistance. The model was improved later by Ashour et al. (1998) for multilayered soil, and to account for pile head conditions (i.e. fixed or free). It assumes that the soil in front of the pile is in similar conditions to triaxial test; in which the horizontal stress from the pile resembles the deviatoric stress in the triaxial test. The model parameters are horizontal soil strain, horizontal stress change, and the nonlinear soil modulus. These parameters are analogous to those used in the beam on elastic foundation solution: pile deflection (y), soil reaction force (*p*), and modulus of subgrade reaction (E_{py}). The geometry of passive wedge is characterized by the mobilized friction angle ϕ_m which evolves gradually with pile deflection until it reaches the maximum value of soil friction angle ϕ, see Figure 2.6.

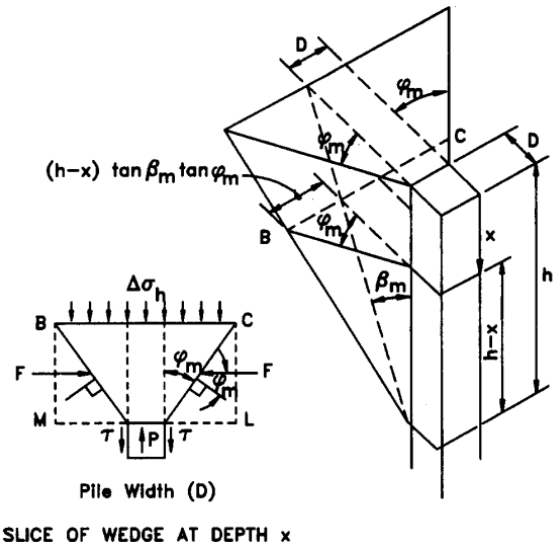

Figure 2.6. Illustration of the strain wedge concept (Ashour et al. 1998)

The main assumption in this model is the linear variation of pile deflection with depth. The depth of passive wedge is assumed initially and then determined by an iterative procedure. The SW model is also capable of solving the problem of multilayered soil by dividing the passive wedge into sublayers that can have different soil properties, see Figure 2.7.

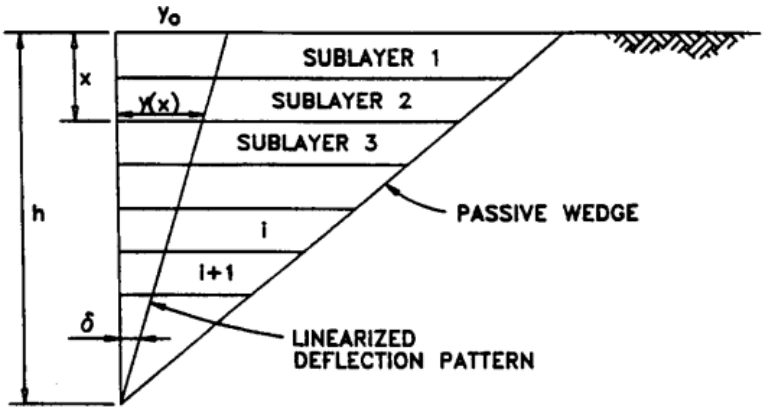

Figure 2.7. The passive wedge for multilayered soil in SW model (Ashour et al. 2004)

The procedure starts by determining the horizontal stress level (SL) from the strain using a power function which relates the stress level with axial strain. The function is normalized using ε_{50} which is the strain at 50% stress level (from stress-strain curve in triaxial test). SL is defined as the ratio of mobilized horizontal stress to the ultimate horizontal stress that the soil can carry. Using SL, one can determine the mobilized friction angle and the horizontal stress increase $\Delta\sigma_h$ from Eq.15 (assuming passive conditions for soil resistance)

$$SL = \frac{\Delta\sigma_h}{\Delta\sigma_{hf}} = \frac{\tan^2(45+\phi_m)-1}{\tan^2(45+\phi)-1} \qquad \text{Eq.15}$$

Where ϕ_m is the mobilized friction angle, $\Delta\sigma_h$ is the change in horizontal stress corresponding to ϕ_m, ϕ is the maximum friction angle for soil, $\Delta\sigma_{hf}$ is the maximum change in horizontal stress corresponding to the ultimate soil resistance (i.e. at maximum ϕ).

Estimation of ϕ_m from Eq.15 is for sands. For clay soil, the model assumes undrained conditions and further estimates the change in pore water pressure to find the effective stresses. The mobilized friction angle is found using Eq.16

$$\tan^2\left(45+\frac{(\bar{\phi}_m)_i}{2}\right) = \frac{(\bar{\sigma}_{vo}+\Delta\sigma_h-\Delta u)_i}{(\bar{\sigma}_{vo}-\Delta u)_i} \qquad \text{Eq.16}$$

Where $\bar{\sigma}_{vo}$ is the effective overburden stress, Δu is the excess pore water pressure.

The resistance force per unit length of pile is determined using Eq.17

$$p_i = (\Delta\sigma_h)_i \overline{BC}_i S_1 + 2\tau_i D S_2 \qquad \text{Eq.17}$$

Where $S_{1,2}$ are shape factors, τ is the shear stress on pile sides, D is pile size.

$\overline{BC}$ is given as (from geometry of the passive wedge, see Figure 2.6)

$$\overline{BC} = D + (h - x)2\tan\beta_m \tan\phi_m \qquad \text{Eq.18}$$

Where h is the passive wedge depth, x is the depth of soil segment, β_m is the base angle of passive wedge ($\beta_m = 45 + \phi_m / 2$).

Having p_i, $y_i (= [h - x_i] * \delta_i)$ estimated for each sub layer, the subgrade modulus E_s is determined as $E_s = p_i / y_i$.

The value of pile head load is estimated using equations as in Norris (1986) depending on pile head condition (i.e. free, fixed). Finally, profiles of pile deflection, soil reaction, and bending moment are determined.

Advantages of the SW model are it addresses the nonlinearity of soil reaction and the subgrade modulus. It is effective since it utilizes basic soil properties (ϕ , S_u, ε_{50}) that are easy to obtain. Another advantage for SW model over Winkler model is the interdependence of soil reactions between each soil segment within the wedge, which is achieved thru the total wedge depth (h). Furthermore, the model is capable of analyzing multi-layered soil. Ashour et al. (1998) indicated that SW model can be used to verify conventional *p-y* curves, since it defines its own parameters from the stress-strain curve from triaxial tests. He also pointed that no unique *p-y* curves for certain soil type exists due to several factors affecting the pile-soil problem. Ashour and Norris (2000) used the SW model and showed that different *p-y* curves can be obtained for same soil type. Their study concluded that the *p-y* curve, in addition to soil properties, is function of pile stiffness, pile head fixity, embedment depth of pile head, and pile cross section shape. The weaknesses of the SW model are (1) it is suitable only for statically loaded piles, (2) and it does not address the effect of pile-soil gapping.

2.2 Static lateral behavior of pile groups

The lateral behavior of piles in group differs than single pile due to the influence of the pile-soil-pile interaction. The soil resistance in case of pile groups is reduced due to the group effect, see Figure 2.8. The soil located within the overlapping zones of the stress bulb is subjected to additional stresses (compared to isolated single pile case). Also, movement of leading pile reduces the confining stress in behind it. Furthermore, soil gapping may occur due to pile movement away from the soil especially in cohesive soils. This combination of overlapping of stress zones along with gapping reduces the resistance of the pile in group configuration.

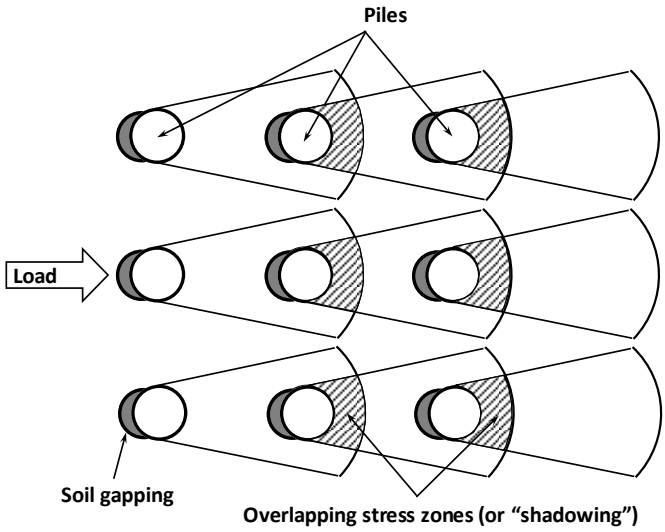

Figure 2.8. Illustration of the pile group effect

Poulos (1980) used his solution, assuming elastic soil continuum, to estimate the group effect using pile-soil-pile interaction factors. The interaction factor reflects the additional passive pile displacement due to active pile displacement. Plots of interaction factors for two-pile groups as function of spacing were presented for cases with different boundary conditions (e.g. fixed head, free head), and flexible/rigid piles. Variation of interaction factors with different parameters showed: (1) larger interaction effect for leading piles (in loading direction) compared to side piles, (2) decreasing interaction with higher slenderness ratio, (3) increasing interaction with higher pile stiffness, (4) increasing interaction with smaller pile spacing. Poulos indicated that the solution for two-pile group can be extended for pile groups with more than two piles, and the total displacement for a pile in group considering the group effect is found by superposition. For example, for a group with *n* piles subjected to horizontal load only, the deflection of pile *i* is estimated using Eq.19

$$u_i = u_0 \left[\sum_{i,j}^{n} \left(P_j * \alpha_{ij} \right) + P_i \right] \qquad \text{Eq.19}$$

where u_i is the total displacement of pile *i* in the group, u_0 is the unit displacement of single pile subjected to unit horizontal load, P_j is the load on pile *j*, P_i is the load on pile *i*, α_{ij} is the interaction factor between piles *i* and *j*.

Leung and Chow (1987) presented a semi-theoretical solution for pile groups considering the pile-soil-pile interaction. Their solution utilized the *p-y* curve approach for individual pile response. The pile is divided into segments and the stiffness matrix for single pile-soil system is determined. The pile-soil-pile interaction is estimated using Mindlin's solution,

and the soil displacement is assumed to be in the horizontal direction only. The total soil displacement at a node is estimated using Eq. 20

$$y_i = \sum_{j}^{n} f_{ij} * P_{sj} \qquad \text{Eq.20}$$

Where y_i is soil displacement at node *i*, f_{ij} is the flexibility factor for displacement at node *i* due to unit horizontal load at node *j*, P_{sj} is the horizontal force at node *j*.

The flexibility factors in the previous equation are obtained from Mindlin's equation for the influence of a unit horizontal point load in a homogeneous isotropic elastic half-space. The vector of soil displacements at all nodes in the group is found as in Eq.21

$$\{y_s\} = [F_s] * \{P_s\} \qquad \text{Eq.21}$$

Eq.21 is substituted in the force-deformation matrix of pile group system assuming (1) pile and soil displacements are equal, (2) pile force equals soil force but with a negative sign. The global load-displacement equations for the pile group-soil system is given as in Eq.22

$$\left([K_p] + [K_s]\right) * \{y_s\} = \{Q\} \qquad \text{Eq.22}$$

Where $K_{p,s}$ is the stiffness matrix for the pile and soil, respectively, y_s is the deflection of soil at pile nodes, Q is the vector of external horizontal forces.

Leung and Chow (1987) solution was in good match with Poulos (1980) solution. However, the first tends to overpredict pile shear force and bending moment at large deflections.

2.2.1 Strain wedge model for pile groups

Ashour et al. (2004) extended the single pile SW model and added the capability to solve for pile groups. The model extension accounts for the group effect by estimating the additional soil stresses due to the overlapping of passive soil wedges. This is achieved by determining the area of overlap for a pile's wedge with surrounding piles' wedges (Figure 2.9). The additional stresses from the surrounding piles result in larger deflection at certain load compared to the isolated pile case.

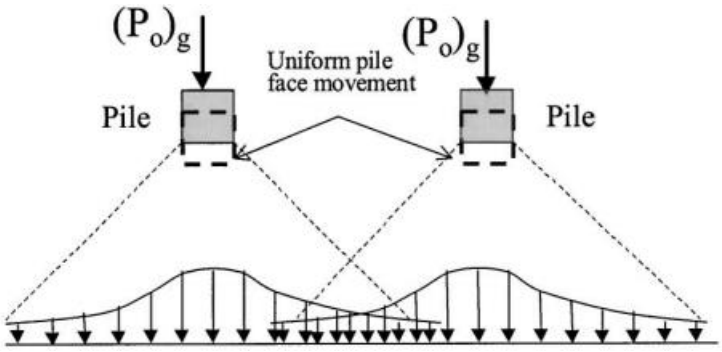

Figure 2.9. Soil wedge overlap in pile groups for SW model (Ashour et al. 2004)

The SW solution for pile groups starts by analyzing each pile in the group individually (Ashour et al. 1998). The overlapping between piles' wedges is determined from the resulted passive wedges geometry for all piles in the group. The increased stress level SL_g in the passive wedge for pile *i* in the group is estimated using the empirical relationship Eq. 23

$$\left(SL_g\right) = SL_i\left(1 + \sum R_j\right)^{1.5} \leq 1 \qquad \text{Eq.23}$$

Where SL_i is the stress level from single pile solution, R_j is the ratio between the length of overlapped portion of passive wedge face and the total length of the passive wedge face from neighboring pile *j*.

The final value of SL_g is determined by iterative procedure, and consequently a modified fanning angle (ϕ_m) is obtained for the pile group. The solution proceeds by constructing subgrade modulus profile over pile length which represents the influence of the group effect.

The advantage of SW model for pile groups is that it implicitly accounts for the group effect without using empirical factors such as *p*-multipliers which are applied to *p-y* curves for pile groups (see next section). Furthermore, the response of each pile in a group can be assessed individually and can be unique for each pile, unlike the *p*-multipliers approach which assumes similar response for all piles in the same row.

2.2.2 Pile groups behavior using p-multipliers

First introduced by Brown et al. (1987), the *p*-multiplier is a factor that modifies (softens) single pile *p-y* curve to obtain the *p-y* curve for a pile-in-group. The *p*-multiplier simplifies the design of pile groups by predicting their response using *p-y* curves for single piles. It is defined as the ratio of lateral load resisted by a pile-in-group and causes a certain deflection, to the lateral load resisted by isolated single pile at the same deflection, see Figure 2.10. The value of *p*-multiplier is less than or equal to unity.

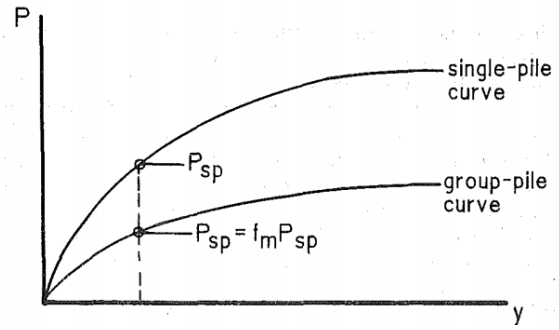

Figure 2.10. The *p*-multiplier concept (Brown et al. 1987)

The *p*-multiplier concept is analogous to the group efficiency factor (Poulos and Davis 1980), which is defined as ratio of the ultimate lateral capacity of a pile-in-group to the ultimate lateral capacity of an isolated single pile.

Several studies indicated that the *p*-multiplier in pile groups is a function of soil type, soil profile, pile spacing in both directions (longitudinal and transversal), pile location in the group (inside or outside pile), pile group deflection, and depth (e.g. Brown et al. 1988; McVay et al. 1998; Rao et al. 1998b; Patra and Pise 2001a; Rollins et al. 2005a; Ashour and Ardalan 2011). It should be noted that, in practice, the *p*-multipliers assumes a constant value over the pile length.

Table 2.1. Reported *p*-multipliers in literature

Reference	Group size	s/D	*p*-multipliers			Soil type
			Leading row	2nd row	Trailing row	
Brown et al. (1987)	3x3	3	0.7	0.6	0.5	clay
Brown et al. (1988)	3x3	3	0.8	0.4	0.3	sand
McVay et al. (1995)	3x5	3	0.8	0.4	0.3	dense sand
		3	0.65	0.45	0.3	loose sand
		5	1.0	0.85	0.7	sand
Ruesta et al. (1997)	4x4	3	0.8	0.3	0.3	sand
McVay et al. (1998)	3x3-3x7	3	0.8	0.4	0.3	sand
Rollins et al. (2003)	3x3	3	0.82	0.61	0.45	clay
		3.3	0.82	0.61	0.46-0.51	
		4.4	0.9	0.8	0.73	
		5.6	0.94	0.88	0.77	
Ilyas et al. (2004)	4x4		0.65	0.49	0.46	clay
Chandrasekaran et al. (2009)	3x3	3	0.61	0.41	0.44	clay
AASHTO (2012)	-	3	0.8	0.4	0.3	-
		5	1.0	0.85	0.7	-

In general, closer pile spacing in both directions leads to higher group interaction, and hence, smaller *p*-multiplier value. This was observed in experimental and numerical studies (e.g. Rao et al. 1998b; Chandrasekaran et al. 2009; Ashour and Ardalan 2011). In the same context, the group effect is larger for piles located in the interior columns of the group compared to the piles on the edges or corners. This is because a smaller number of piles participates in the overlapping of stress zones (e.g. Ruesta and Townsend 1997). Table 2.1 shows *p*-multipliers reported by a number of experimental studies. Figure 2.11 and Figure 2.12 show suggested values for *p*-multipliers at different pile spacing.

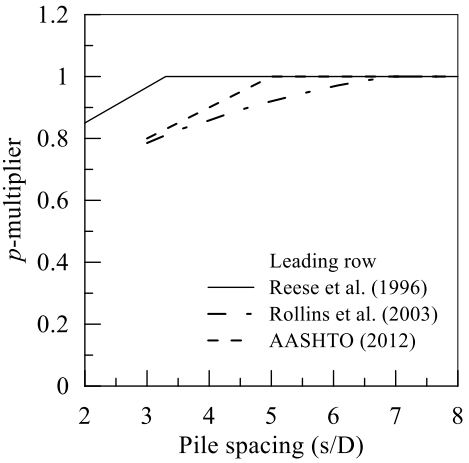

Figure 2.11. Suggested *p*-multiplier vs. pile spacing for the leading row

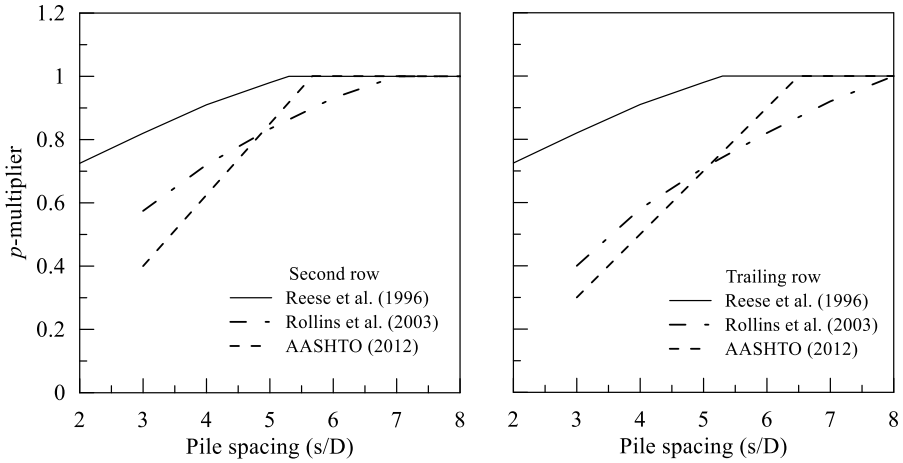

Figure 2.12. Suggested *p*-multiplier values for the trailing row with pile spacing

The influence of pile group deflection is related to the size of mobilized stress zones. At small deflections, the stress zones are not fully developed and minimal overlapping occurs. With increased deflection, the stress zones gradually continue to evolve so that the group interaction fully mobilizes. This is also noticed on the value of *p*-multipliers which start at values close to unity at low deflection, and gradually degrade with larger deflection (e.g.

Rollins et al. 1998; Ashour et al. 2004; Ashour and Ardalan 2011). Therefore, *p*-multiplier values at relatively small pile deflections might not be reliable for design purposes. The variation of *p*-multipliers with depth is also related to the size of stress zones. At greater depths, the stress zones are smaller and hence the influence of the group effect is less (e.g. Brown et al. 1988; Rao et al. 1998b).

The effect of group configuration is more evident in case of non-square groups (i.e. the number of rows and columns not equal). The lateral resistance of non-square pile group differs according to the direction of loading. This effect is clearly observed in case of pile groups in single line arrangement. The lateral resistance of such pile groups is larger when the loading direction is perpendicular to the line of arrangement (e.g. Rao et al. 1998b; Patra and Pise 2001a; Chandrasekaran et al. 2009). This is related to the size of mobilized soil zone and area of overlapped stress zones. For example, for a pile group in single line arrangement, the mobilized soil zone is wider when the direction of loading is perpendicular to the line of arrangement (Figure 2.13). Also, the group effect is smaller in this case of loading (perpendicular to the line of arrangement) compared to in-line loading direction due to smaller overlapped stress zones.

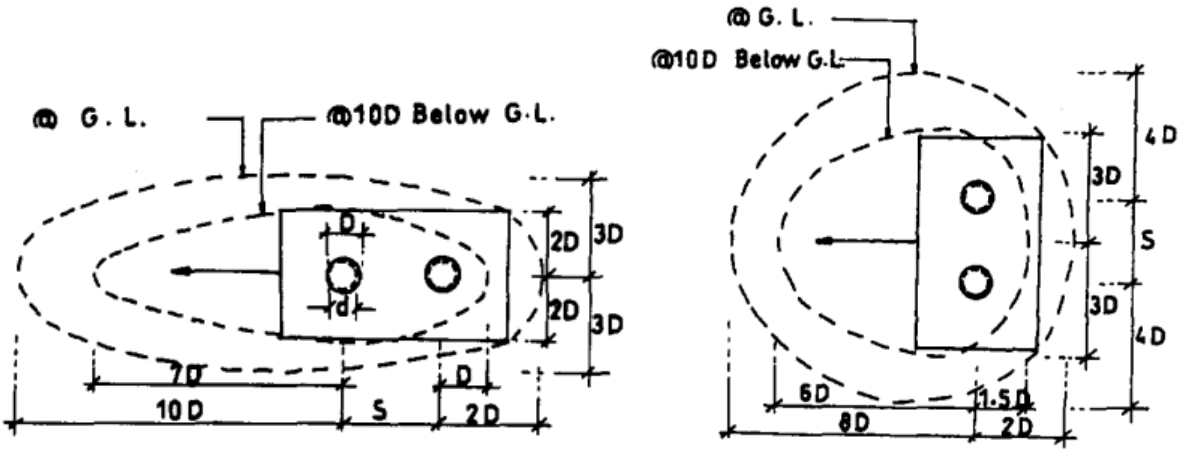

Figure 2.13. Stress zones around pile groups loaded in-line and transverse to piles arrangement line (Rao et al. 1998b)

2.3 Dynamic lateral behavior of single piles

The dynamic lateral behavior of piles differs than the static behavior in the inclusion of inertia and damping effects. The equation of motion for the pile considering the inertia effect and ignoring the pile's material damping is written as

$$EI\frac{d^4y}{dx^4} + \mu_p\ddot{y} + P_s(x,y) = Q(x) \qquad \text{Eq.24}$$

Where y is pile deflection, $\ddot{y}$ is the acceleration, μ_p is the mass per unit length of pile, EI is the flexural rigidity of the pile, $P_s(x,y)$ is the soil reaction per unit length, and $Q(x)$ is the external load acting on pile.

The soil reaction includes both the static and damping resistance. Assuming compatibility at the soil pile interface, the soil reaction is then a function of pile deflection and deflection rate. Neglecting the soil inertia, the equilibrium equation for the soil component is given as

$$P_s(x,y) - k(x)y - c(x)\dot{y} = 0 \qquad \text{Eq.25}$$

Where $\dot{y}$ is the deflection rate, $k(x)$ is the static soil stiffness, and $c(x)$ is the soil's viscous damping coefficient.

Substituting Eq.25 into Eq.24 gives the general equation of motion for the pile-soil system

$$EI\frac{d^4y}{dx^4} + \mu_p\ddot{y} + k(x)y + c(x)\dot{y} = Q(x) \qquad \text{Eq.26}$$

Eq.26 can be solved by assuming the pile under harmonic lateral excitation and solved in the frequency domain using the suitable boundary conditions. The lateral deflection of the pile (y) is assumed to be harmonic in the form $y(x,t) = y(x)\exp(i\omega t)$, in which ω is the cyclic frequency. Thus, the equation for the pile-soil system is rewritten

$$EI\frac{d^4y}{dx^4} + \left[k^*(x) + i\omega c(x) - \mu_p\omega^2\right]y(x,\omega) = Q(x) \qquad \text{Eq.27}$$

There are two types of soil damping considered in Eq.27: material (hysteretic) damping, and viscous (radiation) damping. The effect of material damping can be observed under cyclic load conditions, in which the damping ratio is estimated from the area enclosed by the hysteresis loop. Material damping is frequency independent and difficult to separate from the static material stiffness. Therefore, the static stiffness and material damping are usually combined and represented by the complex stiffness $k^* = k(1 + i\eta)$, where η is the hysteretic damping ratio. On the other hand, viscous damping is frequency dependent and can be modeled as a dashpot with its coefficient estimated by assuming that the radiation energy is fully absorbed by the dashpot.

There are two main approaches used in literature to solve the pile-soil system equations: continuum, and Winkler approach. the continuum approach considers the pile and soil as continuous domain and accounts for radiation damping. However, this approach neglects two main aspects of the problem: the soil plasticity and gap formation. The Winkler approach builds on Winkler's hypothesis by modeling the soil as a separate element with stiffness and damping properties.

Using the continuum approach, Novak (1974)) presented an approximate analytical solution for the lateral dynamic resistance of single piles. He assumed an infinite cylindrical pile embedded in an infinite soil cylinder. The cylinder is discretized into infinitesimal slices (circular discs) that extend to infinity in a plane strain condition. The dynamic soil reaction was obtained for the pile under harmonic motion considering the damping properties of the soil (material and radiation). The differential equation for the problem is then solved in the frequency domain. It was concluded from the solution that pile foundations have higher natural frequency than shallow foundations, and the dynamic stiffness and damping are insensitive to the vibration frequency for piles with slenderness ratio greater than 25. Later, Nogami and Novak (1977) used the same solution technique and presented analytical expressions for the dynamic soil reaction for piles subjected to vertical, horizontal, rotational, and torsional vibrations.

On the other hand, Winkler's approach has been used more often by researchers for it's ability to account for soil nonlinearity, damping, and gap formation. Gazetas and Dobry (1984) presented a simplified realistic method for estimating the lateral dynamic stiffness of piles. They solved the problem for fixed-head piles subjected to harmonic excitation. They assumed that the additional damping resistance only affects the magnitude of the static deflection pile while the deflected shape remains the same. They estimated the dynamic pile resistance by assuming a single spring (static stiffness) and dashpot (damping) at the top of the pile. The static spring stiffness is obtained using the established static approaches such as the *p-y* curve method. The overall dashpot constant was estimated from the material and radiation damping coefficients of soil. The overall dashpot constant was found by integrating over the pile length.

Nogami and Kanagai (1988) presented a time-domain solution for the dynamic lateral resistance of piles using Winkler's soil spring approach. They estimated the dynamic soil reaction by modeling the soil as series of springs and dashpots connected to a mass (Figure 2.14).

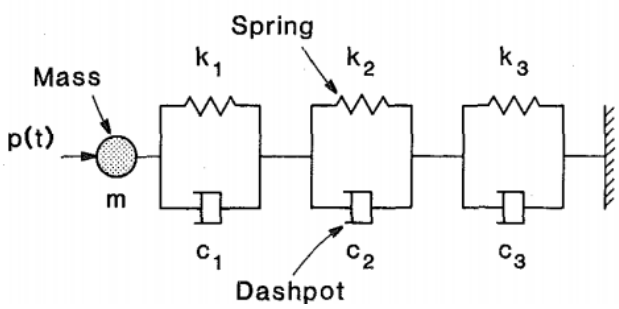

Figure 2.14. Illustration of the Winkler soil model by Nogami and Kanagai (1988)

In the figure, p(t) is the pile-soil interaction force, m_s represents the mass of soil element, k_n is the spring stiffness, c_n is the dashpot coefficient. The dynamic soil reaction at time t_i is estimated as

$$p_i = m_s \ddot{u}_i + k u_i + d_i \qquad \text{Eq.28}$$

Where $m_s \ddot{u}_i$ is the inertial resistance of the soil element, $k u_i$ is the increment in soil resistance from the spring and dashpot combined, d_i is the mobilized soil reaction from the previous time steps.

The pile-soil domain is divided into slices and the beam differential equation for the pile combined with Eq.28 is solved in time using numerical integration scheme.

Later, Nogami et al. (1992) built on and improved the solution by Nogami and Konagai (1988). They divided the soil model into two elements: near field (accounting for the nonlinear soil behavior near the pile) and far field (accounting for the elastic behavior and damping away from the pile). Additionally, they introduced an interface model to account for the gap formation (Figure 2.15). El-Naggar and Novak (1996), used the concept from Nogami et al. (1992) by assuming the soil model comprised of inner and outer field elements. For the inner field element, they used the solution by Novak and Sheta (1980) for the stiffness of the nonlinear spring, while for the outer field they used the solution from Novak (1974). They also accounted for the soil gapping by introducing separate elements for the front and back of the pile with the use of no tension springs. Using El-Naggar and Novak (1996) model and regression analysis, El-Naggar and Bentley (2000) proposed a simplified formula for the dynamic soil resistance (dynamic *p-y* curves) as a function of the static reaction and load frequency

$$P_d = P_s \left[\alpha + \beta a_o^2 + \kappa a_o \left(\frac{\omega y}{d} \right)^n \right] \qquad \text{Eq.29}$$

Where P_d, P_s are the dynamic and static soil reactions, a_o is the dimensionless frequency, y is pile deflection, d is pile diameter, α, β, κ, n are fitting parameters.

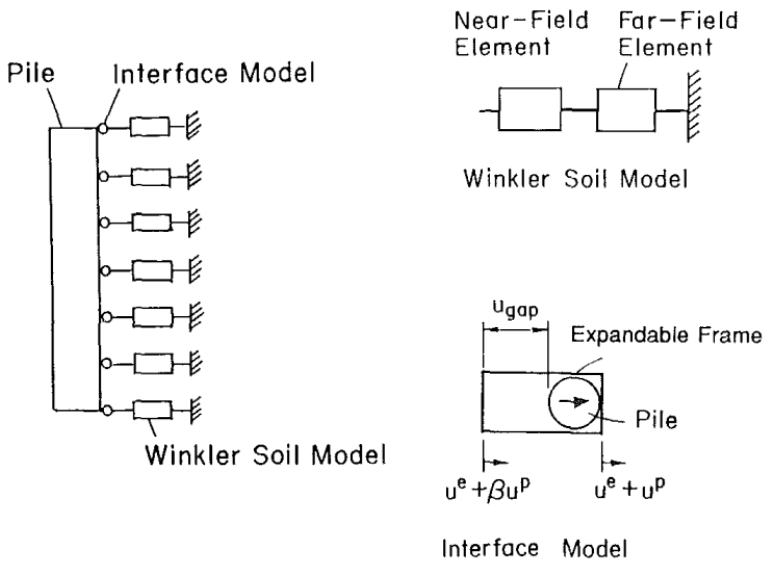

Figure 2.15. Illustration of the pile-soil model by Nogami et al. (1992)

The value of P_d in the equation is limited to the ultimate soil resistance that can be estimated using one of the established methods (e.g. Matlock 1970). Validations of the dynamic *p-y* curve model showed that the model works better with loading frequencies greater than 4 Hz where the dynamic effects are more prominent.

In summary, the dynamic lateral behavior of piles requires additional considerations over the static behavior for the influence of pile and soil inertia, and soil damping. The inertial effects are incorporated by adding the inertia terms for the mass of pile and soil elements in the beam differential equation. Soil damping influences the pile behavior by two mechanisms: hysteretic soil behavior or material damping, and radiation damping. Material damping is accounted for by using the complex form for the soil stiffness and is considered frequency independent. The radiation damping accounts for the energy dissipation at the far region from the pile.

2.4 Dynamic lateral behavior of pile groups

In addition to the group effect from the static behavior, the dynamic lateral behavior of pile groups is influenced by the stress waves emitted from the source piles. The problem was approached in several ways such as the analytical solution (Kaynia and Kausel 1991), dynamic interaction factors based on analytical solutions (Dobry and Gazetas 1988; Gazetas et al. 1991; Makris and Gazetas 1992; Mylonakis and Gazetas 1999), dynamic interaction factors based on Winkler soil model (El Naggar and Novak 1996; e.g. Mostafa and El Naggar 2002).

Kaynia and Kausel (1991) presented a rigorous numerical solution for the dynamic resistance of pile groups. The solution was used to evaluate the validity of the superposition assumption and the dynamic interaction factors for pile groups. The dynamic

interaction factor is defined as the ratio of the displacement of the passive pile due to the dynamically loaded active pile to the displacement of the pile under static load (Gazetas et al., 1991). One of the interesting conclusions from the study was that piles closer to the center of the footing carry the largest share of loading. The study also indicated that the dynamic pile group behavior is highly frequency dependent, and the superposition assumption is valid for low-frequency dynamic loads.

Dobry and Gazetas (1988) defined the dynamic interaction factor as the ratio of the displacement of the passive pile due to the active pile motion to the displacement of the active pile under dynamic loading. They assumed that the stress waves over the length of the source pile are emanated at the same time (i.e. no phase lag) and travels away from the pile's axis in a cylindrical fashion. The displacement field from the source pile periphery was estimated using the wave equation

$$y(r) \cong A\frac{1}{\sqrt{r}}\exp\left(-\frac{\beta\omega r}{V_s}\right)\exp\left[i\omega\left(t-\frac{r}{V_s}\right)\right] \qquad \text{Eq.30}$$

Where A is the displacement amplitude at the source, r is the radial distance from the pile axis, β is the damping ratio, V_s is the shear wave velocity.

The dynamic interaction factor was found as the ratio of the displacement at the passive pile located at a radial distance (r) to the displacement at the source pile using radial distance ($r = 0$). The dynamic interaction factors were found for the cases of two piles in-line ($\theta = 0$) and side-by-side ($\theta = 90°$) and interpolated for the cases of piles located at angles ($0 < \theta < 90°$). Later, Gazetas et al. (1991) presented plots for the dynamic interaction factors using Dobry and Gazetas (1988) solution. The dynamic interaction factors were in complex form, and were influenced by frequency, piles spacing, damping ratio, and pile-soil stiffness ratio.

In a similar approach, Makris and Gazetas (1992) obtained an expression for the dynamic interaction factors using the solution for the equation of motion in the frequency domain. Mylonakis and Gazetas (1999) followed the same approach by Makris and Gazetas (1992) to obtain the dynamic interaction factors. The difference in their solution was in the displacement field functions for the source pile and the receiver pile, respectively.

El Naggar and Novak (1996) used a slightly different approach by modeling the pile-pile interaction using a viscoelastic spring. They used the expression of the attenuation function from Dobry and Gazetas (1988) to estimate the displacement at the passive pile due to the displacement of the active pile. The group interaction force is then added to the equation of motion in the outer field element and the system of equations is solved for two piles (Figure 2.16).

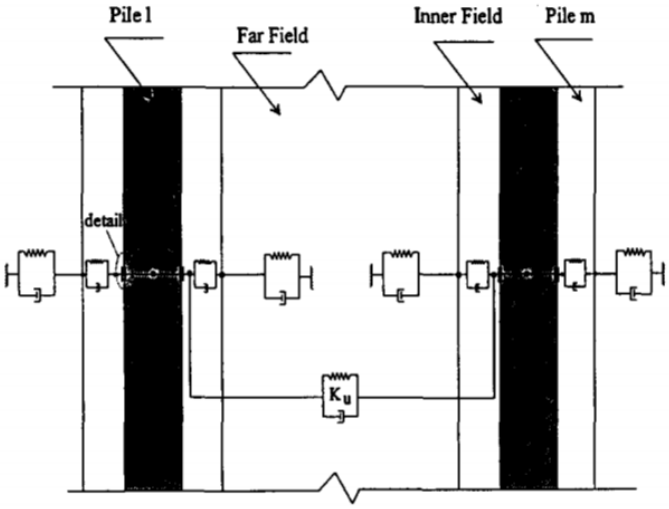

Figure 2.16. Viscoelastic spring model for pile group interaction (El Naggar and Novak 1996)

Mostafa and El Naggar (2002) attempted to extend the *p*-multiplier concept for the dynamic behavior of pile groups. They conducted a parametric study using the dynamic *p-y* curve formula by El Naggar and Bently (2000) and investigated the influence of several parameters on the *p*-multipliers, and concluded that the *p*-multipliers increase with increased pile spacing, deflection, stiffness ratio, and pile size. They also found that pile installation method and head-fixity condition have major influence on the *p*-multipliers.

Chapter 3. Methodology

3.1 Finite element modeling

The three-dimensional (3-D) finite element (FE) method is used in this study to simulate the lateral behavior of pile groups. This method allows modeling and analyzing complex engineering problems that are not possible to solve using traditional methods. Some of the advantages of the FE method are

- Ability to model linear or nonlinear material response,
- Ability to include more than one material type in the same problem,
- Ability to include surface-to-surface interaction between different geometries,
- Ability to solve static or dynamic problems,
- Ability to perform parametric studies,
- theoretically, no limits for the problem size

However, there are some limitations for the FE method such as it requires strong knowledge and expertise in the numerical methods, the output is highly dependent on the modeling choices by the user, and it requires a long time to solve large size problems.

For the current study, the choice of 3-D FE is based on necessity. The pile-soil-pile interaction is essentially a 3-D problem in which the surrounding piles influence the lateral response of the pile in interest. Also, the pile- pile spacing is a major factor in the pile-soil-pile interaction problem and can be varied in two directions (i.e. row spacing and column spacing).

The components of the FE modeling can be summarized as:

- problem geometry
- materials constitutive model
- loads
- boundary conditions
- interface behavior

These components are described in detail in the following sections.

3.1.1 Geometry

The FE model geometry is the first step in the FE simulation and is considered the basis for creating the FE mesh for the object. The input geometry for the current study has two main parts: pile group part, and soil body part (Figure 3.1). Owing to the symmetry of the problem, only half of the pile group and soil body is considered in the FE model. The pile group part is composed of the pile cap and a set of piles (in 4x2 or 4x3 arrangement) which are either vertical or battered. The dimensions of the pile group model follow the design of the M19 pier foundation of the I-10 twin span bridge. Each pile has a square

cross-section with 3 ft width and is 110 ft long. The pile to pile spacing will vary throughout the study parts and will be mentioned later in the discussion and results section. The pile cap is 7 ft thick and has varying planar dimensions depending on the pile to pile spacing.

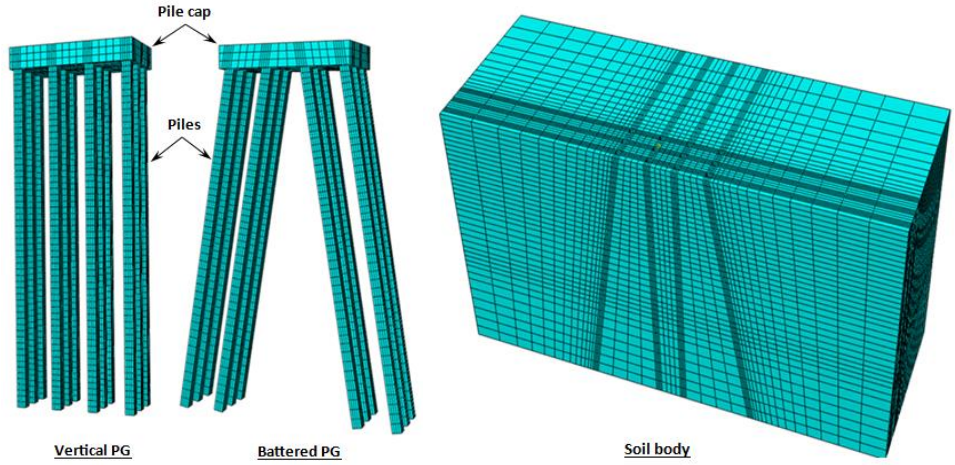

Figure 3.1. Example of pile group and soil body FE models

The soil body part is a solid block with cutout holes for each pile. It should be noted that pile installation effects are ignored in the current study. The soil body can be treated as a single layer or multiple layers. A multiple layer soil body has planar divisions (in the global horizontal direction) for each soil layer and assumes full bond between different layers at the interface. Each layer can be assigned with different constitutive model and parameters. The dimensions of the soil body vary depending on the pile to pile spacing and are determined by finding the least dimension at which the deformation in the boundary elements is negligible.

Another special pile group model is used in the study to obtain the soil resistance for single piles. This model is composed of three piles: vertical, negative battered, and positive battered (Figure 3.2). The pile to pile spacing at the pile cap level is 10D (D is the pile width), which is considered as large enough to eliminate pile-soil-pile interaction. The pile's behavior in this model is assumed as the equivalent for an isolated single vertical or battered pile. The reasons for using this model is to closely simulate the fixed head pile condition in a similar way to the pile group, and save time by running single model to obtain results for three single pile cases.

3.1.2 Load

Two types of load are applied in the FE model: gravity load, and lateral load. In the initial state, the gravity load (i.e. self-weight) is in equilibrium with the stresses in the soil. initializing the soil stresses is necessary because the stiffness in the AMCC and DP models exists only under confining stress. The initial equilibrium is achieved by applying the gravity load and a predefined stress field in the soil (i.e. geostatic stress). Then, a

dummy static step is performed. An acceptable equilibrium state is obtained once the deformation in the soil body due to the gravity load is negligible. The gravity load is defined by providing the gravitational acceleration (g = 32.2 ft/s^2), the density for all materials, and the direction which is the global vertical direction (z-dir), see Figure 3.3.

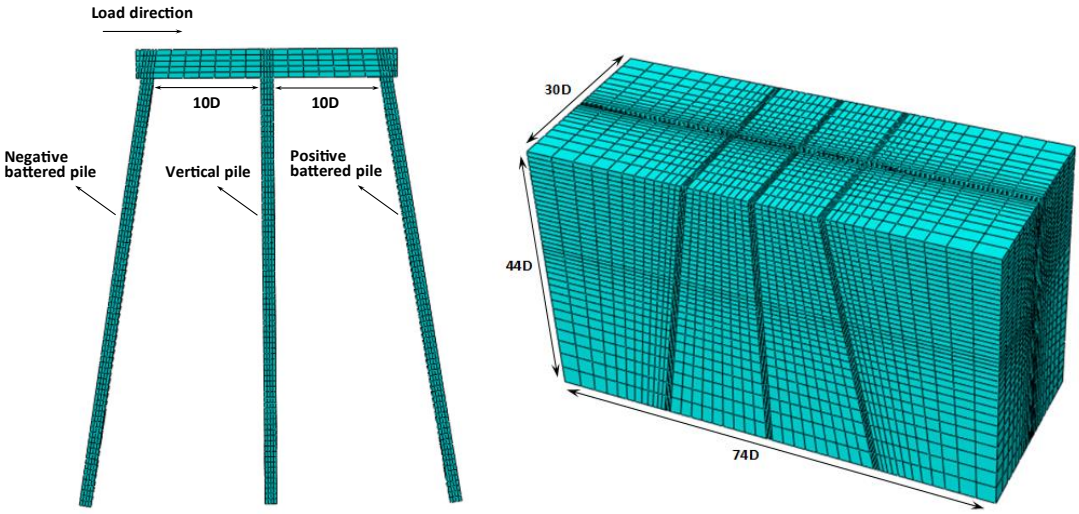

Figure 3.2. Special pile group model for single pile results

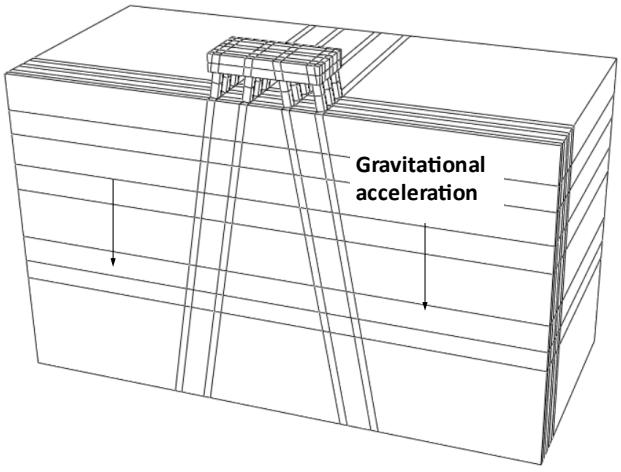

Figure 3.3. Direction of gravity load

The lateral load is applied at the side of the pile cap to produce lateral deformation. It is defined as uniform distributed area load and is assumed in the global horizontal direction parallel to the symmetry plane, see Figure 3.4.

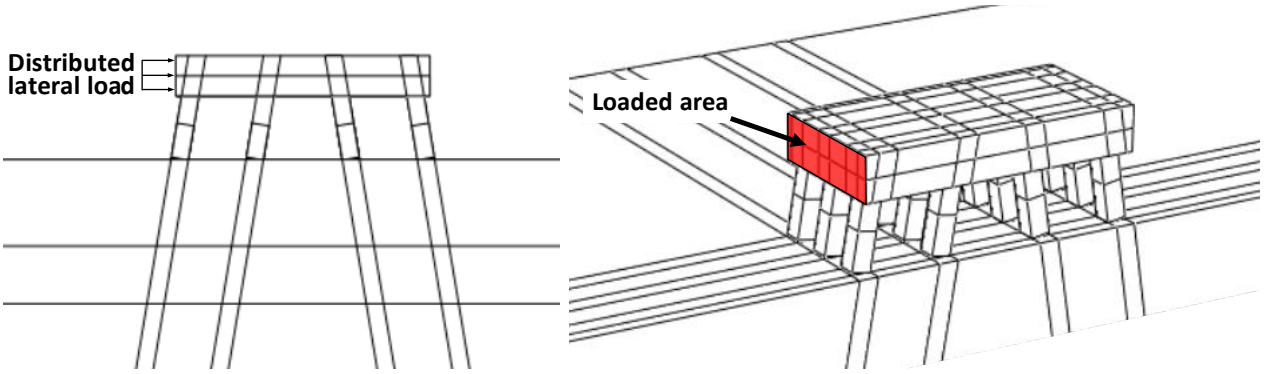

Figure 3.4. The lateral load applied as uniform distributed load

3.1.3 Boundary conditions

The global static equilibrium in the FE model is enforced by applying boundary conditions. The boundary conditions are displacement constraints used on the soil body boundaries and on the symmetry plane, see Figure 3.5. The pin-type boundary condition was used for the far boundaries to restrain the displacement in all directions. The roller-type boundary condition was used for the symmetry plane, which constrains the displacement in one axis and the rotations on the other axes. For example, a roller-type boundary condition for the x-direction restrains the displacement in the x-direction and rotations in the y- and z-directions.

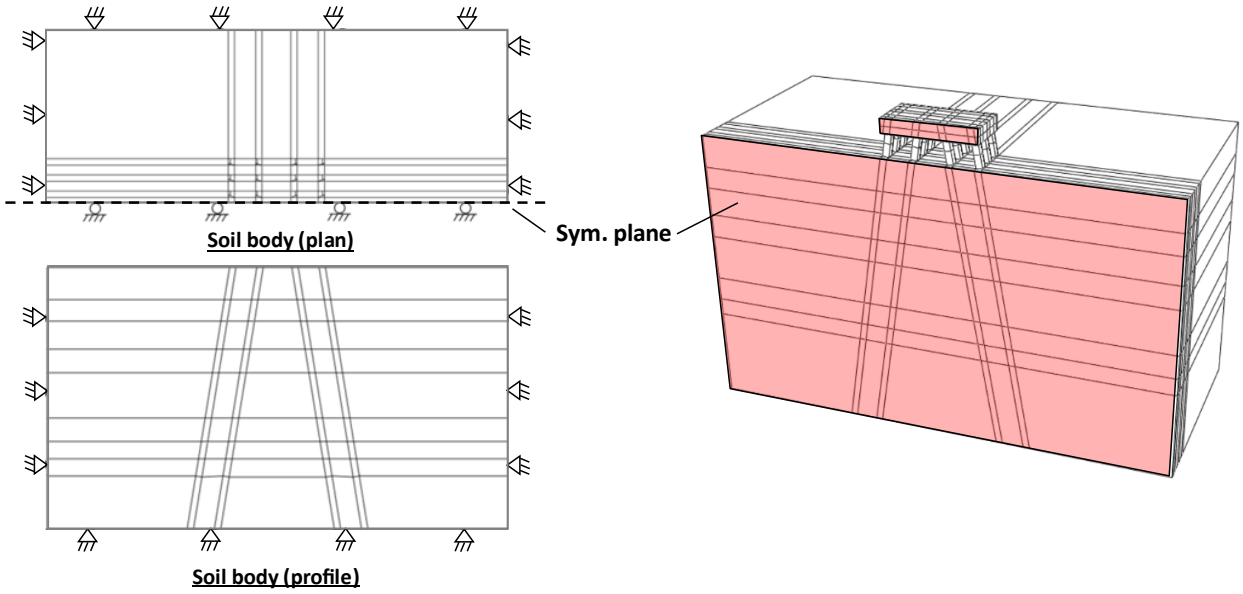

Figure 3.5. Displacement boundary conditions used for the soil model

3.1.4 Pile-soil interface model

The pile-soil interface is modeled using the contact feature in Abaqus. There are two main mechanisms at the interface that is considered: the normal (to surface) behavior, and the

tangential behavior, see Figure 3.6. The normal behavior refers to the interaction between the pile and soil in the direction of surface normal, which comes in the form of separation or interpenetration. For the pile-soil problem, the normal behavior should allow separation (i.e. the tensile stress is not transmitted to the soil, and hence pile-soil gap forms), and prevent interpenetration (i.e. on pile movement, bearing stress is transmitted and the soil moves at equal distance). The normal behavior as mentioned before is referred to as “hard contact”. The magnitude of the normal stress is found by an iterative numerical procedure, which determines the global equilibrium state after an increment of pile displacement.

The tangential behavior refers to the interaction in the direction parallel to the pile-soil surface, which comes in the form of sticking or sliding (Figure 3.6). For the pile-soil problem, the tangential behavior in sticking mode transfers the shear stress to the soil with no relative pile-soil displacement. In sliding mode, the transferred shear stress is limited to the maximum limit with the occurrence of relative pile-soil displacement. The maximum shear stress limit for sliding (τ_{lim}) is governed by the Coulomb friction criteria characterized by the friction coefficient (μ) and the user defined ultimate friction stress (τ_{max}) (Figure 3.6). The Coulomb friction criteria defined the limit as $\tau_c = \mu\sigma_n$, where σ_n is the mean stress at the interface, μ is the coefficient of friction ($= \tan\frac{2}{3}\phi$), and ϕ is the friction angle of soil.

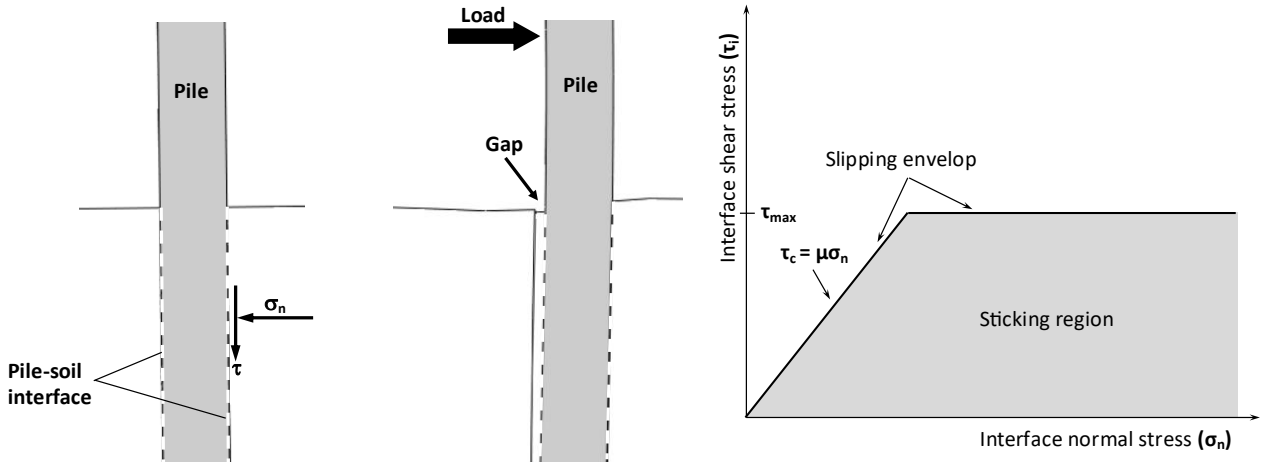

Figure 3.6. Illustration of the pile-soil interface model

3.1.5 Steel reinforcement model

The concrete piles have main steel reinforcement (or rebars) in the form of prestressed steel strands. Each strand has 0.6-inch diameter and made of low relaxation Grade 270 steel wires (ASTM A416). In 3-D FE, rebars geometry can be represented by either beam (line) elements (for individual rebars) or shell elements (for rebars layers). The interaction between rebars elements and concrete elements is modeled using the embedded elements technique (Abaqus 2011). In this technique, the nodes of the embedded (rebars)

elements are tied to the host (concrete) elements nodes. Another advantage of the embedded elements technique is the ability to define the prestress force in rebars elements. The prestress force enforces an initial state of compression in the concrete elements, which eliminates the possibility of premature concrete failure in tension. The structural behavior of the embedded shell elements also mimics the behavior of individual rebars, which only carries axial forces (Abaqus 2011). The actual prestress force magnitude (35.1 kips per rebar) is estimated following AASHTO bridges design standards and considering 20% prestress loss from the design value. Figure 3.7 shows the rebars FE model and pile section detail. Each shell layer resembles nine strands for a total of 36 strands in the pile's section. The layers are positioned at 3 inches from the pile's faces.

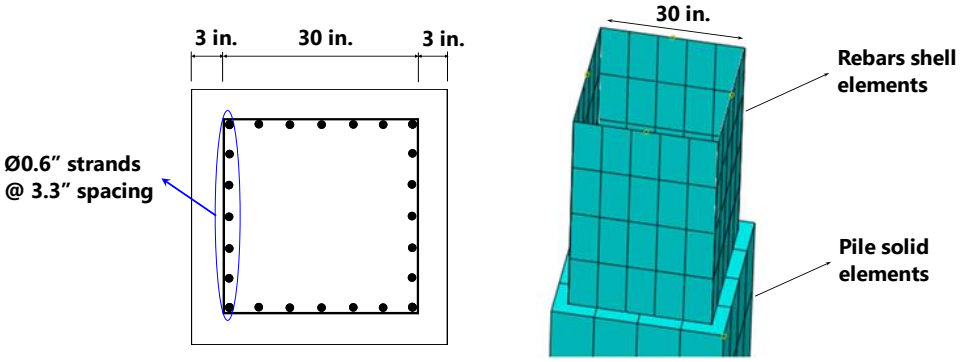

Figure 3.7. Illustration of pile's section detail and rebars FE model

3.2 Material constitutive models

One of the advantages of the FE method is the ability to simulate various types of materials behavior. This is achieved by defining the constitutive model for each material, which governs the stress-strain material response at the element level. The constitutive model is based on a mathematical function that relates the stress rate to the strain rate.

In the following sections, the material constitutive models used in the FE simulation are discussed in details. The materials and their corresponding constitutive law are summarized here:

Material		Constitutive model
Concrete	→	Concrete damaged plasticity
Steel	→	von Mises
Clay	→	Anisotropic Modified Camclay
Sand	→	Drucker-Prager

3.2.1 Concrete

The concrete nonlinear behavior is modeled using the concrete damaged plasticity model (CDP). This model is plasticity based and features distinct material behavior in tension and

compression. The distinction in the concrete's tensile and compressive behavior is necessary due to the large contrast in the tensile and compressive concrete strength (typically $\frac{f_c'}{f_t'} \approx 10$). Also, CDP model applies damage to the concrete material (i.e. reduction in the concrete elastic modulus) once failure (in tension) or yielding (in compression) is exceeded.

In damage mechanics, the effective stress ($\bar{\sigma}$) is obtained from Cauchy stress (σ) using the scalar damage variable d as

$$\bar{\sigma} = (1 - d)\sigma \qquad \text{Eq.31}$$

The effective stress is essentially used in the yield and the plastic potential functions for plasticity calculations. Numerically, the damage effect is applied to the elastic stiffness

$$D^{el} = (1 - d)D_0^{el} \qquad \text{Eq.32}$$

Where $\mathrm{D^{el}}$ and $\mathrm{D_0^{el}}$ are the damaged and undamaged elastic stiffness, respectively.

The elastoplastic stress-strain relation with damage is given by

$$\bar{\sigma} = D^{el}(\varepsilon - \varepsilon^{pl}) \qquad \text{Eq.33}$$

Where σ is Cauchy stress, $\varepsilon \text{ and } \varepsilon^{\mathrm{pl}}$ are the total and plastic strains, respectively.

The damage variable d is a function of two distinct damage variables for tension d_t and compression d_c. For multiaxial conditions, it is estimated from the damage variables d_t and d_c using the multiaxial stress factor r

$$(1 - d) = \big(1 - d_t.(1 - w_t.r)\big).(1 - d_c.(1 - w_c.r))$$
$$r(\sigma) = \frac{\sum_1^3 \langle \sigma_i \rangle}{\sum_1^3 |\sigma_i|} \qquad \text{Eq.34}$$

Where $\langle\ \rangle$ are the Macauley brackets, $\mathrm{w_t}$ and $\mathrm{w_c}$ are weight factors ($\mathrm{w_t}$=0, $\mathrm{w_c}$=1 are assumed).

The damage variables d_t and d_c in the CDP model are function of plastic strains ($\varepsilon_t^{pl}, \varepsilon_c^{pl}$), and assume values in the range ($0 \leq d \leq 1$). These variables are usually determined from extensive experimental tests on concrete, but unfortunately are not available for the current study. Therefore, concrete models in literature are used to obtain the damage variables versus strain, see Figure 3.8 (Mander et al. 1988; Jankowiak and Lodygowski 2005; Cicekli et al. 2007).

In the tension zone, the model assumes linear elastic behavior up to the failure stress σ_{to} (i.e. onset of cracking in concrete), and then followed by gradual softening in the plastic zone; this softening behavior is called tension stiffening. Tension stiffening refers to the region of interaction between the concrete and steel reinforcement during crack progression in tension (e.g. Gupta and Maestrini 1990). For the CDP model, tension stiffening is defined by providing values of the post failure stress (i.e. $\sigma > \sigma_{to}$) as a function of the cracking strain (ε_t^{ck}). The cracking strain is estimated from the total strain (ε_t) and the elastic strain as in Eq. 36

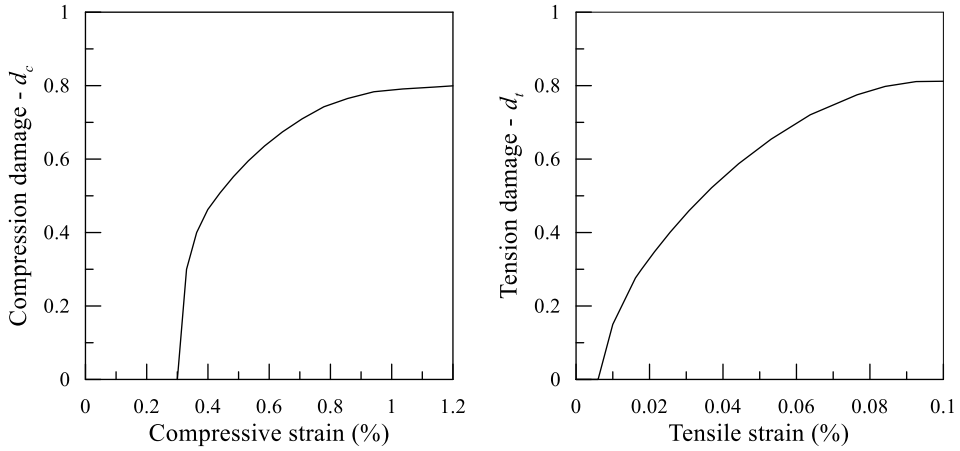

Figure 3.8. Compression damage and tension damage variables versus strain

$$\varepsilon_t^{ck} = \varepsilon_t - \varepsilon_{0t}^{el} \quad \text{Eq.35}$$

Where ε_{0t}^{el} is the elastic strain for the undamaged concrete material ($\varepsilon_{0t}^{el} = [D_0^{el}]^{-1} : \sigma_t$).

The tensile plastic strain ε_t^{pl} necessary for plasticity calculations are obtained as follows

$$\varepsilon_t^{pl} = \varepsilon_t^{ck} - \frac{d_t}{(1-d_t)}\varepsilon_{0t}^{el} \quad \text{Eq.36}$$

The cracking strain ε_{t0}^{ck} at the failure tensile stress σ_{to} is estimated from the tensile concrete strength and the elastic modulus as

$$\varepsilon_{t0}^{ck} = \frac{f_t'}{E_0} \quad \text{Eq.37}$$

Where f_t' is the concrete tensile strength ($f_t' = 7.5\sqrt{f_c'}$), E_0 is the undamaged elastic concrete stiffness ($E_0 = 57000\sqrt{f_c'}$), and f_c' is the concrete compressive strength which was 8000 psi.

The stress-strain curve for the tension stiffening region was obtained following Gupta and Maesterini (1990). In their work, they proposed a model for the tensile stress-strain curve in concrete. The model defines a dimensionless stress-strain curve which is converted to a true stress-strain curve using the reinforced concrete section properties such as the tensile strength of concrete, the yield stress of steel, the yield strain of steel, and the reinforcement ratio. The resulted curve used in the current is shown in Figure 3.10b.

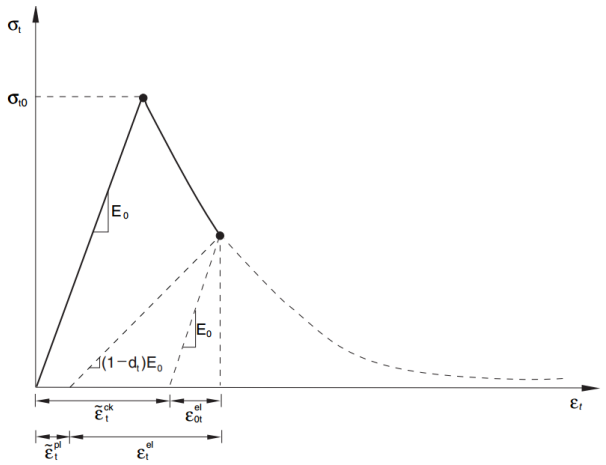

Figure 3.9. Illustration of concrete stress strain curve in tension region, and definition of tensile strains (Abaqus 2011)

In compression, the model assumes linear elastic behavior up to the initial yield stress σ_{co}. In the plastic region, the response exhibits some hardening up to the ultimate compressive strength σ_{cu} followed by softening. The stress-strain curve in for the compression region is obtained using the analytical model by Mander et al. (1988), and following the work of Pam and Park (1990) for prestressed concrete piles. Complete details regarding the concrete model in compression can be found in the aforementioned references. The resulted stress-strain curve for compression zone is shown in Figure 3.10a.

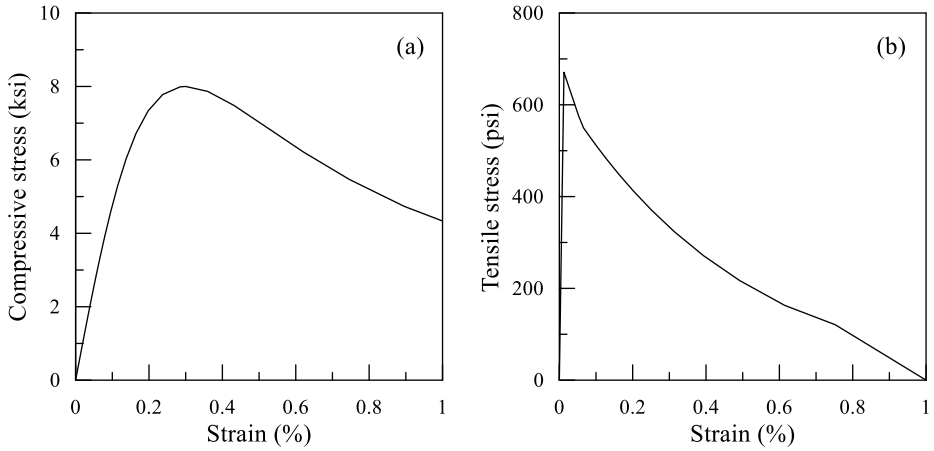

Figure 3.10. Stress-strain curves in (a) compression, and (b) tension

In a similar way to the tension region, the compressive stress values are provided as function of inelastic strain (ε_c^{in}), where the inelastic strain is obtained from the total (ε_c) and elastic strains as

$$\varepsilon_c^{in} = \varepsilon_c \ - \varepsilon_{0c}^{el} \qquad \text{Eq.38}$$

Where $\varepsilon_{0c}^{\mathrm{el}}$ is the elastic strain for the undamaged concrete material ($\varepsilon_{0c}^{el} = [D_0^{el}]^{-1} : \sigma_c$).

The plastic compressive strain is calculated from the inelastic strain as follows (Figure 3.11)

$$\varepsilon_c^{pl} = \varepsilon_c^{in} - \frac{d_c}{(1-d_c)}\varepsilon_{0c}^{el} \qquad \text{Eq.39}$$

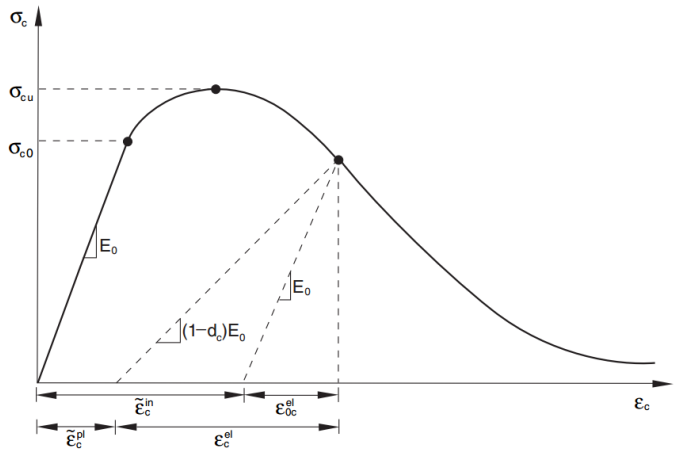

Figure 3.11. Illustration of concrete stress strain curve in compression region, and definition of compressive strains (Abaqus 2011)

The yield function for the CDP model is the one proposed by Lubliner et al. (1989) with some modifications by Lee and Fenves (1998) for the evolution of strength in tension and compression. The function is given in terms of effective stress values

$$f = \frac{1}{1-\alpha}[\bar{q} - 3\alpha\bar{p} + \beta\langle\hat{\sigma}_{max}\rangle - \gamma\langle-\hat{\sigma}_{max}\rangle] - \bar{\sigma}_c \qquad \text{Eq.40}$$

Where $\bar{q}$ is the deviatoric component of the effective stress, $\bar{p}$ is the hydrostatic component of the effective stress, α and γ are material constants, $\hat{\sigma}_{max}$ is the maximum principal stress, and β is

$$\beta = \frac{\bar{\sigma}_c}{\bar{\sigma}_t}(1-\alpha) - (1+\alpha) \qquad \text{Eq.41}$$

Where $\bar{\sigma}_t$ and $\bar{\sigma}_c$ are the effective tensile and compressive cohesion stress, respectively.

The model assumes a non-associative flow rule for the calculations of the plastic strain rate

$$\dot{\varepsilon}^{pl} = \dot{\lambda}\frac{\partial G}{\partial \bar{\sigma}} \quad \text{Eq.42}$$

The plastic potential G is the Drucker-Prager hyperbolic function

$$G = \sqrt{(\epsilon\sigma_{t0}\, tan\psi)^2 + \bar{q}^2} - \bar{p}\, tan\psi \quad \text{Eq.43}$$

Where ψ is the dilation angle, σ_{t0} is the uniaxial tensile stress at failure, ϵ is the eccentricity.

In summary, the use CDP model is advantageous in the 3-D FE since it allows modeling of nonlinear concrete behavior. This is achieved thru the distinct treatment of the tension and compression stress-strain behavior and reduction of material stiffness thru damage. The input parameters for the model are the stress-strain curves (tension, compression), the damage variables as a function of cracking/inelastic strains, the elastic modulus, and Poisson's ratio.

3.2.2 Steel

The material behavior of the main reinforcement steel in the prestressed concrete piles is modeled using the classical elastoplastic von Mises model. This model is suitable for metals which exhibit similar behavior under monotonic tensile or compressive loading (Chen and Han 2007). The model assumes isotropic linear elastic behavior up to the yield stress point. The plastic behavior is triggered by the yield surface which is mathematically written as

$$f = J_2^2 - k^2 \quad \text{Eq.44}$$

Where J_2 is the second invariant of the deviatoric stress tensor ($= \sqrt{3/2\, s_{ij}s_{ij}}$), s_{ij} is the deviatoric stress tensor, k is estimated from the uniaxial yield strength as $\sqrt{2/3}\sigma_y$.

The yield function has the shape of a cylinder in the 3-D principal stress space, and the radius of the cylinder is k, see Figure 3.12.

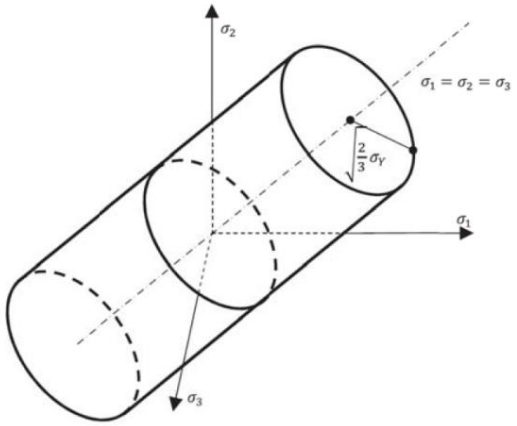

Figure 3.12. von Mises yield surface in the 3-D principal stress space

In the plastic region, the model assumes perfectly plastic behavior (i.e. no hardening). The plastic strain rate, assuming associated flow rule, is given by

$$\dot{\varepsilon}^p = \dot{\lambda}\frac{\partial f}{\partial \sigma} \qquad \text{Eq.45}$$

Where $\dot{\lambda}$ is the plastic multiplier determined from the consistency condition ($df = 0$).

The model is best suited for monotonic load and requires three parameters: the elastic modulus, Poisson's ratio, and the yield strength.

3.2.3 Clay

Natural clays tend to have a significant degree of anisotropy which develops during deposition, one-dimensional consolidation, and any subsequent straining (e.g. Zdravković et al. 2002). There are two forms of anisotropy in soils: inherent anisotropy from natural deposition, and induced anisotropy due to straining. The anisotropic modified Cam clay (AMCC) model is able to account for the anisotropic behavior of clays. The AMCC model is based on the modified Cam-clay (MCC) model, which is derived from the critical state soil mechanics (Roscoe and Burland 1968). It incorporates a specialized rotational hardening rule for the yield surface, which allows simulating the anisotropy of naturally deposited soils (Voyiadjis and Song 2000; Wei 2004; Elias 2008; Abu-Farsakh et al. 2015). The anisotropic form of the model was first proposed by Dafalias (1986) and later updated to simulate the softening behavior of clays by Dafalias et al. (2006). The model in its updated form is used in the current work.

For small strains, the additive decomposition of elastic ε_{ij}^{el} and plastic ε_{ij}^{pl} strains is assumed

$$\varepsilon_{ij} = \varepsilon_{ij}^{el} + \varepsilon_{ij}^{pl} \qquad \text{Eq.46}$$

For the elastic part, the isotropic hypoelastic stress-strain relation is adopted, which is written in the rate form as

$$\dot{\varepsilon}_{ij}^{el} = \frac{\dot{p'}}{K}\delta_{ij} + \frac{\dot{s}_{ij}}{2G} \quad \text{Eq.47}$$

Where *p'* is the effective hydrostatic (or mean) stress component ($p' = \frac{\sigma_{ii}}{3}$), s_{ij} is the deviatoric stress component, K and G are the bulk and shear moduli, respectively.

The bulk modulus K is mean stress dependent and given by

$$K = \frac{(1+e_0)}{\kappa}p' \quad \text{Eq.48}$$

Where e_0 is the initial void ratio, κ is the slope of the unload-reload line in e_0-ln *p'* space.

The shear modulus G is related to the bulk modulus K and Poisson's ratio ν

$$G = \frac{3(1-2\nu)}{2(1+\nu)}K \quad \text{Eq.49}$$

For the plastic part, the plastic strain rate is given by the flow rule

$$\dot{\varepsilon}_{ij}^{pl} = \langle L \rangle \frac{\partial \Pi}{\partial \sigma_{ij}} \quad \text{Eq.50}$$

Where L is the plastic multiplier, Π is the plastic potential.

The flow rule is assumed to be associative, which means the direction of plastic strain rate follows the direction of the normal to the yield surface f (i.e. $f = \Pi$). The yield function for multi-dimensional stress space is the one suggested by Dafalias et al. (2006), and written in terms of effective stress as

$$f = \frac{3}{2}\left(s_{ij} - p'\alpha_{ij}\right)\left(s_{ij} - p'\alpha_{ij}\right) - (M^2 - \frac{3}{2}\alpha_{ij}\alpha_{ij})p'(p'_0 - p') \quad \text{Eq.51}$$

Where M is the slope of critical state line in the triaxial stress space, p'_0 is the preconsolidation pressure, α_{ij} is the non-dimensional deviatoric anisotropy tensor. The critical state line slope M acquires different values for triaxial compression (M_c) and extension (M_e). This can be achieved by means of the Lode angle (θ). Using Argyris et al. (1974) proposition, the slope of the critical state line in the multi-dimensional stress space can be adjusted according to the following formula

$$M = \left[\frac{2n}{(1+n) - (1-n)cos3\theta}\right]M_c \quad \text{Eq.52}$$

Where $n = M_e/M_c$ (0.8 is typically assumed), triaxial compression occurs when θ=0, and triaxial extension when $\theta = \pi/3$.

The Lode angle is calculated based on the stress ratio r_{ij} and the anisotropy tensor α_{ij}

$$cos3\theta = \sqrt{6}k_{ij}k_{jm}k_{mi}\,, \qquad k_{ij} = \frac{r_{ij} - \alpha_{ij}}{\|r_{ij} - \alpha_{ij}\|}\,, \qquad r_{ij} = \frac{s_{ij}}{p'} \qquad \text{Eq.53}$$

There are two hardening mechanisms in the AMCC model: isotropic and kinematic (rotational). The isotropic hardening variable is controlled by the preconsolidation pressure p'_0, which represents the size of the yield surface. During elastoplastic loading, the evolution of the hardening variable p'_0 is proportional to the volumetric plastic strain developed. This is evident in the evolution formula of p'_0

$$\dot{p'_0} = \langle L \rangle \left(\frac{1 + e_0}{\lambda - \kappa}\right) p'_0 \left(\frac{\partial \Pi}{\partial \sigma_{ii}}\right) \qquad \text{Eq.54}$$

Where λ is the slope of the virgin compression line in e_0-ln p' space.

The kinematic hardening variable is the anisotropy tensor α_{ij}, which represents the inclination of the yield surface in the stress space, see Figure 3.13.

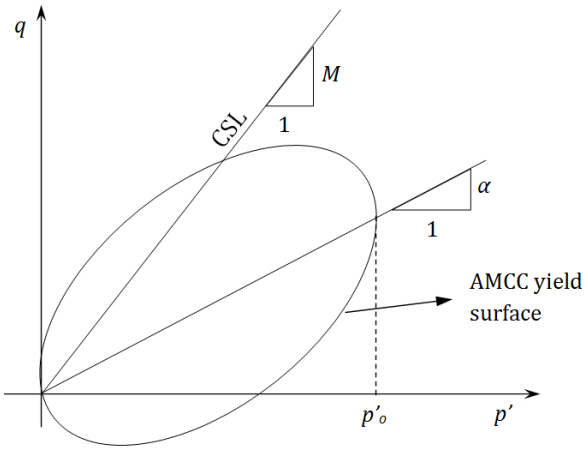

Figure 3.13. AMCC yield surface shape in the triaxial stress space

The inherent part of soil anisotropy is incorporated by defining an initial value for α_{ij} , while the induced part develops during elastoplastic loading.

The initial value for α_{ij} tensor components can be estimated from the initial earth pressure stress ratio $K_0 = \sigma^0_{22,33}/\sigma^0_{11}$ (where σ^0_{11} is in the global vertical direction) (Ling et al. 2002)

$$\begin{gathered} \alpha^0_{11} = 2k\ ,\ \alpha^0_{22} = \alpha^0_{33} = -k \\ k = \frac{1-K_0}{1+2K_0} \\ \alpha^0_{12} = \alpha^0_{23} = \alpha^0_{13} = 0 \end{gathered} \qquad \text{Eq.55}$$

The induced anisotropy develops with the evolution of the anisotropy tensor α_{ij} which is given as

$$\dot{\alpha_{ij}} = \langle L \rangle \left(\frac{1+e_0}{\lambda-\kappa}\right) C \left(\frac{p'}{p'_0}\right)^2 \left|\frac{\partial \Pi}{\partial \sigma_{ii}}\right| \left[\sqrt{\frac{3}{2}(r_{ij}-x\alpha_{ij})(r_{ij}-x\alpha_{ij})}\right] \left(\alpha^b_{ij}-\alpha_{ij}\right) \qquad \text{Eq.56}$$

Where C and x are material constants which control the evolution rate, α^b_{ij} is the bounding anisotropy tensor which limits the values of α_{ij} to guarantee the existence of real stress states σ_{ij}. The bounding anisotropy tensor α^b_{ij} is defined as

$$\alpha^b_{ij} = \sqrt{2/3}\, M n_{ij}\ , \quad n_{ij} = \frac{\frac{r_{ij}}{x}-\alpha_{ij}}{\left\|\frac{r_{ij}}{x}-\alpha_{ij}\right\|} \qquad \text{Eq.57}$$

The model parameters C and x are typically determined from CK_o triaxial test results However, for the current study, the values of C and x are assumed (Dafalias et al. 2006).

In summary, AMCC model is suitable to model the anisotropic behavior of clays, and it is simple since it requires two additional parameters over the original MCC model.

3.2.4 Sand

The Drucker-Prager (DP) constitutive model is well known and best suited for pressure dependent materials (Chen and Han 2007). Cohesionless materials such as sand are known to have small cohesion strength, negligible tensile strength, and become stronger with increasing confining pressure (i.e. pressure dependent).

For the DP model, the small strain theory and additive decomposition of elastic and plastic strains are assumed. The elastic part is governed by the hypoelastic stress-strain relationship similar to AMCC model

$$\begin{gathered} \varepsilon_{ij} = \varepsilon^{el}_{ij} + \varepsilon^{pl}_{ij} \\ \dot{\varepsilon}^{el}_{ij} = \frac{\dot{p'}}{K}\delta_{ij} + \frac{\dot{s}_{ij}}{2G} \end{gathered} \qquad \text{Eq.58}$$

$$K = \frac{(1+e_0)}{\kappa} p'$$
$$G = \frac{3(1-2\nu)}{2(1+\nu)} K$$

The plastic strain is triggered by the DP yield surface which has a distorted cone shape in the 3-D stress space, see Figure 3.14. The yield function is written as

$$f = t - p' tan\beta - d \qquad \text{Eq.59}$$

Where $p'$is the mean component of the effective stress, d is the internal cohesion,

β is the friction angle for DP model, and is related to the friction angle for Mohr Coulomb criteria $tan\beta = \frac{6sin\phi}{3-sin\phi}$, t is the deviatoric stress measure defined as

$$t = \frac{q}{2}\left[1 + \frac{1}{K}\left(1 - \frac{1}{K}\right)\left(\frac{r}{q}\right)^3\right] \qquad \text{Eq.60}$$

Where $q = \sqrt{\frac{3}{2} s_{ij} s_{ij}}$, $r = \sqrt[3]{\frac{9}{2} s_{ij} s_{jk} s_{ki}}$, K is the ratio of yield in triaxial extension and triaxial compression (typically K =0.8).

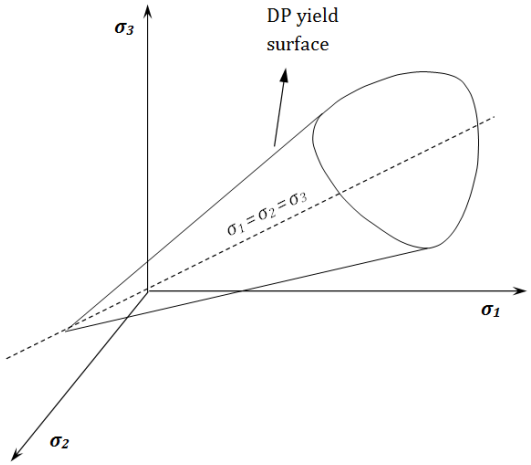

Figure 3.14. DP yield surface in the 3-D stress space

A non-associative flow rule is assumed in the DP model which controls the dilative behavior during the plastic flow. The plastic potential function is

$$\Pi = t - p' tan\psi \qquad \text{Eq.61}$$

Where ψ is the angle of dilation, which is typically $\psi = \phi/3$.

Chapter 4. Simulation of the Static Load Test at M19 Pier Foundation

4.1 Introduction

In this chapter, FE simulation of the static load test conducted at the I-10 twin span bridge (Abu-Farsakh et al. 2011a) is presented. A 3-D model of the M19 pile group foundation was developed and verified using the experimental results from the field test. The results obtained from the field test are limited to (1) displacement profiles for some piles, (2) and bending moment at two elevation level from strain gages. The FE simulation provided additional results for each pile in the pile group such as complete bending moment profile, axial and shear forces profiles, and visualization of damage zones. Furthermore, the soil resistance was deduced the shear force profile from FE.

4.2 Description of the lateral load test of M19 pier foundation

The static lateral load test is briefly described here, and greater details are found in the reference (Abu-Farsakh et al. 2011a).

The lateral load test was conducted on the M19 eastbound pier of the I-10 Twin Span Bridge over Lake Pontchartrain, LA. The pier comprised of 24 prestressed concrete battered piles arranged in 4x6 configuration (Figure 4.1). The adjacent rows of piles were battered at slope of 1H:6V, so that two rows were battered to the east and the other two to the west. Each pile was 110 ft long (at casting) and had 3 ft x 3 ft square section. The pile spacing at the cap level was 4.3D between rows and 2.5D between columns. The average embedded length of the piles was 87 ft, and the mudline was located 11 ft from the bottom of the pile cap. The pile cap dimensions were 44 ft L × 42.5 ft W × 7 ft D. Figure 4.1 shows the layout and numbering of the piles for the pile group foundation. Numbers are used for columns, and L/ML/MT/T refers to leading, middle-leading, middle-trailing, and trailing rows, respectively. A column refers to the piles arranged in the line parallel to the lateral load direction, while a row refers to the piles arranged in the transverse direction to the lateral load. Some of the piles were instrumented with strain gages (SGs) and/or in-place inclinometers (IPI) (Figure 4.1). The SGs were initially installed in pairs at 16 and 21 ft from the pile top at the time of casting. Considering an average cutoff length of 6.5 ft in the piles, the final location of the SGs was estimated at 9.5 and 14.5 ft from the bottom of the pile cap. The inclinometers were installed over the pile length at the following levels: 5, 15, 25, 35, 45, 65 ft from the bottom of the pile cap.

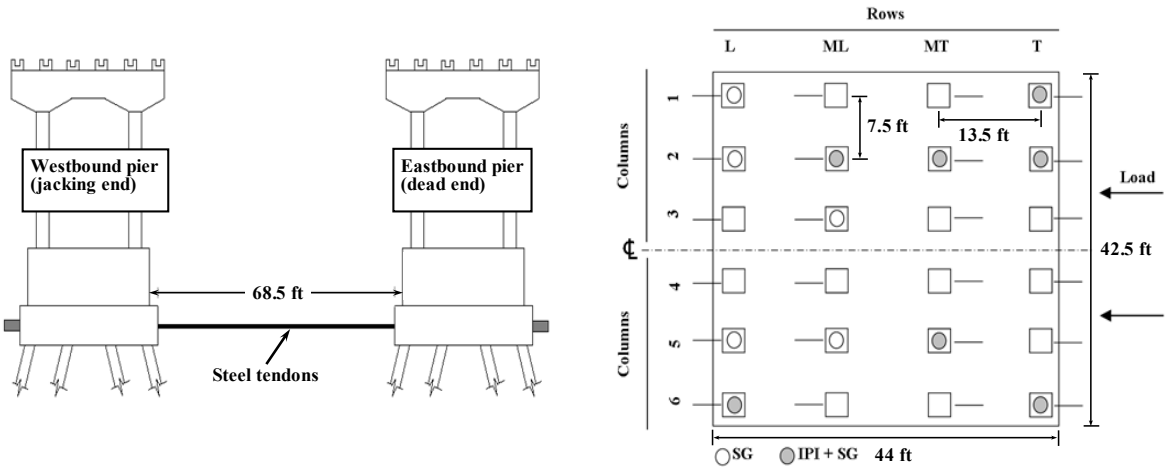

Figure 4.1. Schematic of the lateral load test setup, and piles numbering and instrumentation (after Abu-Farsakh et al. 2011a)

The lateral load test was conducted by pulling the eastbound and westbound piers toward each other using high strength steel tendons run through two 4-inch PVC pipes installed in both pile caps. The steel strands were first anchored at the dead-end side, and then were threaded one-by-one through the two 4-inch PVC pipes from the dead-end at the M19 eastbound pier toward the hydraulic jacks of the live-end at the M19 westbound pier. The total lateral load was applied incrementally and designed to reach a maximum of 2000 kips. However, the maximum load achieved was 1870 kips because one of the strand jacks reached its maximum stroke.

The subsurface soil conditions for the M19 pier were characterized by means of in-situ and laboratory tests; this includes soil boring, laboratory testing, standard penetration tests (SPT), and cone penetration tests (CPT). The site investigation revealed that the subsurface soil stratigraphy consists mainly of medium-to-stiff silty clay to clay soil down to about 100 ft deep with a layer of medium dense sand between 38 and 49 ft below the mudline. A dense sand layer was found at depths greater than 100 ft below the mudline.

Figure 4.2 shows the assumed soil stratigraphy and the CPT profile.

4.3 Finite element model description

A 3-D geometry of the M19 pier and the soil domain was created in Abaqus v6.12, see Figure 4.3. Owing to the symmetry in both load and geometry, only half of the M19 pier foundation was modeled (i.e. the model has four rows and three columns). The pile group and the soil domain models were created from two separate meshes and were allowed to interact with each other using the contact feature. The piles' holes were cut out of the soil domain, and then the piles were placed into the holes (i.e. wish-in-place, installation effects omitted). Roller-type boundary conditions were applied at the soil domain boundaries and the symmetry plane as shown in Figure 4.3. The dimensions of the soil domain were 220 ft

L x 80 ft W x 120 ft D. The size of the soil domain was checked to be large enough to eliminate the boundary effects. The mesh was designed to be finer near the piles and gradually become coarser near the boundaries.

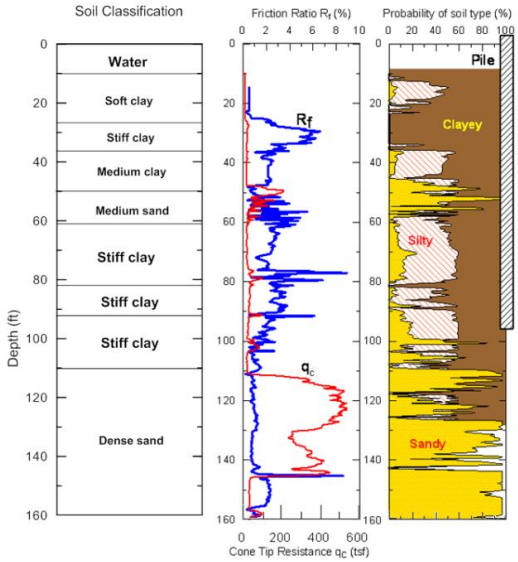

Figure 4.2. Soil stratigraphy and CPT profile

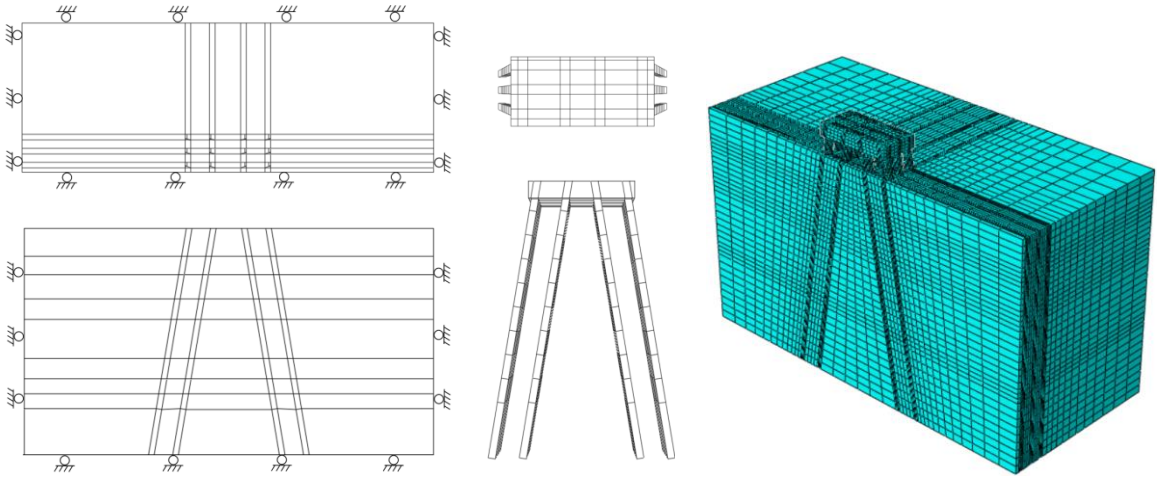

Figure 4.3. Geometry and mesh of the FE model for the battered pile group

Initially, the geostatic (or in-situ) stresses were established by applying gravity load on both soil and pile models, and then performing a static equilibrium step. Once equilibrium was achieved, the lateral load was applied incrementally on the side of the pile cap as: 570, 770, 970, 1180, 1580, 1745, 1870, 2500, 3500, 4500, 5500 kips. The lateral load increments up to 1870 kips followed the field test loading sequence. The soil-pile interaction was introduced using Abaqus's contact feature, which allows soil-pile separation and models frictional behavior at the interface. The frictional behavior was

governed by the classical Coulomb friction law with coefficient of friction $\tan\delta = 0.5$, where δ is the angle of interface friction. Different values for δ were also considered in FE trial tests; however, the influence was negligible on the lateral behavior of the pile group. The latter was similarly observed in the FE study by Mroueh and Shahrour (2009).

4.3.1 Pile group model

The pile group model comprised of 10206 linear continuum brick elements (C3D8R). Two constitutive laws for the concrete were used at the same time: linear elastic, and concrete damaged plasticity (CDP) described in section 3.2.1. The main advantage in CDP is it allows distinct behavior in tension and compression, which is a major aspect of the concrete material behavior. The other advantage is material damage which allows better simulation of the nonlinear concrete behavior in addition to plasticity.

The linear elastic law was chosen for the pile cap and the upper 5 ft of the piles, and the CDP model was used for the remaining portion of the pile's body. This assumption was made to avoid the issue of premature damage in the concrete elements at the pile cap connection under relatively small lateral load (< 500 kips), which resulted in the early termination of the numerical solution by the FE solver. The 5 ft distance came after the choice of three elements (the element size was 1 ft) below the pile cap-piles connection, which were assigned with linear elastic model to overcome the issue. The value of Poisson's ratio for both linear elastic and CDP models was 0.2.

4.3.2 Steel reinforcement in piles

The piles were built with prestressed steel strands as the main reinforcement. Each steel strand was made of seven-wire, low relaxation Grade 270 bundled steel strands, and had a diameter of 0.6 inch. The total number of strands per pile was 36 spaced at 3.3 inches, and the concrete cover was 3 inches. The estimated prestress force per strand after considering the prestress losses was 35.1 kips.

The steel reinforcement was modeled using embedded shell elements (S4R), as described previously in section 3.1.5. The von Mises elastic-perfectly plastic model was used to describe the behavior of the steel material. The elastic properties used were Young's modulus E_s = 29000 ksi, Poisson's ratio ν = 0.2, and the yield stress was 234 ksi (ASTM 2012, standard A416).

4.3.3 Soil model

The soil domain was composed of eight layers: six clay and two sand layers, following the in-situ soil stratigraphy. The soil domain was modeled using linear continuum brick elements (C3D8R) with a total of 72160 elements. The constitutive laws for the soil layers were the Anisotropic Modified Cam-clay (AMCC) model for clays (Dafalias et al. 2006), and the Drucker-Prager elastic-perfectly plastic model for sand (both previously described in section 3.2). The parameters for both AMCC and DP models and the soil layering are

summarized in Table 4.1. The parameters (κ, λ, K_o, β) were estimated with the aid of the CPT results and correlations found in the reference for CPT (Robertson and Cabal 2015). For the DP model, d' represents the cohesion in the sand material and was assumed 10 psf to avoid numerical problems. The constants *x* and C were reasonably assumed following Dafalias et al. (2006).

Table 4.1. AMCC and DP model parameters

Soil Type	Depth from Mudline (ft)	Total Unit Weight (pcf)	Poisson's ratio (ν)	K_0	AMCC						DP		
					α_{ini}	M	κ	λ	x	C	κ	β	d' (psf)
Soft Clay	0-15	123	0.25	0.95	0.034	0.9	0.03	0.14	1.33	4	-	-	-
Stiff Clay	15-25	119	0.20	0.85	0.111	1.1	0.01	0.12	1.33	4	-	-	-
Medium Stiff Clay	25-38	108	0.25	0.73	0.219	1.0	0.02	0.13	1.33	4	-	-	-
Medium Sand	38-49	120	0.38	0.70	-	-	-	-	-	-	0.003	53	10
Stiff Clay	49-70	113	0.20	0.65	0.271	1.2	0.01	0.12	1.33	4	-	-	-
Stiff Clay	70-81	122	0.20	0.65	0.271	1.2	0.01	0.12	1.33	4	-	-	-
Stiff Clay	81-99	128	0.20	0.60	0.363	1.2	0.01	0.12	1.33	4	-	-	-
Dense Sand	>99	124	0.40	0.60	-	-	-	-	-	-	0.003	58	10

4.4 Results and discussion

The FE model was verified using the results from the lateral load test conducted on the M19 pier (displacement profiles from IPIs, and bending moments from SGs). Furthermore, additional lateral load was applied in the FE model to induce more deformation and study the aspects of the lateral behavior of the battered pile group under extreme load conditions. In addition to deflected shapes and bending moments, internal forces such the axial and shear forces in the piles, soil resistance, and *p-y* curves were extracted.

4.4.1 Load-displacement curves

Figure 4.4 shows the lateral load versus displacement for the pile cap and the average for each row in the pile group. Recall that the maximum lateral load from the field test was 1870 kips. Good agreement between the field test results and the FE model results is observed. The cap displacement from the experiment at 1870 kips was 0.65 in. compared to 0.76 in. from the FE model. In the FE simulation, the lateral load was further increased until the piles were severely damaged and unable to sustain additional load. The maximum lateral load achieved in the FE model was 5500 kips, which resulted in pile cap displacement of 2.9 in. The load-displacement curve for the pile cap exhibited slight non-linearity, which is attributed to the nonlinear behavior of the piles and the soil as well. Figure 4.4 also depicts the average lateral load carried by the piles in each row, which shows that the middle rows (ML, MT) carried larger lateral load compared to the leading (L) and trailing (T) rows. It is noticed that rows ML and MT carried approximately similar load percentage, which also applies to rows L and T. At 5500 kips, the average lateral load percentage carried by each row was 22%, 31%, 28%, and 20% in rows L, ML, MT, and T, respectively. The slight difference between rows ML and MT was due to the tension-

damage in row MT, which initiated earlier at a total lateral load of 3500 kips. The distribution of lateral load per row observed here is different from the case of vertical piles groups. For vertical pile groups, the largest share of lateral load is usually carried by the leading row followed by the 2nd, 3rd, and 4th rows, respectively (Brown et al. 1988; Ruesta and Townsend 1997; McVay et al. 1998). Such difference is attributed to the effect of the batter angle, which modifies the mechanism of lateral resistance in battered piles. In the vertical case, the pile resists the lateral load by carrying shear load only, while in the battered case the pile carries both axial and shear loads. As will be shown later, the axial reaction in the middle rows ML and MT was approximately three times larger than the reaction in rows L and T.

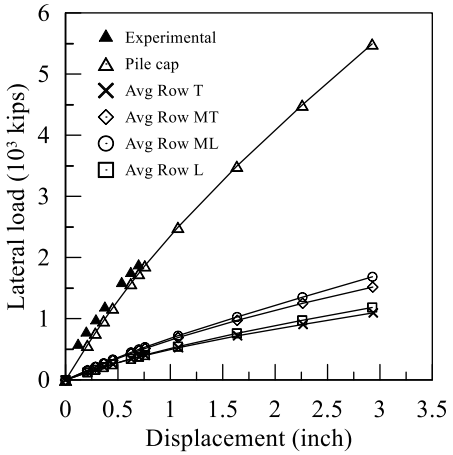

Figure 4.4. Load-displacement curve at pile cap level

4.4.2 Damage in piles

The CDP constitutive law introduces damage by reducing the concrete modulus. This occurs in tension and/or compression when the strength limit is exceeded. When damage is introduced, the concrete material becomes weaker and, consequently, stresses are transferred to the embedded reinforcing steel. In the current FE study, only damage from tension was observed following the fact that the tensile strength is significantly smaller (10 times less) than the compressive strength. The first elements to get damage were in row MT piles at 3500 kips, and located 5 ft below the pile cap. This was expected since the material damage was not a property of the elements within the top 5 ft of the piles.

The damage parameter d represents the reduction to the elastic stiffness of the material, and assumes values within the range $0 < d < 1.0$. A zero value for d means the material is damage free, while a value of 1.0 means the material stiffness vanished. In numerical modeling, a value of 1.0 is not applicable and introduces numerical problems; therefore, the maximum value of d is typically below 0.99. Figure 4.5 shows the damage progression in the piles with lateral load. Damage first appeared in row MT at 3500 kips, followed by rows T and L at 4500 kips, and finally in row ML at 5500 kips. At 5500 kips, the elements

located at 5 ft below the pile cap in the trailing rows (MT and T) were severely damaged with d > 0.7 (notice the dark colored areas in the figure), and the damaged area expanded to the elements further below 5 ft. Piles in the leading row (L) exhibited lesser degree of damage with d < 0.5 compared to the trailing rows. The lowest damage level was observed in row ML with d < 0.2. It should be noted that the FE solver aborted the solution at a total lateral load less than 6000 kips (the load increment in the FE solution was 500 kips). Therefore, it was assumed that the last load increment completed in the FE solution (5500 kips) was the maximum lateral load that the pile group can carry.

The damage sequence in the rows can be explained by investigating the axial load carried in each pile. Figure 4.6a summarizes the variation of the axial load in each pile with increasing group lateral load. In the figure, positive axial load means compression while negative is tension. The axial loads in the leading rows (L and ML) were in compression and increased with increasing lateral load, while in the trailing rows (T and MT) the axial loads increased in tension. Additionally, it is noticed that the edge piles (column 1) were subjected to the largest magnitude of axial loads among other piles in the same row. For the damage sequence, piles in row MT were the first to get tension damage due to the relatively large tensile axial load, which in combination with bending moment initiated tension-damage earlier than other rows. The second to experience tension-damage was the trailing row (T), which was subjected to a lesser tensile axial load. Lastly, the leading rows (L and ML) exhibited damage at later stages due to the compressive axial load, which counteracts the action of the bending moment. Moreover, within the same row, the edge piles (column 1) received more damage compared to the interior piles (columns 2 and 3) due to the larger bending moment. For example, Figure 4.6b shows the bending moments developed at the top of piles in the leading row (L). The edge pile (L1) carried larger bending moment (8% more) compared to the interior piles (L2 and L3). Similar behavior was observed in other rows (ML, MT, T) as well (not shown here).

4.4.3 Lateral displacement profiles

The lateral deformation profiles for piles L6, ML2, MT2, T1, T2 are shown in Figure 4.7. Note that the results of pile L6 from the full-scale test are compared to the mirror or symmetry pile L1 from the FE model. The deflected shapes are shown for two load levels: 1870 kips from the field test and FE, and 5500 kips from FE analyses only. Good agreement can be observed between the field test and FE results at 1870 kips. It can be noticed that the majority of the deformation occurred within the clay layers (11 - 49 ft), and diminished at the (medium dense) sand layer located at 49 - 60 ft below the mudline.

The lateral deformation for column 2 and row ML piles at 5500 kips are depicted in Figure 4.8a and Figure 4.8b, respectively. For column 2 piles, it is noticed that the deflections for piles ML2 and MT2 (middle rows) were slightly greater than piles L2 and T2. Similarly, for row ML, piles ML2 and ML3 had slightly greater deformation compared to the edge pile ML1, Figure 4.8b. The latter observation is also valid for the other columns/rows.

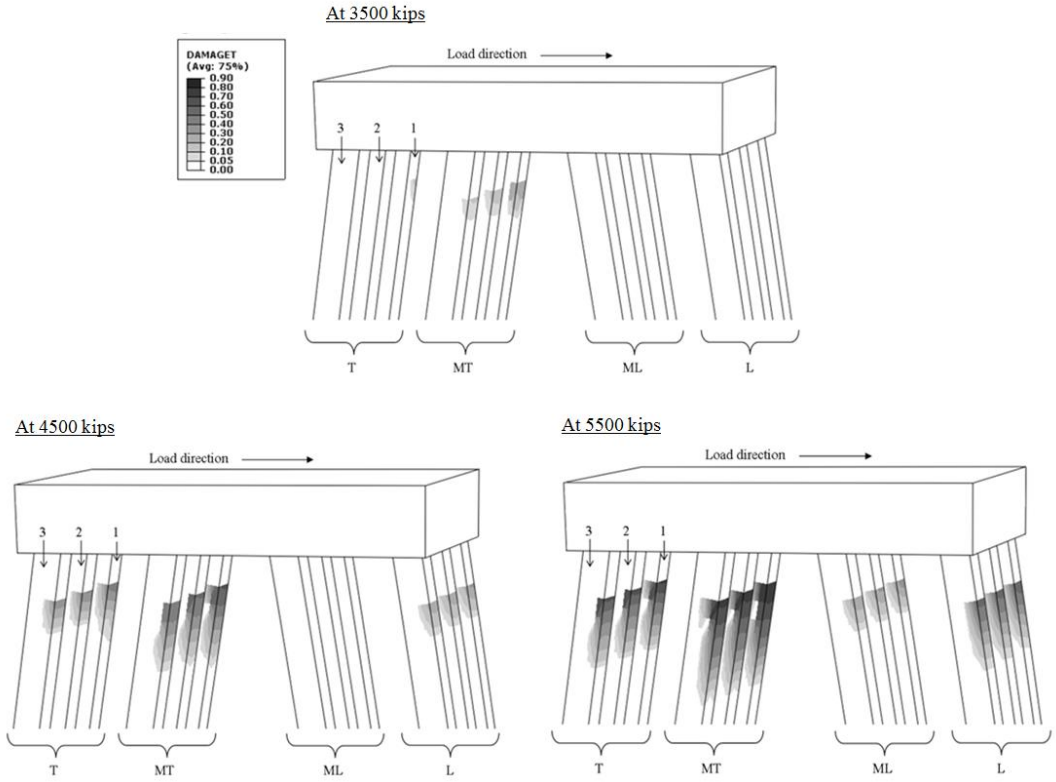

Figure 4.5. Damage progression in the piles with increased loading

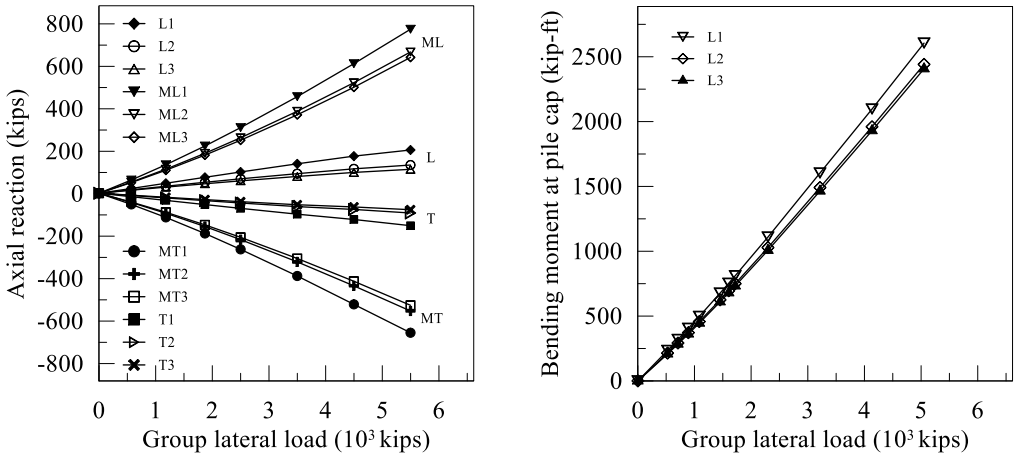

Figure 4.6. Variation of the axial reaction and bending moment in row L

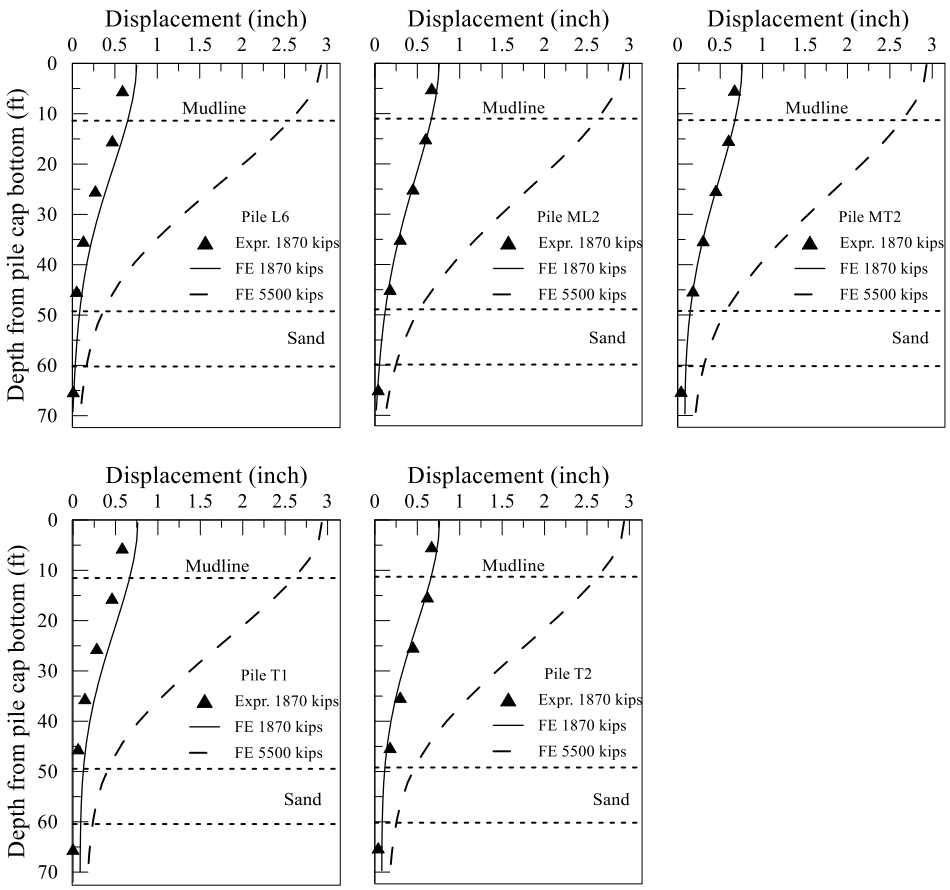

Figure 4.7. Displacement profiles for instrumented piles

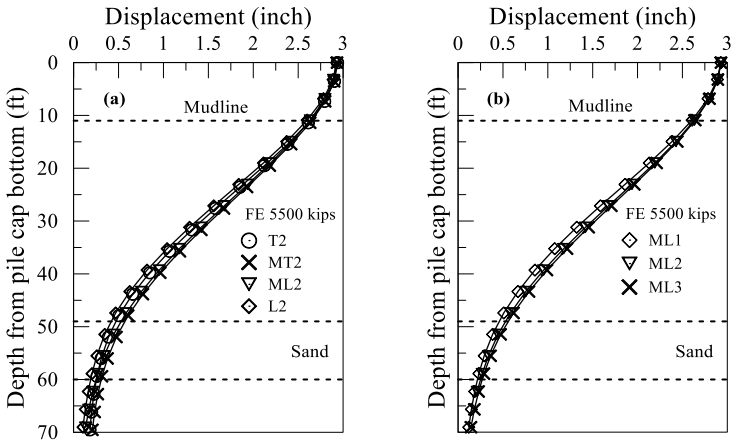

Figure 4.8. Displacement profiles comparison for (a) same column piles, (b) same row piles

4.4.4 Bending moment profiles

The bending moments from the field were deduced from the strain gage readings at 12 and 16 ft from the bottom of the pile cap in each of the instrumented piles. For 3-D solid continuum elements, Abaqus provides the results of bending moment, axial force, and shear force for defined cross sections in the piles. It performs the integration of stresses for cross sections defined in the mesh and appends the results to the output file. To obtain the bending moment profiles, multiple cross sections were defined in the pile group mesh at the pile cap-piles connection and at 5, 15, 25, 35, 45, 55, 65, 75, and 85 ft from the bottom of the pile cap. A comparison between the field results and the FE bending moments at lateral loads of 570 kips and 1745 kips is shown in Figure 4.9. Good agreement is observed between the field measurements and FE results. The bending moment profiles from FE show that the inflection point (i.e. zero moment) was located within 21-25 ft from the bottom of the pile cap. The location of the maximum positive moment was at the pile cap connection, while the maximum negative moment was located at 39-45 ft from the bottom of the pile cap. Within the same column, the leading and trailing rows (L and T) had shallower inflection and maximum negative moment points compared to the middle rows (ML and MT), as shown in Figure 4.10a. Within the same row, the inflection and maximum negative moment points were slightly shallower for the edge piles (column 1), see for example the bending moment profiles for row L piles in Figure 4.10b. It is also noticed that both points (inflection and maximum negative moment) shift deeper with increasing lateral load, as noticed in Figure 4.10c.

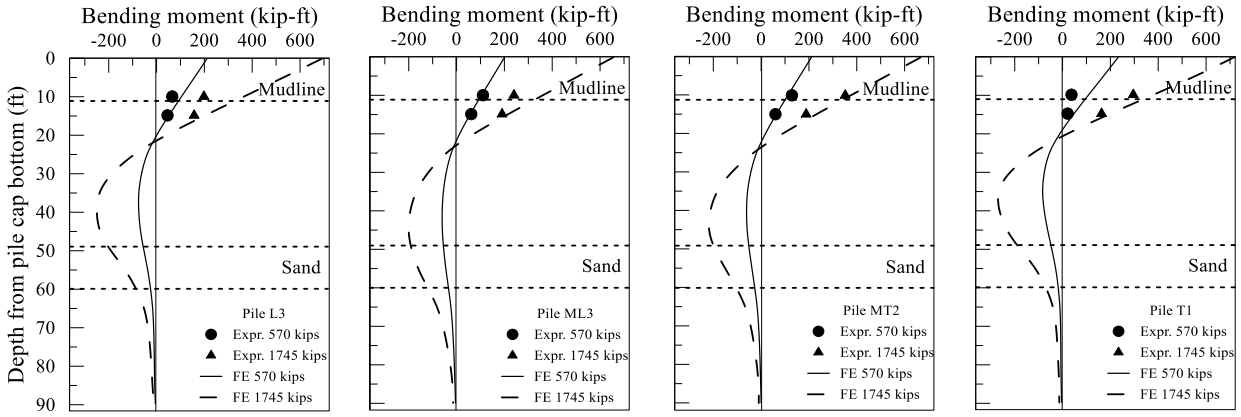

Figure 4.9. Bending moment results from strain gages and FE profiles for instrumented piles

4.4.5 Soil resistance

The soil resistance is investigated with the aid of soil resistance profiles and *p-y* curves. The soil resistance profiles were obtained using the traditional method by double differentiating the bending moment curve, which was fitted using high-order polynomial fit (Wilson 1998; Ilyas et al. 2004; Nip and Ng 2005; Abu-Farsakh et al. 2011b).

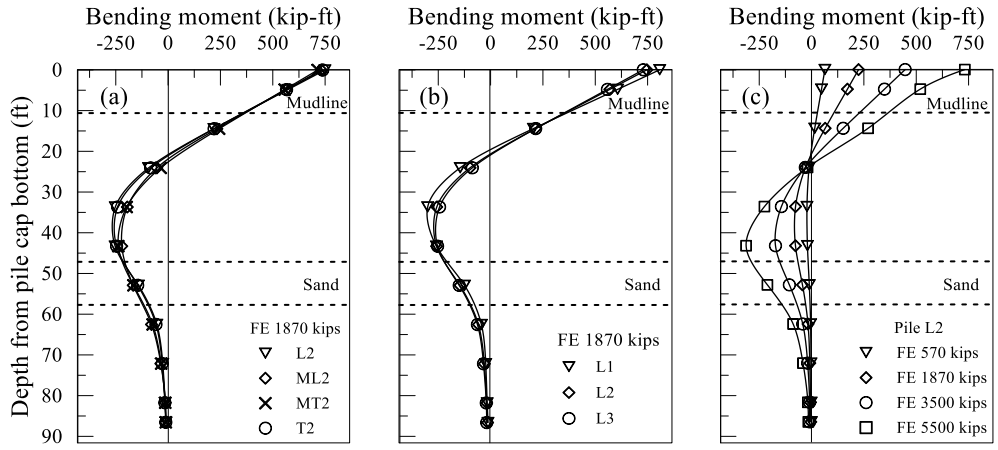

Figure 4.10. Bending moment profiles for (a) column 2 piles, (b) row L piles, (c) pile L2

Figure 4.11 presents the soil resistance profiles for column 2 piles. It should be noted that the reference depth in the following discussion as well as in the figures is taken from the mudline unless otherwise specified. The profiles show that the soil resistance changed direction at an approximate depth of 45 ft in all piles. The soil resistance increased with increasing lateral load in all piles, but at different rates. The largest increase in soil resistance was in the leading row pile L2, which is mainly due to the group effect. The resistance was also influenced by soil layering; this can be noticed in the larger resistance in layer 2 (stiff clay, 15-25 ft) compared to layer 3 (medium stiff clay, 25-38 ft). In addition, a sharp increase in the resistance at 5500 kips in the sand layer is noticed, which can be attributed to the larger stiffness of the sand layer compared to the clay layers.

The soil resistance is also investigated using the *p-y* curves. A *p-y* curve represents the soil resistance per unit pile-length versus displacement at certain depth. For brevity, only column 2 and row ML *p-y* curves are presented here, and the following discussion applies to other columns/rows as well. Figure 4.12 shows the *p-y* curves for column 2 piles at different depths. The *p-y* curves for pile L2 in the leading row were stiffer than those in other rows (ML2, MT2, T2). In addition, the *p-y* curves for piles ML2 and T2 were approximately similar and stiffer than pile MT2, which had the lowest soil resistance.

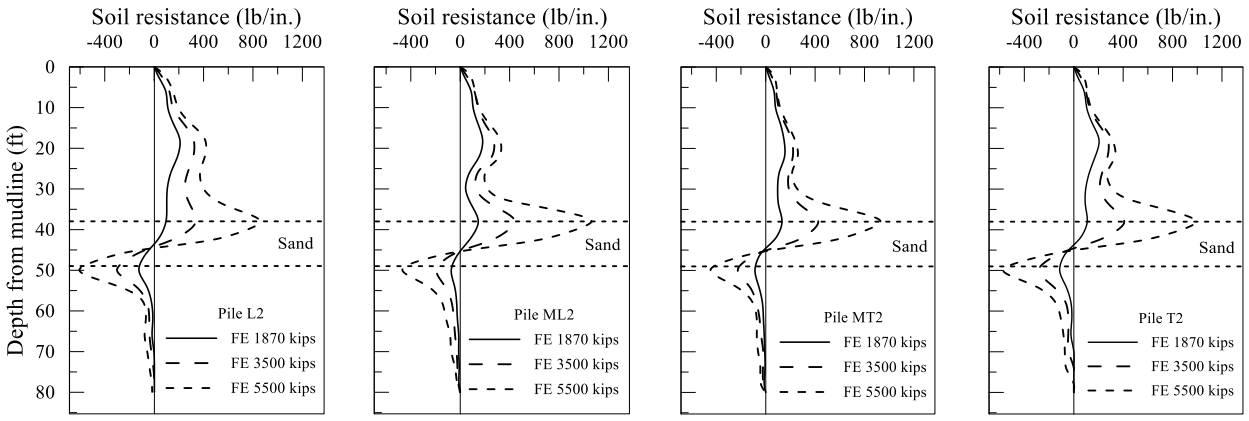

Figure 4.11. Soil resistance profiles for column 2 piles

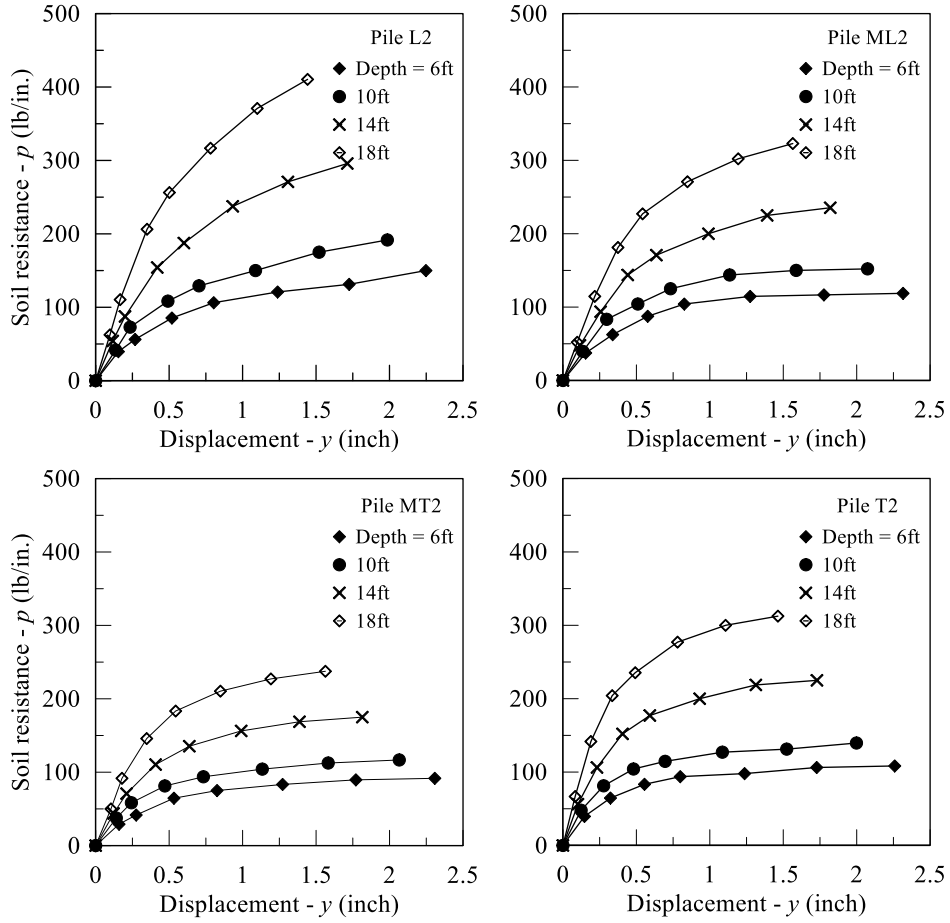

Figure 4.12. *p-y* curves for column 2 piles

Figure 4.13 compares the *p-y* curves for column 2 piles and row ML piles at depth of 10 ft. The comparison also includes the *p-y* curve for an isolated single vertical pile, single positive battered pile, and single negative battered pile. Those *p-y* curves were obtained from a separate FE models for each single pile case. These FE models maintained the

same pile dimensions, pile head condition (i.e. fixity), batter angle for battered piles, material properties (soil, steel, and concrete), constitutive models, soil layering, and embedded shell elements for steel reinforcement. The *p-y* curves for single pile cases show that the single positive battered pile was subjected to slightly higher soil resistance compared to the vertical and negative battered cases, which can be attributed to the effect of the batter angle.

Within the same column (Figure 4.13a), the soil resistance was notably reduced for all piles in the group compared to the single pile case, again, due to the group effect. The largest reduction in the soil resistance was in row MT followed by rows T then ML, and finally row L. Within the same row (Figure 4.13b), the soil resistance was largest in the edge pile ML1 followed by ML2 and ML3, which had almost the same *p-y* curves.

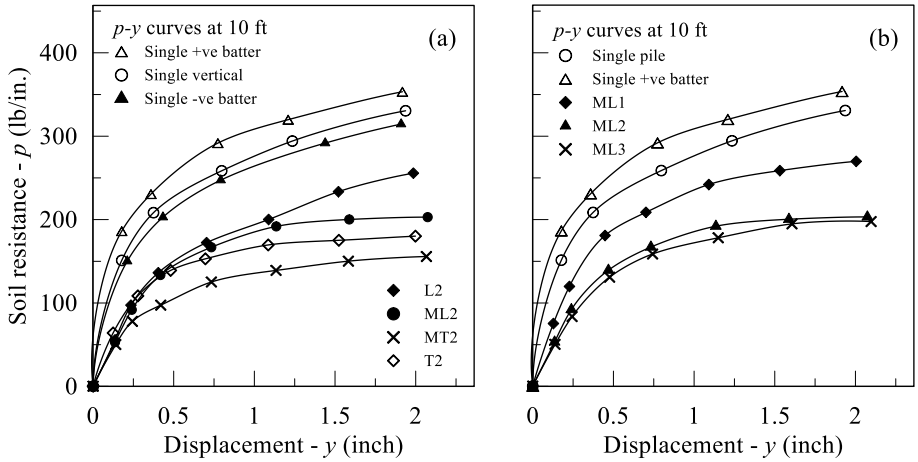

Figure 4.13. *p-y* curves comparison for (a) column 2 piles and (b) row ML piles

The influence of the group effect is quantitatively evaluated using the *p*-multiplier concept. Brown et al. (1988) defined the *p*-multiplier as the factor that reduces the *p-y* curve from a single pile case to give the *p-y* curve for a pile-in-group configuration. The typical value of the *p*-multiplier is less than unity. The *p*-multiplier is affected by pile group arrangement (i.e. number of rows and columns), piles spacing (row and column spacing), and soil properties (McVay et al. 1995; Chandrasekaran et al. 2009; Ashour and Ardalan 2011). Table 4.2 summarizes the *p*-multipliers for all piles in the current study obtained using the *p-y* curves at depth of 10 ft, in which the *p-y* curve for the single vertical pile was taken as the reference case. The *p*-multipliers in Table 4.2 are the average values of *p*-multipliers calculated at displacements of 3, 4, and 5 cm, following the suggestions from previous studies. McVay et al. (1998) reported that 2-3 cm displacement is needed to develop the average *p*-multipliers. Ashour and Ardalan (2011) showed that the *p*-multiplier value stabilizes at displacements greater than 1 inch.

Table 4.2. Summary of *p*-multipliers at 10 ft depth

	Row			
	L	ML	MT	T
Column 1	0.96	0.78	0.57	0.72
Column 2	0.74	0.59	0.46	0.55
Column 3	0.70	0.57	0.43	0.51
Average	0.80	0.64	0.49	0.59

The *p*-multipliers were highest in the edge piles (column 1) followed by the interior columns 2 and 3 for which the multipliers were almost the same. The average *p*-multiplier was largest in the leading row L followed by rows ML, T, and MT, respectively. The *p*-multipliers for the current study are comparable to those from experimental studies on vertical pile groups with 4-rows (e.g. Ilyas et al. 2004; Chandrasekaran et al. 2009). The *p*-multipliers from the study by Ilyas et al. were 0.65, 0.49, 0.42, 0.46, and from the study by Chandrasekaran et al. were 0.76, 0.56, 0.46, 0.54 for the 1st, 2nd, 3rd, and 4th row, respectively. The most notable similarity is in the value of the *p*-multiplier for the 3rd row, which was the lowest multiplier among other rows. The slightly higher *p*-multipliers for the battered pile group for the current study can be attributed to the larger row spacing, which was 4.3D in the current study versus 3D in the referenced studies.

4.5 Conclusions

The lateral behavior of 4x6 battered pile group foundation was studied using 3-D finite element modeling in Abaqus. The FE model utilized advanced elastoplastic constitutive laws for the concrete and soil materials. The constitutive model for the concrete allowed distinct behavior in tension and compression and introduced stiffness degradation once the failure limit stress is exceeded. The constitutive model for the clay layers was the Anisotropic Modified Camclay, and the classical Drucker-Prager adopted for the sand layers. The FE model was verified using the results of full-scale static lateral load test that was conducted on the M19 eastbound pier of the I-10 Twin Span Bridge over Lake Pontchartrain, LA. Based on the findings of this study, the following conclusions can be drawn:

- Good agreement was obtained between the field results and FE predictions in terms of lateral deformations and bending moments.
- The lateral load distribution indicated that the middle rows carried 8-10% more lateral load than the leading and trailing rows. The latter was different from the load distribution in vertical pile groups in which the leading row carries the largest share of lateral load.

- The comparison between the piles in the same row showed that the edge piles carried larger axial loads and bending moments than the other piles in the same row. Also, the edge piles were subjected to larger soil resistance.
- Bending moment profiles showed that the maximum positive moment was located at the pile cap connection and the maximum negative moment within 10D from the mudline. The inflection point (or zero bending moment) was found within 5D from the mudline.
- At large lateral loads, only tensile failure in the concrete piles was observed and was initiated near the connection with the pile cap in the trailing rows with negative batter.
- The soil resistance profiles showed that the soil resistance was influenced by soil layering. This was observed in the higher resistance in the stiff clay and sand layers compared to the soft and medium stiff clay layers. In addition, the profiles showed that the influence depth for soil resistance was within 14-16D from the mudline.

When compared to isolated single pile case, the soil resistance in the pile group was notably reduced due to the group effect. The group effect was quantitatively represented by the *p*-multipliers. The average *p*-multipliers per row for the battered pile group were 0.80, 0.64, 0.49, 0.59 for the 1^{st}, 2^{nd}, 3^{rd}, and 4^{th} row, respectively. The *p*-multipliers values were comparable to the *p*-multipliers reported in previous studies for vertical pile groups.

Chapter 5. The Effect of Pile Group Configuration on the Static Lateral Behavior of Pile Groups

5.1 Introduction

Bridge piers and offshore structures are usually supported by pile foundations that are designed to resist vertical and lateral loads. The lateral behavior of the pile-soil system is dependent on both pile stiffness and soil reaction. The soil reaction is a nonlinear function of deflection, depth, pile stiffness, and soil stiffness and strength. Established methods for prediction of the lateral capacity of single pile are: the *p-y* curve method (Matlock 1970; Reese et al. 1974), elastic solution (Poulos and Davis 1980), the strain wedge model (Ashour et al. 2004), and the finite element (FE) method (e.g. Muqtadir and Desai 1986; Brown and Shie 1990; Trochanis et al. 1991; Yang and Jeremić 2002; Comodromos and Pitilakis 2005; Isenhower et al. 2014). Pile foundations are usually used in groups, in which the lateral capacity of a pile in the group is less than the case of isolated single pile. The soil in front of the pile in interest is weakened by the overlap of stress zones from surrounding piles, which is referred to as the group effect (e.g. Rollins et al. 1998). Pile group solutions based on *p-y* curves account for the group effect using empirical factors called "*p*-multipliers" (Brown et al. 1988). Site-specific *p*-multipliers are estimated thru an iterative procedure to match the experimental load-displacement curve with the solution's curve. Several studies suggested values for *p*-multipliers for vertical pile groups based on soil type and pile-pile spacing (Brown et al. 1988; McVay et al. 1995; Ruesta and Townsend 1997; Rollins et al. 1998, 2003, 2005b; Chandrasekaran et al. 2009). Additionally, the lateral capacity of vertical pile groups is also influenced by vertical load, piles arrangement, and slenderness ratio (e.g. Rao et al. 1998a; Patra and Pise 2001b; Ilyas et al. 2004; Hussien et al. 2012).

Single battered piles were less studied experimentally compared to single vertical piles (e.g. Tschebotarioff 1953; Murthy 1964; Meyerhof and Yalcin 1993; Zhang et al. 1999). Depending on the direction of inclination, battered piles are called "negative battered" when inclined in the load direction, and "positive battered" when inclined opposite to the load direction. When compared, negative battered piles have greater lateral resistance than positive battered and vertical piles, respectively (Murthy 1964; Meyerhof and Yalcin 1993; Zhang et al. 1999).

In contrast to vertical pile groups, there is a limited number of experimental studies available for battered pile groups (Ranjan et al. 1980; Chow 1987; McVay et al. 1996; Zhang et al. 2002; Abu-Farsakh et al. 2011b). Ranjan et al. (1980) showed that mixed pile groups of both vertical and battered piles have greater lateral resistance than groups of only vertical piles. McVay et al. (1996) evaluated the lateral performance of battered pile groups in-centrifuge at different pile spacing and pile-head fixity conditions. Zhang et al. (2002) concluded that greater vertical load increases the lateral resistance of battered pile

groups. Abu-Farsakh et al. (2011b) conducted a full-scale field study to evaluate the lateral capacity of 4x6 battered pile group in the I-10 twin span bridge in Louisiana.

Battered piles were also studied using numerical methods. Rajashree and Sitharam (2001) performed analysis of single battered piles under static and cyclic load using hyperbolic soil model. Mroueh and Shahrour (2009) investigated the influence of load inclination on the capacity of single battered piles and found that the lateral capacity of battered piles decreases when load inclination increase. Chow (1987) evaluated the lateral capacity for a number of mixed vertical and battered pile groups using the stiffness method. Isenhower et al. (2014) analyzed flood barrier battered pile group using 3-D finite element modeling, and estimated the long-term lateral loads and bending moments in the piles due to settlement and storm surge. Souri et al. (2015) used 3-D finite element modeling for the case study of 4x6 battered pile group in the I-10 twin span bridge, and back-calculated *p-y* curves and *p*-multipliers per pile.

In this chapter, the lateral performance of three pile group configurations (vertical, battered, and mixed) is investigated using 3-D FE modeling. The study is an extension to a previous field and numerical investigations for the lateral performance of M19 pier battered pile foundation of the I-10 twin span bridge (Abu-Farsakh et al. 2011b; Souri et al. 2015). The three FE models are based on the M19 battered pile group case study, in which the same cap size, pile spacing, material models, concrete and soil parameters were used. The comparison of lateral performance considered: load-displacement curves, axial load, damage in piles, bending moment, soil resistance, and back-calculated *p-y* curves and *p*-multipliers.

5.2 Static lateral load test on M19 pier foundation

The field test conducted on the M19 pile foundation is briefly described here (Abu-Farsakh et al. 2011b). The foundation composed of 3 ft-square prestressed concrete piles arranged in 4x6 configuration, which were inclined at 1H:6V batter angle (Figure 5.1). The eastbound and westbound piers were pulled toward each other using two high capacity strand jacks and steel tendons. The lateral load was applied incrementally and reached a maximum value of 1870 kips. Selected piles were instrumented with IPI inclinometers for pile slope and deflection, and two sets of strain gages for bending moment estimation.

The subsurface soil conditions were characterized by in-situ and laboratory tests; this includes soil boring, laboratory testing, standard penetration tests (SPT), and cone penetration tests (CPT). The subsurface soil stratigraphy consisted mainly of medium and stiff silty clay down to 100 ft below the mudline, and a layer of medium dense sand within 38-49 ft depth from the mudline. The pile tip bearing layer was dense sand located at depths greater than 100 ft from the mudline. The assumed soil stratigraphy in the FE models is depicted in Figure 5.1. A layout map for piles numbering shown in Figure 5.1 is used throughout the study. Numbers were used for pile columns, and L/ML/MT/T refers to

leading, middle-leading, middle-trailing, trailing rows, respectively. A column refers to piles arranged parallel to the load direction. A row refers to the piles arranged in the transverse direction to the lateral load.

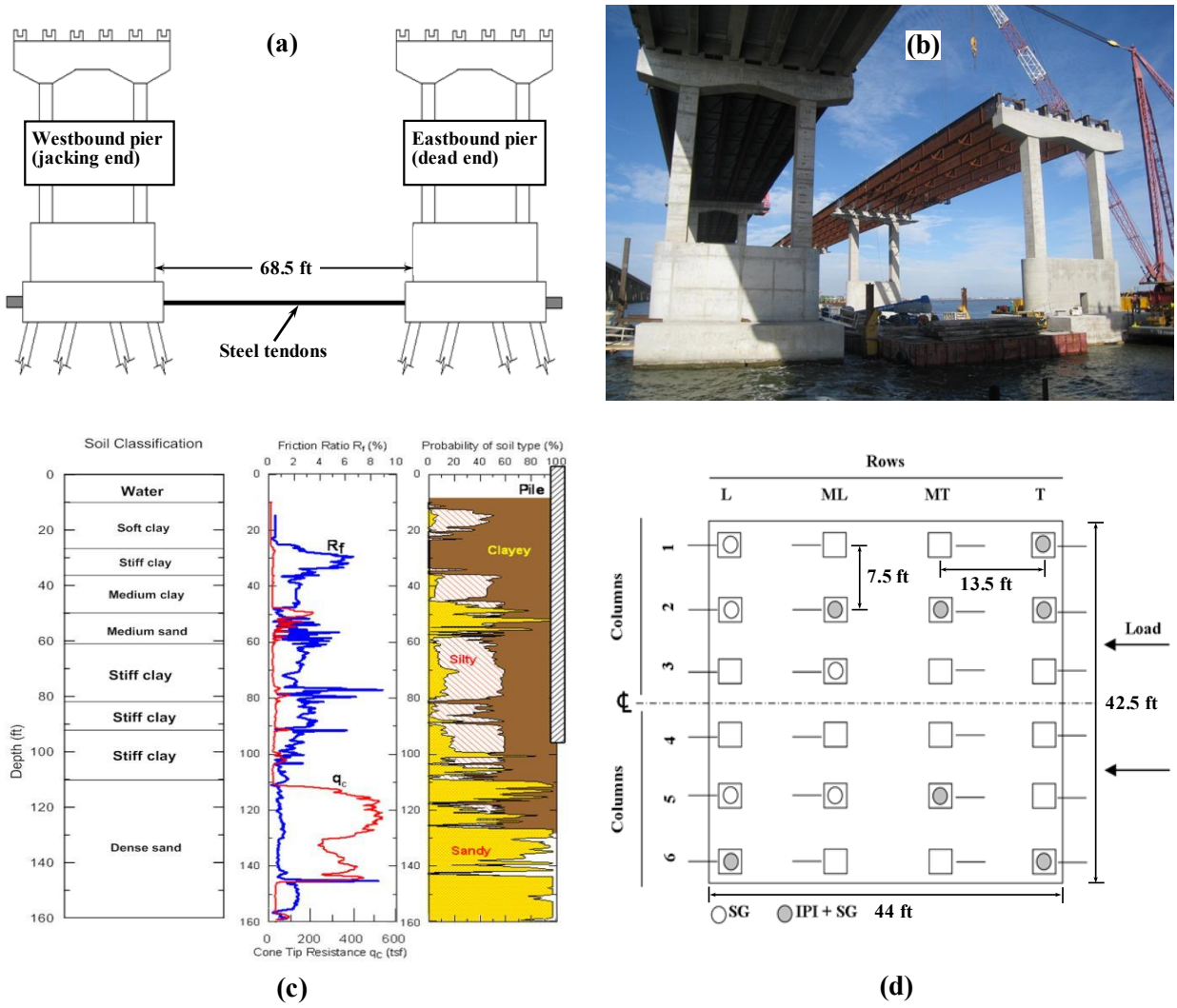

Figure 5.1. Lateral load test of M19 pier foundation (a), test site (b), soil profile and CPT sounding (c), and pile cap dimensions and piles' numbering (d)

5.3 Finite element model description

Three FE models were developed in Abaqus v6.12 for three pile group configurations: Vertical PG, Battered PG, and Mixed PG. Following the previous FE study by Souri et al. (2015), the Vertical and Mixed PGs models were developed based on the Battered PG model of the M19 pier foundation. The three FE models have similar characteristics as will be described in the following, with the only difference in piles' inclination.

The FE models resembled half of the foundation geometry exploiting the symmetry to reduce the solution cost. The pile group (including the cap) and soil body were created

from two separate meshes using the 8-nodes linear continuum brick element (C3D8R). The soil mesh was designed so that the element size increased gradually in the direction away from the pile group. The number of elements for the pile group mesh was ~10500, and ~72000 for the soil mesh. The geometry and dimensions of the three FE models are shown in Figure 5.3. The soil domain boundaries were located far away from the pile group to eliminate their influence on the response. Pile installation effects were ignored in the study, and the piles were placed in pre-bored holes in the soil mesh (i.e. wish-in-place). The connection between the piles and the cap was assumed fixed-head connection. The main steel reinforcement in the piles was included in the FE models to introduce the prestress force. This was achieved using the embedded shell elements (S4R), which was numerically formulated to simulate rebars (Abaqus 2011). Each row of steel tendons in the pile section was replaced by one shell with a total of four shells per pile in a box shape, Figure 5.2.

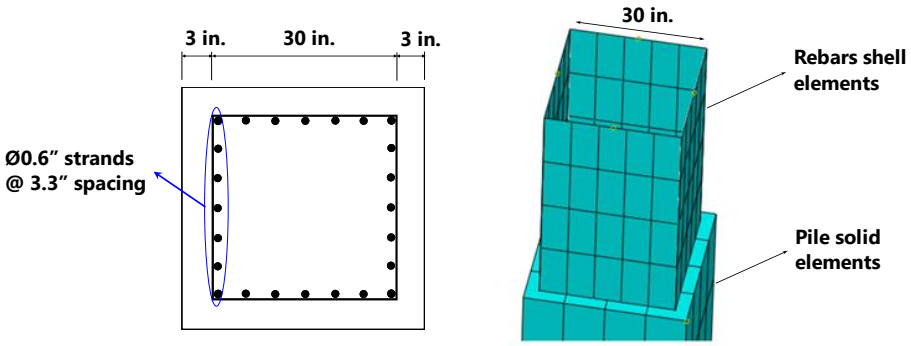

Figure 5.2. Embedded shell elements in the pile's section

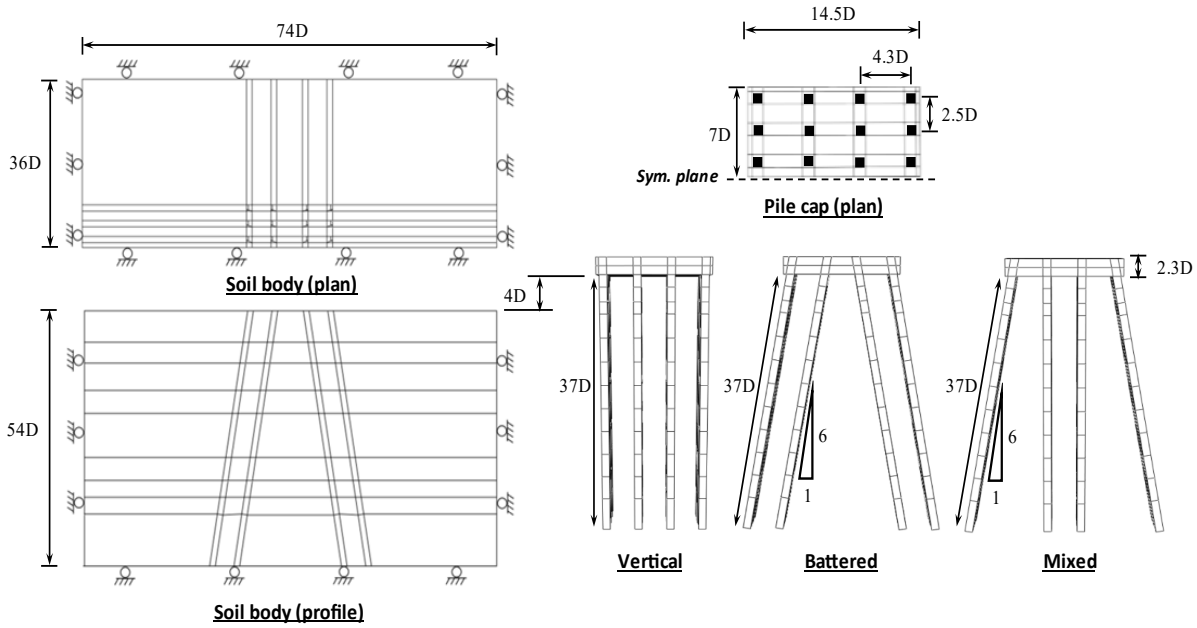

Figure 5.3. Geometry and dimensions of FE models

5.4 Material constitutive and interface models

The laterally loaded pile is a nonlinear problem due to the nonlinear material behavior of concrete piles and soil, and gap formation at the pile-soil interface (e.g. Matlock 1970; Trochanis et al. 1991; Mroueh and Shahrour 2009). In the current study, the nonlinear material behavior is incorporated using advanced elastoplastic constitutive models which are described next followed by the interface model.

5.4.1 Concrete

The concrete damaged plasticity (CDP) was used for pile's concrete material as described previously in section 3.2.1. The parameters used for the CDP model were E_c = 5000 ksi (ACI 318) for f_c' = 8 ksi, Poisson's ratio ν = 0.2. The yield stresses in compression and tension were determined after Mander et al. (1988) and Gupta and Maestrini (1990), respectively.

5.4.2 Clay

The Anisotropic Modified Camclay (AMCC) model was used for clay soils (Dafalias et al. 2006), which was described previously in section 3.2.3. The AMCC model was incorporated in Abaqus thru the UMAT subroutine with a Fortran code written for the model algorithm. The AMCC model parameters used in the study are summarized in Table 5.1.

Table 5.1. Parameters for AMCC and DP models

Soil Type	Depth from Mudline (ft)	Unit Weight (γ) (pcf)	Poisson's ratio (ν)	AMCC						DP		
				κ	λ	M	α_{ini}	*x*	C	κ	β	*d*' (psf)
Soft Clay	0-15	123	0.25	0.03	0.14	0.9	0.034	1.33	4	-	-	-
Stiff Clay	15-25	119	0.20	0.01	0.12	1.1	0.111	1.33	4	-	-	-
Medium Stiff Clay	25-38	108	0.25	0.02	0.13	1.0	0.219	1.33	4	-	-	-
Medium Sand	38-49	120	0.38	-	-	-	-	-	-	0.003	53	10
Stiff Clay	49-70	113	0.20	0.01	0.12	1.2	0.271	1.33	4	-	-	-
Stiff Clay	70-81	122	0.20	0.01	0.12	1.2	0.271	1.33	4	-	-	-
Stiff Clay	81-99	128	0.20	0.01	0.12	1.2	0.363	1.33	4	-	-	-
Dense Sand	>99	124	0.40	-	-	-	-	-	-	0.003	58	10

* κ is slope of unload-reload line in *e*-log *p* plot; λ is slope of virgin consolidation line in *e*-log *p* plot; M is slope of critical state line; α_{ini} is the degree of initial anisotropy ($\alpha_{ini} = \frac{1+3K_o}{1-2K_o}$); *x* and C are model constants; β is friction angle in DP model; d' is the cohesion in DP model; K_o is coefficient of lateral earth pressure (σ_h/σ_v)

5.4.3 Sand

The Drucker Prager (DP) model was used for sand layers, which is well known for modeling the behavior of pressure dependent materials (Chen and Han 2007). The model details were described previously in section 3.2.4. The DP model parameters used in the study are shown in Table 5.1.

5.4.4 Pile-soil interface model

The pile-soil interface was modeled using the contact interface model described in section 3.1.4. The model provides the mechanism for transferring the normal (non-tensile) and tangential stresses at the interface, and pile-soil gap formation. The interface model properties were assumed as $\mu = 0.5$, and τ_{max} was averaged for the soil profile using the undrained shear strength per layer results (1760 psf). The sensitivity of the FE solution to interface friction parameters was found negligible for the laterally loaded piles problem, as similarly reported by Mroueh and Shahrour (2009).

5.4.5 Loads and boundary conditions

The loads applied in the FE models were: gravity, the weight of superstructure, and lateral load. Gravity load was necessary to establish the geostatic stress equilibrium and was applied by defining the gravitational acceleration g = 32.2 ft/s^2. The dead load due to superstructure weight was applied as uniform distributed load on top of the cap in the global vertical direction. The lateral load was applied as uniform distributed load on the side of the cap in the global horizontal direction. For boundary conditions, a pin-type boundary condition was used for the far sides and bottom boundaries of the soil mesh, whereas a roller-type condition was applied on the symmetry plane. The FE solution proceeded as follows: in the first step, the gravity load was activated to establish the geostatic stress in the soil and initial equilibrium. Then, the dead load of the superstructure was activated in the second step. The lateral load was applied in increments up to 5500 kips in subsequent steps (Souri et al. 2015).

5.5 Results

5.5.1 Load-displacement curves

Comparison of the load-displacement response for the PGs is shown in Figure 5.4. Under the same lateral load, the vertical PG exhibited lesser lateral resistance compared with the battered and mixed PGs, which was due to the additional lateral resistance from the battered piles. For instance, at the maximum load, the displacement in the vertical PG was 11 inches while it was 3 inches in the battered PG and 6.5 inches in the mixed PG. The figure also depicts the average lateral load carried by each row in the PGs. It is noticeable that the load distribution is affected by the presence of battered piles. In the vertical PG, the largest load share was carried by the leading row L (31% at max load) followed by rows ML (24%), MT (23%), and T (22%). For the battered PG, the middle rows carried larger share with 31% and 28% for rows ML and MT, and 22% and 19% for rows L and T, respectively. For the mixed PG, the load share distribution was 36%, 17%, 18%, and 29% for rows L, ML, MT, T, respectively. The load share percentages indicate that the lateral load is likely to be closely distributed in vertical PGs, and nonuniformly distributed in the battered and mixed PGs.

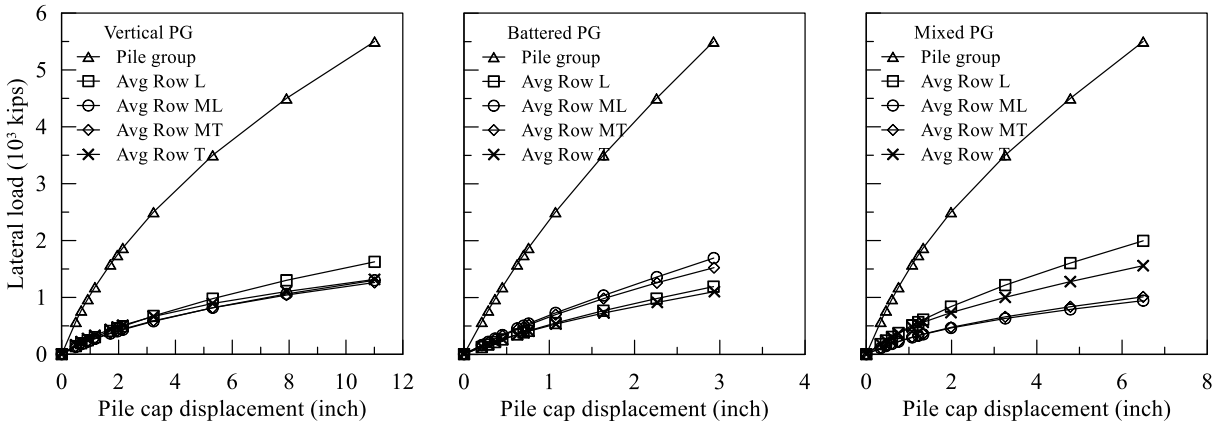

Figure 5.4. Load-displacement response for the vertical, battered, and mixed pile groups

The lateral stiffness of the PGs are compared in Figure 5.5. It can be noticed that the lateral stiffness decreased nonlinearly with displacement in all PGs at a similar rate. The relative stiffness results show that the battered PG was 120% stiffer than the vertical PG, while for the mixed PG it was about 48% stiffer.

5.5.2 Axial reaction in piles

The axial reaction (F_{axial}) per pile versus the group lateral load (H) results are shown in Figure 5.6. Note that the positive sign means the force is compressive (i.e. push in), while the negative sign means it is tensile (i.e. pull out). First, it is noticed that the axial load in a pile and its mirror pile was similar in magnitude, assuming that the mirror axis passes between the middle rows and perpendicular to the load direction. For example, the axial reaction in pile L1 and its mirror pile T1 was similar in magnitude and different in load sign. Second, in any row for all PGs, the axial reaction was largest in piles within the edge column (i.e. column 1), which was due to the weaker influence from the group effect. Third, the average axial reaction per row differs between the PGs. In the vertical PG, the axial reaction was largest in the leading and trailing rows (L and T) with a row average of 8% and stabilized with increased lateral load. In the battered PG, the axial load was largest in the middle rows (ML and MT) and increased linearly with lateral load from 10% to 12.5%. For the mixed PG, the largest axial reaction was in rows L and T with 8.5% row average. One interesting observation was that the axial reaction was compressive in row MT and tensile in row ML in the mixed PG, which is opposite to the observation in the vertical and battered PGs.

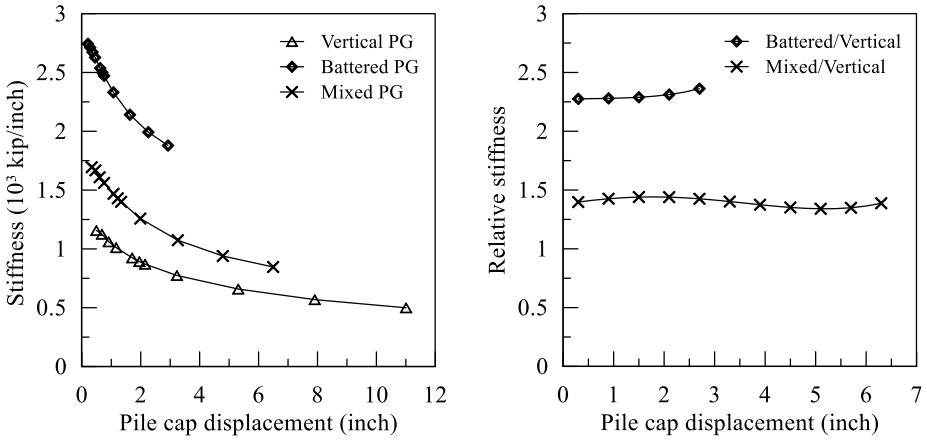

Figure 5.5. Comparison of the PGs lateral stiffness

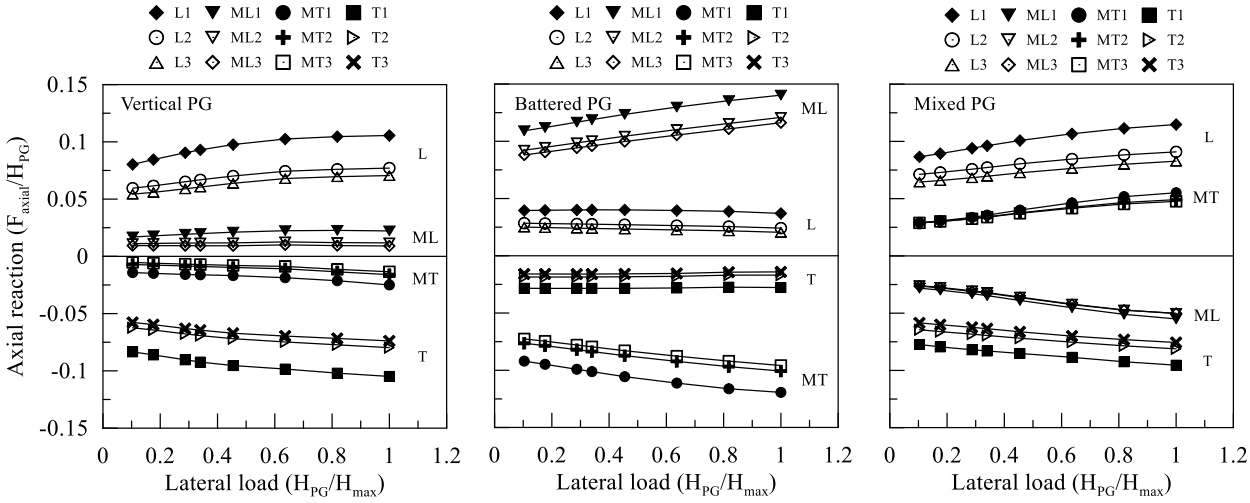

Figure 5.6. Variation of the axial reaction in the piles

5.5.3 Lateral load distribution

The lateral load distribution per pile for all PGs is depicted in Figure 5.7. It should be noted here that the sum of piles' loads (in the plots) for each PG is 50%, which is due to the fact that the FE model represents half of the PG foundation. For the vertical PG case, the lateral load share varied only in rows L and T and remained fairly constant in rows ML and MT. The lateral load in row T decreased steadily to reach a similar load as in rows ML and MT, while in row L the load kept increasing. In the battered PG case, the lateral load distribution exhibited slight variation with lateral load while keeping same order for rows share. In a similar way to axial load, rows ML and MT carried a larger share of lateral load compared to rows L and T. For the mixed PG, a larger contrast in load share is noticed between rows L, T, and ML, MT (2-3%) compared to the vertical and battered PGs. Load share in rows L and T exhibited notable variation, similar to the vertical PG case. When

comparing pile columns, the edge column (column 1) exceeds columns 2 and 3 load share by 0.5-1.0% for all PGs.

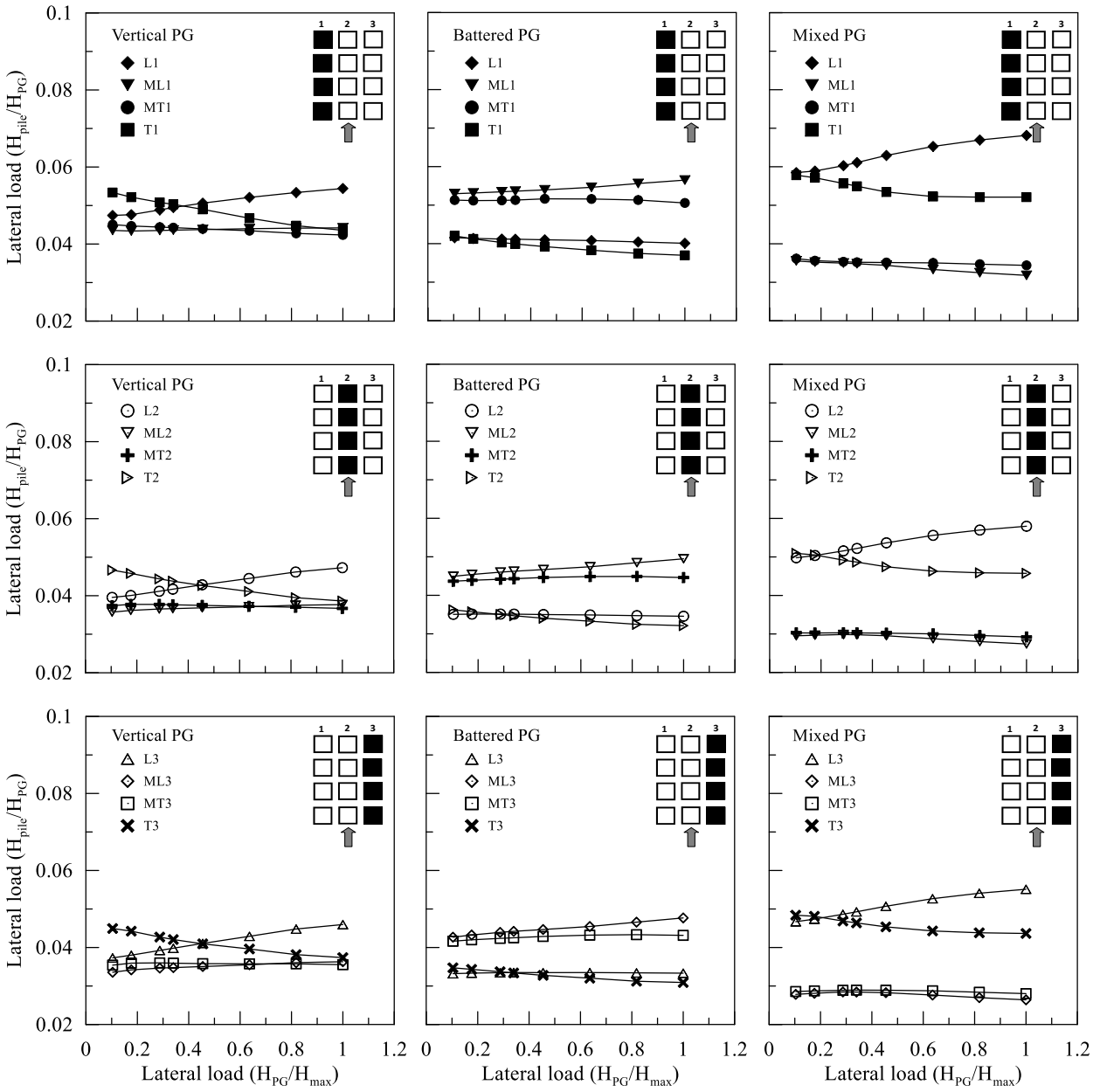

Figure 5.7. Comparison of the lateral load distribution

5.5.4 Bending moment

Bending moment (BM) variation at the pile-pile cap connection is shown in Figure 5.8. BM in the vertical PG kept increasing with lateral load and was higher than battered and mixed PGs. In the battered PG, the rate of increase in BM was much less compared to other PGs. Similar to previous observations, piles in the edge column (column 1) carried higher BM magnitude compared to columns 1 and 2.

A comparison of BM profiles is shown in Figure 5.9. First, the point of BM inflection (i.e. sign change) was located at a similar depth in all PGs (7-8D). Second, the area under the BM curve was largest in the case of vertical PG, and it took greater depth to approach zero value (32D). In the battered PG case, the area under the BM curve was less, and it approached zero at a shallower depth (25D). For the mixed PG, the area under the BM curve varied between the piles with row T piles carrying the lowest BM, and the depth at which the BM approached zero was 30D.

5.5.5 Damage in piles

The damage in the piles is visualized by damage parameter "*d*" contour plot. The damage parameter "*d*" reflects the reduction in concrete stiffness, and is a function of plastic strain. The value of "*d*" evolves with the accumulated plastic strain from zero (i.e. no damage) to 1.0 (i.e. fully damaged). The concrete material damage initiates when the strength limit (compression or tension) is exceeded. Figure 5.10a,b,c are contour plots for damage variable "*d*" highlighting the damaged regions in the piles, in which the darker color means greater damage level. For the vertical PG (Figure 5.10a), the damage regions were near the pile cap and at depth 16D from the cap bottom in all piles. These two areas are located near the maximum BM as noticed in BM profiles (Figure 5.9). Near the pile cap, the damage appeared in the front side of piles, in which concrete elements were in tension, with similar damage intensity observed between all piles. At depth 16D, the damage appeared in the rear side and spread in a larger area with milder intensity. For the battered PG (Figure 5.10b), the damaged regions were located near the pile cap in all rows, and in row MT only at depth 16D from the cap bottom. Near the pile cap, the damage appeared in the front side with higher intensity in the trailing rows (MT, T). The leading rows (L, ML) exhibited smaller damage area and milder intensity compared to the trailing rows. This is referred to the combined effect of the axial load and BM. In the trailing rows, the axial load was tensile and had a combined effect with BM so that the concrete in the front side fail earlier in tension. While for the leading rows, the axial load was compressive and negated BM action. At depth 16D, the damage was minimal and limited to the rear side in row MT. For the mixed PG (Figure 5.10c), the damaged regions were located near the pile cap in all rows, and in rows L, ML and T at depth 16D. The damage intensity, in this case, was lesser than the vertical and battered PGs (notice the lighter color). At depth 16D, the damage was more notable in rows ML and T due to the combined effect of tensile axial load and BM.

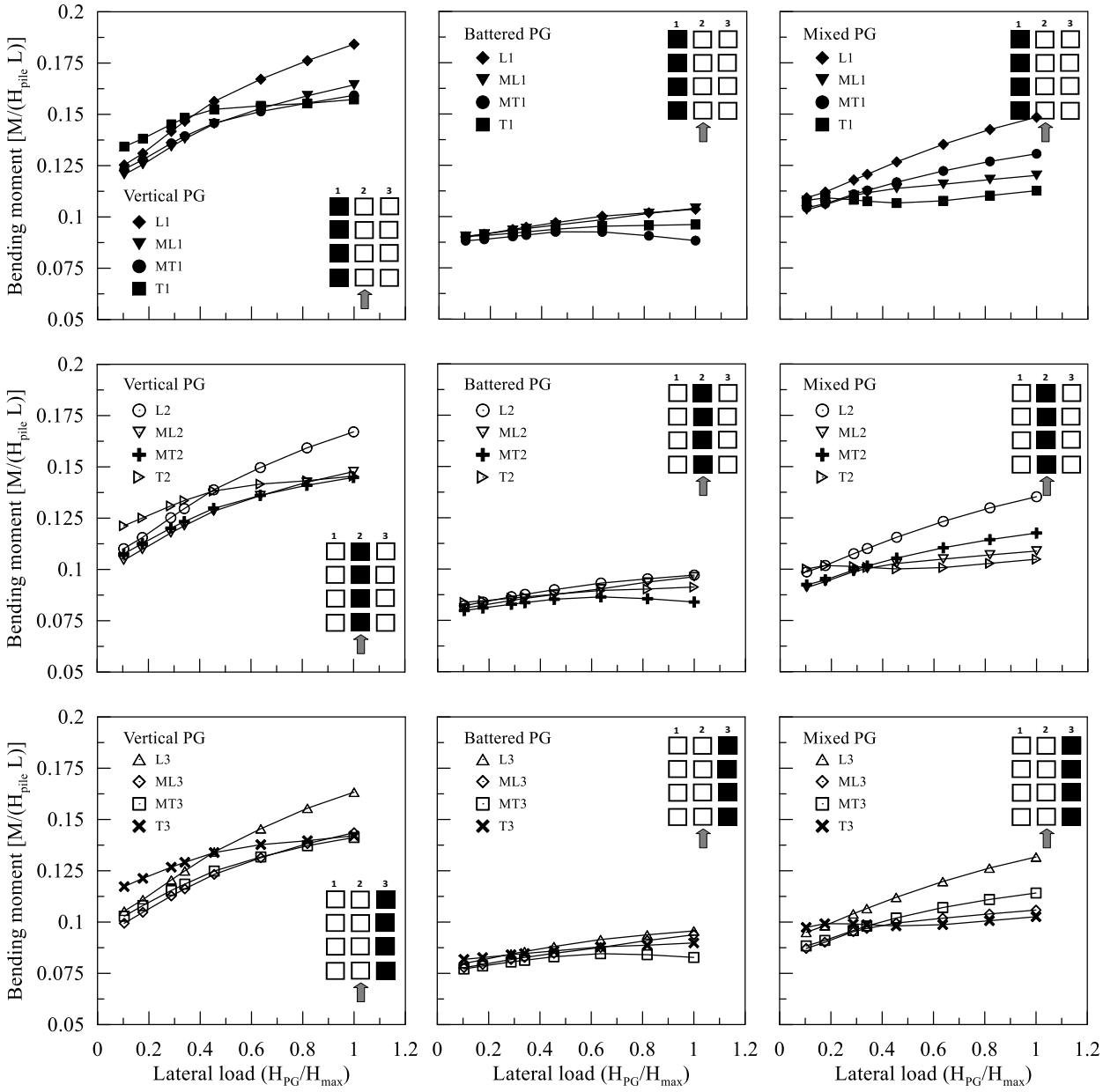

Figure 5.8. Bending moment variation with lateral load at the pile cap connection

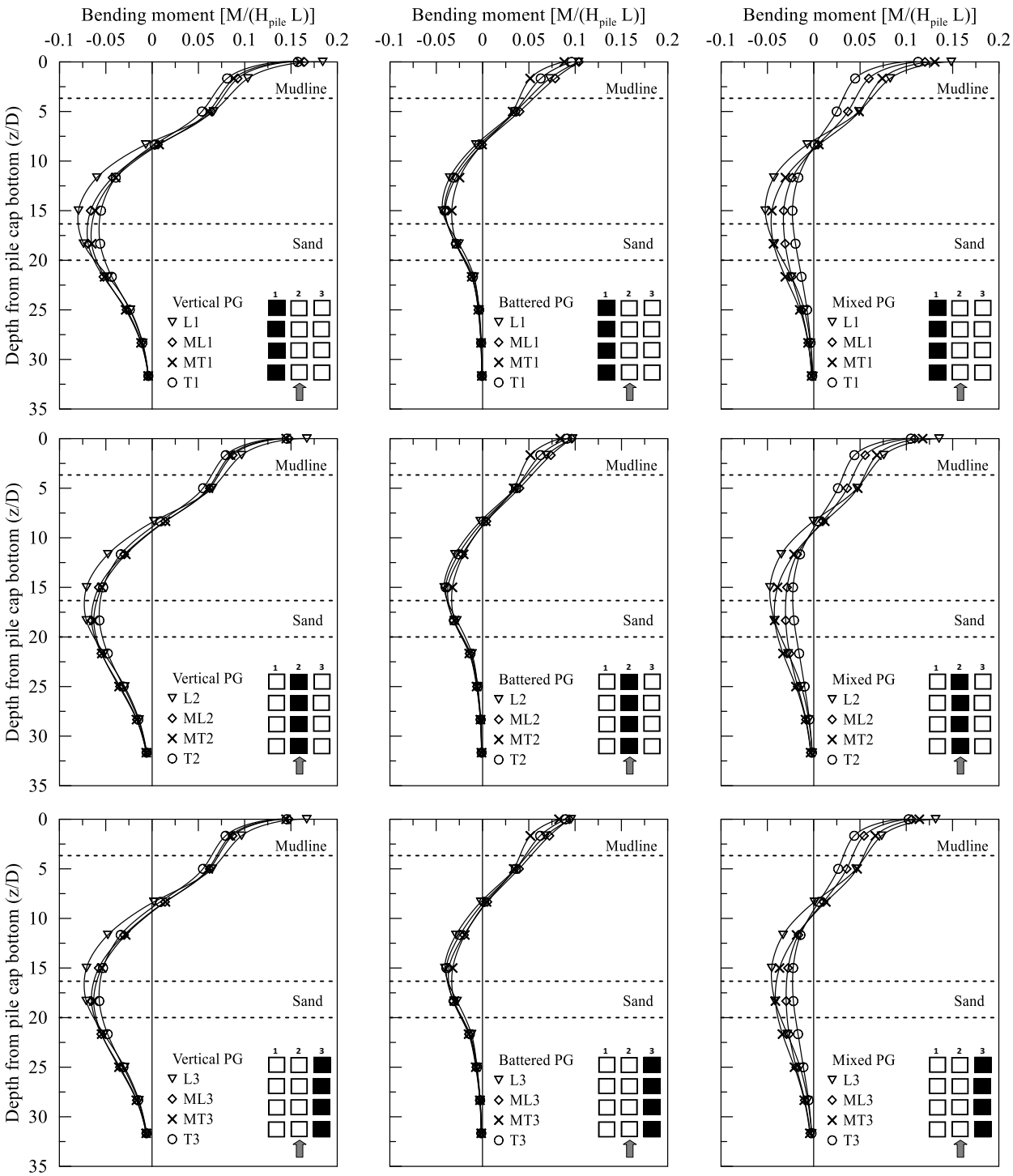

Figure 5.9. Bending moment profiles at 5500 kips

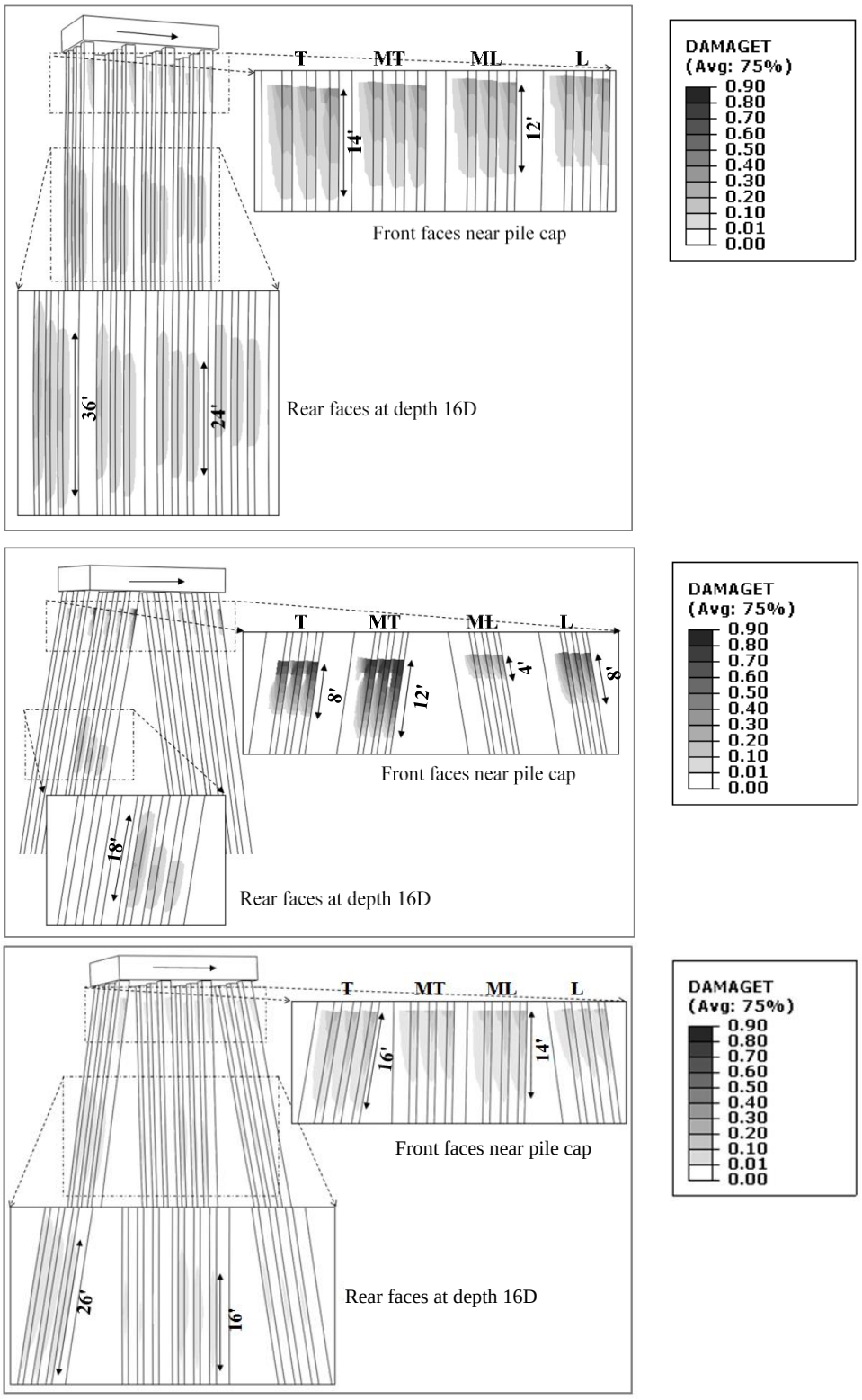

Figure 5.10. Damage contours at 5500 kips for (a) vertical, (b) battered, and (c) mixed PGs.

5.5.6 Soil resistance profiles

Soil resistance profiles in each pile were obtained using the double differentiation of BM curve technique (e.g. Ilyas et al. 2004; Nip and Ng 2005; Abu-Farsakh et al. 2011b). Figure 5.11 shows soil resistance profiles for all piles in the PGs. It should be noted that the zero-depth reference in the figure is the mudline. The sign convention in the figure refers to the acting direction of soil resistance. Positive resistance value means it acted in a direction opposite to pile movement direction, and vice versa. First, it is noticed that profiles are similar for all piles in the same PG, even though the mixed PG has both vertical and battered piles. The soil resistance in all PGs switched to a decreasing trend within the sand layer, which can be referred to the higher stiffness of sand material. The depth at which soil resistance changed sign was greater in the vertical PG (18-20D) compared to 15D in the battered PG and 16-18D in the mixed PG. The soil resistance diminished at shallower depth in the battered PG (20D) compared to the vertical and mixed PGs which reached to greater depths (29D). On the side of positive resistance, the vertical PG mobilized greater soil resistance in front of the piles compared to other PGs (58% greater than battered PG, and 43% than mixed PG based on average area under the curves).

5.5.7 *p-y* curves

The variation of normalized soil resistance (*p*) with lateral pile displacement (*y*) at certain depth is a nonlinear curve called "*p-y* curve". In the beam-springs model representing the lateral pile behavior problem, the nonlinear spring stiffness in the model is given by the *p-y* curve. In the current FE study, *p-y* curves are back-calculated using soil resistance and pile deflection values. Figure 5.12 shows *p-y* curves for all PGs obtained at selected depth z/D=4.6. Each sub-figure contains *p-y* curves for piles in the group and for isolated single piles (vertical, positive battered and negative battered). Note that the *p-y* curves for single piles in all sub-figures are the same, and may look different due to the different scale of the horizontal axis. When comparing *p-y* curves for the PGs with single piles, the influence of the group effect is noticeable in the softer *p-y* curves in all PGs. Also, columns 2 and 3 piles had softer *p-y* curves compared to column 1 piles (edge piles) due to the higher influence of the group effect from neighboring columns. When comparing piles rows, the soil resistance was highest in the leading row. The Middle rows (ML and MT) had similar *p-y* curves in all PGs.

The *p-y* curves from the FE solution allows back calculating the *p*-multipliers (Brown et al. 1987), which provide quantitative measure for the group effect in PGs. The *p*-multiplier is defined as the ratio of soil resistance for pile-in-group (p_g) to the soil resistance for isolated single pile (p_{single}) at certain displacement (*y*), and typically assumes values less than unity. Figure 5.13 shows variation of *p*-multipliers with pile displacement in all PGs. overall, the *p*-multipliers were higher and more stable with displacement in the battered PG, which was due to the increased pile-pile spacing with depth. The vertical and mixed PGs had closely similar *p*-multipliers for rows ML, MT, T, and notably differ only in row L, which was higher

in the mixed PG. The largest change in the *p*-multiplier is noticed in row T for all PGs. This indicates that soil resistance mobilized early in row T with limited influence from the group effect, and then gradually decreased due to the movement of piles in the rows ahead.

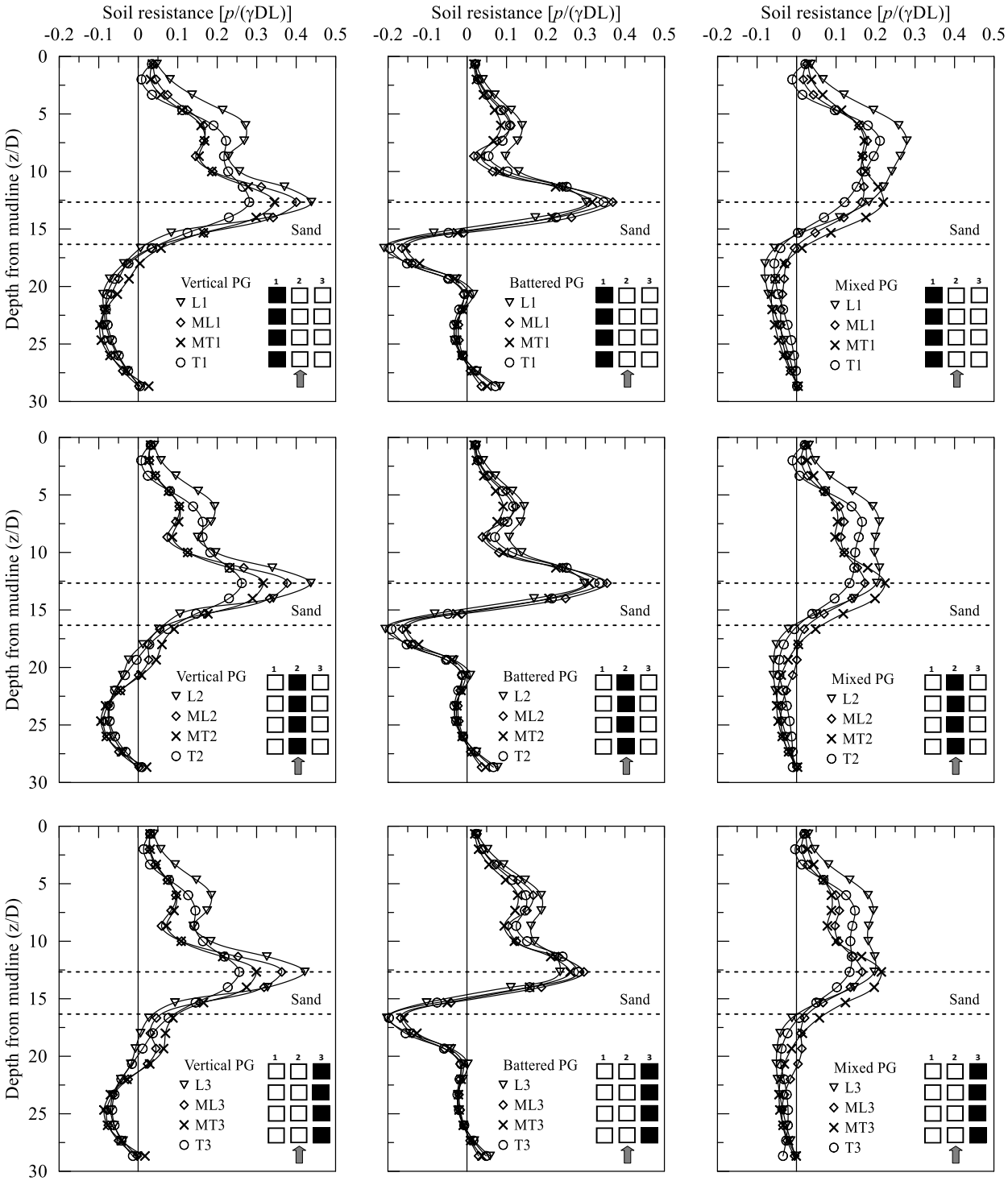

Figure 5.11. Soil resistance profiles at 5500 kips

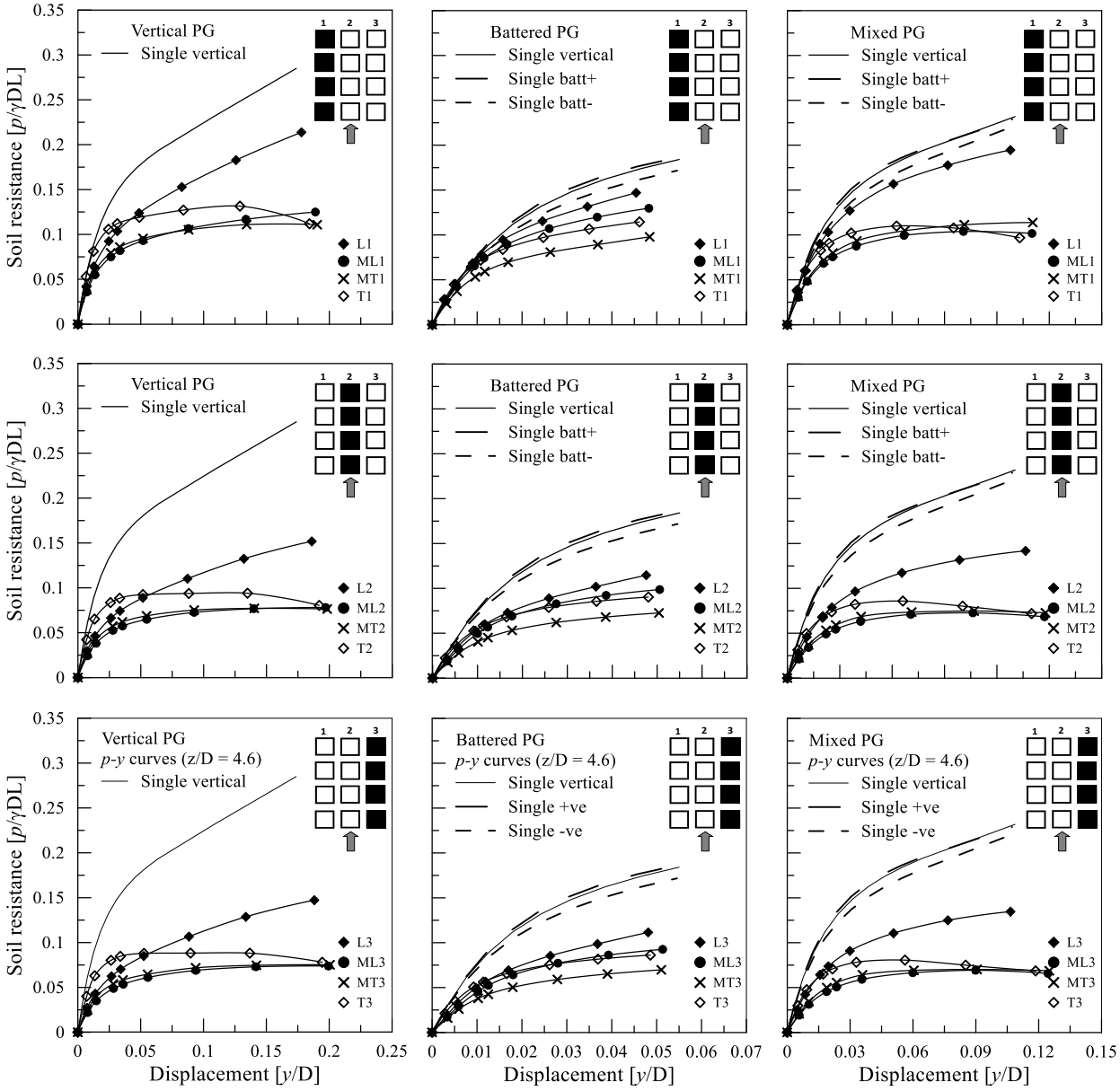

Figure 5.12. Back-calculated *p-y* curves at depth z/D = 4.6

The *p*-multipliers averaged over the displacement are summarized in Table 5.2, Table 5.3, Table 5.4 for each PG. The *p*-multipliers for column 1 (edge column) is notably higher than columns 2 and 3 in all PGs with 0.2 difference. This observation leads to the conclusion that the average *p*-multiplier for a row would decrease with increasing number of columns. This is following the fact that there are only two edge columns in any PG, and their influence on the average *p*-multiplier would decrease with increasing number of interior columns.

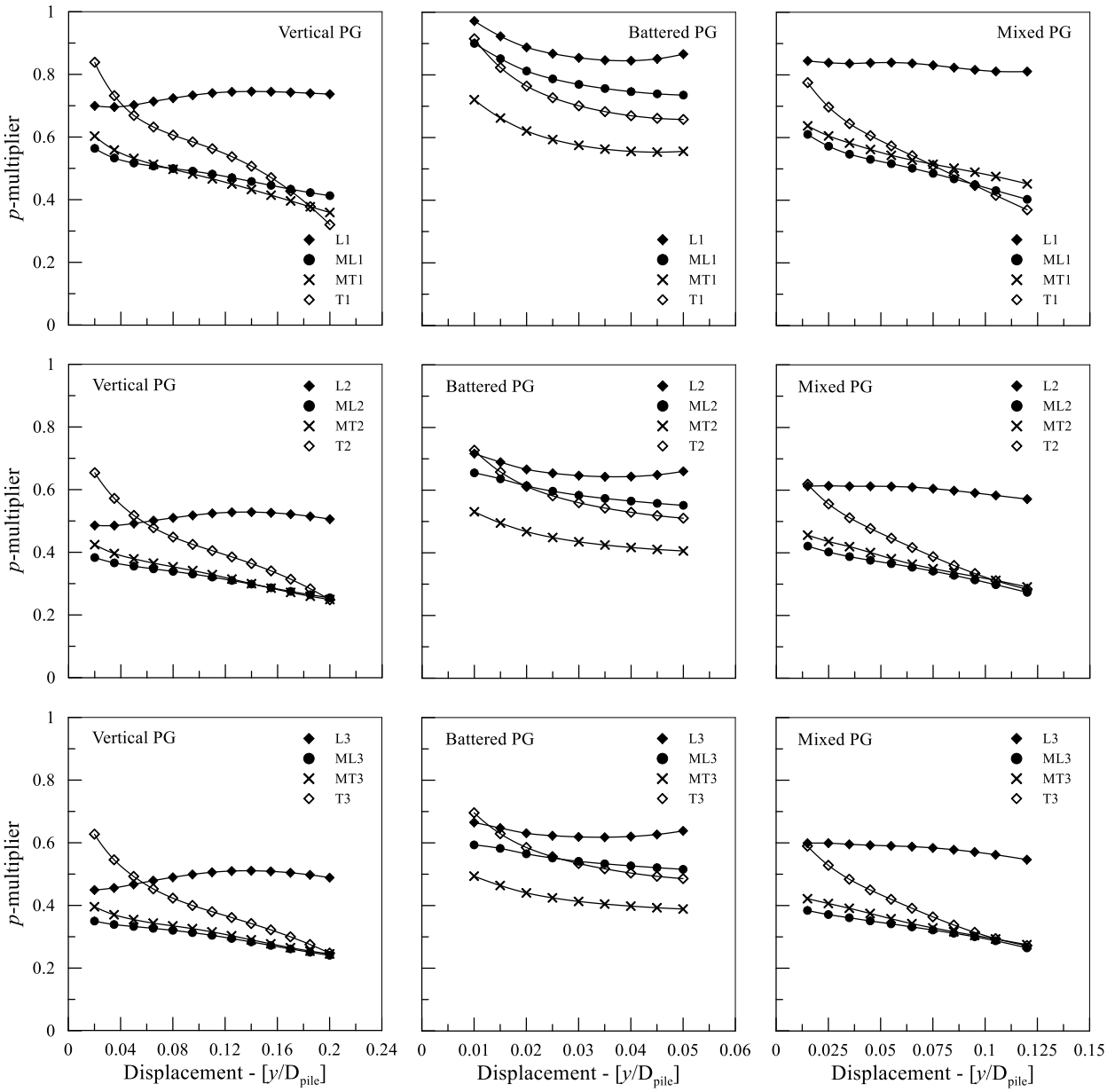

Figure 5.13. Back-calculated *p*-multipliers at depth z/D=4.6

The *p*-multipliers for the leading and trailing rows for all PGs are compared to the recommended values from literature in Figure 5.14. The recommended values of *p*-multipliers in the figure are provided as a function of pile spacing in the loading direction (S_L) only, while it assumes similar pile spacing for the transverse direction ($S_L = S_T$). In the current study, the *p*-multipliers for the leading and trailing rows in the PGs are notably below the recommended values, with the exception of row T in the battered PG. This is possibly due to the fact that pile spacing was non-symmetric at the pile cap level in all PGs

(S_L = 4.3D, S_T = 2.5D). The smaller spacing in the transverse direction resulted in a greater influence of the group effect. Finally, the large number of columns is another factor that lowered the average *p*-multiplier as mentioned previously.

Table 5.2. Average *p*-multipliers for vertical PG at depth z/D=4.6

	Row			
Column	L	ML	MT	T
1	0.73	0.49	0.48	0.59
2	0.51	0.32	0.34	0.44
3	0.49	0.30	0.32	0.42
Row average	0.58	0.37	0.38	0.48

Table 5.3. Average *p*-multipliers for battered PG at depth z/D=4.6

	Row			
Column	L	ML	MT	T
1	0.89	0.81	0.62	0.77
2	0.67	0.60	0.46	0.61
3	0.64	0.55	0.43	0.58
Row average	0.73	0.65	0.51	0.65

Table 5.4. Average *p*-multipliers for mixed PG at depth z/D=4.6

	Row			
Column	L	ML	MT	T
1	0.87	0.54	0.57	0.61
2	0.63	0.37	0.39	0.47
3	0.61	0.35	0.37	0.44
Row average	0.70	0.42	0.44	0.51

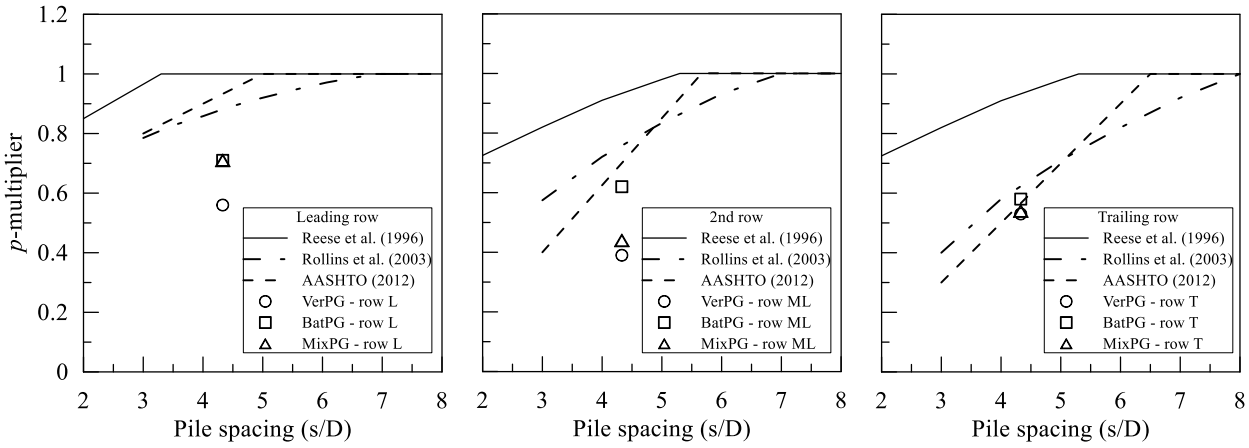

Figure 5.14. *p*-multipliers from current study compared to recommended values in literature.

Chapter 6. Parametric Study for the Effect of Pile Spacing and Clay Soil Type on the Lateral Behavior of Pile Groups

6.1 Introduction

In this chapter, the results of a parametric investigation for the effect of pile spacing and clay soil type is discussed. For the effect of pile spacing, three pile group (PG) types are considered at three pile spacings. Additionally, a pile group composed of four vertical piles in one line at similar pile spacings is also studied. For the effect of soil type, clay strength parameters corresponding to soft, medium, and stiff clays are considered. The variables investigated are the axial reaction, shear force, pile group efficiency, and *p*-multipliers.

6.2 FE models

6.2.1 Geometry and FE mesh

The effect of pile spacing and clay soil type is studied for three PG types: vertical, battered, and mixed. Each PG comprised of eight concrete piles in a 4x4 arrangement, in which each pile had a square cross-section and measured 3 ft wide (D) and 110 ft long. Due to model symmetry, the FE model resembled half of the PG geometry. The three pile spacings (S) considered were: 3D, 5D, and 7D measured at the pile cap level (Figure 6.1). The soil body was created from single soil material and was sized large enough to eliminate the influence of boundaries. The PG and soil body models were made of two separate FE meshes, in which the piles were placed in holes pre-cut into the soil body (i.e. wish in place). The interaction between the PG and soil models was governed by the interface model. The total number of solid continuum brick element with 8 nodes (C3D8R) used was ~70000.

In addition to the three PGs, a group composed of four vertical piles arranged in single line was studied. The influence of pile spacing and clay soil type for this PG was investigated for two loading conditions; the first is when the loading direction is concurrent with the line of piles (termed as single-column), while the second is when the loading is transverse to the line of piles (termed as single-row), see Figure 6.2. Similar to the previous PG models, the pile spacings was varied from 3D to 7D, and the PG and soil body models were made of two separate FE meshes. The total number of solid elements (C3D8R) used was ~50000.

Table 6.1 summarizes the pile groups cases considered in the parametric study. Each PG type was analyzed at three spacings (3D, 5D, 7D) and three clay soil types (soft, medium, stiff), which resulted in a total of nine unique cases per PG.

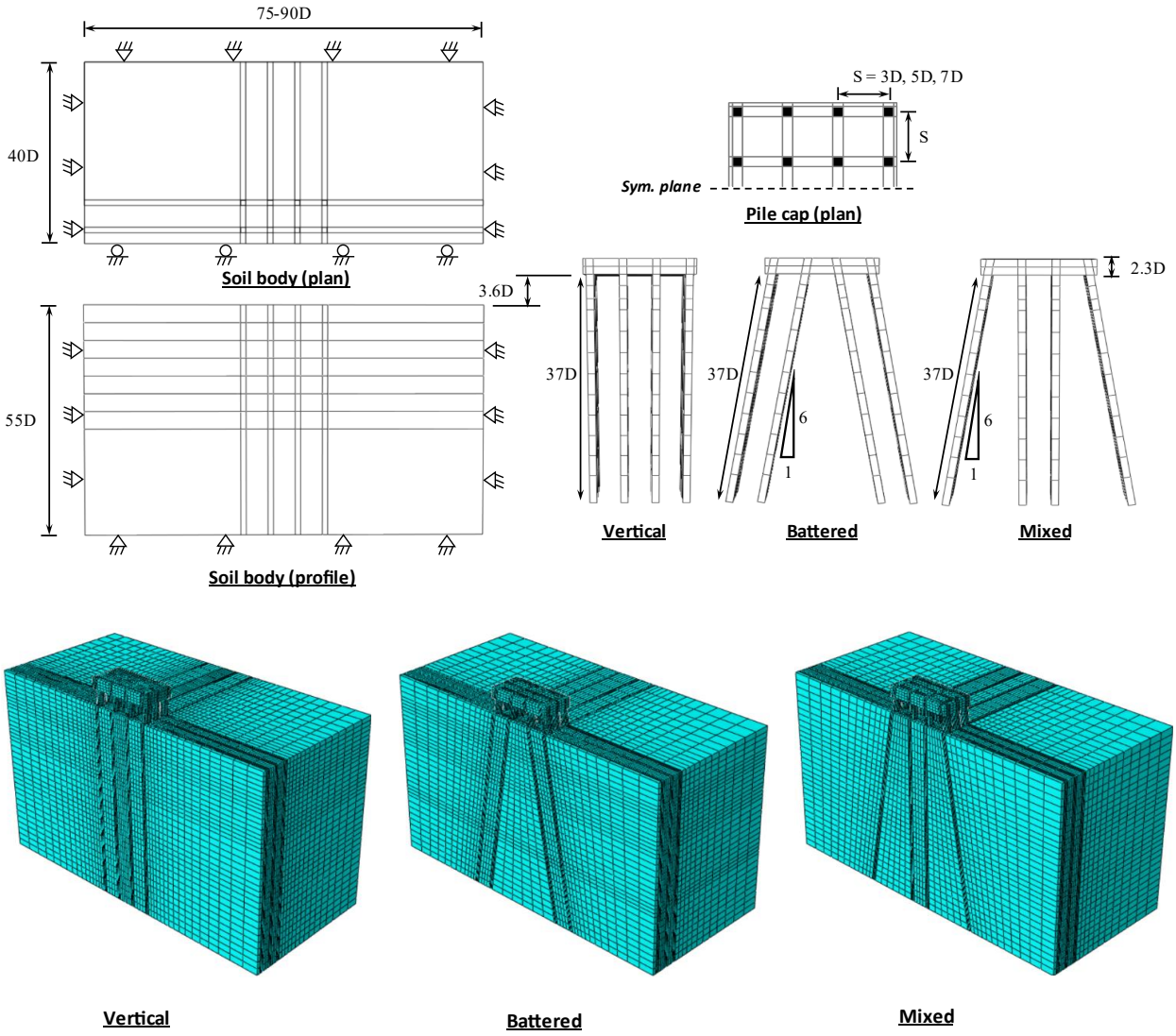

Figure 6.1. PGs FE models used in the parametric study

Table 6.1. PG cases considered in parametric study

Pile group type	Pile-pile spacing (w.r.t pile size D)	Clay soil type
Vertical	3, 5, 7	Soft, Medium, Stiff clay
Battered	3, 5, 7	Soft, Medium, Stiff clay
Mixed	3, 5, 7	Soft, Medium, Stiff clay
Single column	3, 5, 7	Soft, Medium, Stiff clay
Single row	3, 5, 7	Soft, Medium, Stiff clay
Total number of cases = 45		

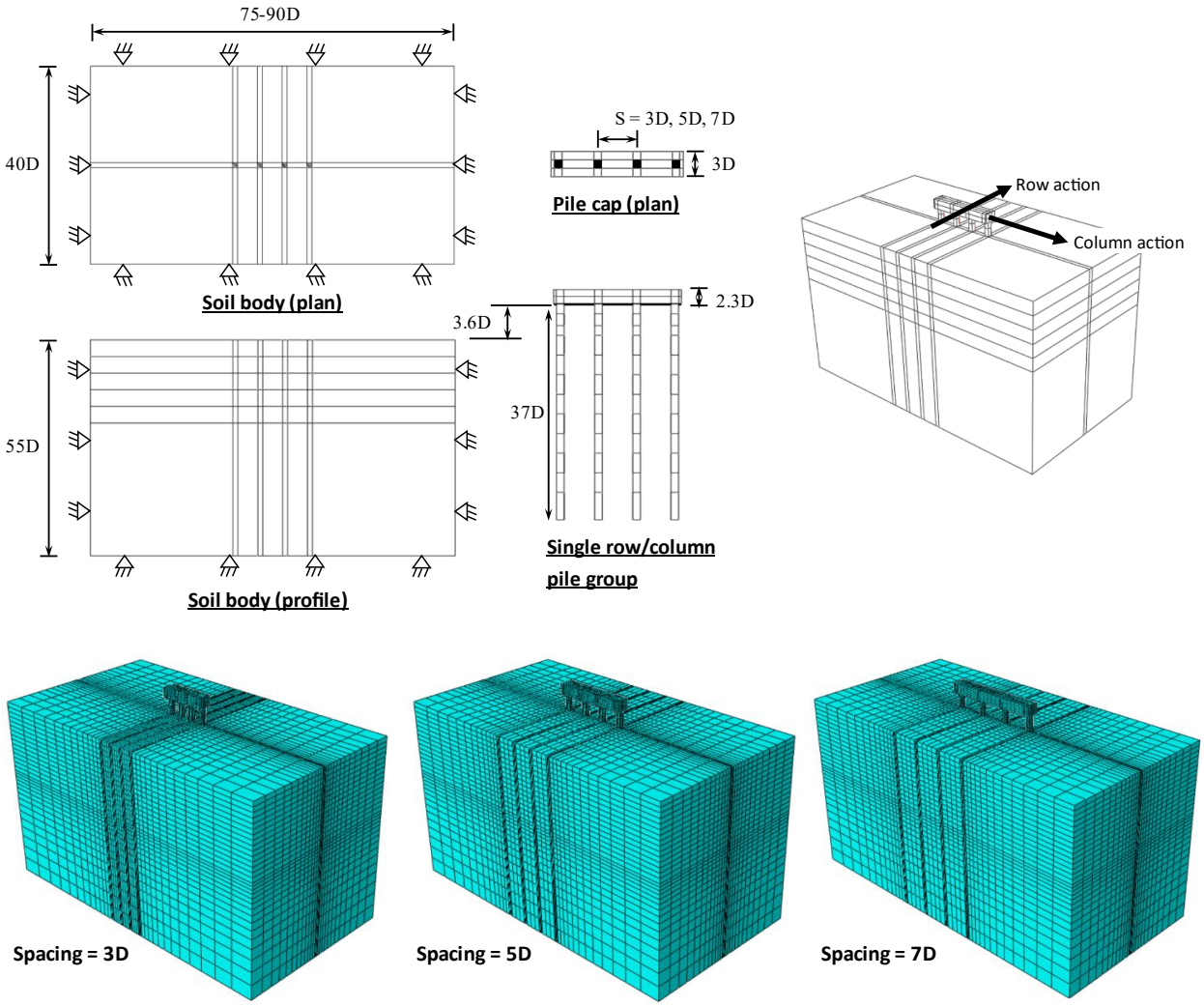

Figure 6.2. Dimensions and FE models for the single row PG

6.2.2 Material constitutive and interface models

The constitutive models, previously described in Chapter 2, were used in the parametric study. The concrete constitutive behavior was modeled using the elastoplastic CDP model, and the clay soil material using the AMCC model. The CDP model parameters used here are given in section 3.2.1. The soil body was made of single clay material, and the AMCC model parameters for three clay soil types soft, medium, and stiff are summarized in Table 6.2. The soil strength and stiffness properties for each clay category were obtained from the literature (Das 2011; Day 2012) and were used to estimate the clay model parameters. The pile-soil interface was modeled using the contact feature described in Chapter 2, assuming interface friction coefficient $\mu = 0.5$, and slipping shear stress limit of $\tau = 2000$ psf.

Table 6.2. Clay soil material properties used in the parametric study

Soil type	Unit weight (pcf)	Undrained shear str. s_u (psf)	Poisson's ratio (ν)	K_o	AMCC model parameters						
					e_o	α_{ini}	M	κ	λ	x	C
Soft clay	120	250	0.25	1.0	0.8	0.03	0.6	0.030	0.17	1.33	4
Medium clay		750			0.8	0.03	0.8	0.010	0.11	1.33	4
Stiff clay		1500			0.8	0.03	1.4	0.007	0.09	1.33	4

6.2.3 Loads and boundary conditions

The loads applied in the FE models were (1) gravity, (2) weight of superstructure, and (3) lateral load. The lateral load was applied as uniform distributed load on the side of the pile cap, and its magnitude was determined at the corresponding pile cap displacement. For boundary conditions, the displacement on the far side and bottom soil boundaries were restrained using pin-type condition, and for the symmetry plane, a roller-type condition was used as shown in Figure 6.1 and Figure 6.2.

6.3 Results

The results for the effect of pile spacing on the axial reaction, piles' shear, pile group efficiency, and *p*-multipliers are reported here for the medium clay soil only. This is because the influence of clay soil type vanishes by the normalization of the axial reaction, piles' shear, pile group efficiency results. Therefore, the effect of clay soil type is discussed only for the *p*-multipliers.

6.3.1 Effect of pile spacing on the axial reaction

The effect of pile spacing on piles axial reaction generated from lateral loading is discussed. The axial reaction here refers to the net change in the axial force in the piles due to lateral load. The axial force in total remains compressive in the piles due to the self-weight of the structure. The axial reaction was obtained at the pile cap elevation at four pile cap displacements (0.5, 1.0, 1.5, 2.0 inches). The results for axial reaction was normalized using the group lateral load (H_{PG}) at the corresponding pile cap displacement. The influence of pile cap displacement on the axial reaction is investigated in Figure 6.4. It can be seen that the normalized axial reaction was fairly constant in all PGs, and therefore considered independent of the pile cap displacement.

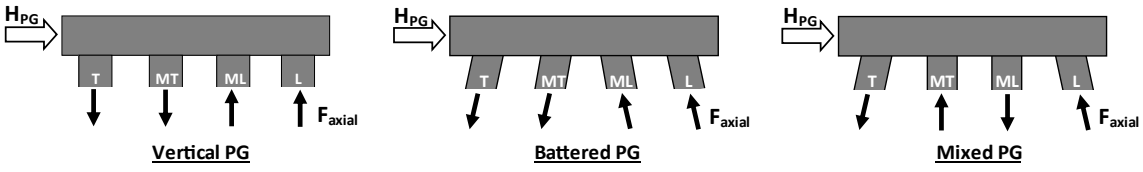

Figure 6.3. Definition of the axial reaction in the PGs

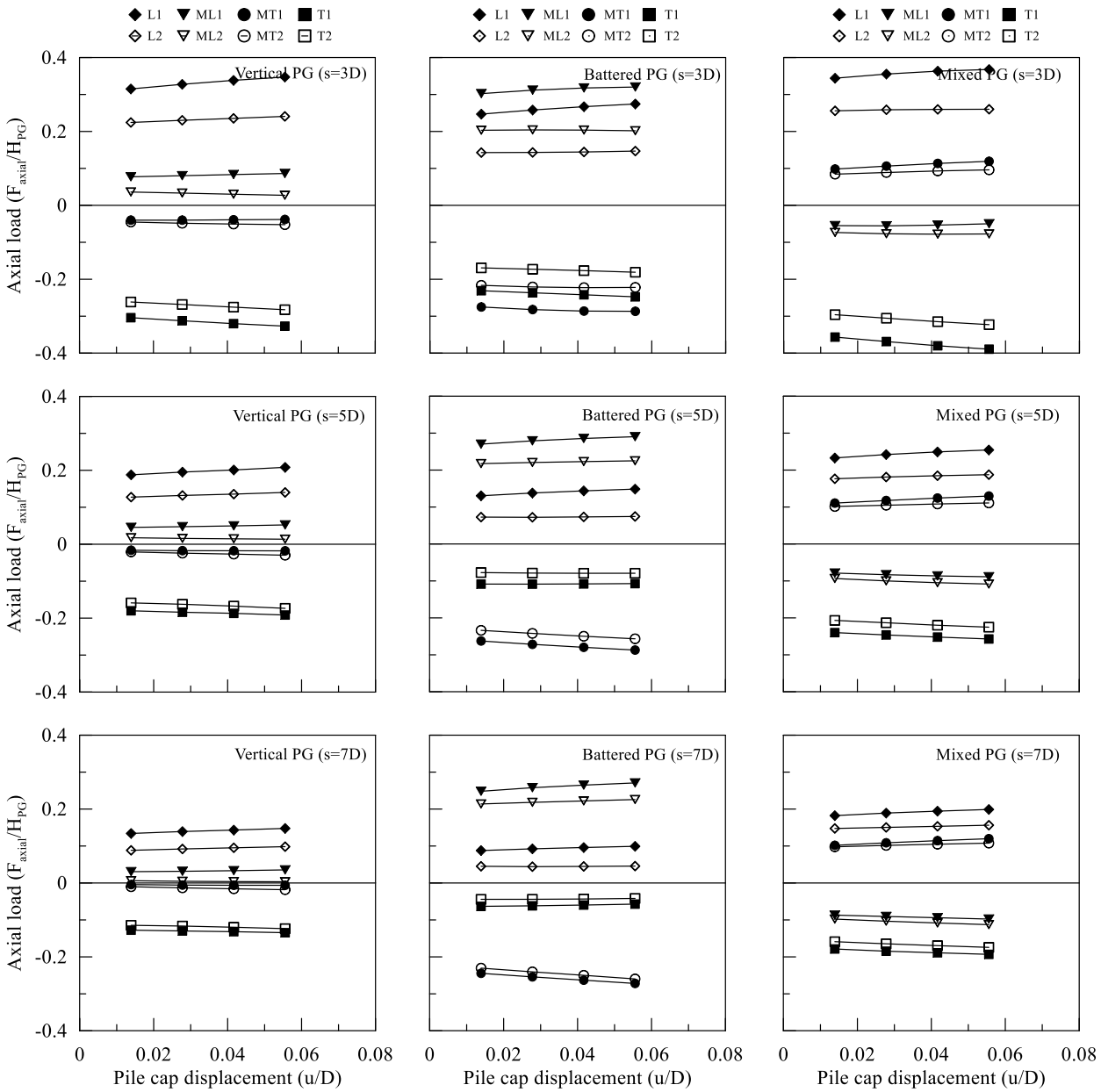

Figure 6.4. Effect of pile cap displacement on axial reaction

The effect of pile spacing on the normalized axial reaction is depicted in Figure 6.5Figure 6.6 and Figure 6.6. From statics, the axial reaction is expected to decrease at larger pile spacing due to the increased moment arm from the pile axis to the axis of rotation of pile cap. In the vertical PG, the significant percentage of axial reaction was found the leading and trailing rows (L, T) with an average of 57% at 3D spacing. The axial reaction percentage decreased with increased pile spacing in all piles. The largest decrease was in the leading and trailing rows at an average of 34% when the spacing increased from 3D to 7D. In the middle rows (ML, MT), the axial reaction percentage was relatively small at 10% and the percentage dropped to 4% at 7D spacing.

In the battered PG, the axial reaction percentage was significant in all piles with an average of 40% in the leading and trailing rows and 50% in the middle rows at 3D spacing. The decrease in axial reaction when spacing increased was notable only in the leading and trailing rows with 28% reduction on average, while in the middle rows the average percentage remained fairly constant.

In the mixed PG, the axial reaction percentage was highest in the leading and trailing rows with an average of 65% at 3D spacing and dropped 30% when the spacing increased to 7D. The middle rows showed a slight change in the percentage and remained around 20%. Moreover, the axial reaction in rows ML and MT was tensile and compressive, respectively, which was in contrary to the observation in the vertical and battered PGs. The common observation in the three PG cases is that the axial reaction significantly decreased only in the leading and trailing rows when the pile spacing increased.

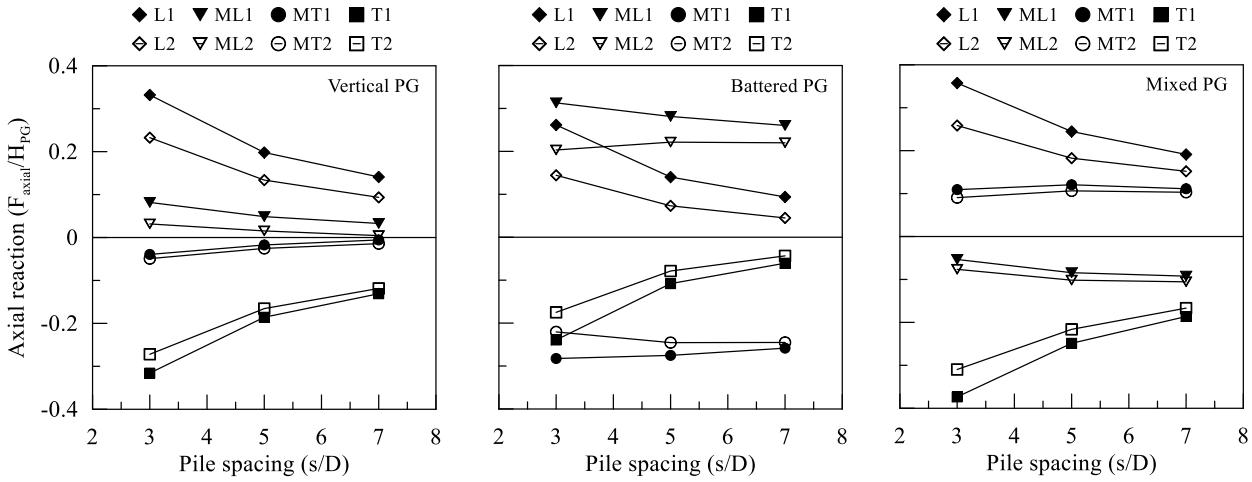

Figure 6.5. Effect of pile spacing on normalized axial reaction per pile

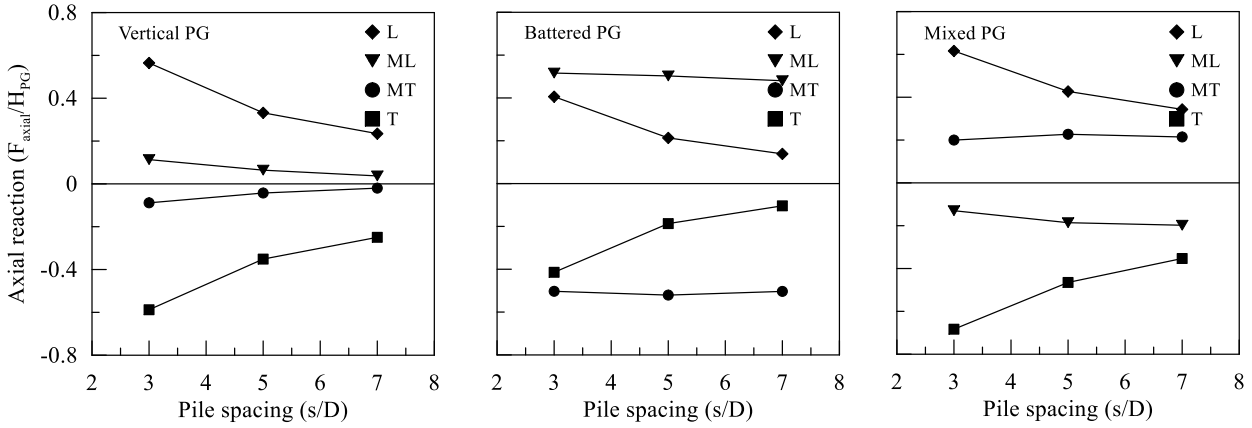

Figure 6.6. Effect of pile spacing on normalized axial reaction per row

6.3.2 Effect of pile spacing on piles' shear

The effect of spacing on piles' shear was investigated. The pile shear (V) refers to the internal shear component normal to the pile's major axis, as depicted in Figure 6.7. Following this definition, the sum of shears in all piles in the vertical PG is equivalent to the group lateral load (H_{PG}), while it is not in the cases of battered and mixed PGs.

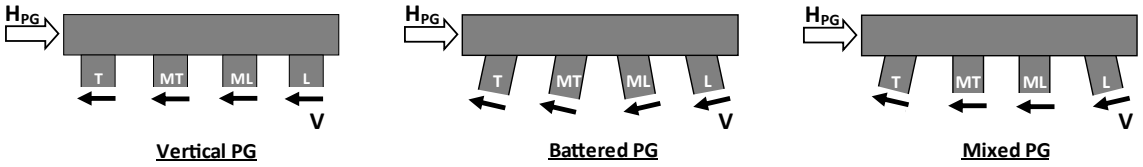

Figure 6.7. Pile shear definition in the pile groups

Piles' shear results at the pile cap elevation are presented in Figure 6.8 versus pile cap displacements (0.5, 1.0, 1.5, 2.0 inches). Similar to the axial load, piles shear results were normalized using the group lateral load (H_{PG}). The figure shows that the piles' shear was slightly affected by the cap displacement, in which it decreased with increased displacement in some piles.

The effect of pile spacing on the piles' shear per row is summarized in Figure 6.9. In the vertical PG, the pile spacing increase from 3D to 7D caused a slight change in piles shear (<1%). In the battered PG, the shear increased 2% in rows L and ML, and less than 1% in rows MT and T. In the mixed PG, the shear increased 1.5% in all rows. The change in piles shear observed was very small in all PGs with no clear trend, and therefore the influence of pile spacing is considered negligible.

6.3.3 Effect of pile spacing on group efficiency

Pile group efficiency is a simple measure of the pile group load capacity in reference to the sum of individual pile capacities and defined as

$$\mathrm{Eff_{PG}} = \frac{\mathrm{H_{PG}}}{n \,.\, \mathrm{H_{single}}}$$

Where H_{PG} is the lateral capacity of the pile group, H_{single} is the lateral capacity of single pile, and *n* is the number of piles in the group.

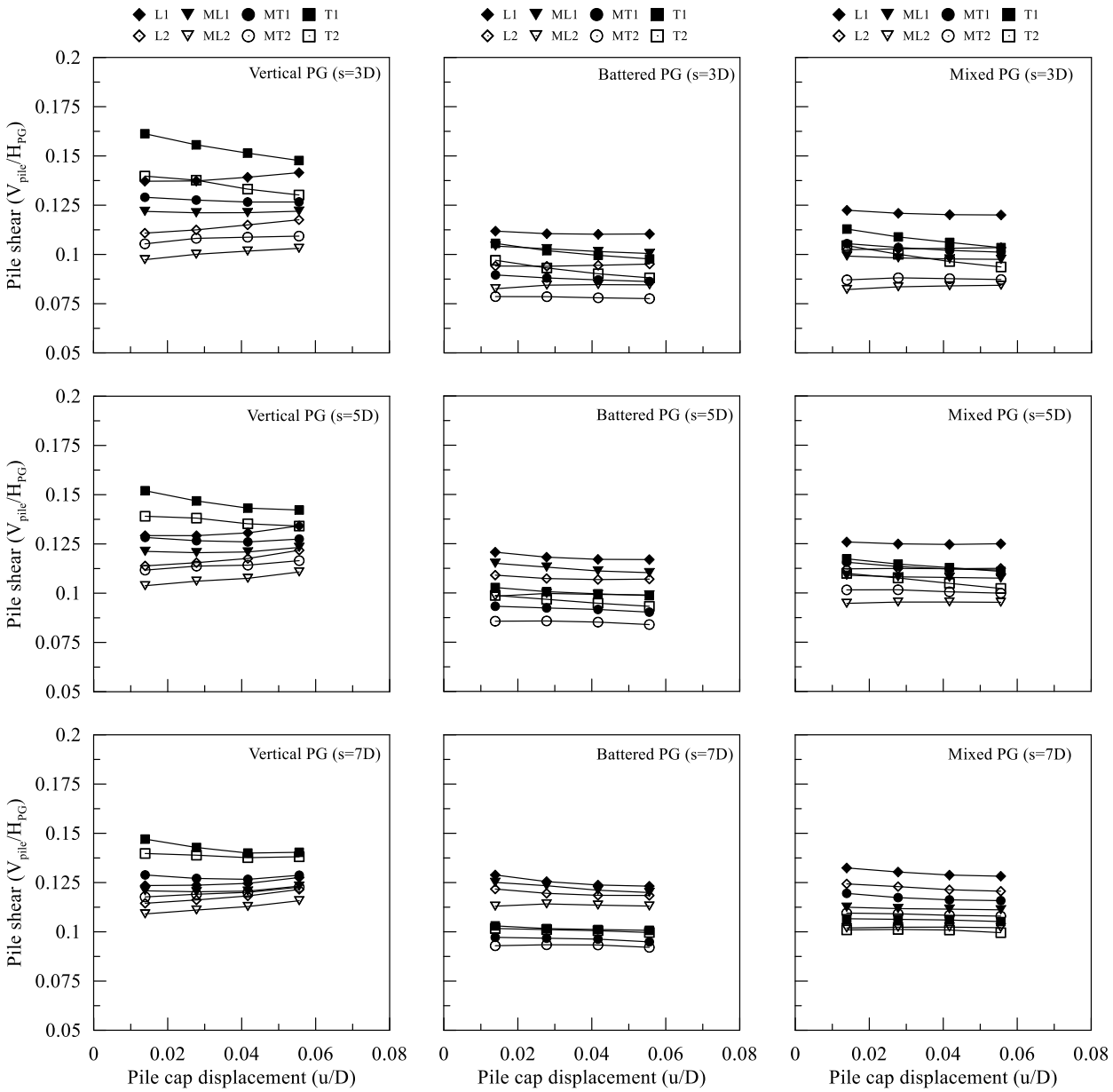

Figure 6.8. Effect of displacement on normalized pile shear

The lateral capacity is defined as the magnitude of lateral load that causes certain displacement at the pile cap (for pile group) or pile top (for single pile). The lateral capacity of the pile groups at different pile cap displacements (0.5, 1.0, 1.5, 2.0 inches) is presented in Figure 6.10. The figure also shows the sum of individual pile capacity ($n \,.\, \mathrm{H}_{\mathrm{single}}$) at similar displacements for number of piles *n* = 16 (recall that the studied PGs have 4 rows and 4 columns). The individual pile capacity was obtained from a separate FE model for single pile with similar pile and soil model properties. Pile group efficiency was estimated using the above equation and presented at different displacements in the bottom plots in

Figure 6.10. It can be seen that the pile group efficiency remained constant at different pile cap displacements in all pile groups.

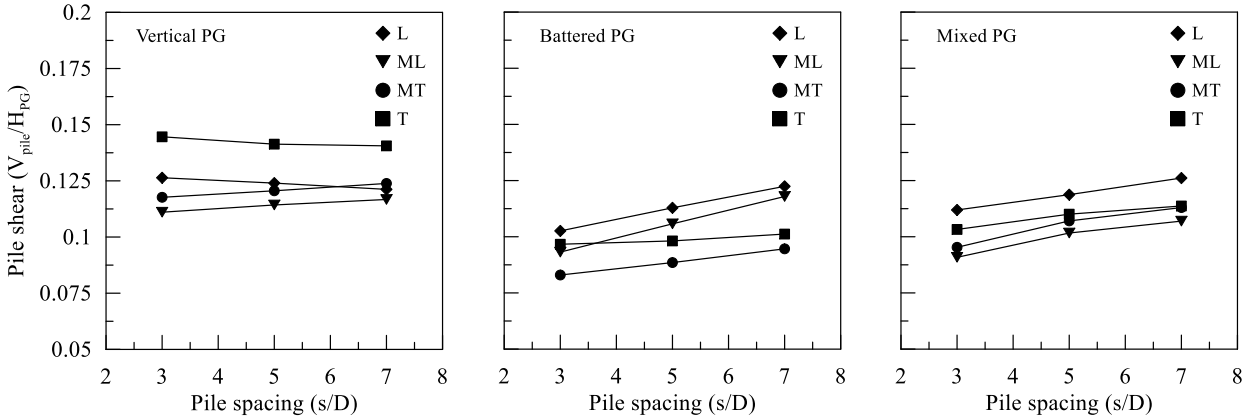

Figure 6.9. Effect of pile spacing on normalized pile shear

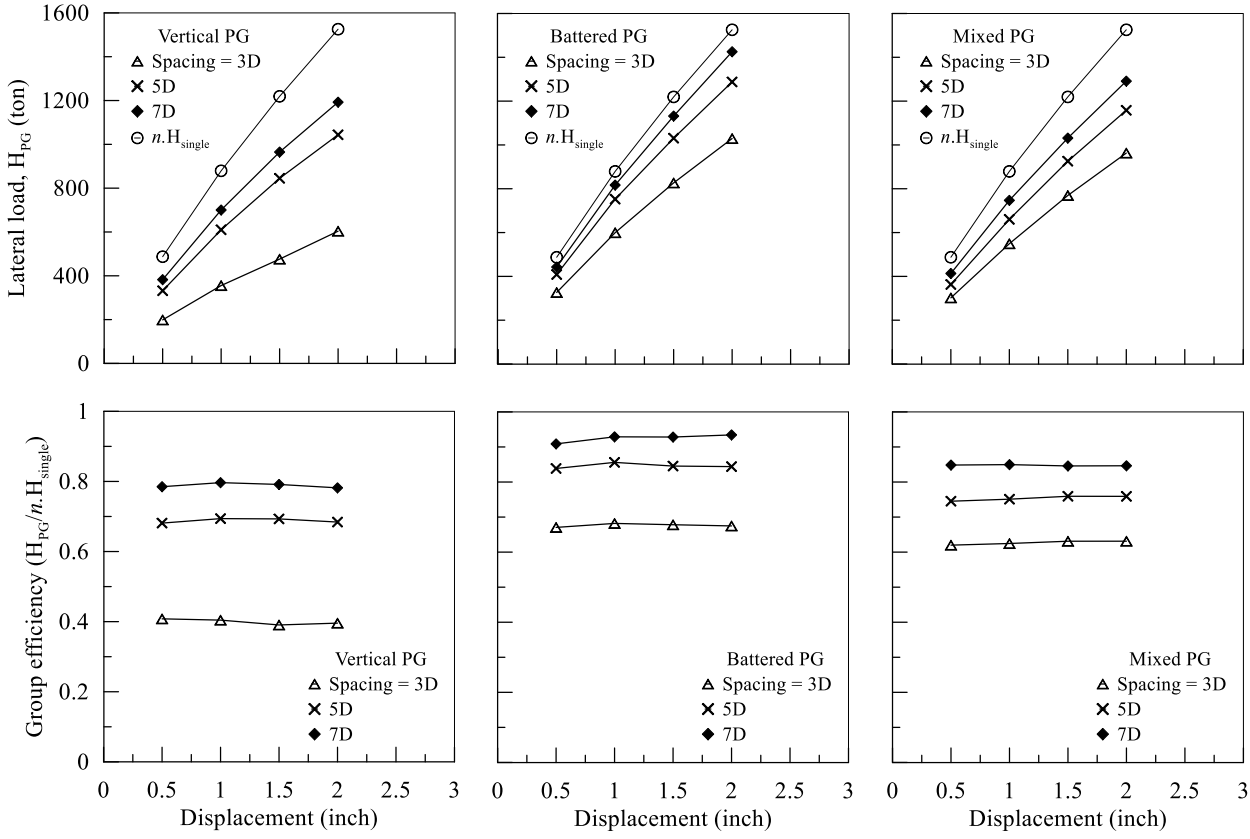

Figure 6.10. Variation of the lateral capacity and group efficiency with displacement

Comparison of PG efficiency at different pile spacing is presented in Figure 6.11. In general, increasing pile spacing resulted in higher efficiency for all PGs types. This follows the fact that the group effect become weaker at larger spacing, and the lateral capacity of

each pile in the group is closer to the individual pile capacity. The battered PG had the highest efficiency followed by the mixed and vertical PGs, respectively. The largest improvement in PG efficiency was in the vertical PG at 28% when the spacing increased from 3D to 5D compared to 12% and 16% in the mixed and battered PGs, respectively. When the spacing was increased from 5D to 7D, the percent improvement was less than 10% in all PGs. The latter indicates that the influence of the group effect becomes minimal at pile spacings greater than 5D (Rollins et al. 2006). The efficiency results for the vertical PG suggests that switching to mixed or battered PG configuration at 3D spacing is an alternative design option to increase the PG lateral capacity in addition to increasing pile spacing.

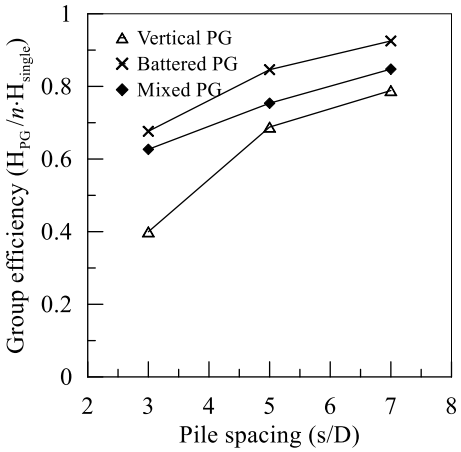

Figure 6.11. Effect of pile spacing on the group efficiency

6.3.4 Effect of pile spacing on *p*-multipliers

The *p*-multiplier is a scalar that accounts for the group effect in the beam-spring FE modeling tools (e.g., FB MultiPier, Ensoft GROUP). This factor is applied to *p*-*y* curves for single pile to obtain the *p*-*y* curves for a pile-in-group, as previously presented in 2.2. One should recall that the *p*-*y* curve is a function of depth, and the number of *p*-*y* curves in an FE model depends on the pile model discretization. In order to back-calculate the *p*-multiplier from the FE model, the *p*-*y* curves at several points over depth are obtained for the single pile and pile-in-group cases, and then the *p*-multiplier is averaged over the depth (Figure 6.12). However, such procedure is laborious and time-consuming when analyzing multiple pile group cases. Instead, a time-efficient procedure for back-calculation of *p*-multipliers is adopted in this section. The new procedure starts with the soil resistance profiles for the single pile and pile-in-group corresponding to a presumed displacement (Δy) for the pile top and pile cap, as illustrated in Figure 6.13. Then, the soil resistance ratio of the pile-in-group to the single pile (p_g/p_s) is estimated over depth. The *p*-multiplier for the pile-in-group is estimated from the average of soil resistance ratios over the influence depth (~15D) excluding outlier points. The pile top/pile cap displacement (Δy) was assumed 0.1D, which was chosen to ensure a fully mobilized soil resistance.

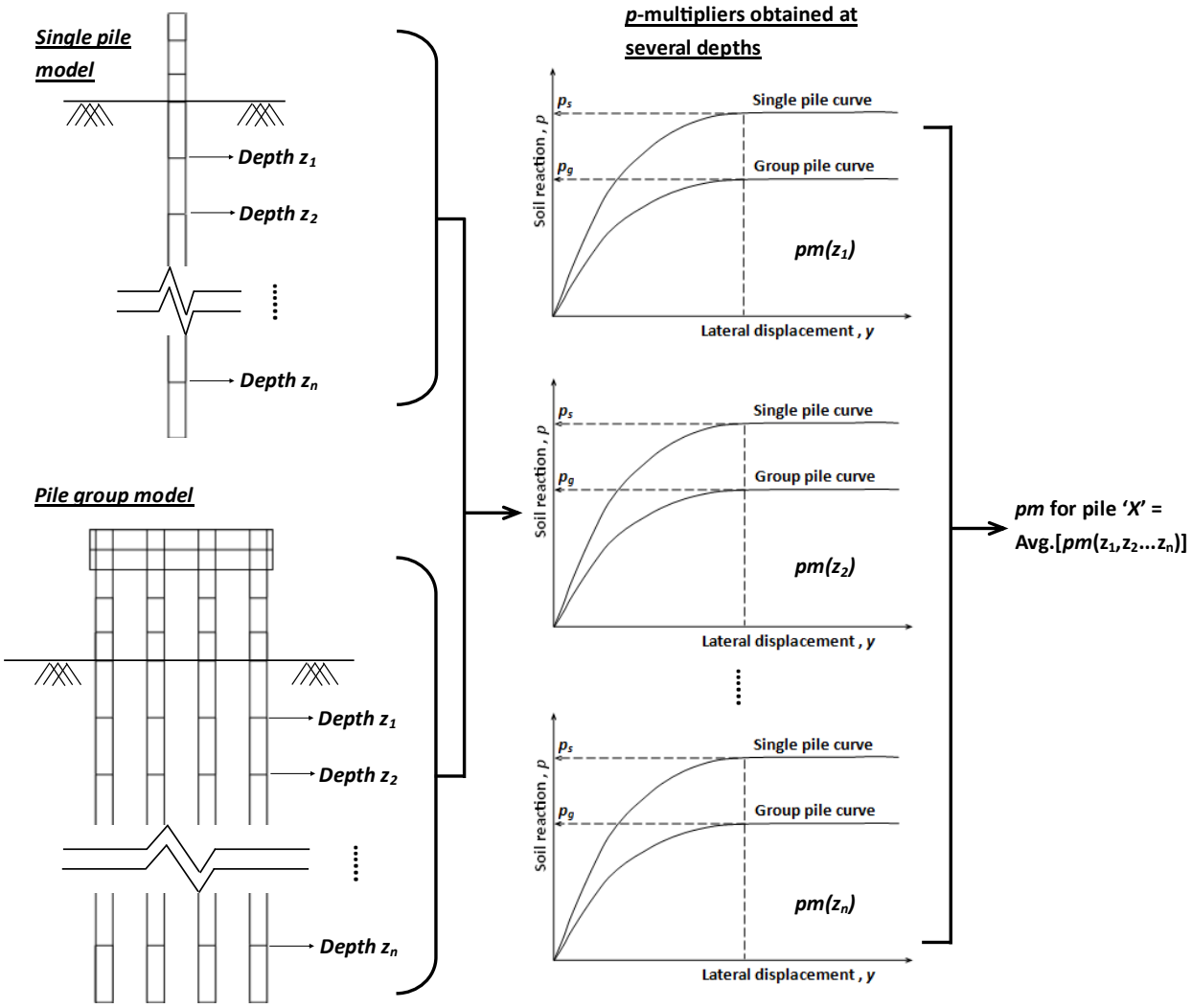

Figure 6.12. Estimation of *p*-multipliers following the definition in literature

The soil resistance profiles for different pile spacings in medium clay soil for the vertical, battered, and mixed PGs are shown in Figure 6.14, Figure 6.15, and Figure 6.16, respectively. The profile from the single pile model used for *p*-multipliers calculation is presented in the top left plot. The effect of pile spacing is clearly seen when the figures of 3D spacing are compared to the figures of 5D and 7D spacings. The mobilized soil resistance in the pile groups increased at larger pile spacing which resulted in *p*-multipliers closer to a value of unity.

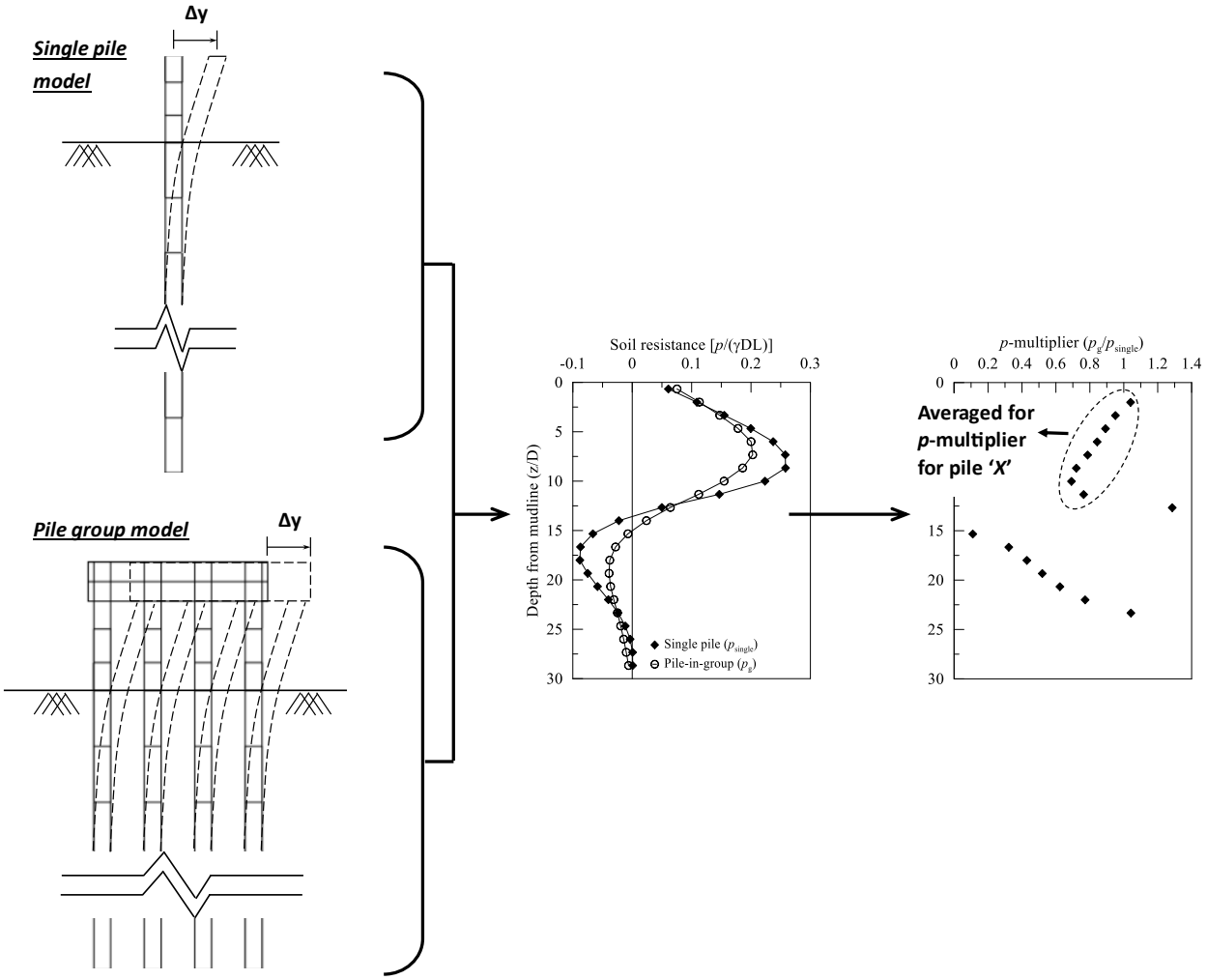

Figure 6.13. Proposed procedure for estimation of the *p*-multiplier using soil resistance profiles

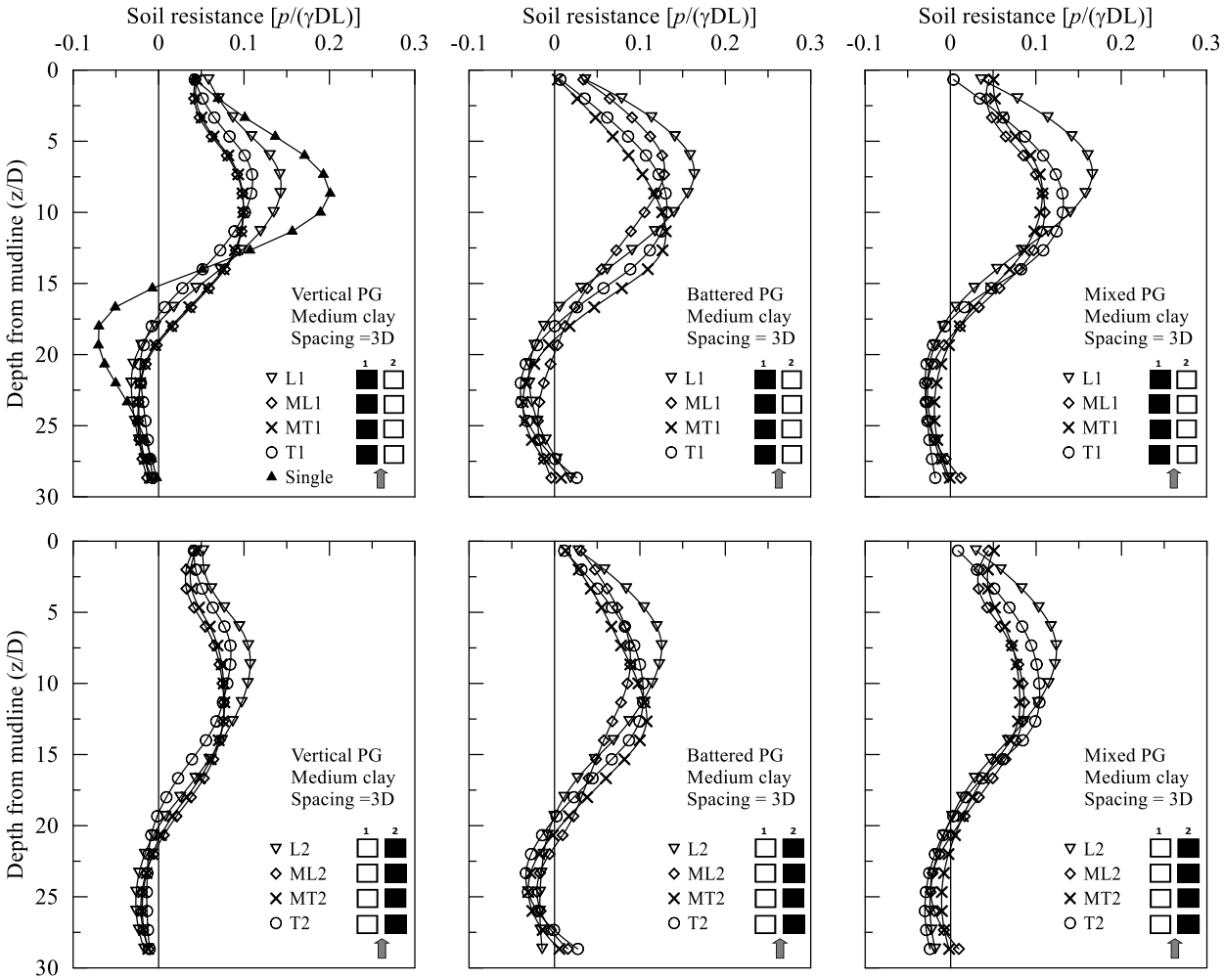

Figure 6.14. Soil resistance profiles for pile groups at 3D spacing

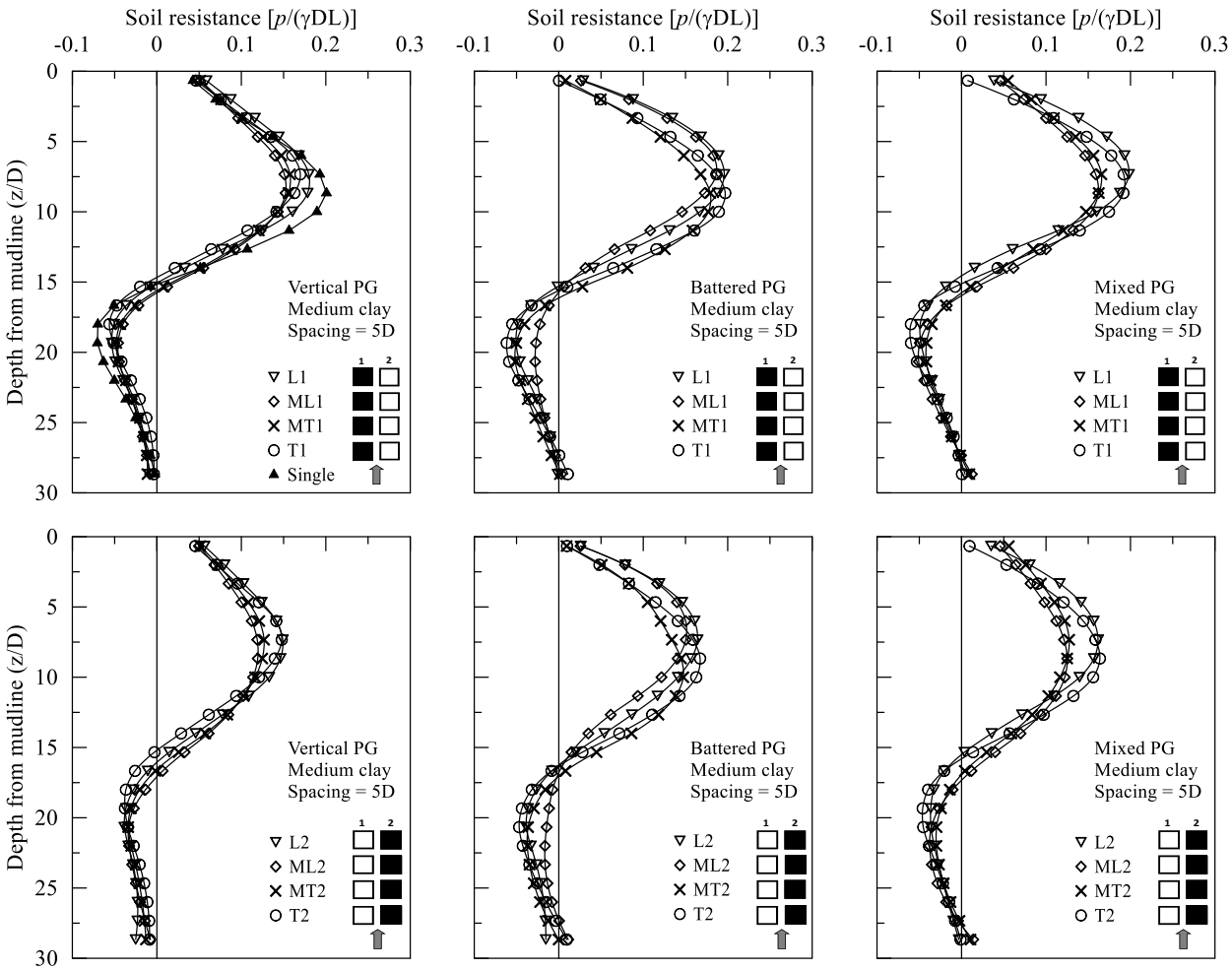

Figure 6.15. Soil resistance profiles for pile groups at 5D spacing

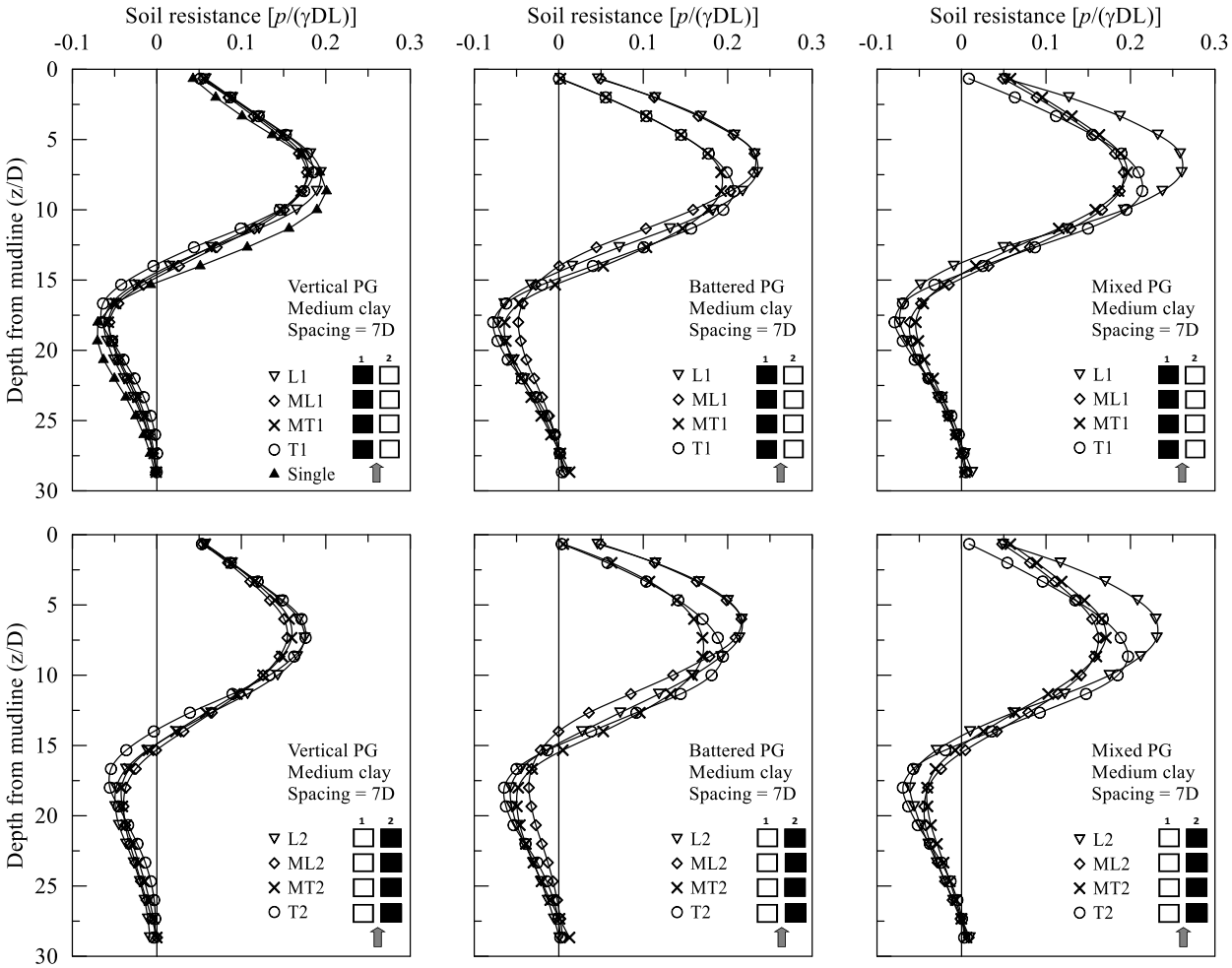

Figure 6.16. Soil resistance profiles for pile groups at 7D spacing

The *p*-multipliers results versus spacing are presented in Figure 6.17 and averaged for each pile row, which follows the practice of reporting *p*-multipliers as a function of spacing and pile location (e.g. AASTHO 2012). The largest increase in the *p*-multipliers in all pile groups was when the pile spacing increased from 3D to 5D. At 5D spacing, the average increase in *p*-multipliers was more notable in rows ML, MT, T with 0.3-point increase, and at a lesser degree in the leading row (L) with 0.2-point increase, approximately. Further increase in pile spacing from 5D to 7D resulted in a smaller increase in *p*-multipliers with 0.1-point increase on average. The latter indicates that the influence of the group effect significantly diminishes at pile spacings of 5D and greater.

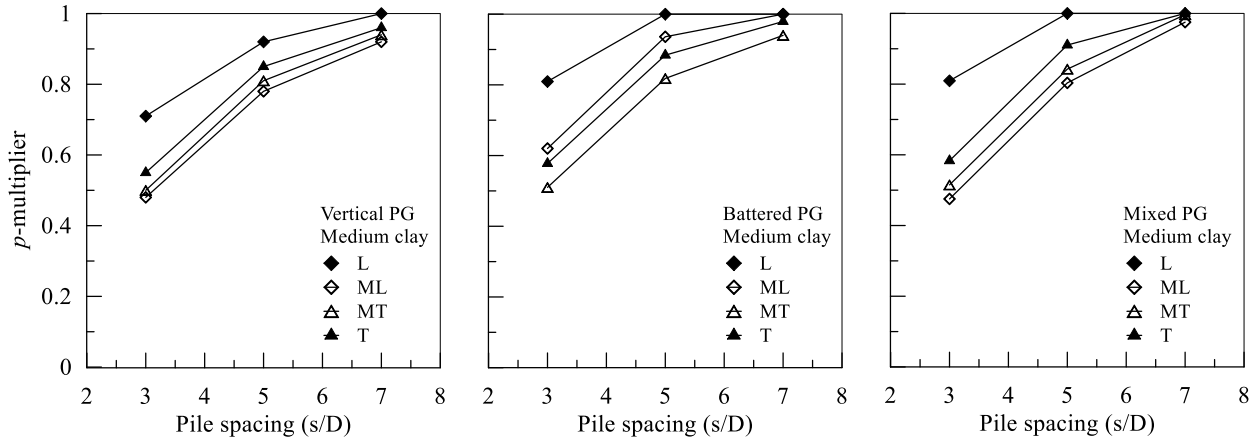

Figure 6.17. Effect of pile spacing on *p*-multipliers for vertical, battered, and mixed pile groups

The results for the single column and single row pile groups are presented in Figure 6.18. Again, increasing pile spacing resulted in higher *p*-multipliers, and the largest increase was when the spacing increased from 3D to 5D. For the single column group, the *p*-multipliers were slightly higher compared to the vertical pile group (Figure 6.17), which is expected due to the absence of neighboring piles. At 7D spacing, the *p*-multipliers approximately reached the unity value. Similar to the vertical pile group, the row with the highest *p*-multipliers was row L, followed by rows T, ML, MT, respectively.

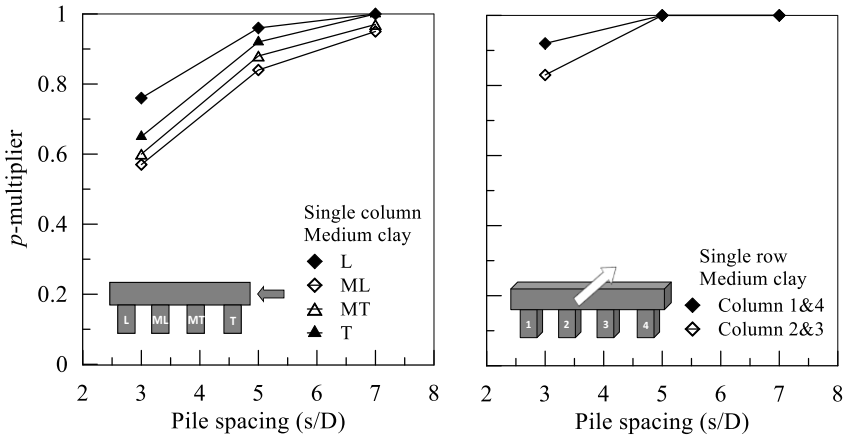

Figure 6.18. Effect of pile spacing on *p*-multipliers for single column and single row pile groups

For the single row group, the influence of the group effect was notably weaker compared to the single column group. The *p*-multipliers at 3D spacing were greater than 0.8 and reached to unity at 5D spacing. The *p*-multipliers at 3D spacing here was the highest value in all pile groups at similar spacing. Notice that piles 1 and 4 had higher *p*-multipliers than piles 2 and 3 because they were at the edges of the pile group. The single row group

results suggest that pile spacing in the loading direction can be used solely to determine the *p*-multipliers for the cases when pile spacing in the transverse (to the load) direction is greater than 3D.

6.3.5 Effect of clay soil type on *p*-multipliers

The recommended *p*-multipliers in literature are given for two main soil categories; sandy or clay soils. In the current study, the focus is on clay soils which were classified into three types; stiff, medium stiff, and soft based on consistency. The soil strength and stiffness properties for each clay category were obtained from the literature (Das 2011; Day 2012), which were used to estimate the clay model parameters presented previously in Table 6.2. The results for the effect of clay soil type on *p*-multipliers in the pile groups are shown in Figure 6.19, in which the average *p*-multipliers per row are presented. It can be noticed that the influence of clay soil is also affected by the pile spacing. At pile spacing 3D, the *p*-multipliers increased (0.1-point) steadily and consistently when the clay soil became stiffer. At pile spacing 5D, the *p*-multipliers increased consistently only in the vertical PG, while in the battered and mixed PGs they increased only when the clay type was changed from soft to medium. At pile spacing 7D, the influence of clay type became negligible.

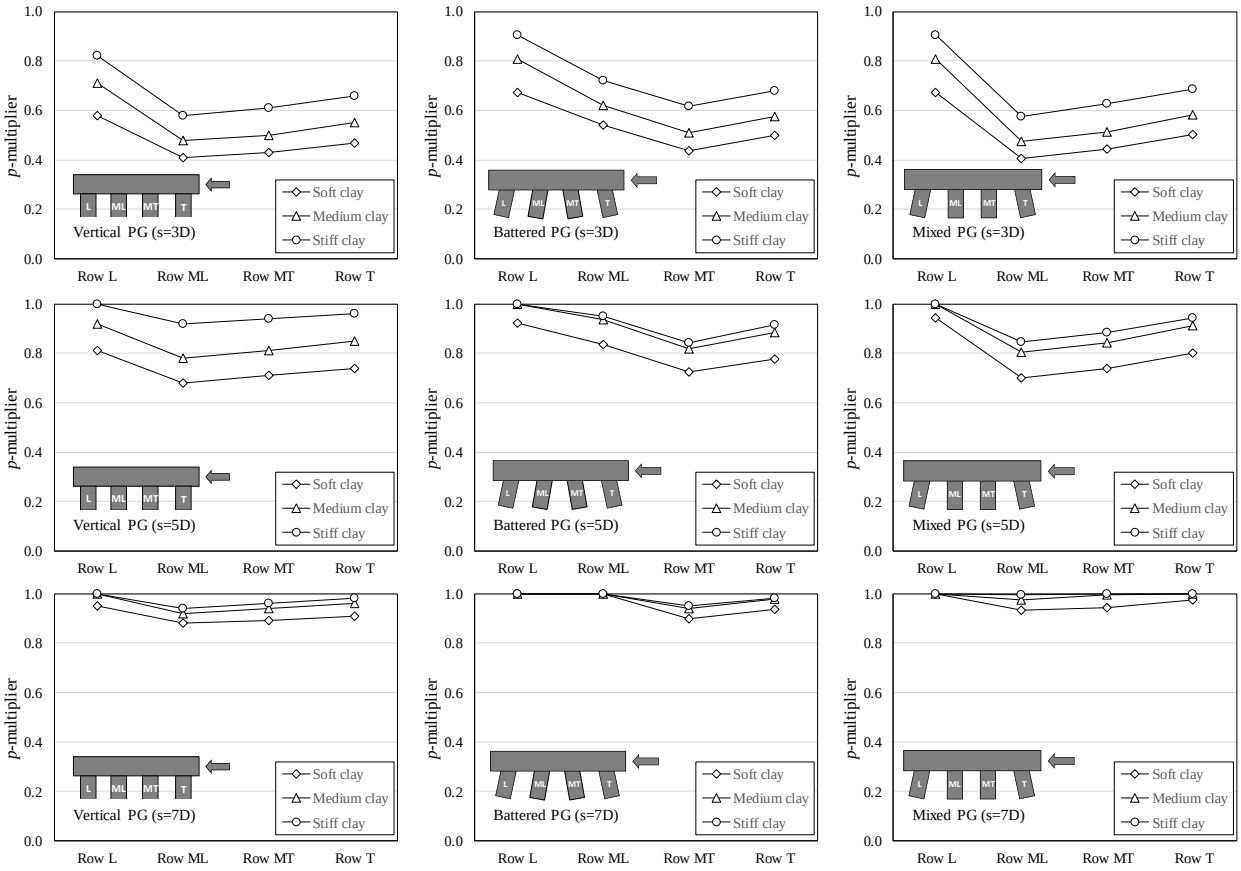

Figure 6.19. Effect of clay soil type on *p*-multipliers for vertical, battered, and mixed pile groups

The influence of clay soil type on the single column/row pile groups is shown in Figure 6.20 and Figure 6.21, respectively. For the single column pile group, the effect of clay soil type was closely similar to the vertical PG, but the increase in the *p*-multipliers was slightly less (0.08-point). For the single row pile group, the influence of clay soil type is noticed only at pile spacing 3D, which follows the previous observation in Figure 6.18 that the group effect vanishes at pile spacings equal or greater than 5D for single row pile groups.

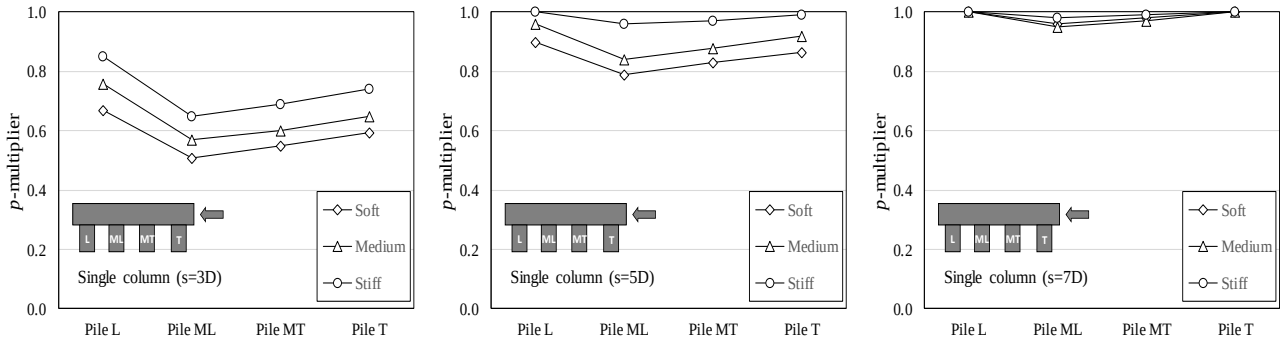

Figure 6.20. Effect of clay soil type on *p*-multipliers for single column pile group

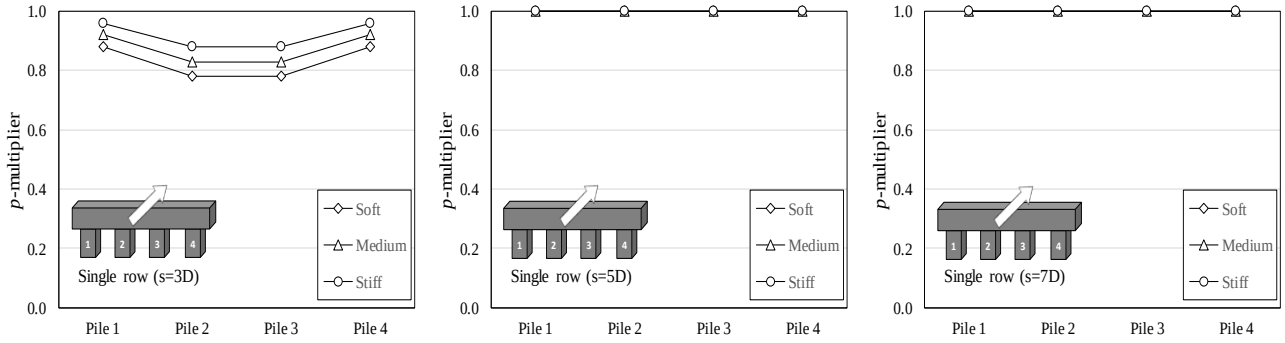

Figure 6.21. Effect of clay soil type on *p*-multipliers for single row pile group

Chapter 7. The Dynamic Lateral Behavior of Pile Groups Subjected to Barge Impact

7.1 Introduction and background

Vessel-bridge collisions became a serious issue due to the increasing number of inland vessels passing underneath bridges over waterways. The subject of vessel-bridge impact has gained more attention after several serious accidents since the 1960s. For example, one of the catastrophic incidents was the collapse of the Sunshine Skyway Bridge in Florida in 1980 after the collision of a freighter into one of the bridge piers (Larsen 1993; Consolazio and Cowan 2003). The current AASHTO bridge design guideline require all bridge components in a navigable waterway crossing to be designed for vessel impact (AASHTO 2012). Determination of loads from vessel-bridge collision should consider factors such as size, type, and frequency of vessels passing, bridge and channel geometry, available water depth, vessel speed and direction, the structural response of the bridge (Larsen 1993). The AASHTO design impact force (equivalent static force) from barges is estimated using empirical relations based on the kinetic energy (KE) and barge bow crush depth (a_B)

$$KE = \frac{C_H W_B V_B^2}{29.2} \quad \text{Eq. 62}$$

$$a_B = 10.2\left(\sqrt{1 + \frac{KE}{5672}} - 1\right) \quad \text{Eq. 63}$$

$$P_B = \begin{cases} 4112a_B \ , & \text{for } a_B < 0.34 \\ 1349 + 110a_B \ , & \text{for } a_B \geq 0.34 \end{cases} \quad \text{Eq. 64}$$

where KE is the kinetic energy (kip-ft), C_H is the hydrodynamic coefficient (= 1.05 for draft ≥ 0.5 ft, 1.25 for draft ≤ 0.1 ft), W_B is the barge weight (ton), V_B is the barge speed (ft/s), a_B is the bow crush depth (ft), P_B is the equivalent static impact force (kips).

In the past decade, several numerical and experimental studies investigated the impact load from barges and the factors affecting it such as speed, pier column shape and width, vessel weight, and bow stiffness (e.g., Consolazio and Cowan 2003; Yuan 2005; Yuan and Harik 2010; Chu and Zhang 2011; Sha and Hao 2012; Kantrales et al. 2016; Zhang et al. 2016). The studies main focus was to propose and validate a simplified model to predict the impact load magnitude. The most notable and versatile studies were performed by the research group at the University of Florida, in which they used both experimental and numerical methods to study and validate the prediction models for the barge impact problem (Consolazio and Cowan 2003; Consolazio et al. 2006, 2009). In one of the barge impact experiments, a tanker barge was used in the collisions conducted on the piers of

the decommissioned St. George causeway bridge. It was concluded from those impact experiments that the peak impact force is amplified by the dynamic response of the bridge pier. Their investigation using numerical methods included high fidelity FE simulations to verify the impact force models for low and high energy impacts. They used the FE model of the Jumbo Hopper (JH) barge to impact flat-face and circular piers with different sizes (Figure 7.2). The numerical results indicated that the current AASHTO equivalent static force model underestimates the impact force magnitude for low to moderate energy impacts and overestimates it for high energy impacts. They also found that the shape of the impacted pier has a significant influence on the peak impact force, and proposed a procedure to determine the peak impact force for flat-faced and round piers from regression analysis (Consolazio et al. 2009).

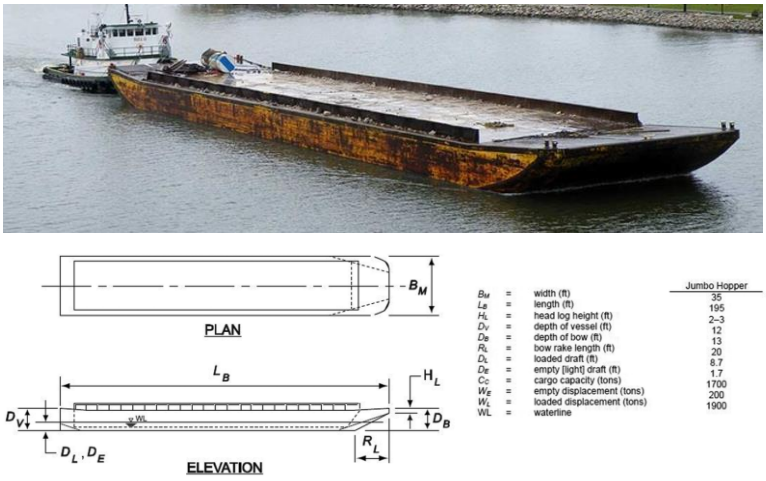

Figure 7.1. The Jumbo Hopper is the common barge type in US waterways

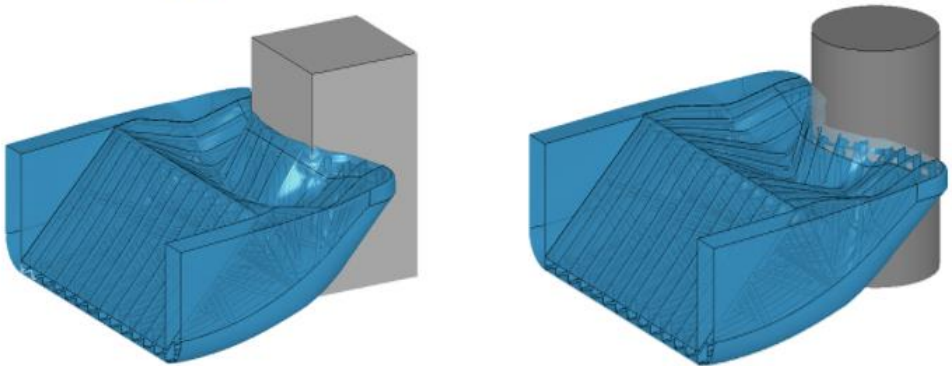

Figure 7.2. Barge impact simulations on flat-faced and round piers (Consolazio et al. 2008)

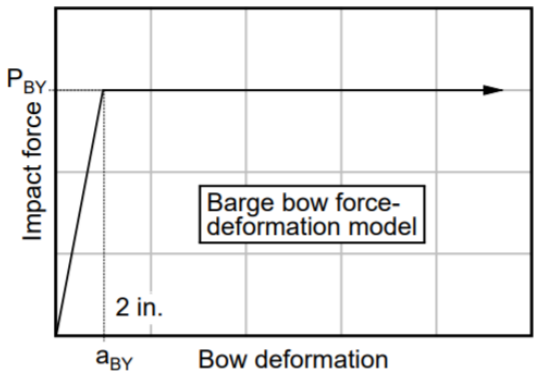

Figure 7.3. The generalized impact force – bow crush depth relationship by Consolazio et al. (2009)

The procedure assumes a generalized linear elastic-perfectly plastic force curve as a function of barge bow crush depth, in which the peak impact force magnitude plateaus after 2 inches of bow crush depth (Figure 7.3). For flat-faced piers, the peak impact force prediction model is bilinear and requires the pier width (w_p) as the only variable

$$P_{BY} = \begin{cases} 1500 + 60w_p \ , & \text{for } w_p < 10 \text{ ft} \\ 300 + 180w_p \ , & \text{for } w_p \geq 10 \text{ ft} \end{cases} \quad \text{Eq. 65}$$

For rounded piers, the model prediction is linear

$$P_{BY} = 1500 + 30w_p \quad \text{Eq. 66}$$

where P_{BY} is the peak impact force (kips), w_p is the pier width (ft).

Furthermore, Consolazio et al. (2009) showed that the impact force for two types of barges (JH, Tanker) is closely similar even though their bow width is different (35 ft vs 50 ft, respectively).

In this chapter, a number of FE simulations for studying the lateral behavior of pile groups subjected to barge impact is investigated using the case of pier M19 of the I-10 twin span bridge. Unlike the previous studies, the superstructure, pile group foundation, and the soil body are included in the FE models, and the differences between the vertical, battered, and mixed pile groups is investigated.

7.2 Additional considerations for dynamic FE simulations

7.2.1 FE simulations using explicit dynamics

Dynamic problems can be solved in FE modeling using implicit or explicit integration schemes. The implicit/explicit schemes in FE simulation refers to the numerical operator used for integrating the time rate equations. In implicit schemes, the variables at the end of the time increment (*dt*) are calculated using the values at the beginning of the time step (t_o)

and the end of the step (t_o+dt) by an iterative procedure. In explicit schemes, the variables at the end of the time increment (dt) are calculated using the values at the beginning of the time step (t_o) only with no iterations. Implicit schemes are robust, have good accuracy, and insensitive to the size of time increment (i.e. unconditionally stable). However, the iterative procedure in implicit schemes requires more computational resources (CPU, RAM) and the solution cost increases exponentially with the number of elements in the model. on the other hand, explicit schemes have faster solution time per increment, require less computational resources, and the solution cost increases linearly with the number of elements in the model. However, the time increment in explicit schemes is very small and limited by the stability condition for convergence.

Solving transient and nonlinear dynamic problems, such as impact and blast problems, is more efficient using explicit schemes. This is because the complete time history of the response is desired and the solution cost (time and computer resources) is significantly less for large models. For example, a single FE model in this chapter for barge impact problem analyzed using the explicit solver required a 1.1 GB of RAM memory space and 7 hours to complete the simulation on a desktop PC. On the other hand, when using the implicit solver, the RAM memory space required was about 16 GB and took 2 days to complete only the geostatic step. Therefore, the explicit solver in Abaqus was used for simulating the barge impact problem in this chapter.

7.2.2 Modeling far boundaries using infinite elements

For problems with semi-infinite domains, the FE model boundaries defined with displacement constraints have to be far enough from the studied region to eliminate their influence on the response. For example, the load-displacement response of FE model for laterally loaded pile would be artificially stiffer if the soil domain boundary is defined at a close distance such as 5D from the pile's front face. The approach to determine the distance from the boundary is to evaluate the response from several FE model trials with increasing mesh sizes. The optimum mesh size is selected as the smallest mesh at which the influence on the response becomes negligible. The latter approach is commonly used for static problems. For dynamic problems, however, another issue arises from the reflection of stress waves by the boundaries, which interferes with the model response. This issue is avoided by using a combination of spring and dashpot elements connected to the ground at the boundaries (Figure 7.4). The spring elements provide the reaction to satisfy the global force equilibrium, while the dashpot elements provide the dissipation mechanism for the stress waves traveling toward the domain boundaries.

Alternatively, Abaqus elements library provides a special type of elements called "infinite elements" (Figure 7.4). The infinite elements, which are similar to the standard solid continuum elements in their nodal structure, have modified numerical formulation that dissipates the energy from the stress waves akin to a dashpot. The advantages of infinite elements are (1) their compatibility with standard solid continuum elements, (2) their

definition in Abaqus is similar to the standard solid elements, (3) they utilize the typical elastic material properties (Young's modulus and Poisson's ratio), (4) they self-provide the equilibrating reaction at the boundaries, (5) they provide the dissipative mechanism for stress waves traveling toward the boundaries. For the current study, the linear infinite elements with eight nodes (CIN3D8) was used on the far boundaries of the soil body.

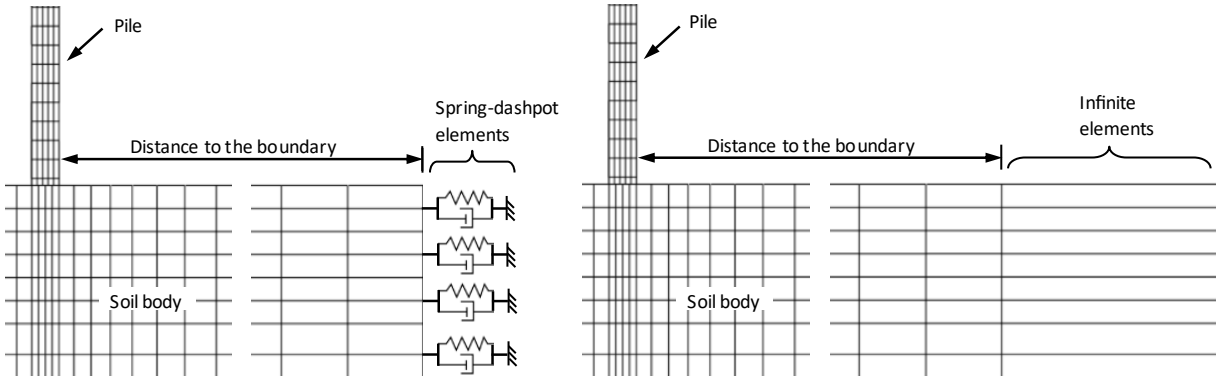

Figure 7.4. Modeling of FE model boundaries in dynamic problems using spring-dashpot elements or infinite elements

7.2.3 Material damping

Damping is one of the energy dissipation mechanisms that cause the attenuation of propagating stress waves. The influence of damping in soils is more prominent during cyclic events such as earthquakes or foundation vibrations. The damping property for soils is represented by the damping ratio (ξ), which can be estimated from the results of cyclic shear tests (Hardin and Drnevich 1972). The soil stress-strain response during cyclic shear forms a loop shape between the loading-unloading stress trajectories. The area of this loop is used to estimate the damping ratio. The main factors affecting the damping ratio in soils are the strain amplitude, effective confining stress, void ratio, and number of cycles.

In FE modeling, the effect of damping can be incorporated using the Rayleigh damping model, which is a simplified approach to introduce damping in FE models without altering the mode shapes and frequencies of the model. The Rayleigh damping model approximates the damping matrix $[C]$ in the dynamic governing equation as a linear combination of the mass $[M]$ and stiffness $[K]$ matrices (Liu and Gorman 1995)

$$[M]\{\ddot{u}\} + [C]\{\dot{u}\} + [K]\{u\} = \{F\} \quad \text{Eq. 67}$$

$$[C] = \alpha[M] + \beta[K] \quad \text{Eq. 68}$$

where $\ddot{u}$, $\dot{u}$, and u are the acceleration, velocity, and displacement vectors, respectively, $\{F\}$ is the external force vector, α and β are the mass and stiffness proportional damping constants.

The damping ratio (ξ) is estimated using α and β in the two-parameters Rayleigh damping model as

$$\xi_i = \frac{\alpha}{2\omega_i} + \frac{\beta\omega_i}{2} \qquad \text{Eq. 69}$$

where i refers to the mode number, ω_i is the circular frequency.

In Eq. 69, the first part in the RHS is the mass proportional part of the Rayleigh model, which mainly dampens the response in the low-frequency range. While the second part is the stiffness proportional part mainly dampens the response in the high-frequency range (Figure 7.5).

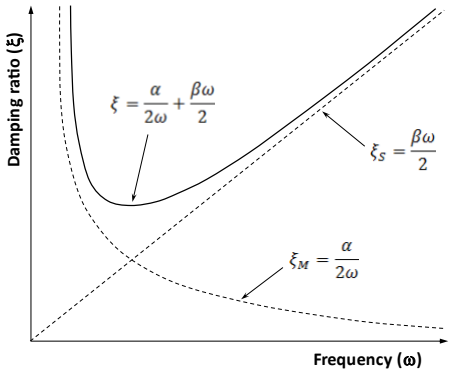

Figure 7.5. The two-parameter Rayleigh damping model

Eq. 69 estimates the damping parameters (α and β) at certain frequency. However, the FE model response covers a range of frequencies. Therefore, the damping is introduced for the selected frequency range 1-10 Hz, which typically applies for soils (Hashash and Park 2002). For frequency range damping, the constants α and β are alternately determined as (Zerwer et al. 2002)

$$\alpha = \frac{2\xi\omega_1\omega_n}{\omega_1 + \omega_n}, \qquad \beta = \frac{2\xi}{\omega_1 + \omega_n} \qquad \text{Eq. 70}$$

where ω_1 and ω_n are the lowest and highest circular frequencies, respectively, in the frequency range.

Zerwar et al. (2002) indicated that constant Rayleigh damping is not achieved over the frequency range using Eq. 70. Instead, they suggested averaging the damping ratio ($\bar{\xi}$) over the frequency range by combining the equations in Eq. 70 and minimize the variance in the damping ratio

$$\bar{\xi} = \frac{\frac{\alpha}{2}\ln\left(\frac{\omega_1}{\omega_n}\right) + \frac{\beta}{4}(\omega_n^2 - \omega_1^2)}{\omega_n - \omega_1} \qquad \text{Eq. 71}$$

$$Var(\bar{\xi}) = \frac{(\omega_n - \omega_1)\left[\frac{\alpha^2}{4}\left(\frac{1}{\omega_1} - \frac{1}{\omega_n}\right) + \frac{\beta^2}{12}(\omega_n^3 - \omega_1^3) + \frac{\alpha\beta}{2}(\omega_n - \omega_1)\right] - \bar{\xi}^2}{(\omega_n - \omega_1)^2} \qquad \text{Eq. 72}$$

To solve for α and β in Eq. 71 and Eq. 72, an average value for the damping ratio is assumed first, and then the constants are determined using an iterative procedure to minimize the variance.

7.2.4 Data sampling and filtering

The numerical solution using explicit schemes proceeds in very small increments, which is dependent on the smallest element size and the propagation speed of stress waves. Requesting data output at every time increment results in huge output file size, which makes the access time for the computer very long and consumes the computer's main memory. Therefore, the user chooses to store the output data at spaced time intervals, which usually referred to as sampling. Care must be taken when choosing the frequency of sampling to avoid the signal corruption by aliasing (Figure 7.6). Aliasing occurs due to the sampling of the source signal at a frequency below the limit defined by the Nyquist sampling rate (f_{Nyq}) and the maximum frequency (f_{max}) of interest in the source signal.

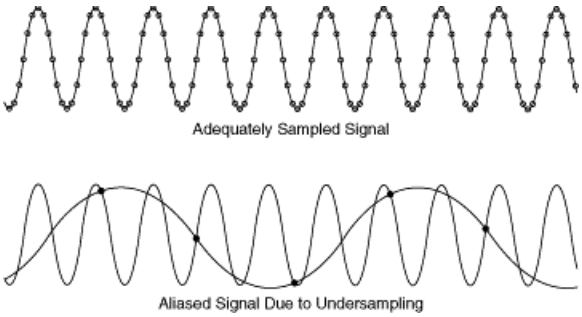

Figure 7.6. Sampling can lead to signal corruption by aliasing

To avoid aliasing the following rules apply

$$f_s > 2f_{max} \ , \qquad f_{Nyq} = \frac{f_s}{2} \qquad \text{Eq. 73}$$

where f_s is the sampling frequency.

The Nyquist sampling rate (f_{Nyq}) defines the minimum sampling frequency to avoid signal corruption by aliasing. Diehl et al. (1999) recommended a sampling frequency $f_s=10f_{max}$ to maintain 95% accuracy in the amplitude. For the barge impact problem, the frequency range of interest is within 1-10 Hz, and therefore, the chosen sampling frequency is 100 Hz.

The output from the dynamic FE analysis in the postprocessing contains a spectrum of frequencies with unwanted components that masks the frequency of interest. The unwanted components are typically in the high-frequency range, which referred to as noise. Noise can be removed from the signal using a low-pass digital filter, which performs mathematical operations to remove the frequency content above a user-defined frequency limit called the cutoff frequency. Examples of well-known low-pass digital filters are the Butterworth and Chebyshev filters (Figure 7.7).

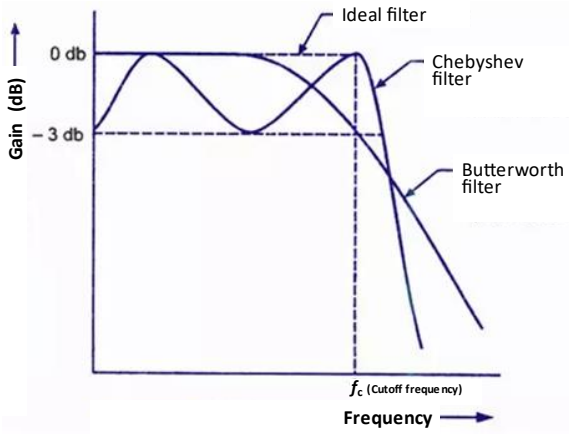

Figure 7.7. Low-pass filter response near the cutoff frequency

Ideally, it is desired that the digital filter removes all frequencies above the cutoff frequency from the signal. However, as shown in Figure 7.7, this is not possible due to the shape of the filter's mathematical function, which produces a transition band that allows some noise in the filtered signal. The cutoff frequency can be determined by several approaches such as the residual analysis method (Winter 2009), and the Jackson knee method (Jackson 1979).

The residual analysis method was adopted in this chapter for its simplicity and ease of implementation in spreadsheets. In this method, the signal is filtered at regularly increasing cutoff frequencies (i.e. 1, 2, 3..., up to 0.5 f_s), and then the residual is estimated for each filtered signal as

$$R(f_c) = \sqrt{\frac{\sum(X_i - \hat{X}_i)^2}{N}} \qquad \text{Eq. 74}$$

where $X_i, \hat{X}_i$ are the unfiltered and filtered signal data points, respectively, and N is the total number of signal data points.

The residual function $R(f_c)$ is plotted against the cutoff frequency f_c and the optimal cutoff frequency is graphically determined as in Figure 7.8. First, the tangent to line ***e-d*** is extended to find point ***a*** on the vertical axis. Then a horizontal line is drawn from ***a*** to

intersect the residual curve at ***b***, and, finally, the abscissa of point ***b*** is taken as the optimal cutoff frequency.

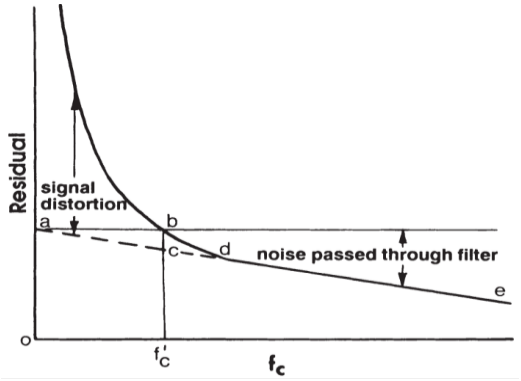

Figure 7.8. Determination of the optimal cutoff frequency using the residual analysis method

The Butterworth digital filter was used in this study for its availability and simplicity. This is because it requires defining only the cutoff frequency unlike the Chebyshev filter, which requires defining two additional constants.

7.3 FE models for the barge impact problem

The lateral behavior of three types of pile groups (vertical, battered, and mixed) was simulated and compared. The FE model for barge impact comprised of several components and discussed in the following sections. The discussion also presents the results of FE simulation of the statnamic test of test pile TP7, which was used to verify the soil model parameters.

7.3.1 Study cases

The study was conducted for three types of pile groups (vertical, battered, and mixed) being hit by the barge at different speeds: 2 knots (3.37 ft/s), 4 knots (6.75 ft/s), and 6 knots (10.12 ft/s). These speeds represent slow to moderate level navigation speeds for barges (AASHTO 2012). The barge weight was maintained at 1873 tons in all cases. In the FE models, the barge was set to hit the middle of the pile cap, which was determined from the mean water level for the M19 pile group foundation (Figure 7.9). The design barge specs by AASHTO suggests that the draft for fully oaded barge is 8.7 ft. In the horizontal plane, the centerline axis for the barge was aligned with the cap central axis.

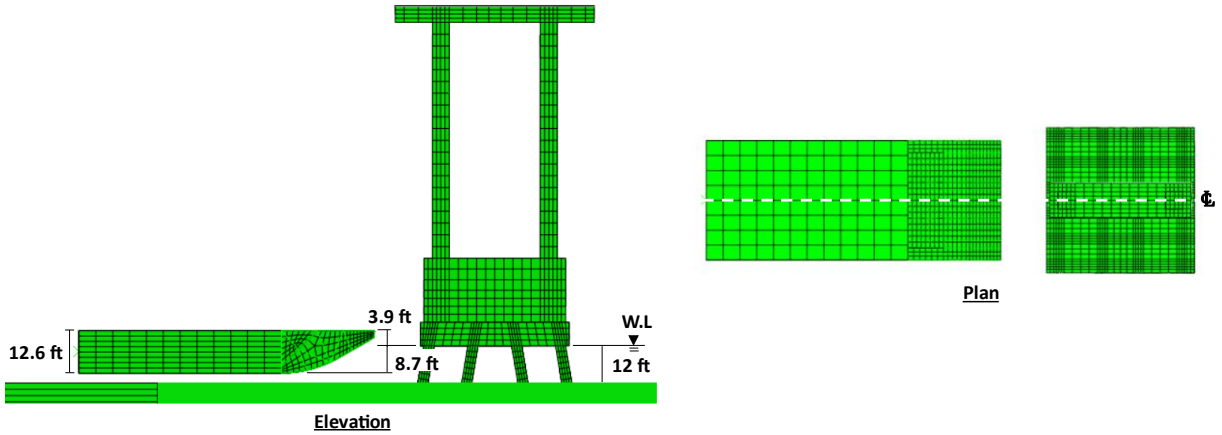

Figure 7.9. Positioning of the barge and impact point

7.3.2 Barge FE model

The JH barge has been used in numerous barge impact FE simulations (e.g., Consolazio and Cowan 2003; Yuan and Harik 2010; Sha and Hao 2013; Getter et al. 2015; Zhang et al. 2016; Kantrales et al. 2016). The standard JH barge specs per AASHTO guidelines (2012) was used in the current study. The actual barge dimensions are 195 ft L x 35 ft W x 12 ft D, and the total weight is 1873 tons for fully loaded barge. The JH barge body can be separated into two main regions: the bow rake and the cargo region (Figure 7.10).

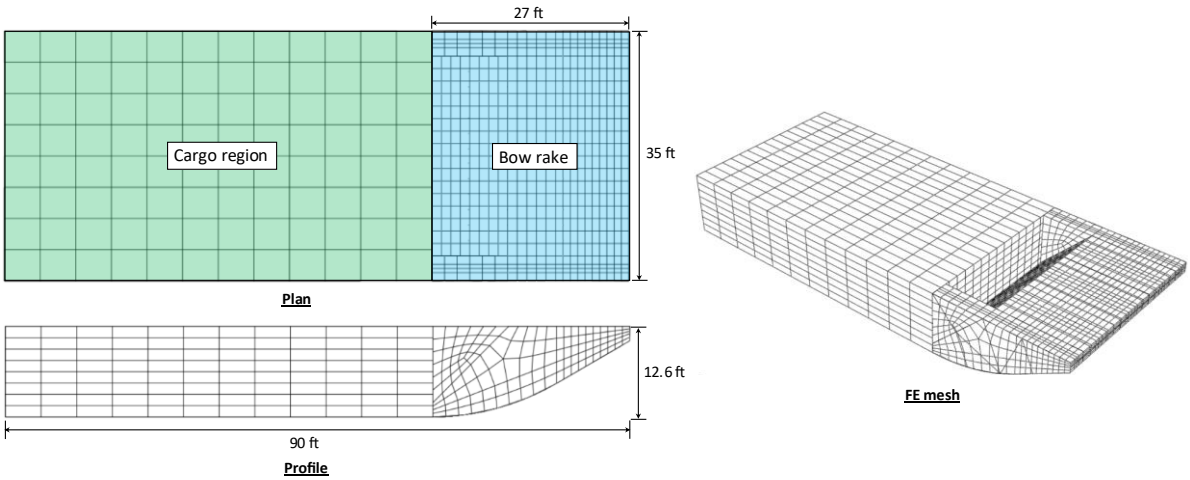

Figure 7.10. FE model for the Jumbo Hopper barge

In reality, the whole JH barge is built from trusses and steel plating. However, modeling the full barge in FE is a challenging task due to the complexity and the large number of elements and constraints required. In previous impact simulation studies, the barge model consisted of highly detailed model for the bow rake and a simplified model for the cargo region. The bow rake is the most important region because it is the part in contact with the pier which suffers significant deformation throughout the impact. For the current study, the bow rake model was built of 3-D beam and shell elements. The beam elements were used to model the internal truss frames, while the shell elements modeled the outer steel

plating. The total number of truss frames was 14 spaced at 2.16 ft in the lateral direction (see Figure 7.11).

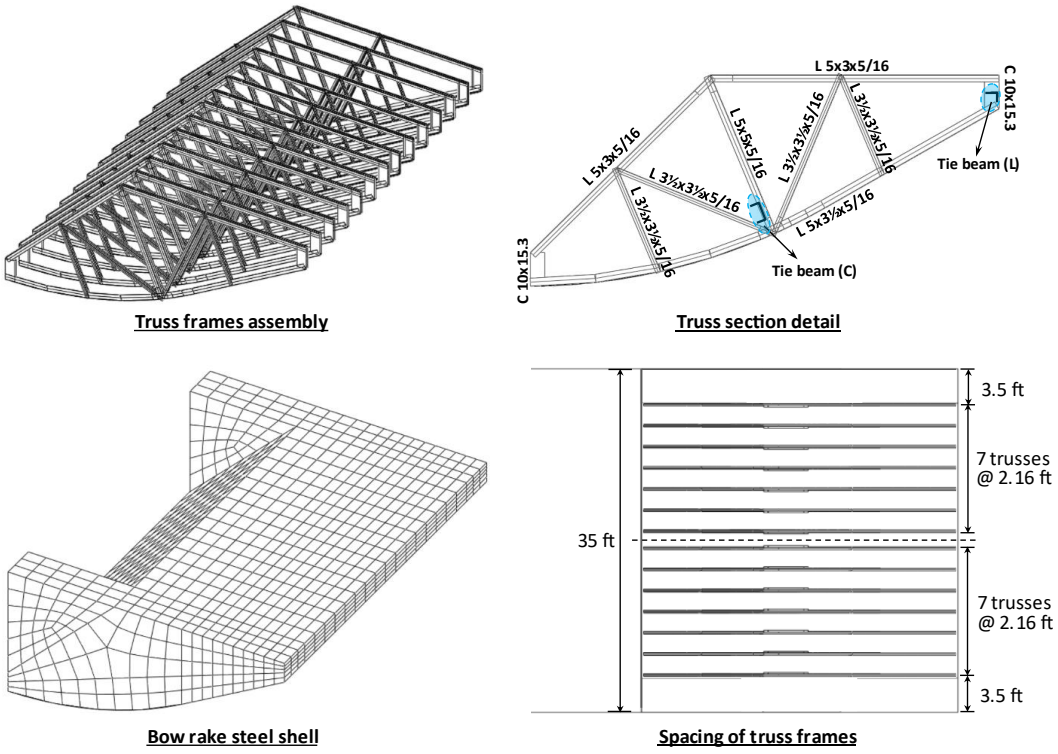

Figure 7.11. Bow rake FE model details

Each truss frame was built from A36 steel beams with L and C structural shapes. The frames were mirrored at the barges' center line and laterally braced by two tie beams (L & C shaped) at the front of the bow and at the bottom of the diagonal member, respectively. All components of the truss frame were modeled using 3-D beam elements (B23), and the beam junctions were numerically constrained to simulate the effect of stiffened joints. The outer shell was built from A36 steel plating with 3/8" thickness and modeled using 3-D shell elements (S4R). The truss frames assembly and the outer shell were connected together using tie constraints to simulate the welding between the plating and the trusses. The total number of elements used in the bow rake model was ~3200.

For the cargo region, the weight of cargo is the only necessary property which influences the barge's inertia. The cargo region was simply modeled as solid block of A36 steel with a total weight of 1873 tons. The elements used were the 3-D solid continuum elements (C3D8R) with a total number of ~500 elements. The bow rake and cargo region were numerically tied using numerical constraints so that they behave as a single unit.

The A36 steel material behavior was simulated using the elastoplastic von Mises constitutive model. The post-yield nonlinear stress-strain behavior was introduced as a

piece-wise linear function to account for the hardening in the large strain region, which was necessary for the large deformation in the bow rake (Figure 7.12). The A36 steel elastic properties used in the model were Young's modulus E_s= 29000 ksi, and Poisson's ratio ν = 0.26.

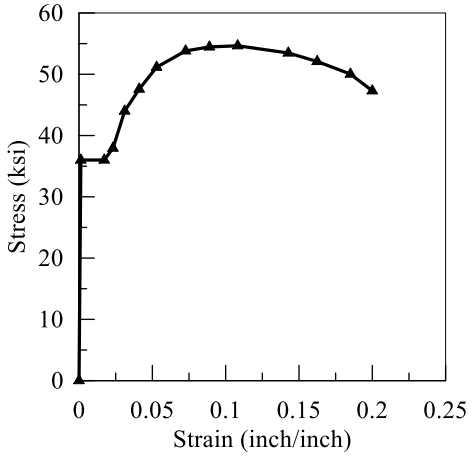

Figure 7.12. A36 steel stress-strain response

7.3.3 Pile group and bridge pier FE model

The M19 pier foundation design was used for studying the differences in the lateral behavior of pile groups subjected to barge impact. The FE model was created from three main components: the pier superstructure, the bridge deck and girders, and the pile group foundation.

7.3.3.1 Pier superstructure

The concrete pier superstructure comprised of the protection wall, columns, and the seating beam for girders (Figure 7.13). The pier superstructure was modeled as a solid part using the 3-D solid continuum element (C3D8R) with a total of ~2200 elements. The concrete material behavior was assumed linear elastic with the elastic properties Young's modulus E_c= 3800 ksi, and Poisson's ratio ν = 0.2. The unit weight of concrete used in the model was 150 pcf. The pier super structure was affixed to the top surface of the pile cap using tie constraints. The separation of the pier and pile group foundation model allowed the reuse and modification of predeveloped pile group models, which resulted in less time spent on recreating FE models.

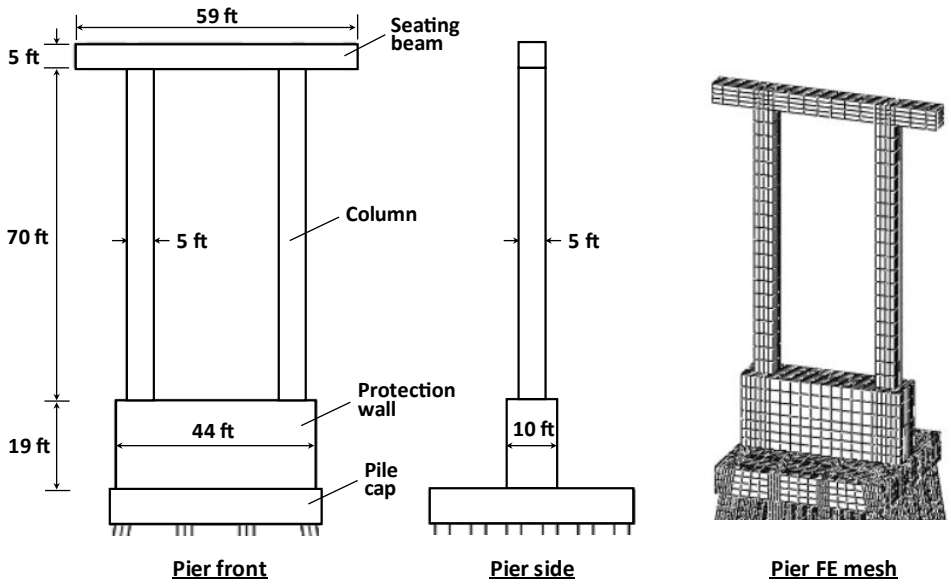

Figure 7.13. Geometry and FE mesh for the pier superstructure

7.3.3.2 Girders and bridge deck

The pier superstructure supported 12 girders (6 per side) and two concrete decks. The girders used in the M19 case were the LG-78 concrete girders (Louisiana bridge design book) spaced at 10.75 ft and had 200 ft span length. The section detail for LG-78 girders was simplified in the FE model to an approximate I-section in terms of cross-sectional area and second moment of area (Figure 7.14).

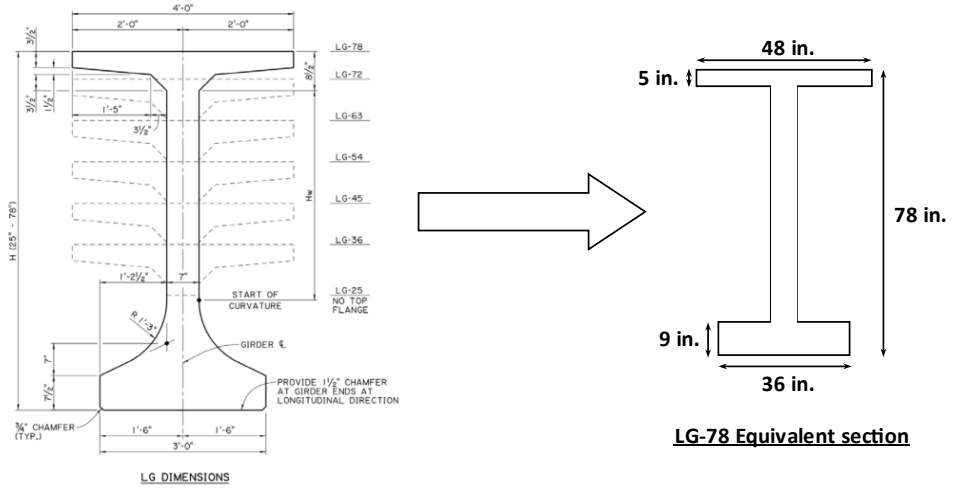

GIRDER DIMENSIONS AND SECTION PROPERTIES										
GIRDER TYPE	H	Hw	Yt	Yb	AREA	Ix	Iy	St	Sb	WEIGHT
	(in.)	(in.)	(in.)	(in.)	($in.^2$)	($in.^4$)	($in.^4$)	($in.^3$)	($in.^3$)	(plf)
LG-78	78	45.58	42.96	35.04	1,086	889,863	77,382	20,714	25,396	1,169

Figure 7.14. LG-78 girder section properties and the equivalent section used in the FE models

This simplification facilitated the modeling of girders using the 3-D beam elements (B23), which required the section definition from standard shapes. The girders were connected to the seating beam using tie constraints to simulated the anchorage. For the far end, the girders were restrained using pin-type displacement constraints. The concrete decks were modeled as solid slab of 8 inches thickness using 3-D shell elements (S4R) and connected to the girders using tie constraints (Figure 7.15). The concrete material behavior for the girders and decks was assumed linear elastic with similar elastic properties to the pier superstructure (Young's modulus E_c= 3800 ksi, and Poisson's ratio ν = 0.2). The unit weight of concrete for girders and deck used in the model was 150 pcf.

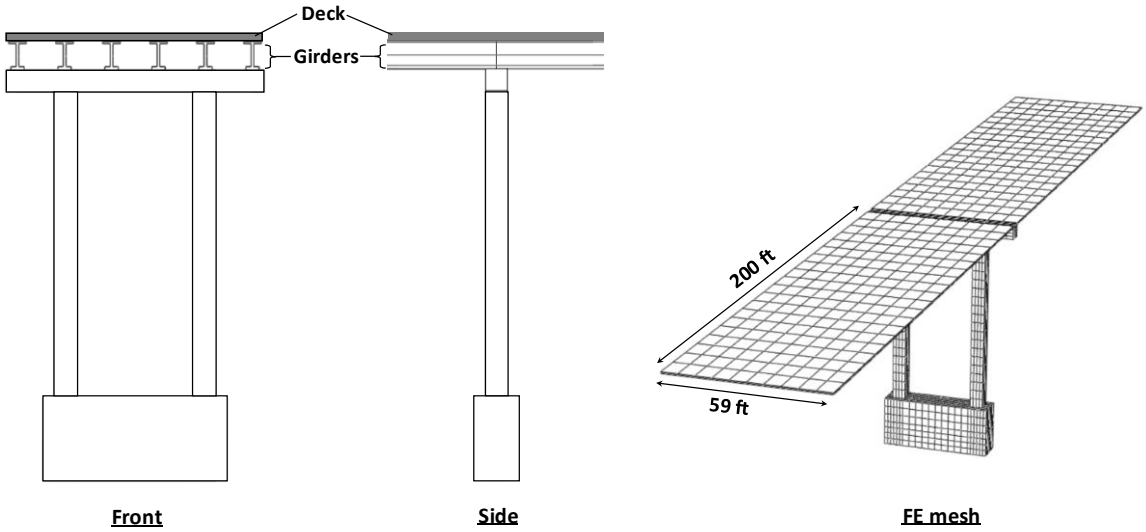

Figure 7.15. Girders and deck FE model

7.3.3.3 Pile group foundation

The M19 pile group foundation comprised of 24 battered piles and the pile cap. In addition to the battered pile group, FE models for vertical and mixed pile group configurations were developed and analyzed for barge impact. The geometry and dimensions of the pile group models were adapted from the M19 battered pile group. The prestressed concrete piles had 3 ft square section and were 110 ft in length. The pile cap was built of cast-in-place concrete and measured 44 ft x 42.5 ft x 7 ft. The main steel reinforcement (Grade 270 steel) in the piles comprised of 36 x 0.6″-dia. steel tendons, which were offset at 3″ within the pile section. The pile group including the pile cap were modeled as a single mesh using the 3-D solid continuum element (C3D8R) with a total of ~21000 elements. The main steel reinforcement was modeled using the embedded shell elements (S4R), which allowed incorporating the prestress force in the piles. The piles were placed in prebored holes created in the soil mesh. The concrete material behavior was modeled using the Concrete Damaged Plasticity (CDP) constitutive model, as presented in chapter 2. The concrete elastic properties for the pile group were Young's modulus were E_c= 5000 ksi, and Poisson's ratio ν = 0.2. The steel material behavior was modeled using the

elastoplastic von Mises model with the elastic properties: Young's modulus E_s= 29000 ksi, and Poisson's ratio ν = 0.26.

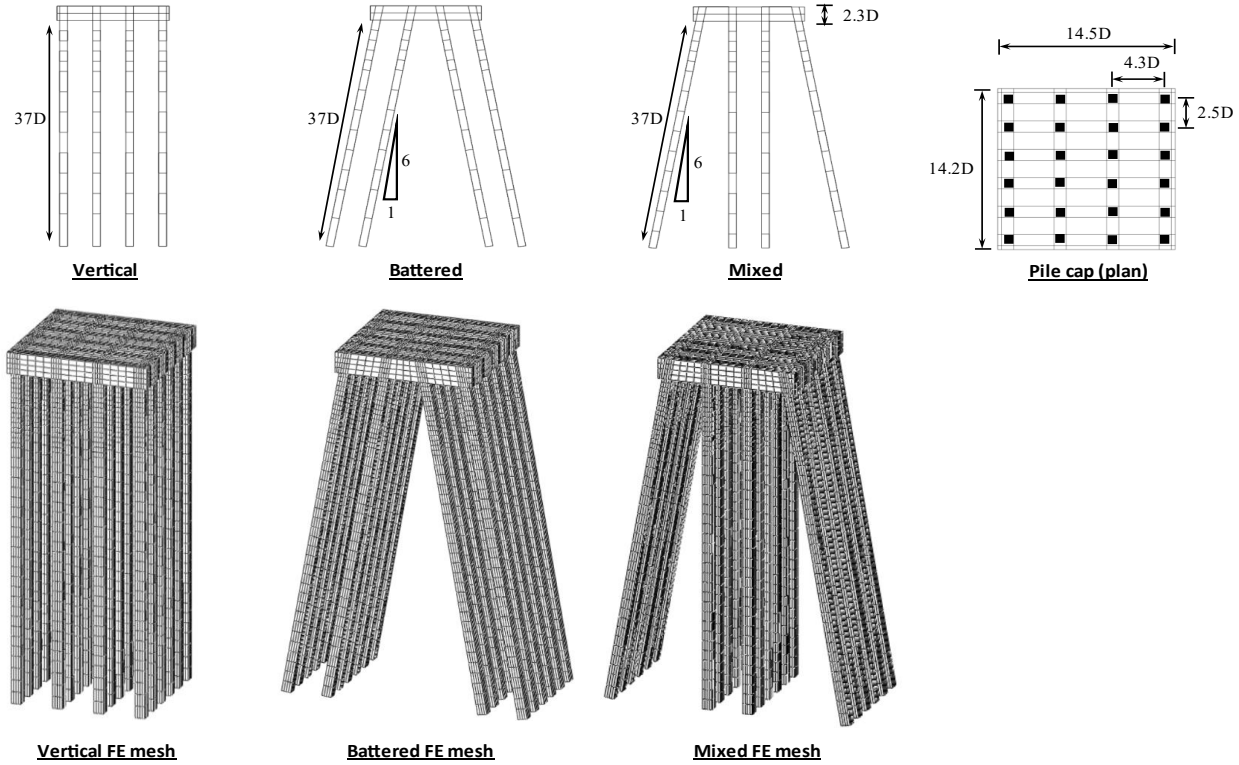

Figure 7.16. Pile group geometry and FE models (D is pile width = 3 ft)

7.3.4 Soil FE model

The soil profile identified in section 4.2 was used in the section too. The soil layering was divided into six clay layers and two sand layers. The FE mesh for the soil layer was built from two types of elements: the standard elements, and the infinite elements. The standard elements were the 3-D solid continuum elements (C3D8R) and were assigned to the central part with elastoplastic material behavior (Figure 7.17). The infinite elements (CIN3D8) were used on the far boundaries to provide the equilibrium reaction and absorb the propagating stress waves, as discussed previously. The total number of elements used in the soil body was ~153000. The clay material behavior was modeled using the Modified Cam Clay model (MCC), while the sand material behavior was modeled using the Drucker Prager model (DP). The material parameters for both models are summarized in Table 7.1. The soil model parameters used in the barge impact problem were different than the properties used in the static analysis (Chapter 4), and were verified using the results of the statnamic test discussed in the following section. Additionally, material damping for the soil material was introduced using the two-parameter Rayleigh damping model described previously. The Rayleigh damping parameters (α, β) was estimated for an average

damping ratio ξ=2% over the frequency range 1-10 Hz. The damping parameters obtained from the iterative procedure were α=0.1, β=0.0013.

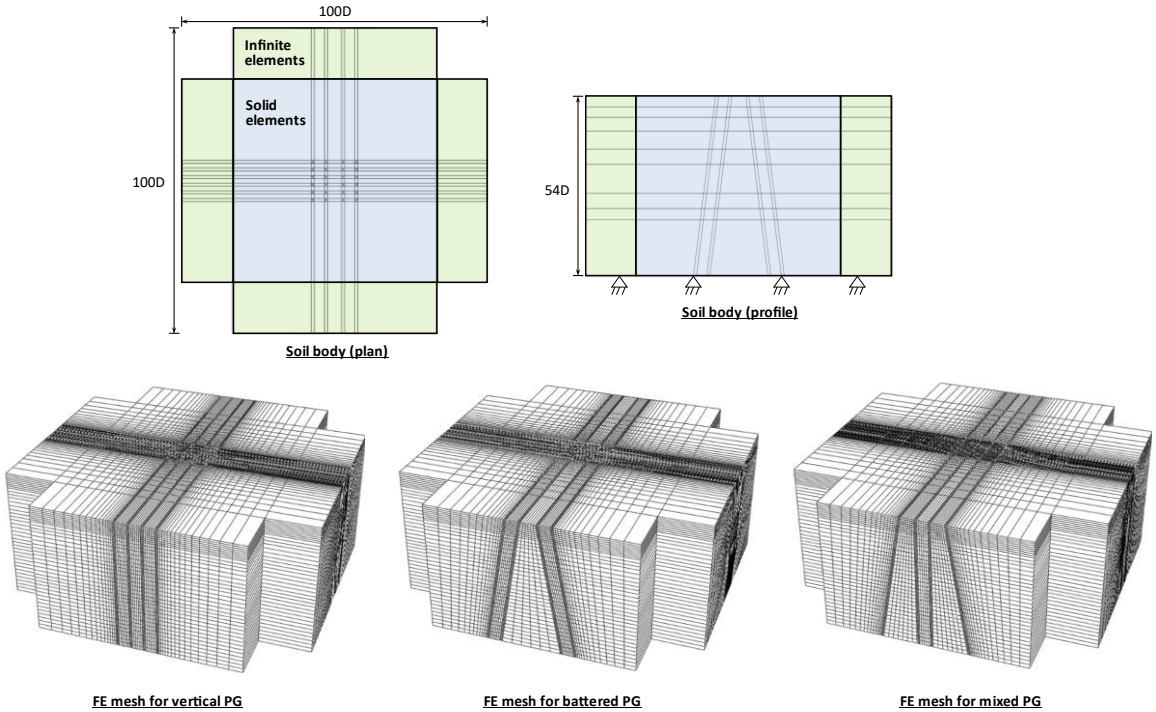

Figure 7.17. Soil body geometry and FE mesh (D is pile width = 3ft)

Table 7.1. MCC and DP model parameters used in the barge impact FE models

Soil Type	Depth from mudline (ft)	Unit weight (pcf)	Poisson's ratio (ν)	MCC			DP		
				E (ksf)	M	λ	E (ksf)	β	d (psf)
Soft Clay	0-15	123	0.40	52	0.9	0.14	-	-	-
Stiff Clay	15-25	119	0.40	239	1.1	0.12	-	-	-
Medium Clay	25-38	108	0.40	259	1.0	0.13	-	-	-
Medium Sand	38-49	120	0.40	-	-	-	360	53	10
Stiff Clay	49-70	113	0.40	528	1.2	0.12	-	-	-
Stiff Clay	70-81	122	0.40	637	1.2	0.12	-	-	-
Stiff Clay	81-99	128	0.40	637	1.2	0.12	-	-	-
Dense Sand	>99	124	0.40	-	-	-	720	58	10

7.3.5 Verification of soil response using pile TP7 statnamic test results

The soil and damping parameters were verified to ensure a realistic response in the pile group models subjected to barge impact. The statnamic test is a dynamic test performed on test piles to back-calculate the static resistance from the dynamic response. During the construction of the M19 pile group foundation, a statnamic test was performed on test pile TP7, which was located 135 ft west of the M19 pile group foundation. An FE model for pile TP7 simulating the statnamic test was developed, in which the soil model and damping

parameters in Table 7.1 were used. The experimental and FE pile response was compared to verify the response from the soil model.

7.3.5.1 The statnamic test of pile TP7

The lateral statnamic test was used on test pile 7 during the construction of the I-10 twin span bridge. Sacrifice test piles are commonly used during construction projects to verify the axial and lateral design capacities of piles. The statnamic test setup comprises of three main parts: piston, cylinder, internal accelerated mass (Figure 7.18). The cylinder houses the fuel and the accelerated mass. When the fuel burns, the pressure inside the cylinder increases and accelerates the internal mass, which generates the reaction force on the pile. The movement of the cylinder assembly is guided by a track when it slides away from the pile. The force-time history is measured by the load cell embedded in the piston. The displacement and acceleration time histories of the pile are obtained from LVDTs and accelerometers. The test is conducted in multiple consecutive load cycles, in which a minimum of two points in the pre-yield region and two in the post-yield region is targeted when deciding the peak load for each cycle. The test results with assumptions regarding the damping ratio are used to back-calculate the static lateral resistance.

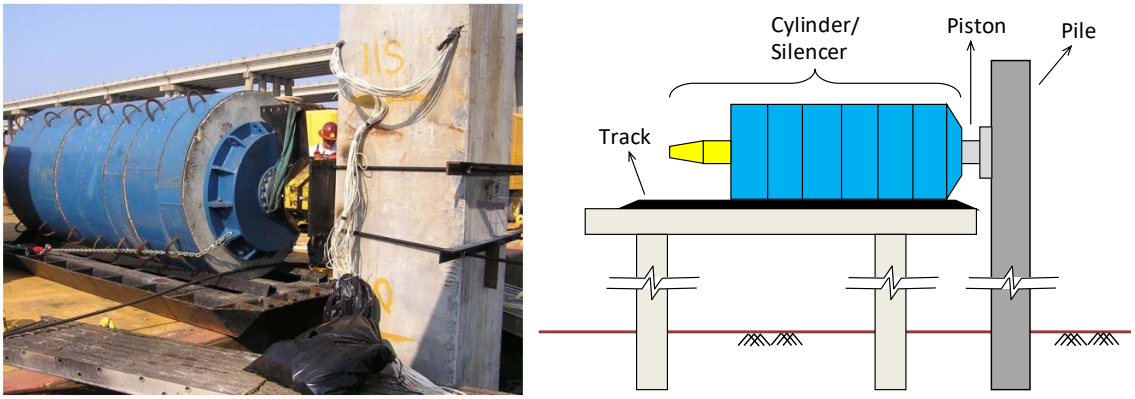

Figure 7.18. Statnamic test setup

Pile TP7, driven near the location of pier M19, was 36-inch squared prestressed concrete pile and 123 ft in total length with similar specs to the piles of M19 pier foundation. It was instrumented with LVDTs, strain gages, and accelerometers over its length (Figure 7.19). The statnamic test on pile TP7 was conducted in five consecutive load cycles with increasing peak load after each cycle (Figure 7.20a). For this study, the test results for pile TP7 were used to verify the soil model parameters and the pile response in the FE model. The load-displacement response and displacement time history measurements from the LVDT are shown in Figure 7.20b, c. The peak load for the first cycle was 33 kips and increased up to 115 kips in the fifth cycle. The peak displacement during the first cycle was 2 inches and reached to 10 inches during the fifth cycle.

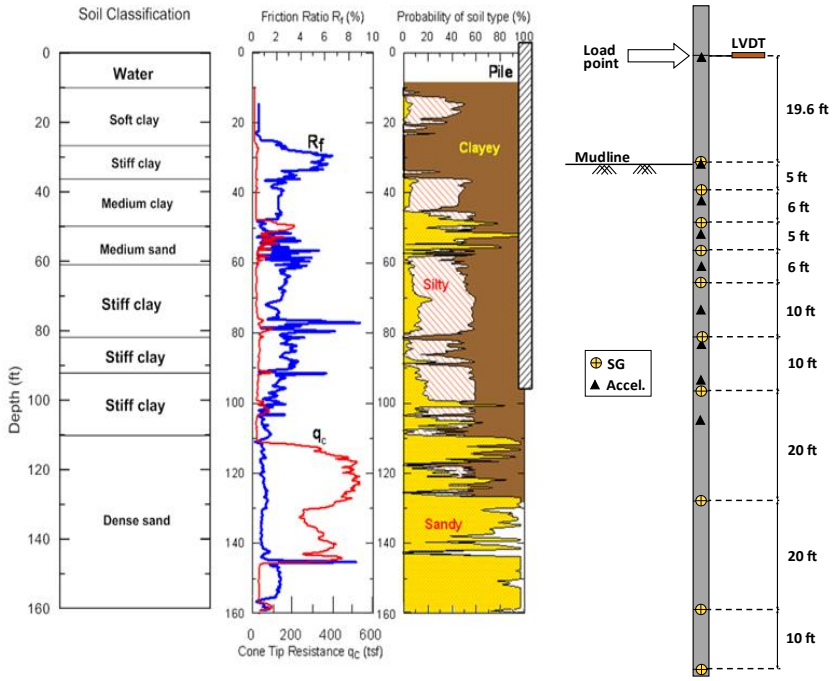

Figure 7.19. Soil profile and instrumentation for pile TP7

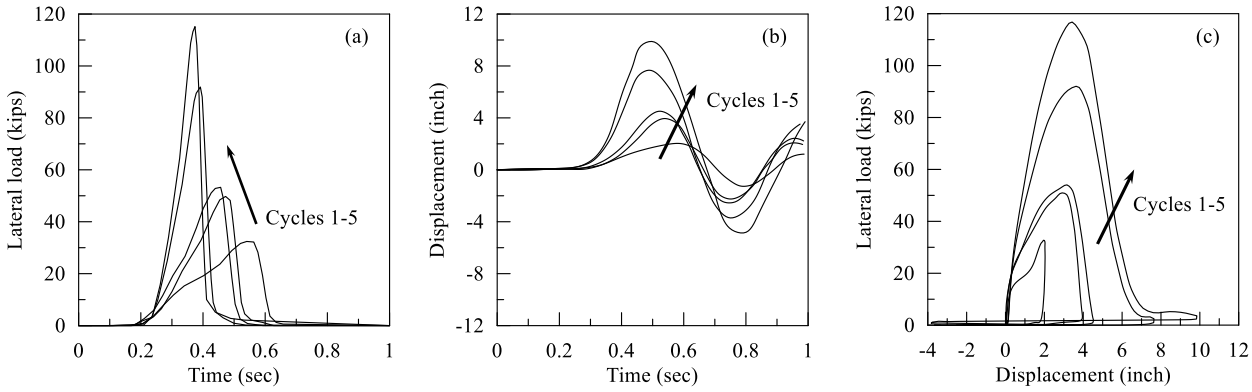

Figure 7.20. Statnamic test results for pile TP7: (a) load time history, (b) displacement time history at loading point, (c) load-displacement curves

7.3.5.2 FE model of pile TP7

The FE model for pile TP7 was created to verify the soil constitutive model parameters and the damping constants. The FE model comprised of the pile and soil body (Figure 7.21). The pile was modeled using the solid continuum element (C3D8R) with the main steel reinforcement modeled using the embedded shell elements (S4R). The soil body was modeled using the solid continuum elements (C3D8R) for the central region (blue colored in Figure 7.21) and using the infinite elements (CIN3D8) for the outer boundary regions (green colored). The number of elements used was ~2300 for the pile model and ~50000 for the soil model. With the use of the infinite elements, the only boundary condition

needed in the FE model was for the bottom boundary using displacement constraints as in to pin.

The loads applied in the FE model were: gravity and the statnamic load. The gravity load is necessary to establish the geostatic stress equilibrium. The statnamic load was applied as uniformly distributed load over a strip area of 1ft width on the pile surface so that the center of the area corresponds to the loading point in the in-situ test (Figure 7.19). The load amplitudes for the five load cycles (Figure 7.20a) was imported into the FE model and used to vary the distributed load magnitude with time.

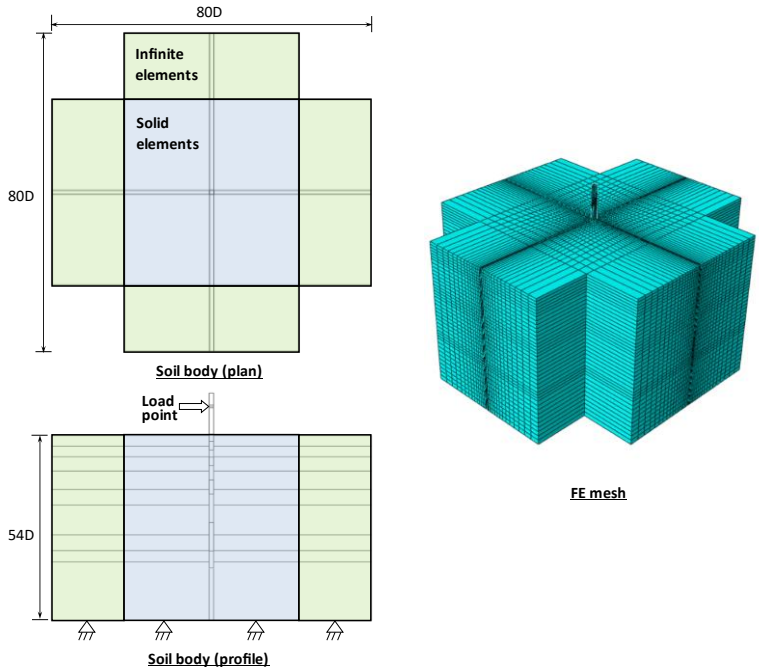

Figure 7.21. Pile TP7 geometry and FE model

The FE simulation was conducted in five consecutive loading steps, similar to the in-situ test, and included a dummy first step to establish the geostatic stress equilibrium (Figure 7.22). The load cycle duration in the statnamic test was less than 1.0 seconds and after each cycle there was 20-30 min gap to reset the statnamic device. The time gap between each load cycle allowed the pile's free oscillation to vanish prior to the next load cycle. For the FE model, the interest was to obtain the pile response for the first 1.0 second. However, the free oscillation of the pile in the FE model continued after the first 1.0 second and it interfered with the pile response in subsequent load cycles. Running an FE model in explicit dynamics for a step duration in the order of minutes is time consuming and not practical. Therefore, an artificial damper was added in the FE model at the loading point elevation to dampen the free oscillation of the pile within seconds. The duration for each load step was fixed at 3.0 seconds and the artificial damper was activated after the first 1.2

seconds. The 3.0 seconds duration was verified to be long enough to stop the free oscillation of the pile (Figure 7.22).

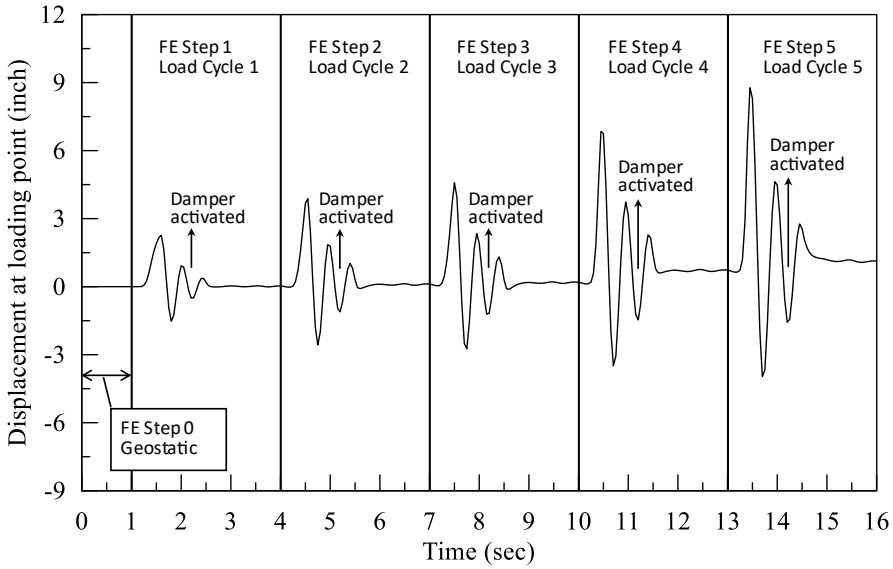

Figure 7.22. Pile displacement response throughout the simulation steps

7.3.5.3 Results

The pile displacement at the loading point was used to verify the response from the FE model.

Figure 7.23 shows the results of pile displacement at the loading point for each load cycle for the statnamic test and the FE model. Very good agreement can be noticed for the first three load cycle. For cycles 4 and 5, there is a notable difference (0.7-0.9 inch) in the peak displacement between the FE model and the statnamic test, which is attributed to the pile damage. The statnamic test report showed that the strain gage readings at depth 16 ft from the mudline were very high (>7000μ strain), which is a sign of pile damage. Furthermore, the FE model results showed significant material damage in the pile at similar depth after the load cycles 4 and 5 (Figure 7.24).

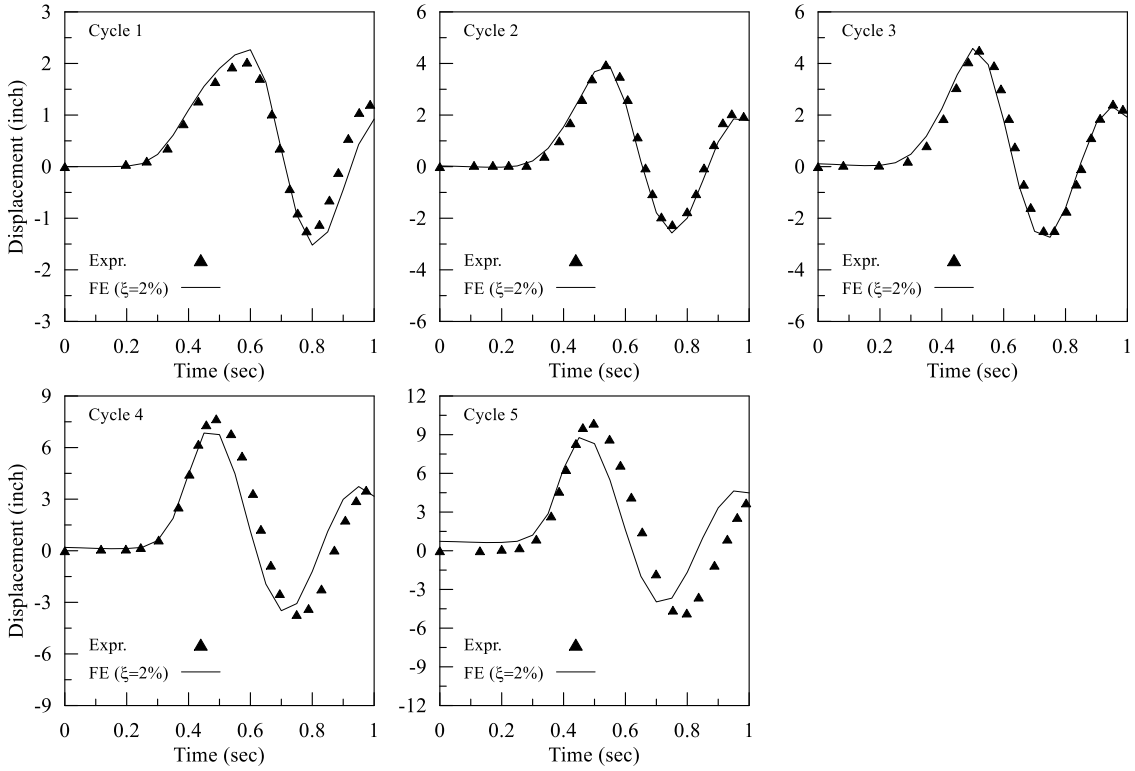

Figure 7.23. Pile displacement results at the loading point from the statnamic test and FE model

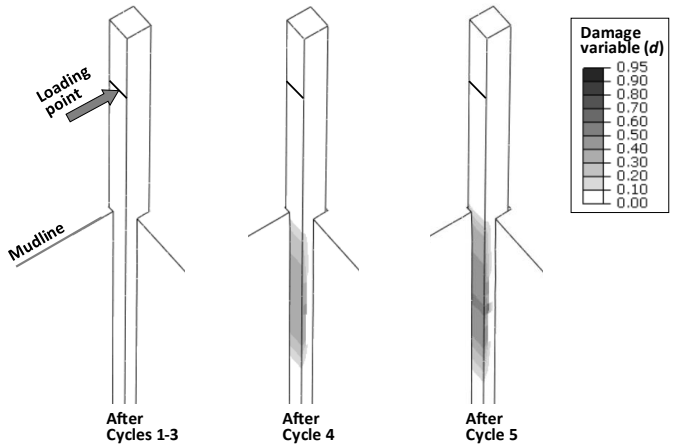

Figure 7.24. 3-D contour plot for the pile damage after each load cycle

7.3.6 Loads, boundary conditions, and solution steps

The loads applied in the barge impact problem were gravity and artificial damping loads. The gravity load (g =32.2 ft/s^2) was applied to the soil body, pier superstructure, girders and deck, and pile group. The impact load by the barge was introduced by assigning an initial velocity in the horizontal direction so that it is generated from the barge momentum and interaction with the pile group. The artificial damping loads were introduced to

eliminate the oscillations in the whole model induced by the gravitational acceleration. The damping loads were removed after the oscillations ceased in the model, so they don't influence the model response during the barge impact. For boundary conditions, the bottom of the soil model and the girders' far ends were assigned with displacement constraints akin to pin. No boundary conditions were used on the side boundaries of the soil body due to the use of infinite elements, as discussed previously.

The barge impact problem was solved in two steps with two seconds step duration; the first was the equilibrium step, and the second was impact step (Figure 7.25). In step 1, the model is brought to near static condition by allowing the soil to reach a state of geostatic stress equilibrium and dissipating the oscillations caused by the gravitational acceleration. The barge is initially positioned at a distance so that the impact occurs after the end of the first step. The distance is estimated from the barge velocity and the step time of two seconds. At the end of step 1, the impact is imminent and the barge bow is barely in touch with the pile cap. In step 2, the barge impact progresses until the barge momentum dissipated and the rebounds away from the pile group.

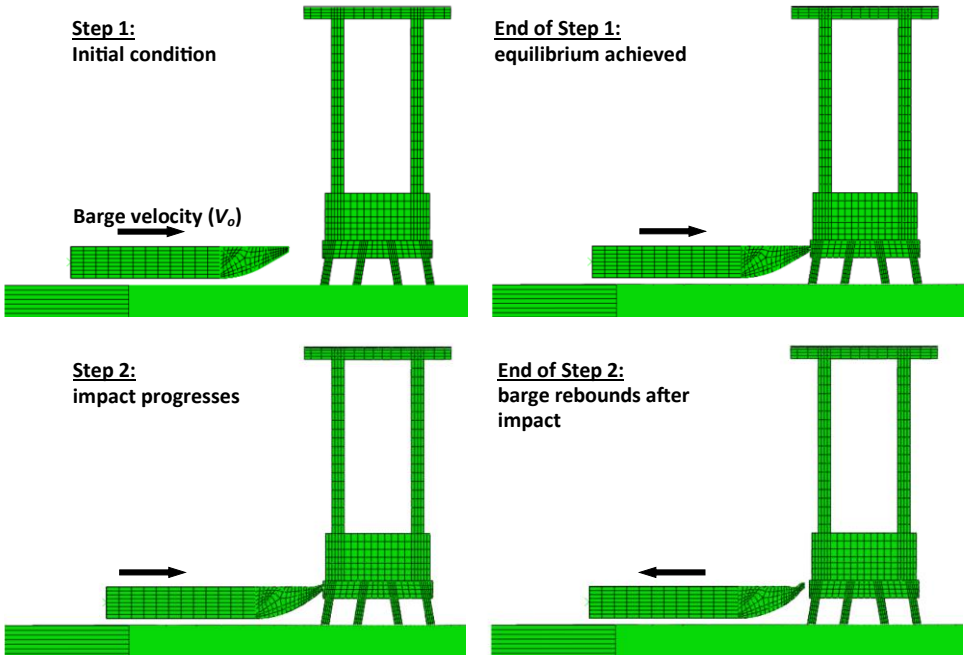

Figure 7.25. Illustration of steps for simulating the barge impact problem

7.4 Results

The barge impact results are presented for pile group displacement, group and piles' shears, axial reaction, and bending moment.

7.4.1 Displacement results

The displacement history at the pile cap and pier top elevations were obtained for all cases and shown in Figure 7.27. The displacement history exhibits a large peak in the first 0.2-

0.4 seconds as a response to the impact force, and subsequent smaller peaks corresponding to the free oscillations of the structure. It is noticed that the displacement vanished in the battered and mixed PGs after 2 seconds, whereas in the vertical pile group it returns to a non-zero value. The latter observation is referred to the gap formation in the front soil and to the significant damage in the piles (Figure 7.26). The damage contours plot is shown only for the vertical PG, while the battered and mixed PGs were free of damage for all impact cases.

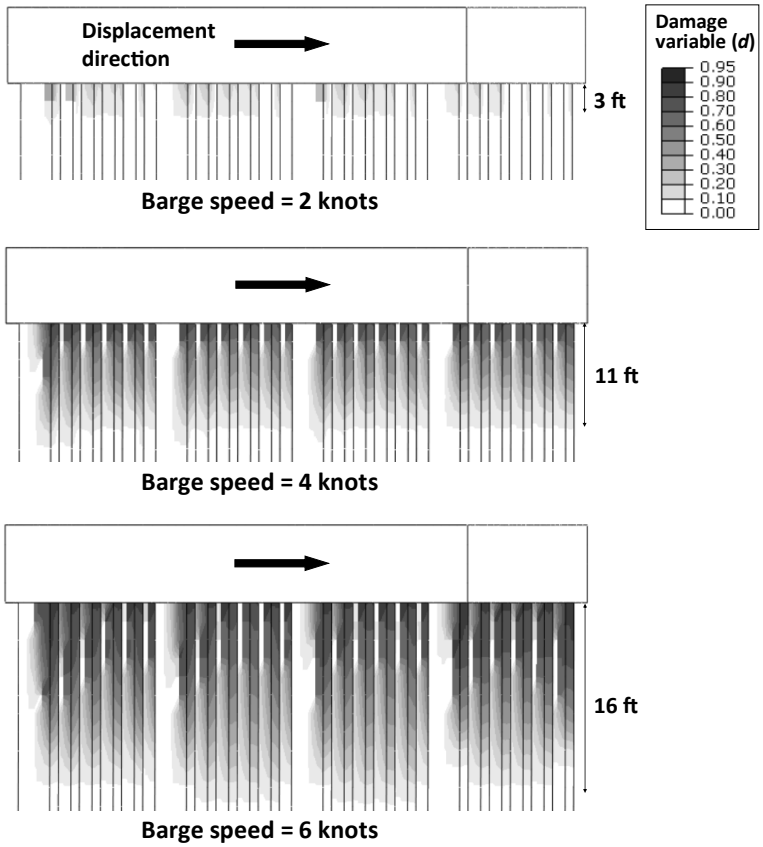

Figure 7.26. Damage contours for the vertical PG after the impact

The peak displacement at the pile cap was notably higher (2-8.4 inches) in the vertical pile group (PG), while in the battered and mixed PGs the peak displacement remained within 2-2.5 inches at all barge speeds. The magnitude of peak displacement was mainly affected by the impact force which is dependent on the lateral PG stiffness and the barge bow stiffness. The barge's kinetic energy is dissipated in the impact by two mechanisms: (1) PG displacement, and (2) barge bow deformation. The PG displacement depends on the lateral PG stiffness, which is a function of PG type and soil resistance. When the PG stiffness is relatively low, a greater portion of the impact energy is dissipated in the PG displacement, while for very stiff PGs the significant portion of the impact energy is absorbed by the bow deformation.

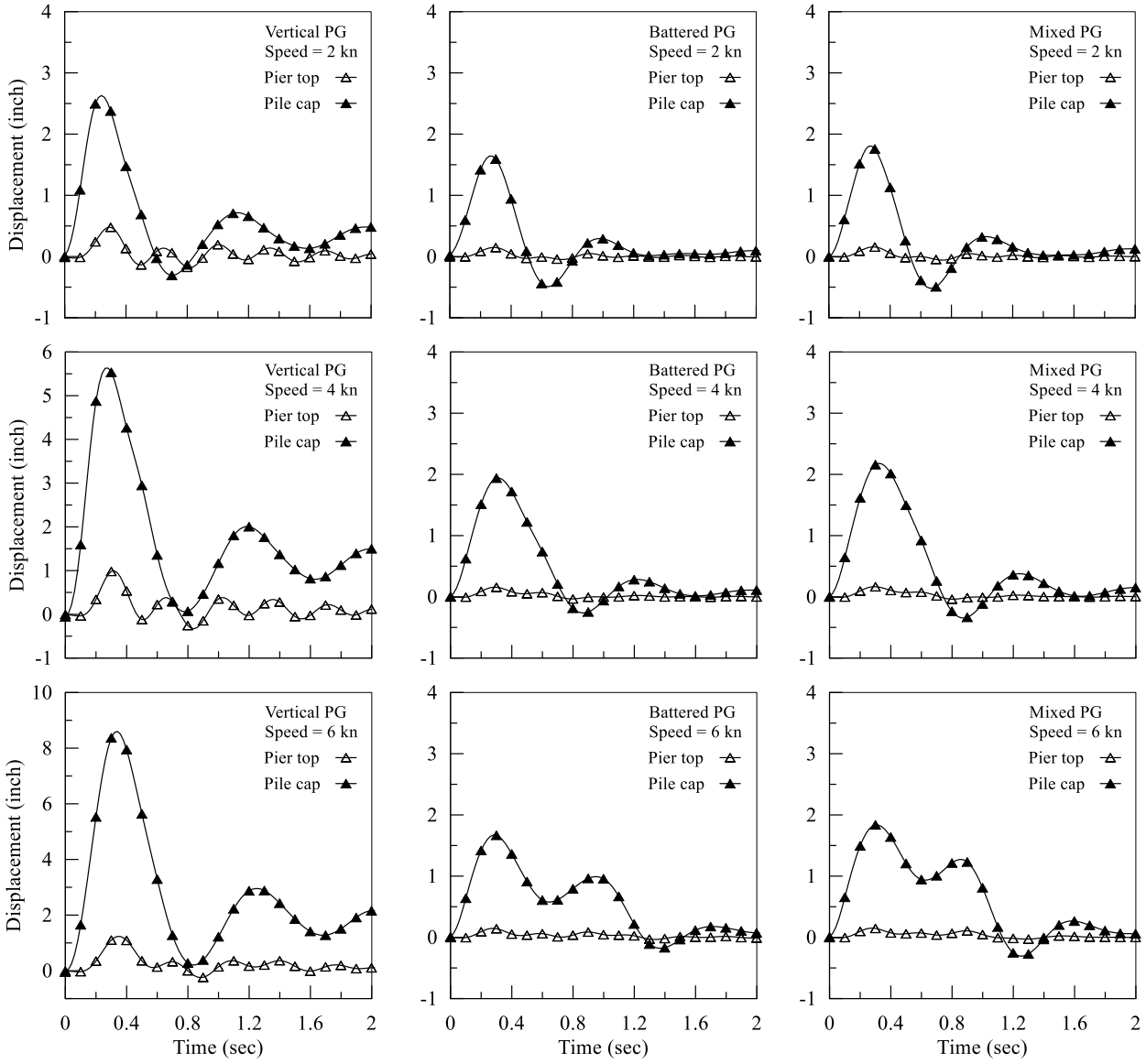

Figure 7.27. Displacement history results

The lateral stiffness of the vertical PG was relatively low so that the impact generated greater lateral force and as a result had greater pile cap displacement. The battered and mixed PGs exhibited closely similar response and had significantly higher stiffness than the vertical PG, which can be deduced from the smaller pile cap displacement and significantly large bow deformation. The relation between the peak displacement and barge speed is investigated in Figure 7.28. A linear relation between the displacement and speed is noticed in the vertical PG. In the battered and mixed PGs, the results show that the displacement was almost constant with increased barge speed. A further look at the peak impact force versus peak displacement provides additional clarification for the battered and mixed PG cases (Figure 7.29). The peak impact force in the battered and mixed PGs was closely similar at all barge speeds.

The barge bow deformation can be separated into two parts: elastic and inelastic. In Figure 7.30, the bow deformation reaches a peak value and then recedes to a lower plateau. The difference between the peak and the plateau represents the elastic bow deformation, whereas the value at the plateau corresponds to the inelastic deformation. It can be noticed from the figure that the inelastic bow deformation in the vertical PG case was significantly lower than the battered and mixed PGs for the barge speeds greater than 2 knots. For example, at barge speed 6 knots, the inelastic bow deformation was 3.5 inches for the vertical PG versus 40-42 inches in the battered and mixed PGs.

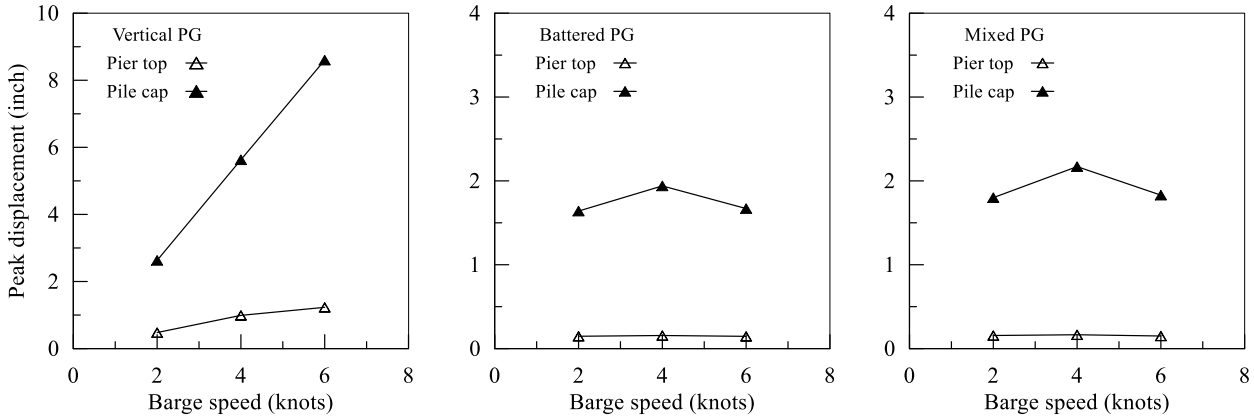

Figure 7.28. Peak displacement at different barge speeds

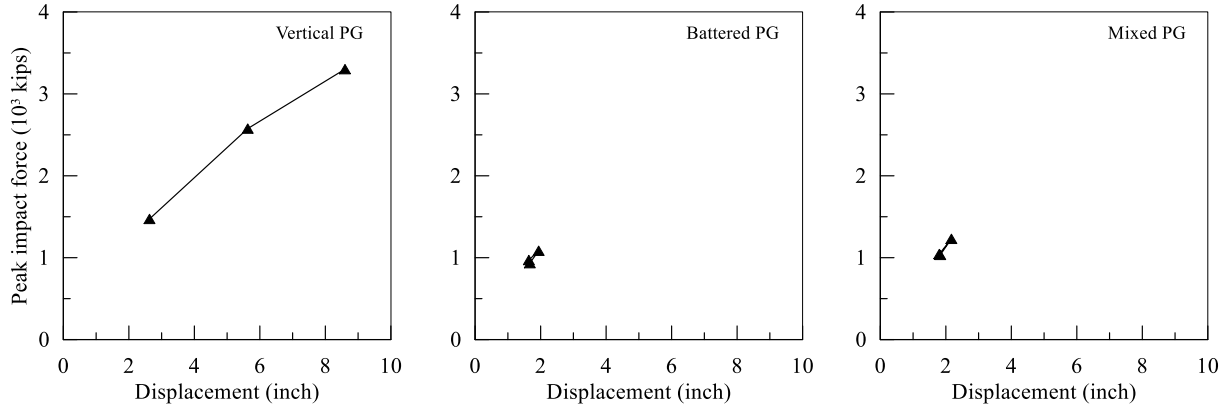

Figure 7.29. Peak impact force vs pile cap displacement

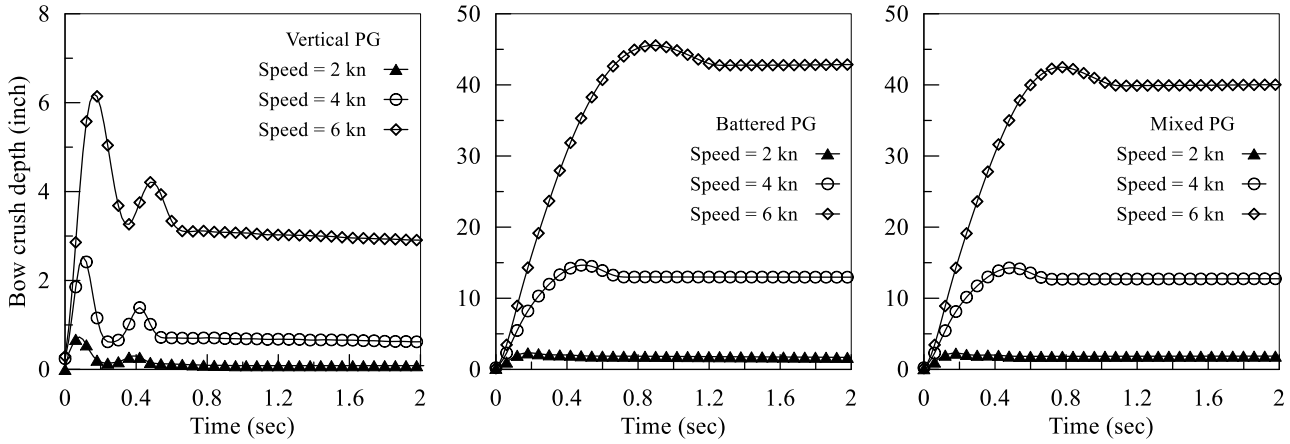

Figure 7.30. Barge bow deformation history results

7.4.2 Impact force and shear force distribution

The shear force history in all piles and pier columns is shown in Figure 7.32, and the shear force sum in both represents the total impact force. Figure 7.31 illustrates the definition of the shear force in the piles and pier columns.

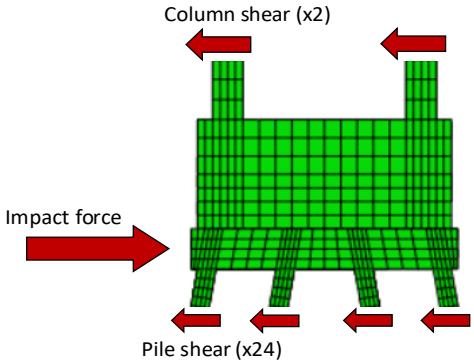

Figure 7.31. Free body diagram illustrating the internal shear forces in the pier

The impact force in the vertical PG case was notably higher than the battered and mixed PGs. The vertical PG behavior facilitated the generation of greater lateral force from the impact by absorbing more kinetic energy. The lower stiffness of the vertical PG allowed greater lateral displacement and greater damage levels in the piles. On the other hand, the battered and mixed PGs absorbed less kinetic energy due to the higher stiffness, which forced the barge bow to greatly deform and absorb significant amount of kinetic energy. The force history in the vertical PG peaks at a higher rate than the other PGs and shows an intermediate peak in the declining limb, which was possible due to the pushing from the pile cap on the barge on reversal. It can be noticed that the force in the piles in the vertical PG returns to a negative value at the end of the impact, which was due to the damage in the piles. The damage in the piles was located on the tension side in the piles and created a negative balance in the pile shears. The negative pile shears were countered by a net

positive shear in the pier columns. In the battered and mixed PGs, the duration of the first peak was longer due to the bow deformation. At barge speed 6 knots, the force history for both PGs shows two consecutive force peaks indicating that the collision was highly inelastic.

The peak force in the piles and pier columns versus barge speed is summarized in Figure 7.33. The results show that the peak force increased linearly with barge speed in the vertical PG, while it remains fairly constant in the battered and mixed PGs. The contribution from the foundation and superstructure in the total resisting force is depicted in Figure 7.34. The results show that the force ratio carried by the piles was constant (82%) in the battered and mixed PGs, while in the vertical PG the force ratio decreased from 75% to 65% when the barge speed increased. The reason for that is the piles damage, which weakened the piles in the in the vertical PG.

A comparison between the peak impact force from the FE analysis and prediction models by AASHTO (2012) and Consolazio et al. (2009) is shown in Figure 7.35. As discussed in the introduction, AASHTO's impact force prediction model is a function of the barge's mass, speed, and bow crush depth, while Consolazio's prediction model is a function of the pier-barge contact width only. It can be seen that Consolazio's model prediction works well in the case of the vertical PG but greatly over-predict the impact force in the cases of battered and mixed PGs. This indicates that the pile group's lateral stiffness is an influencing factor and a distinction for each configuration is needed in the model. On the other hand, AASHTO's prediction model under-predict the impact force in all cases and at a significant level in the vertical PG case.

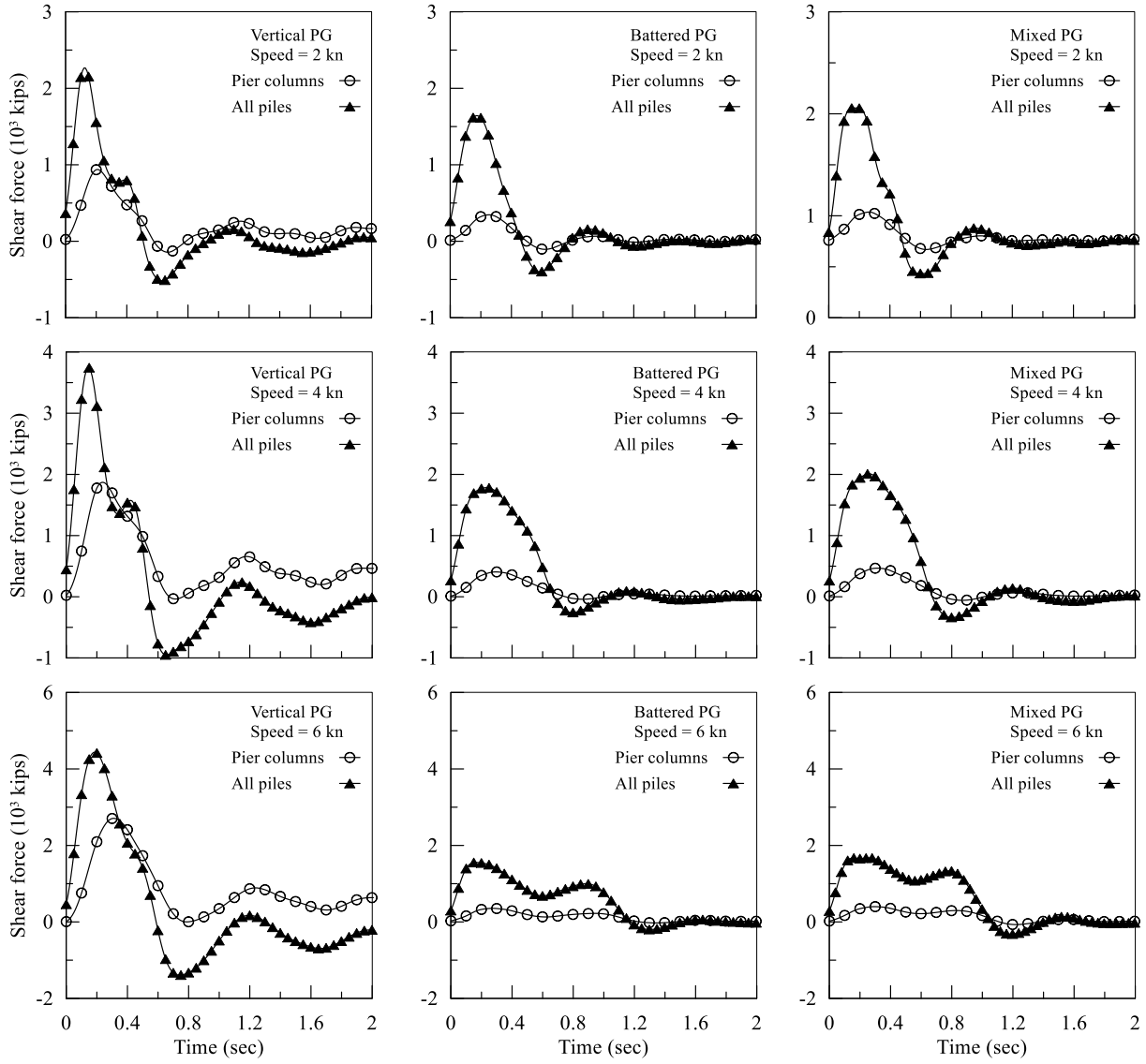

Figure 7.32. Shear force history results

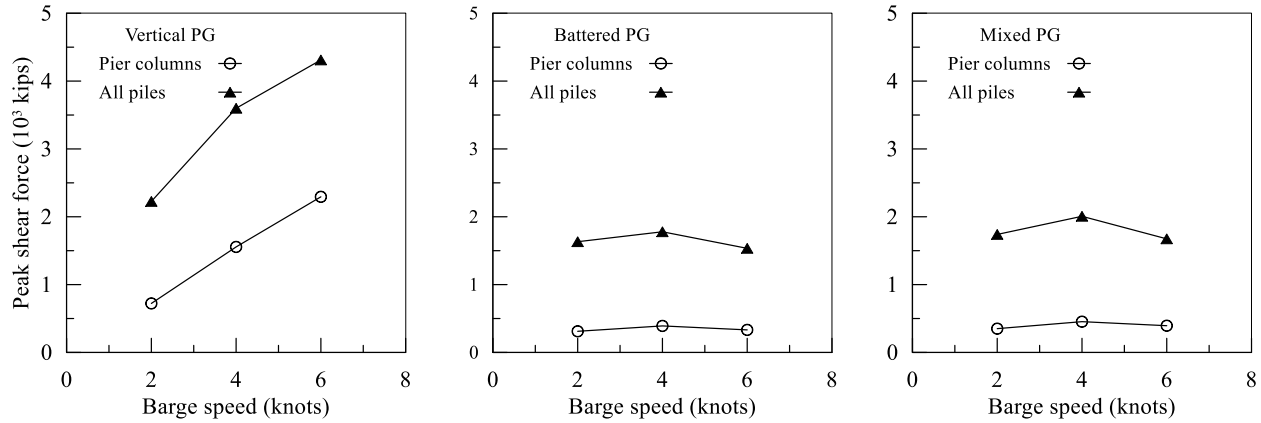

Figure 7.33. Peak shear vs barge speed results

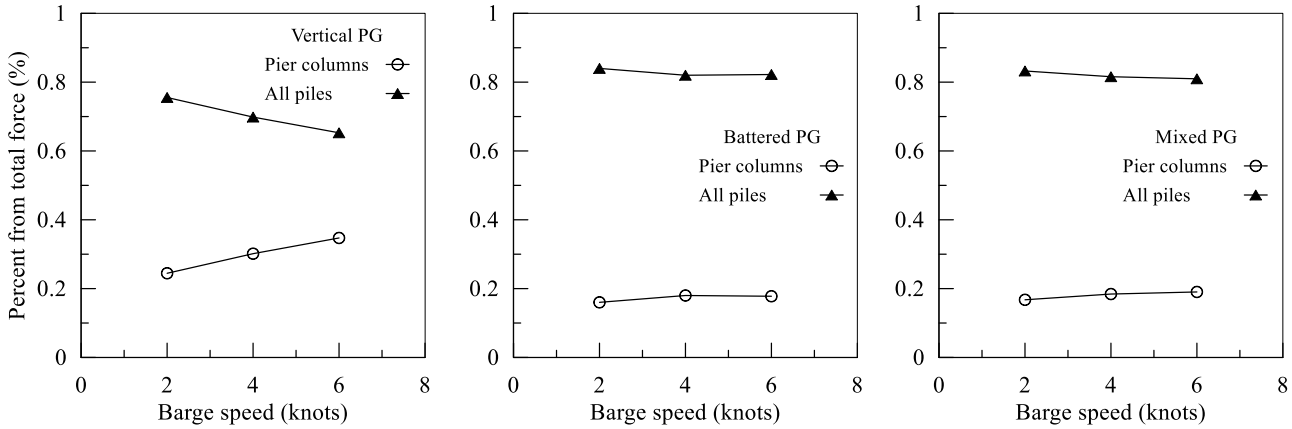

Figure 7.34. Contribution of piles and pier columns in the resisting force

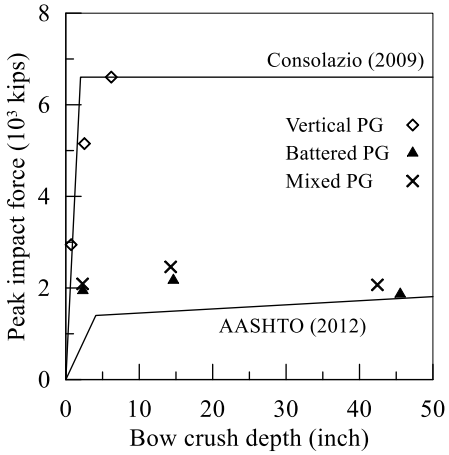

Figure 7.35. Peak impact force vs force prediction models

The contribution of each pile to the total shear force is investigated with the aid of Figure 7.36, Figure 7.37, Figure 7.38, in which each subplot presents the results for piles in the same row (L, ML, MT, T). Notice that the figures include the results for half of the 24-piles due to the symmetry about the pile cap centerline (Figure 7.9). The similarity in the shape of force history for the total force and the individual pile force is noticed, for example, when comparing Figure 7.32 and Figure 7.36. The main observation in the force history per pile is the slightly higher contribution of the piles in the edge column (col. 1). This was also observed in the previous results for statically loaded PGs and the reason for it was the influence of the group effect. The ratio of the peak shear force in each pile to the total shear force is summarized in Figure 7.39. The contribution of the edge column was fairly constant for all barge speeds and notably higher in the battered and mixed PGs. On average, the percentage difference in the shear force ratio between the edge column (col. 1) and the interior columns (col. 2 and 3) was 0.6% in the vertical PG, 1.7% in the battered PG, and 1.5% in the mixed PG.

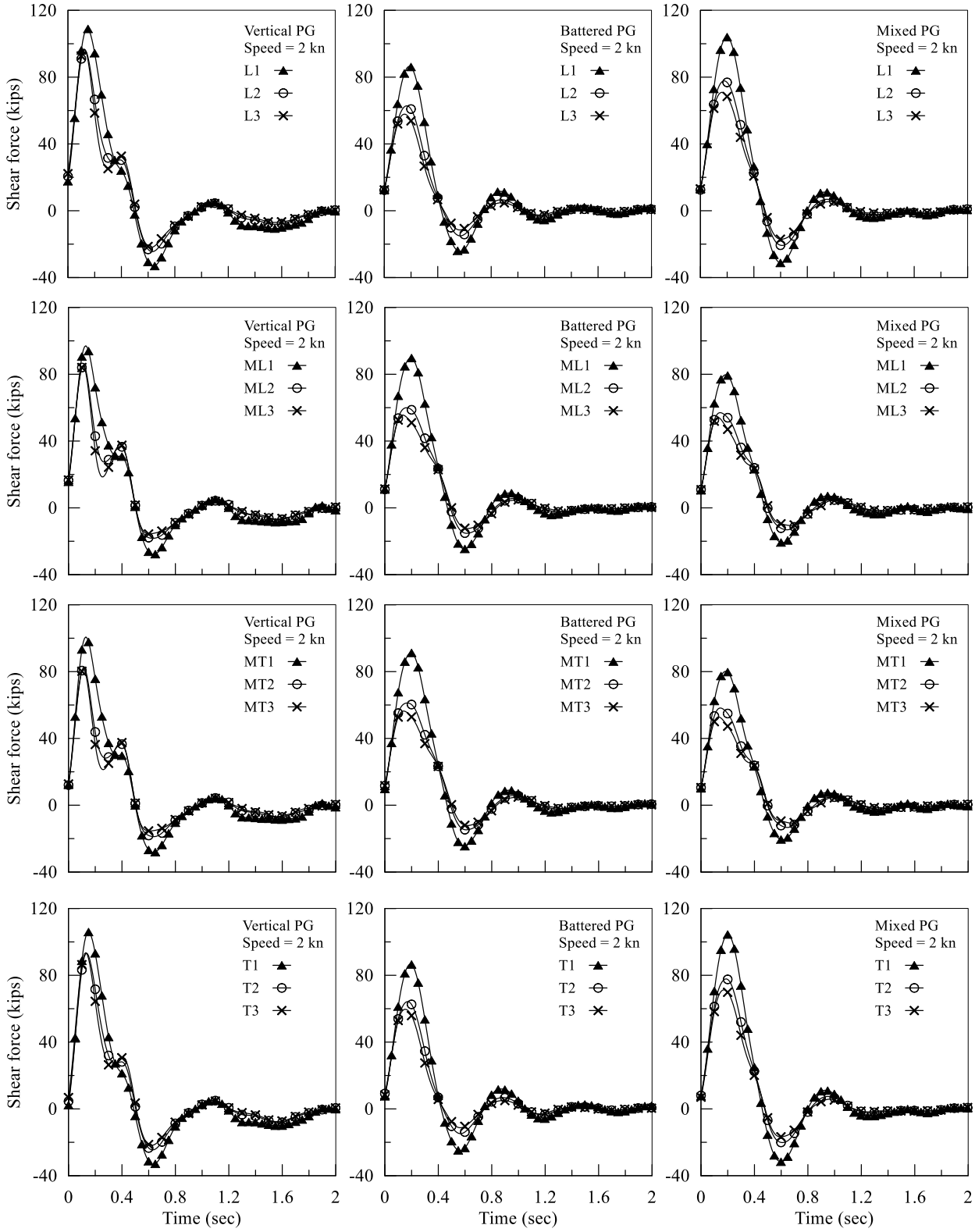

Figure 7.36. Piles' shear force history results at barge speed = 2 knots

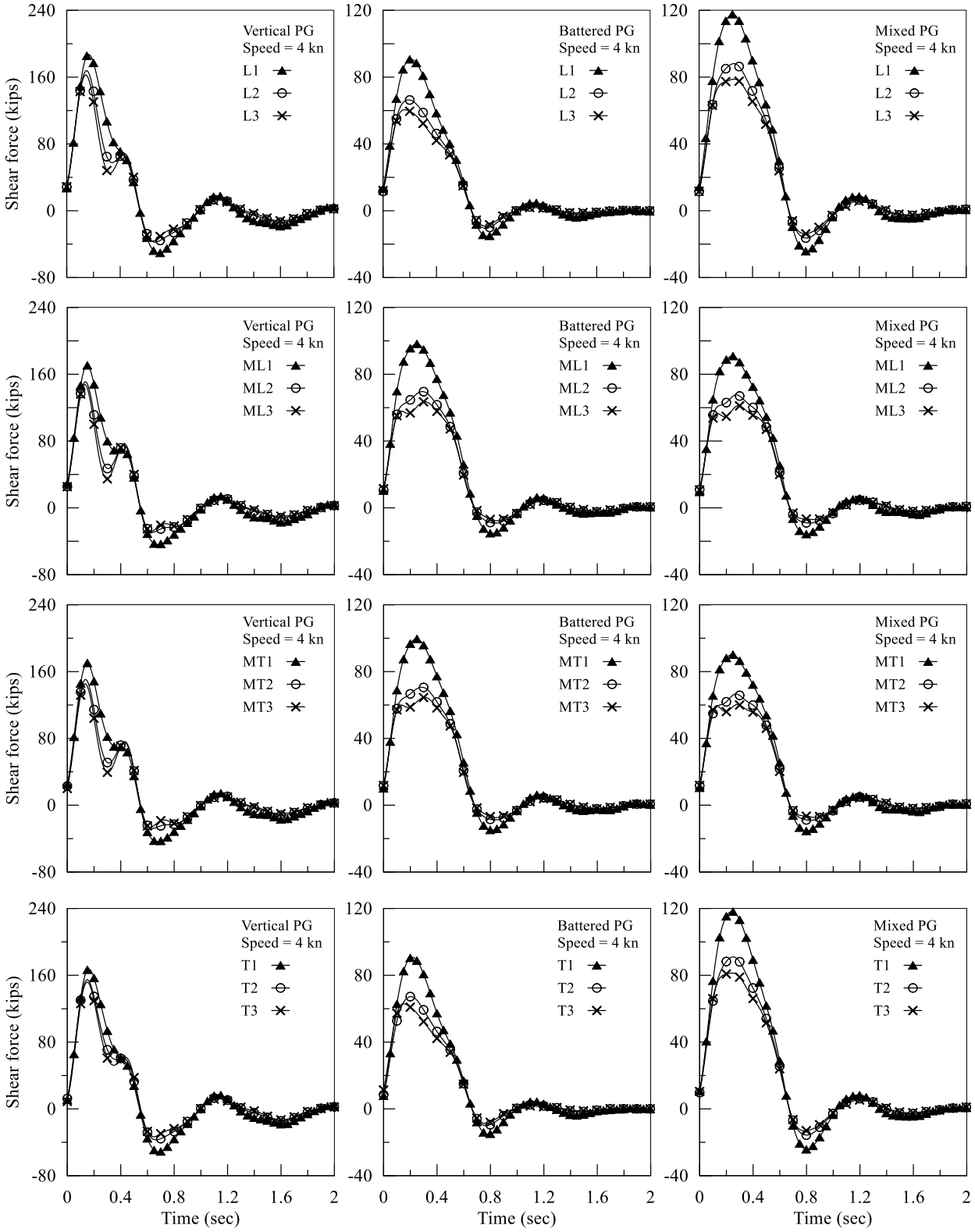

Figure 7.37. Piles' shear force history results at barge speed = 4 knots

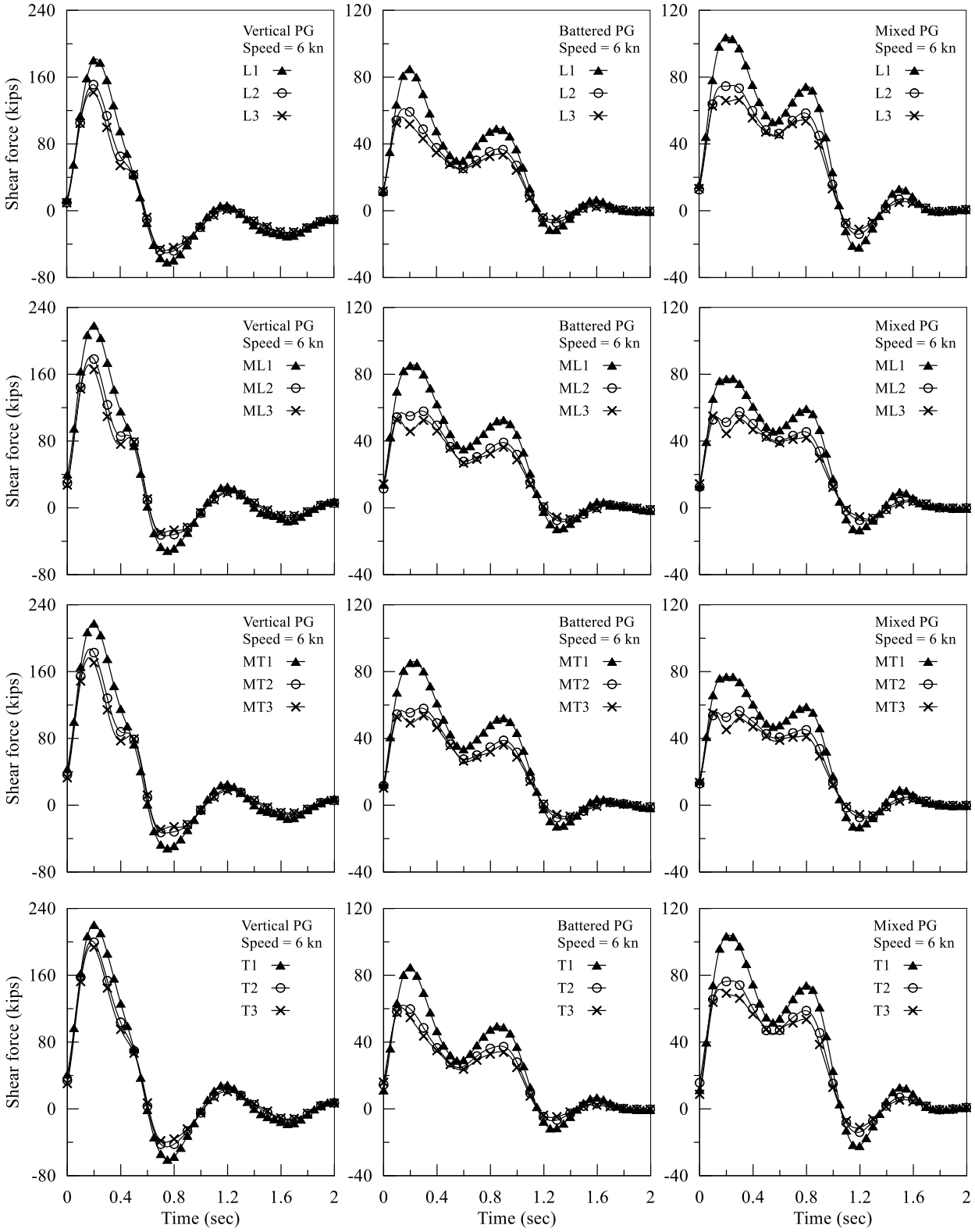

Figure 7.38. Piles' shear force history results at barge speed = 6 knots

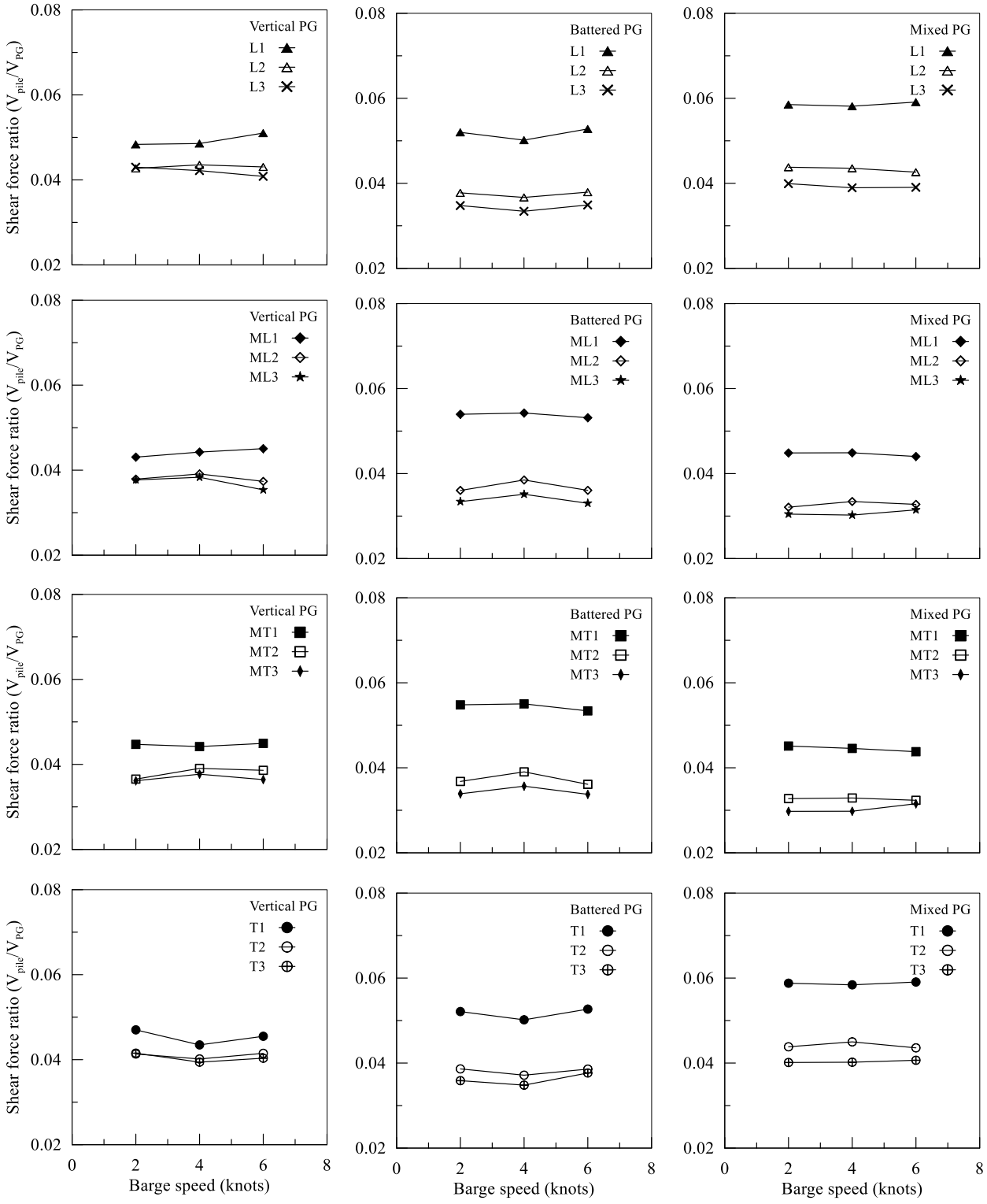

Figure 7.39. Summary of piles' peak shear force ratio for each pile

The contribution of each pile row to the total shear force is summarized in Figure 7.40. in the vertical PG, row L had the highest percentage (27%) followed by row T (25%), and

rows ML and MT (24% each). The battered PG rows had a closely similar percentage at 25%, which is a different distribution than the observed from the static analysis in section 5.5.3. The mixed PG had the largest contrast between the rows with 28% in rows L and T, and 22% in rows ML and MT.

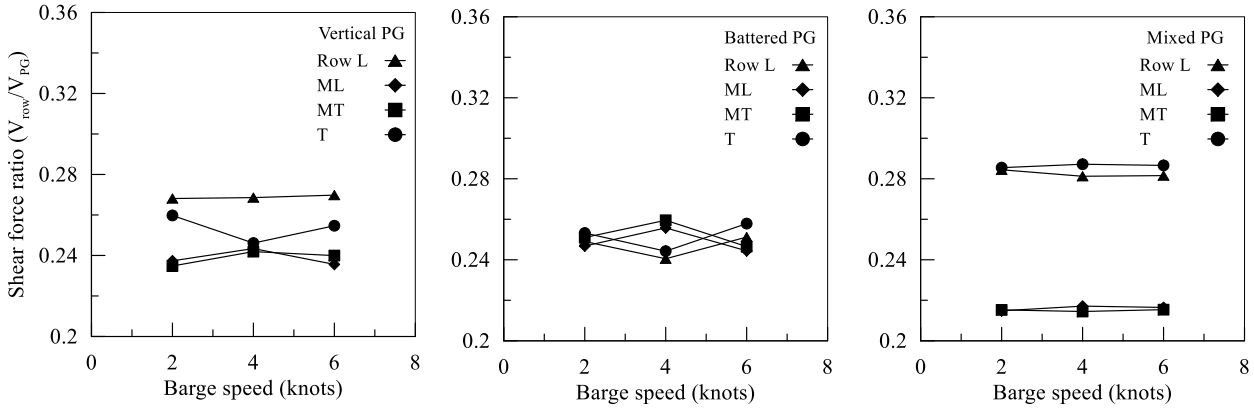

Figure 7.40. Distribution of shear force per row

7.4.3 Axial reaction

The results for the axial reaction developed in the piles is presented next (Figure 7.41). The axial reaction history generated in each pile is shown in Figure 7.42, Figure 7.43, and Figure 7.44. In the figures, a positive force indicates the force action is compressive in the piles, whereas negative means the force action is tensile.

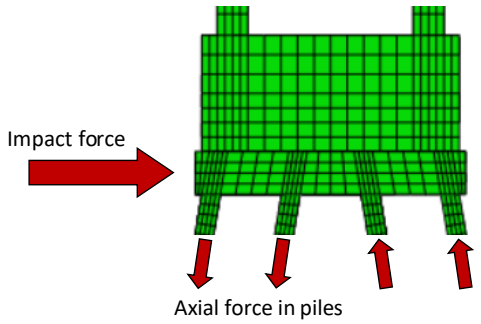

Figure 7.41. Free body diagram illustrating the axial reaction in the piles

The magnitude and direction of the axial reaction is affected by the PG type and row location. In the vertical, the axially active piles can be noticed from the difference in the force magnitude. The piles in rows L and T had a significant magnitude of axial reaction compared to rows ML and MT for the cases with barge speeds 2 and 4 knots. For the case with barge speed 6 knots, the large pile cap displacement and piles' damage influenced the PG behavior so that the piles in rows L and ML generated a greater compressive reaction. In the battered PG, all of the PG rows were axially active with notably higher

contribution from the middle rows (ML and MT). In the mixed PG, all rows were axially active with closely similar contribution from all rows.

The ratio of peak axial reaction per pile to the total shear in the piles is summarized in Figure 7.45. This figure shows the percentage of axial reaction generated in reference to the total shear in the PG. The force ratio in the rows L and T in the vertical PG were similar (3-5%) for the cases with barge speed 2 and 4 knots, while it was relatively small (>1%) in the trailing rows (MT, T). The force ratio in row L and ML showed a sharp increase in the case of barge speed 6 knots, which can be referred to the large pile cap displacement (9 inches) and piles' damage. The piles in the edge column (col. 1) had 2% higher force ratio compared to the interior columns. In the battered PG, the force ratio in the middle rows (ML, MT) was 6% higher than rows L and T, and the edge column piles had 2% higher ratio than the interior columns. In the mixed PG, the pile rows had closely similar force ratio at 15%.

The force ratio per row is presented in Figure 7.46, which is estimated by the sum of force ratio of all piles within the row. The vertical PG results show that rows L and T were the axially active rows at 23%, while the contribution was limited from the middle rows (ML, MT) at 3%. In the battered PG, all the rows were axially active with the middle rows (ML, MT) having the higher axial reaction at 50% compared to 12% in rows L and T. In the mixed PG, the rows had a closely similar force ratio at 33%.

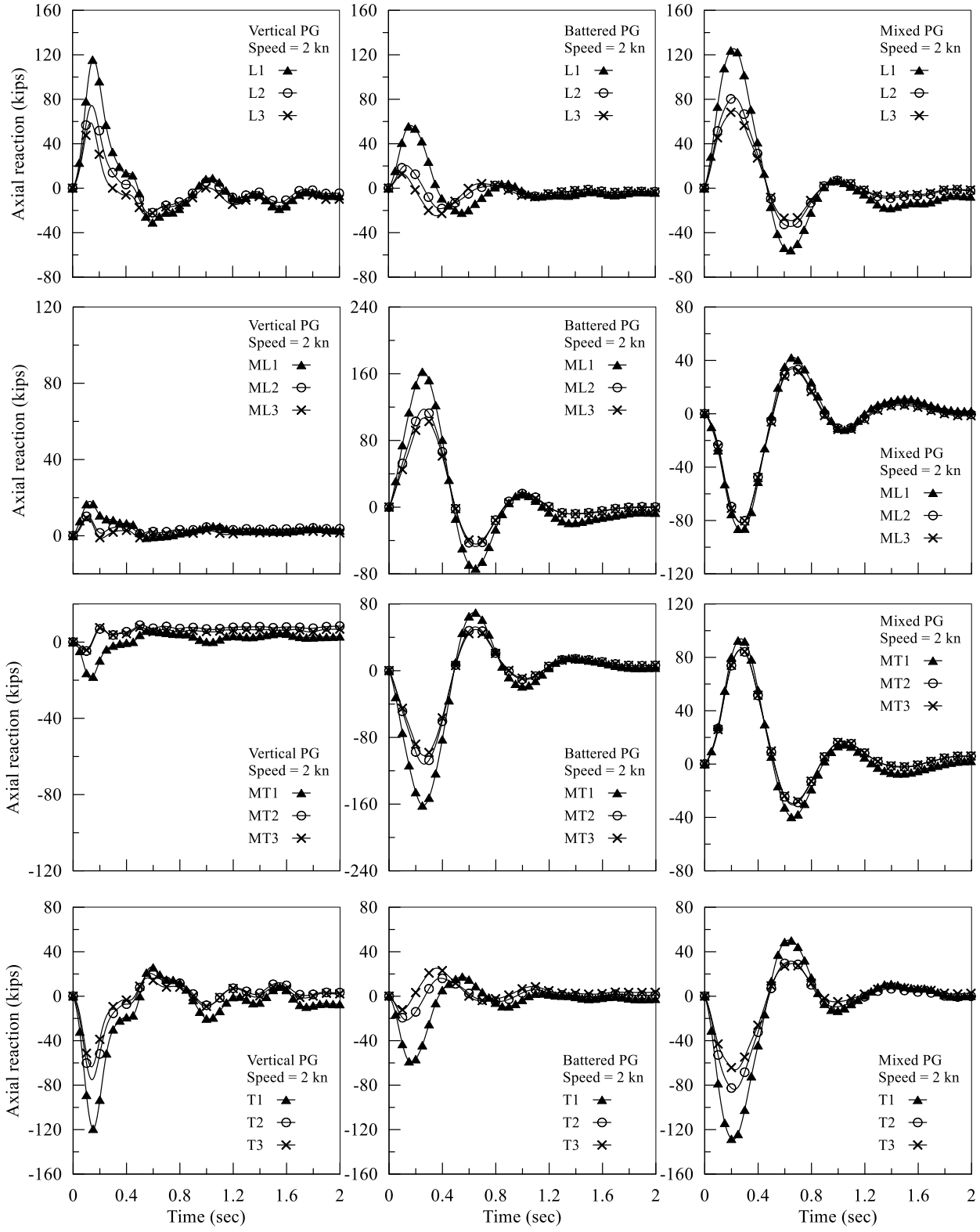

Figure 7.42. Axial force history results at barge speed = 2 knots

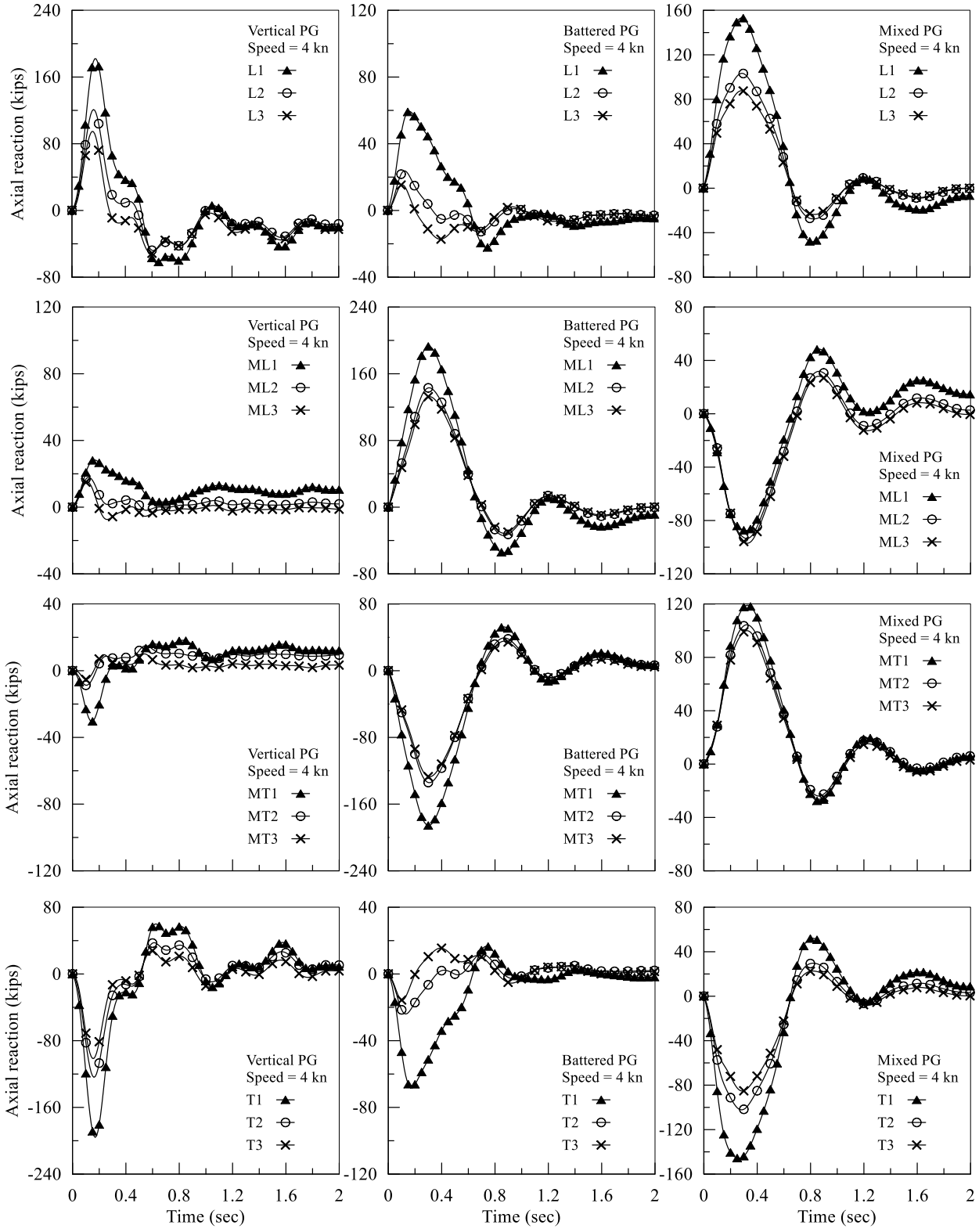

Figure 7.43. Axial force history results at barge speed = 4 knots

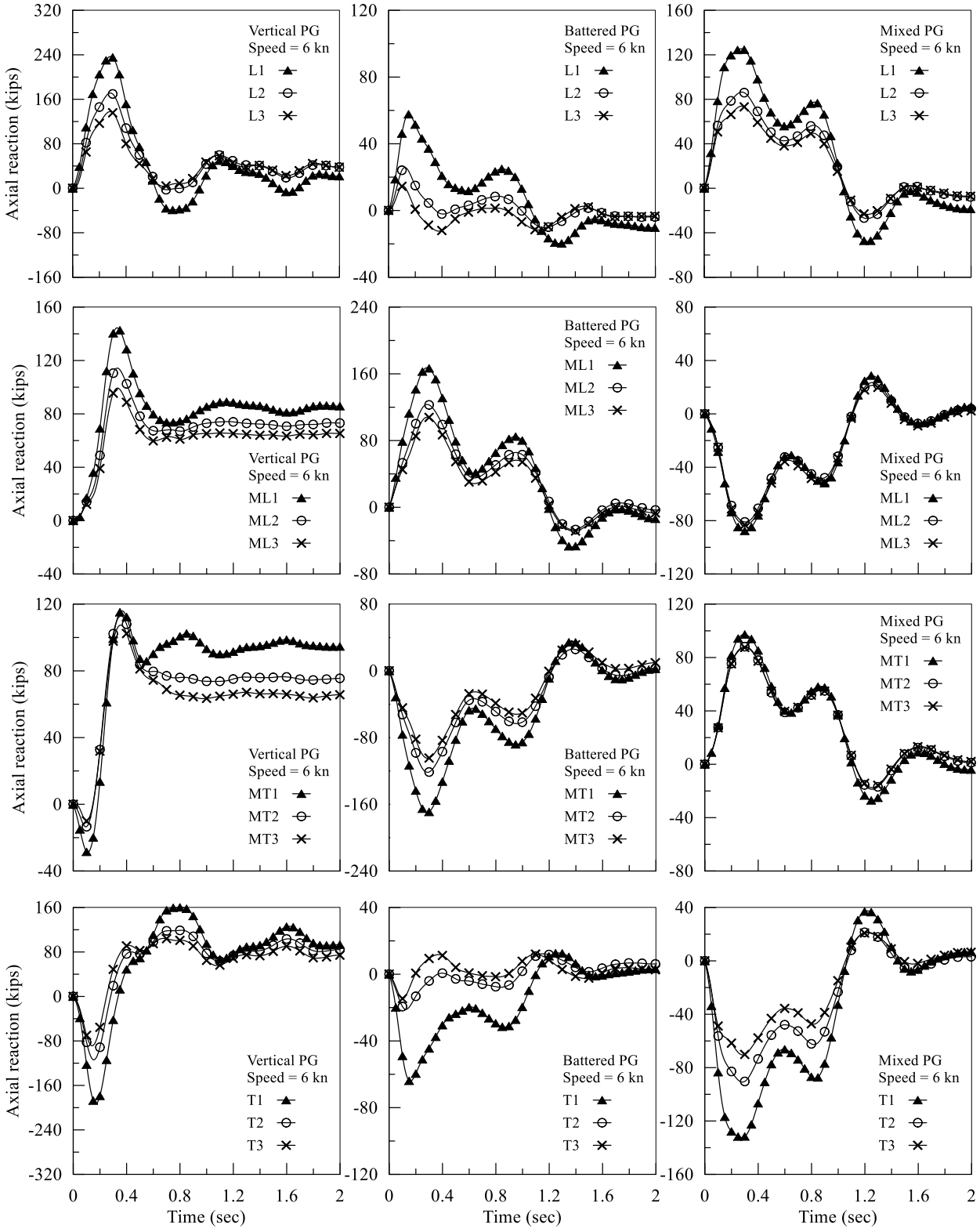

Figure 7.44. Axial force history results at barge speed = 6 knots

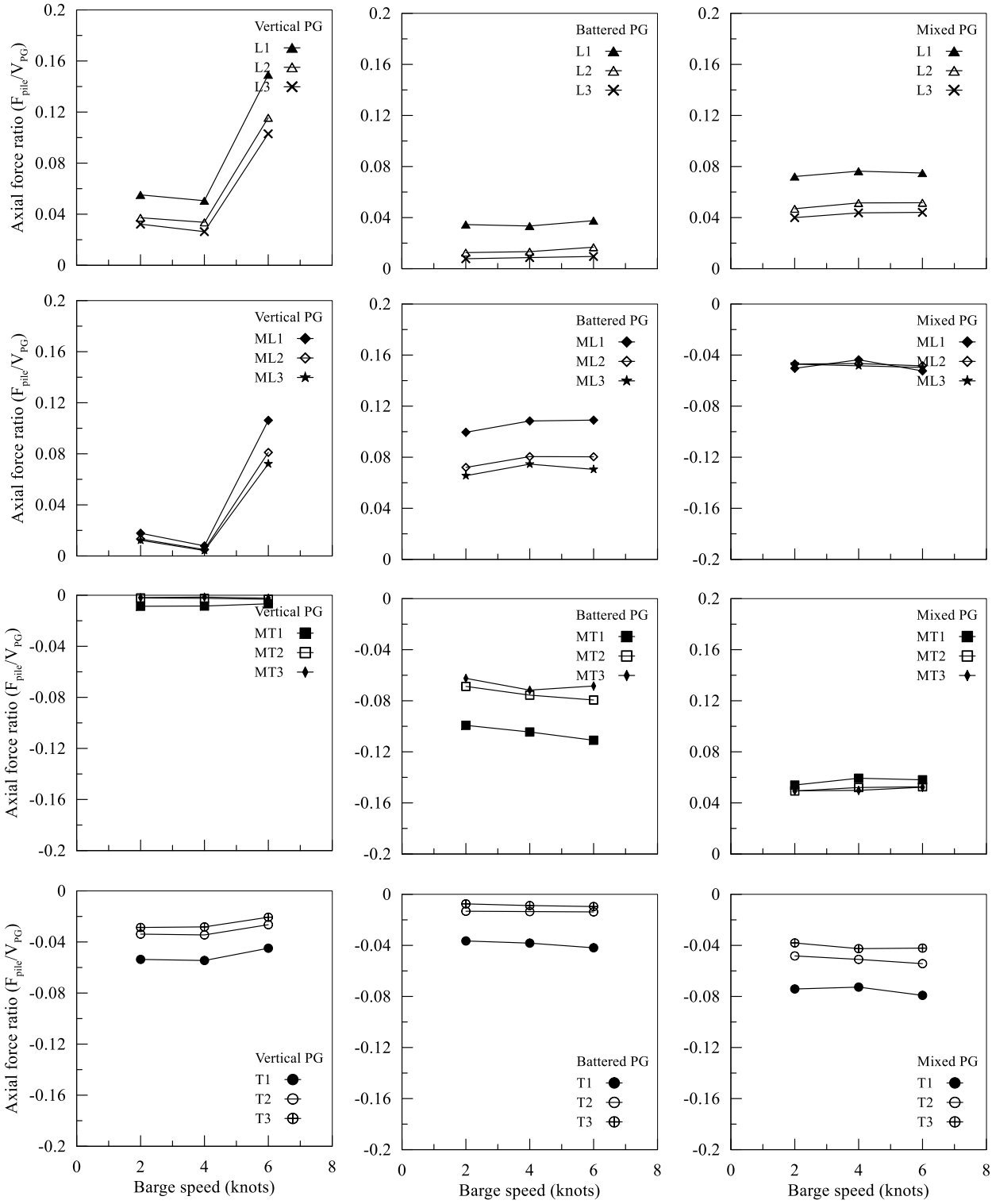

Figure 7.45. Summary of piles' peak axial force ratio

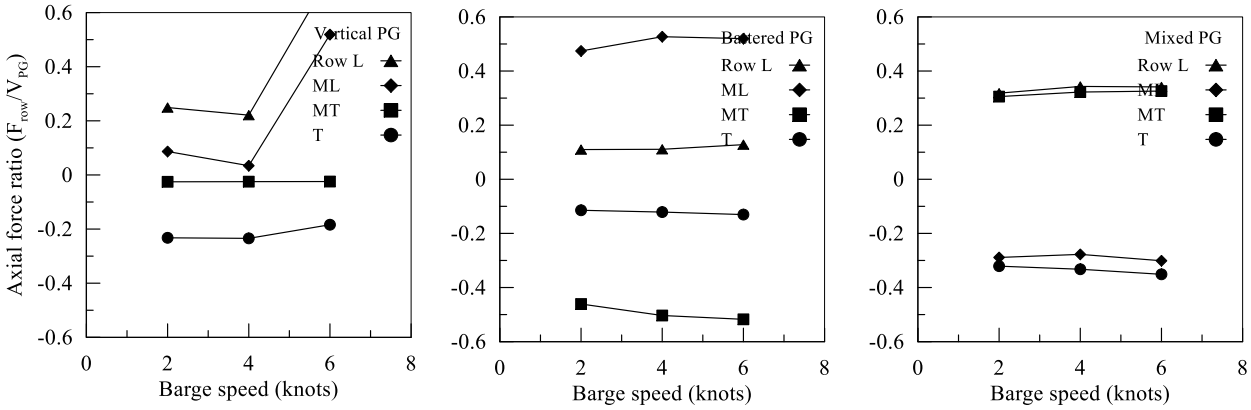

Figure 7.46. Summary of axial force ratio per row

7.4.4 Bending moment

The results for piles' bending moment (BM) at the pile cap elevation is shown in Figure 7.48, Figure 7.49, and Figure 7.50. A positive sign for the BM indicates the direction of action as illustrated in Figure 7.47.

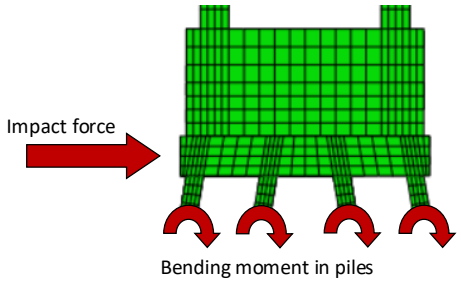

Figure 7.47. Free body diagram illustrating the bending moment in the piles

The BM history results show a closely similar response and contribution from all piles in the PGs. looking at the peak BM magnitude, the piles in the vertical PG had notably higher BM than the piles in the other PGs, which was due to the large pile cap displacement. A closer look at the contribution from each pile is studied with the aid of Figure 7.51. The BM ratio in the figure was obtained by normalizing the peak BM for the individual pile using the PG shear (V_{PG}), pile length (L=110 ft), and the number of piles in the PG (*n*=24). Similar to previously observed, the piles in the edge column (col. 1) had higher BM ratio in all PGs. The difference in BM between the edge column and the interior columns was 1.3% in the vertical PG, 2.3% in the battered PG, and 2.2% in the mixed PG.

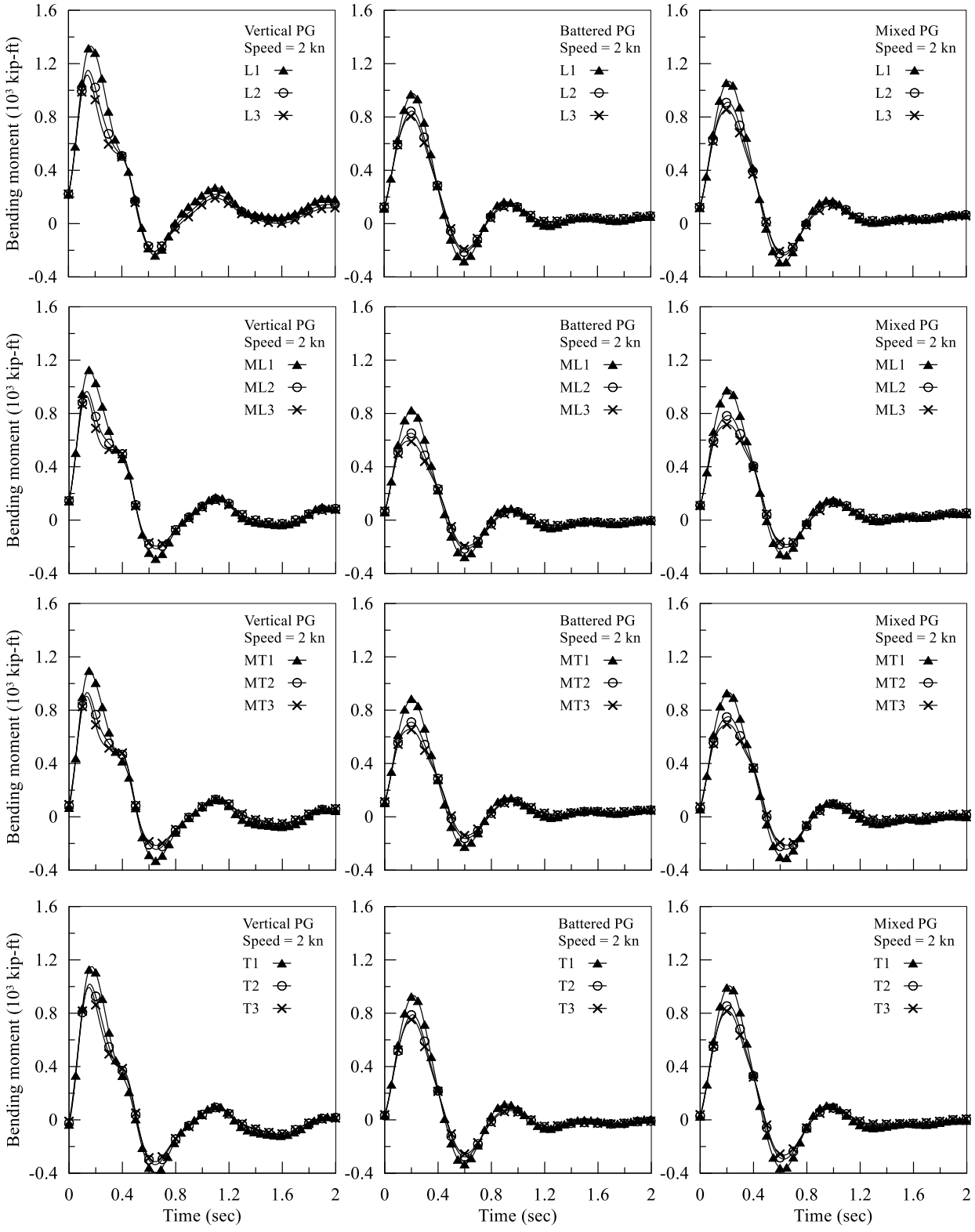

Figure 7.48. Bending moment history results at barge speed = 2 knots

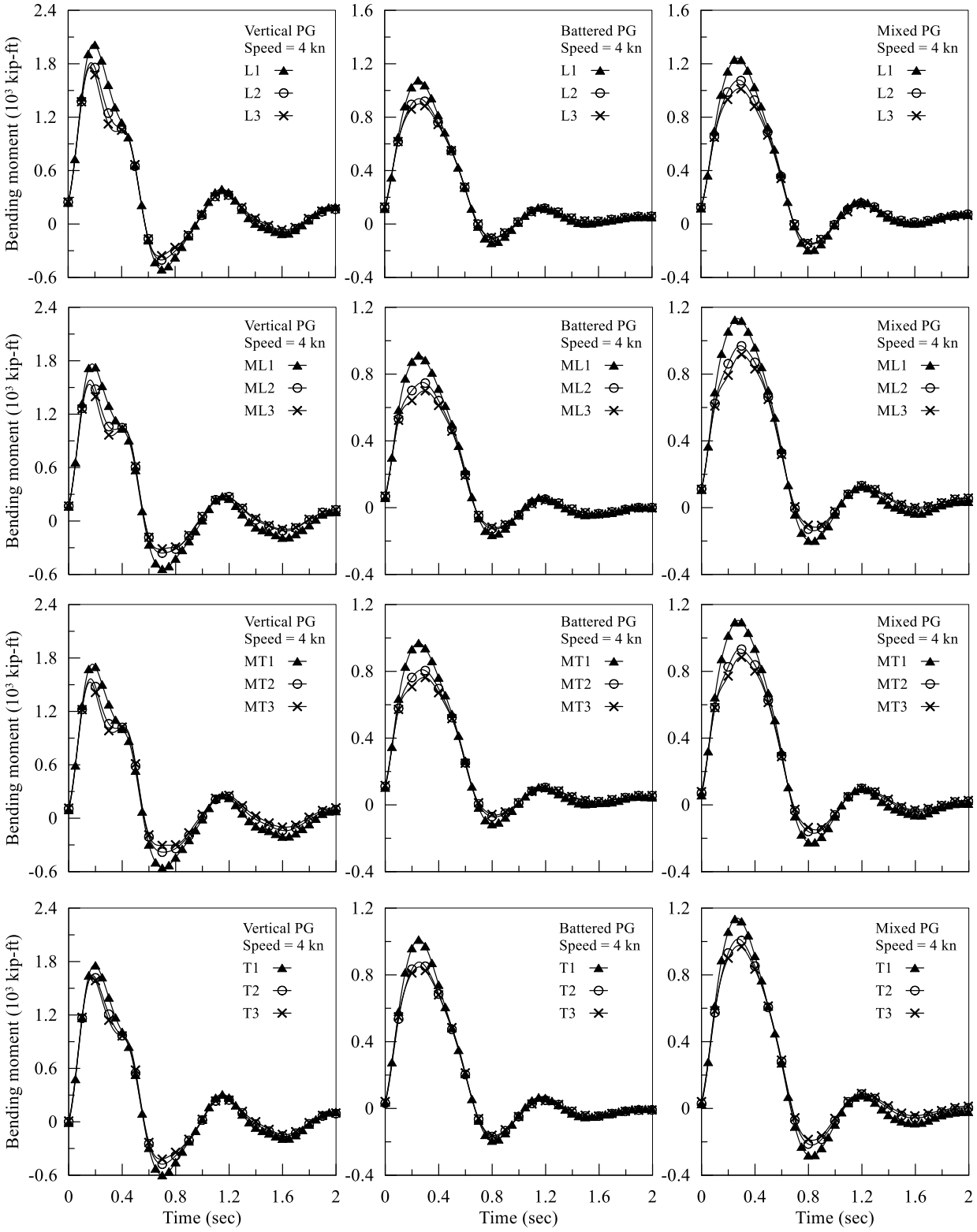

Figure 7.49. Bending moment history results at barge speed = 4 knots

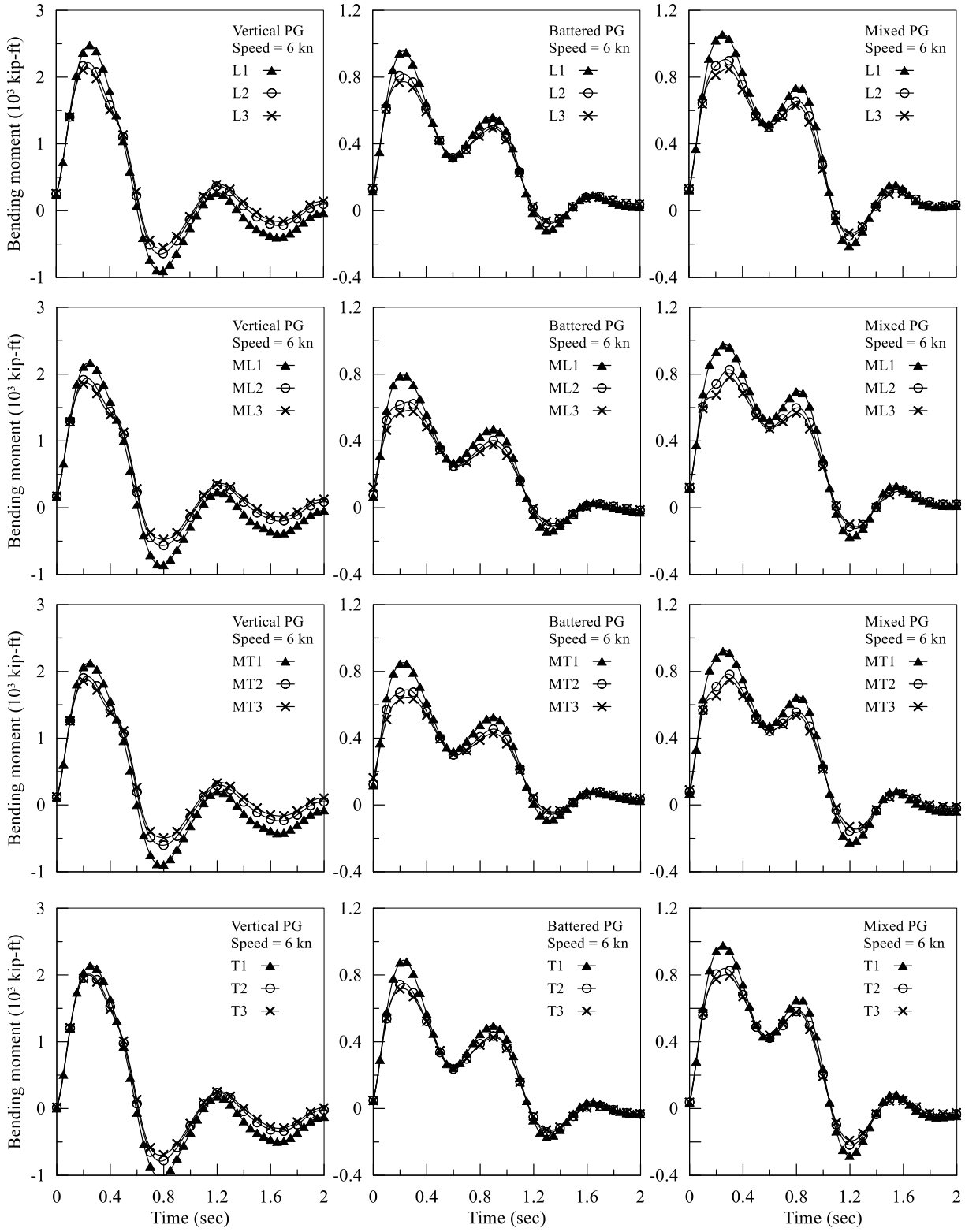

Figure 7.50. Bending moment history results at barge speed = 6 knots

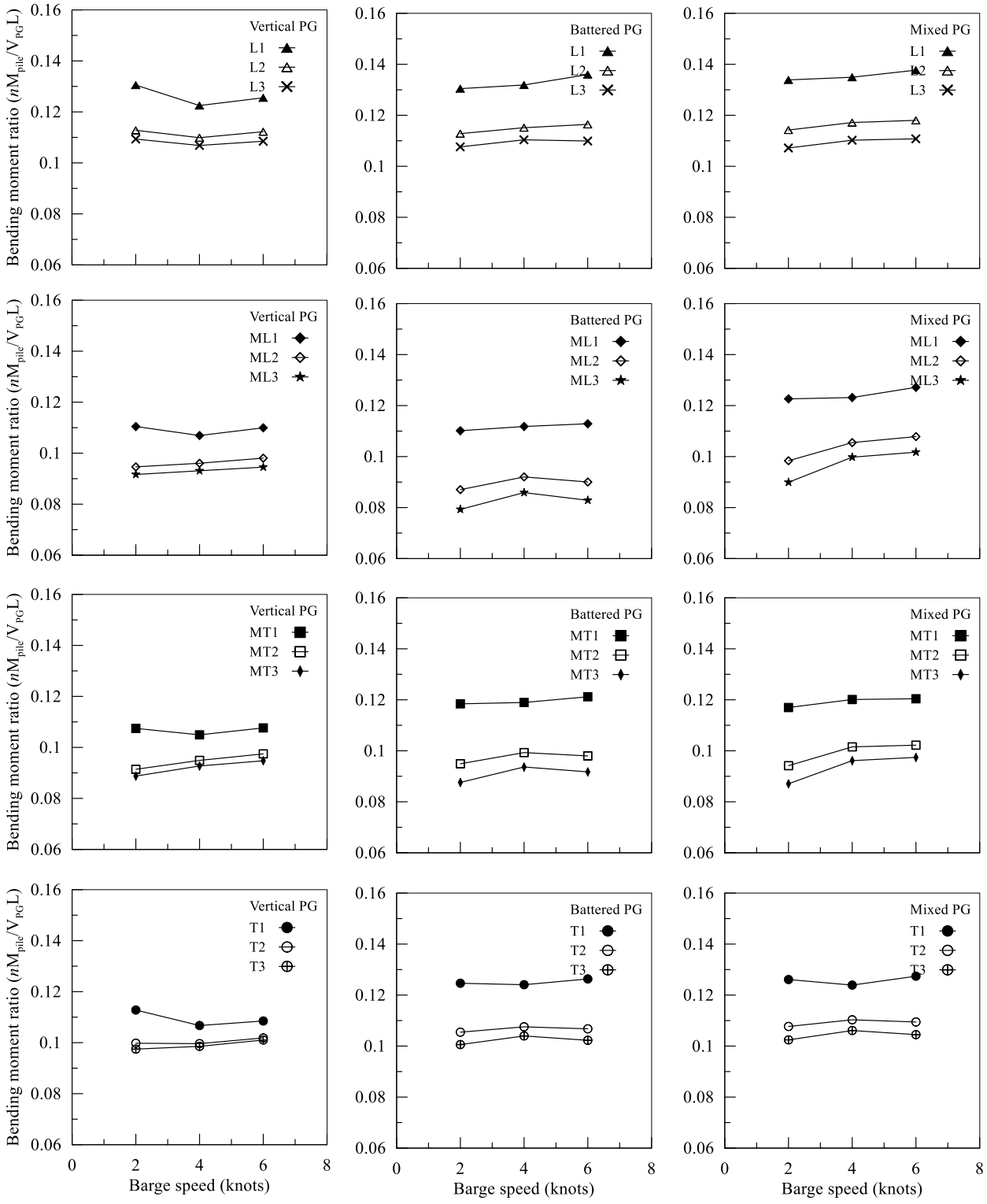

Figure 7.51. Summary of piles' peak bending moment ratio

The BM ratio per row in Figure 7.52 gives an idea about the BM distribution between the rows. The leading row (L) had the highest BM ratio (69-72%) in all PGs. In the vertical PG,

the BM ratio was closely similar in row ML, MT, and T 58-61%, respectively. In the battered, the BM ratios were 71, 57, 61, 67% in rows L, ML, MT, and T, respectively. In the mixed PG, the BM ratios were 72, 65, 62, 68% in rows L, ML, MT, and T, respectively.

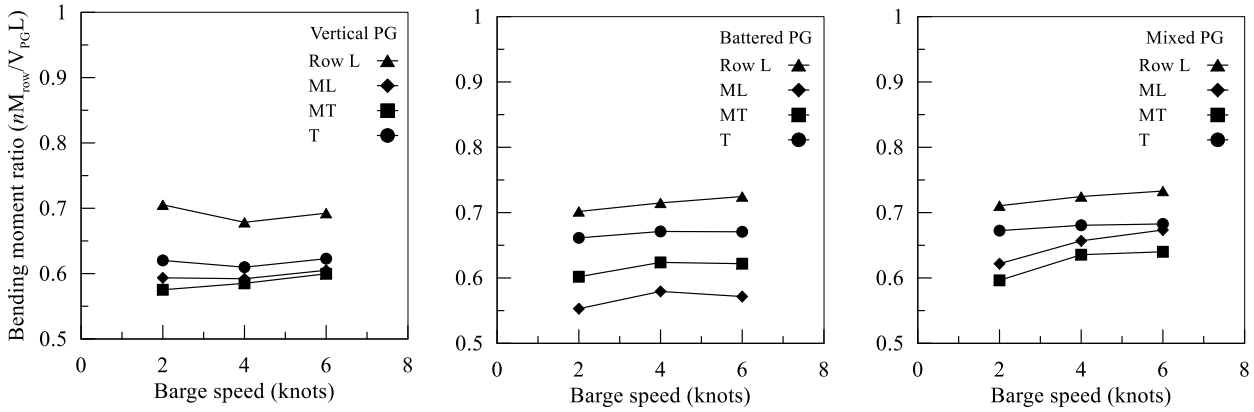

Figure 7.52. Summary of bending moment ratio per row

7.4.5 Results for non-centric impact

The case of a non-centric collision with the pile cap was investigated for the three pile groups. The barge's impact location was shifted so that the side of the barge aligns with the side of the pile cap (Figure 7.53). The non-centric impact simulations were conducted at barge speed of 4 knots only.

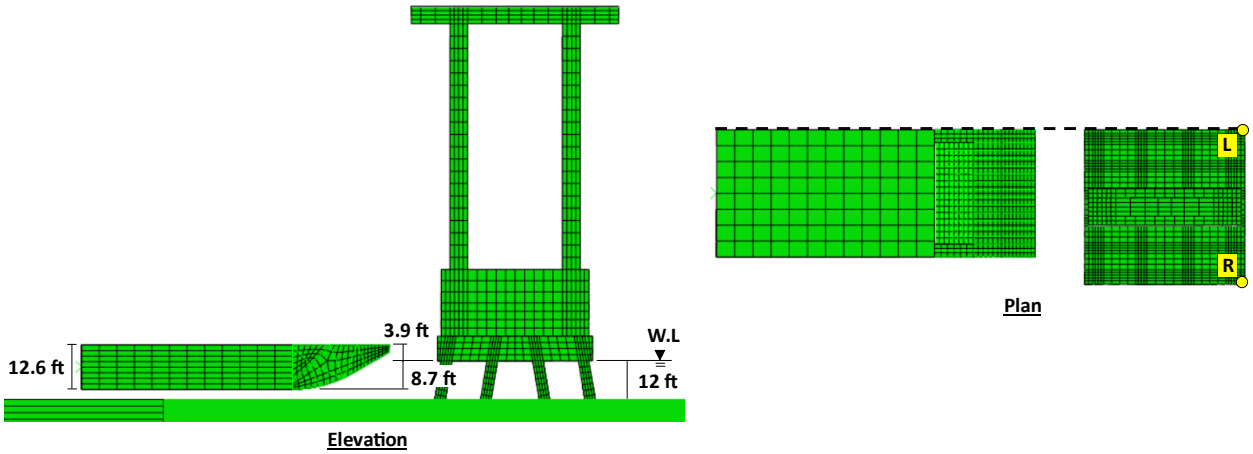

Figure 7.53. Barge alignment for non-centric impact

The displacement results for the three pile groups is shown in Figure 7.54. The figures include the cap displacement at the left (L) and right (R) corners, which shows a slightly higher displacement magnitude (0.2 inch) at the left corner. This small difference indicates that the cap rotation from the impact was minimal. For the peak displacement, the results from the non-centric impact were closely similar to the centric impacts results (Figure 7.55).

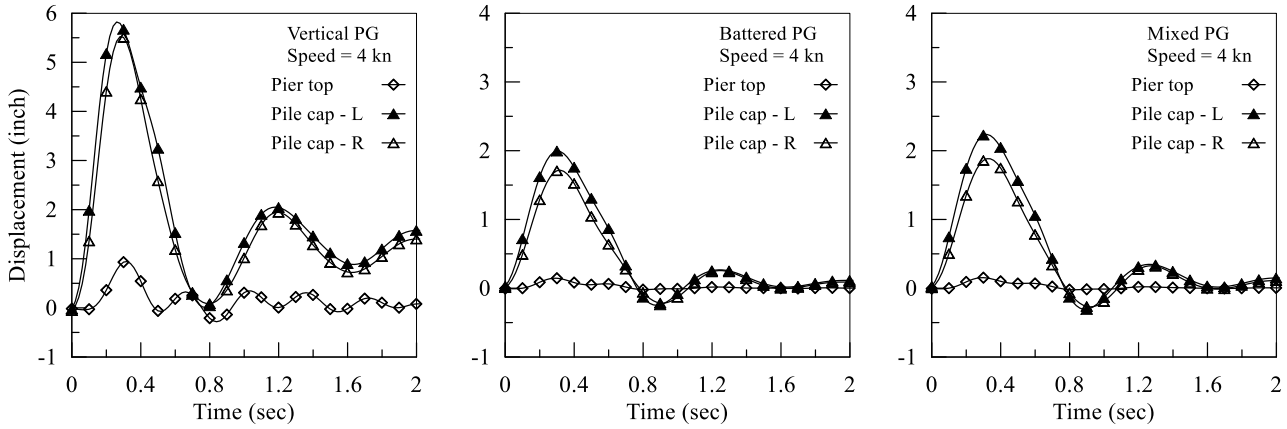

Figure 7.54. Displacement history for non-centric impact

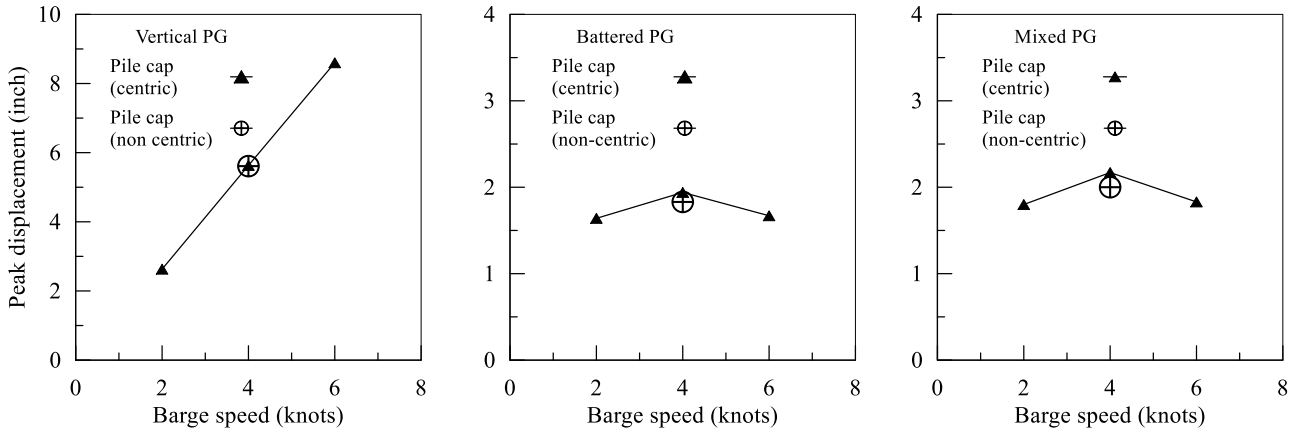

Figure 7.55. Comparison of peak displacement results for centric and non-centric impacts

The impact force results and force distribution in the piles and columns is shown in Figure 7.56 and Figure 7.57. The similarity in the impact force results between the centric and non-centric impact cases is clearly noticed.

The contribution of each pile in the total shear force is presented in Figure 7.58, Figure 7.59, and Figure 7.60 for the vertical, battered, and mixed PGs, respectively. The shear force was unevenly distributed in the piles, as expected, which is noticed in the slightly higher percentages in column 1 piles. However, the deviation in the force distribution was notably higher in the battered and mixed pile groups. The percentage difference between column 1 and column 6 piles was 0.2-0.3% in the vertical PG, while it was 1-1.2% in the battered and mixed PGs.

In summary, the influence of barge impact location (with fixed pier contact width) is considered minimal on the displacement response. The similarity in the force results for centric and non-centric impacts indicates that the impact location is not an influencing factor for the impact force magnitude.

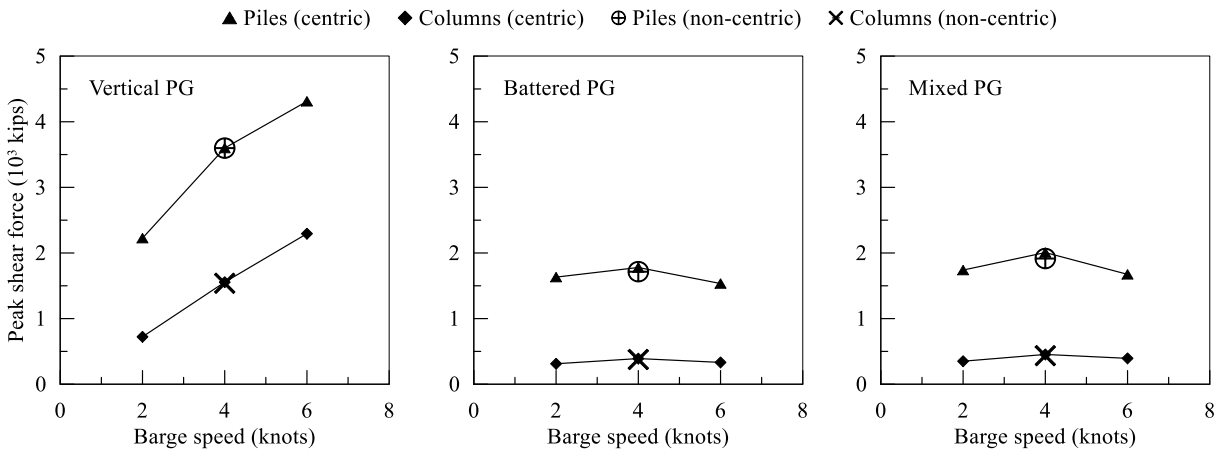

Figure 7.56. Comparison of peak shear force results for centric and non-centric impacts

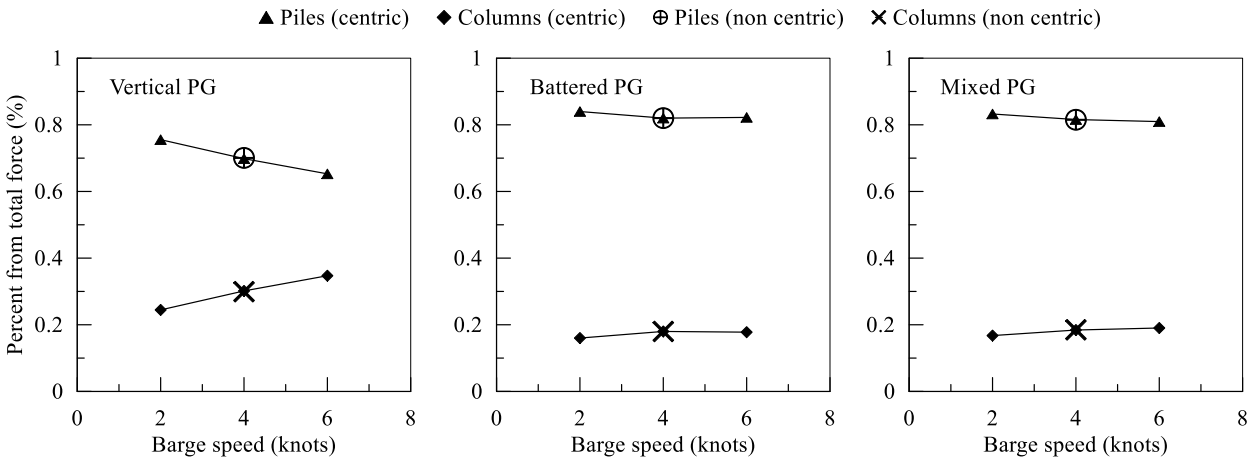

Figure 7.57. Contribution of piles and pier columns to the resisting force in centric and non-centric impacts

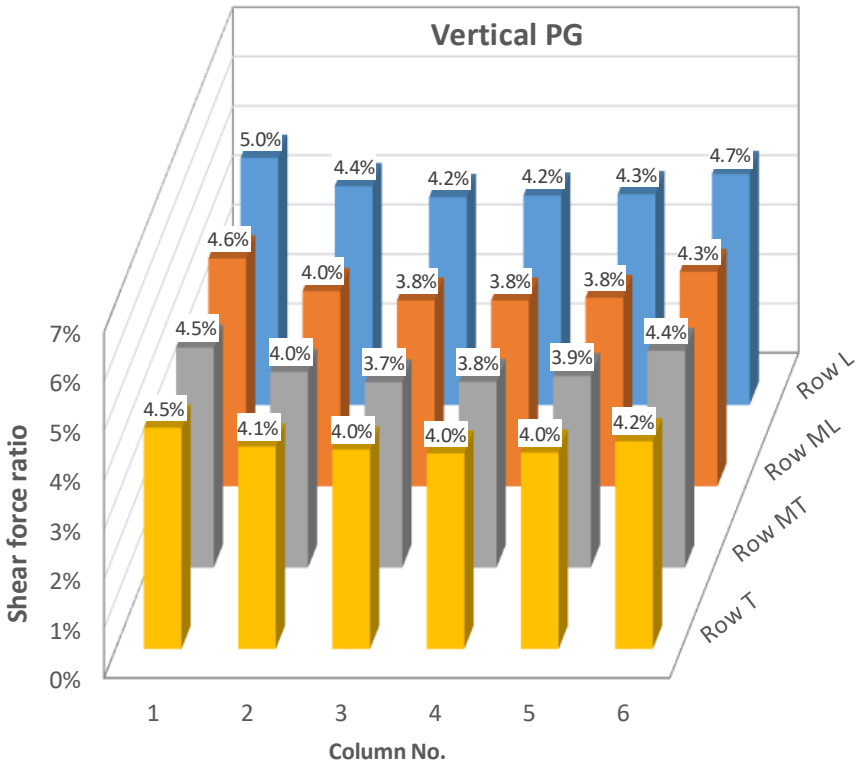

Figure 7.58. Summary of shear force ratio per pile for non-centric impact in vertical PG

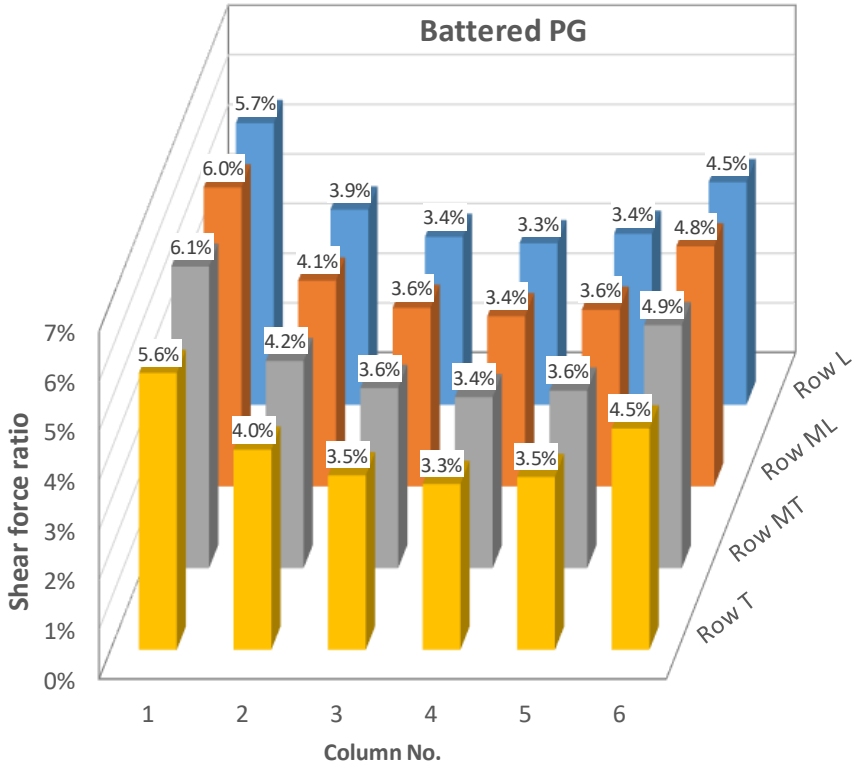

Figure 7.59. Summary of shear force ratio per pile for non-centric impact in battered PG

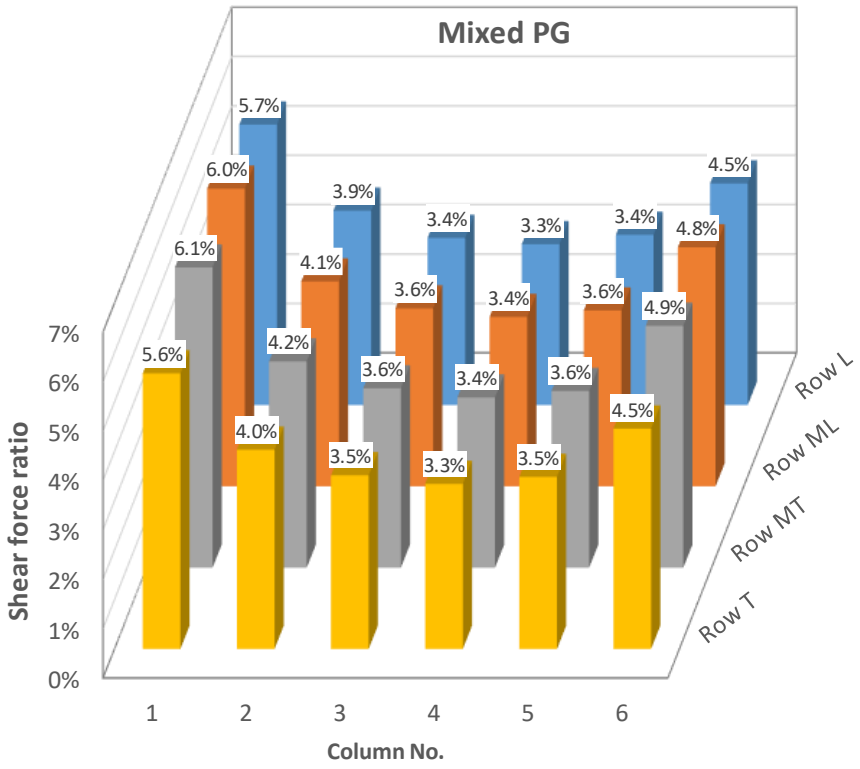

Figure 7.60. Summary of shear force ratio per pile for non-centric impact in mixed PG

Chapter 8. Summary, Conclusions, and Recommendations

8.1 Summary

In this study, the lateral behavior of pile groups is investigated using 3-D finite element (FE) modeling. Experimental investigations for pile groups are costly and demanding. Numerical modeling using the FE method is a feasible and economical alternative to study the problem. In practice, piles are installed vertically or battered (i.e. at an angle). There is extensive literature on the lateral behavior of single vertical piles and vertical pile groups, while it is limited for battered piles and battered pile groups. The lateral capacity of single piles can be predicted using the beam-springs model, in which the empirical *p-y* curves used for the spring reaction. For pile groups, multiple beam-springs models are used simultaneously and the group effect is accounted for using the *p*-multipliers. The *p*-multipliers are given as a function of pile spacing and their values are recommended after studies on only vertical pile groups, which may not be suitable for battered pile groups. In FE modeling, the nonlinear soil reaction is introduced using nonlinear constitutive models and pile-soil interface model. The differences in the influence of the group effect can be studied for the vertical and battered pile groups at various pile spacings. Furthermore, FE modeling allows studying the behavior of pile groups under dynamic loading such as in vessel collisions. Experimental investigations for vessel collisions on bridge piers exists in literature, however, their main focus was to propose models for the magnitude of the impact force. Using FE modeling, the interaction between the vessel and the bridge pier and influence of pile group type can be studied.

The lateral behavior of pile groups is a 3-D problem by nature and is affected by several nonlinearities such as the pile's concrete material behavior, the nonlinear soil reaction, pile-soil gap formation, and pile-soil-pile interaction or the group effect. In FE, the nonlinear material behavior can be accounted for using constitutive models. For pile's concrete material, the concrete damaged plasticity (CDP) model was used. The CDP model accounts for the distinct stress-strain response in concrete and applies stiffness reduction to compensate for the cracking in concrete. For clay soil, the Anisotropic Modified Camclay (AMCC) by Dafalias et al. (2006) was used. The AMCC model incorporates the elastoplastic behavior and the effect of soil anisotropy. For sandy soil, the Drucker-Prager model was used, which is well known for modeling the behavior of granular materials. The pile-soil interface was modeled using the contact approach, which allows soil gap formation and linear elastic-perfectly plastic sticking-sliding behavior. The group effect was accounted for by the interaction of the stress field around the piles and the strain compatibility in the soil elements.

The geometry of the pile groups was adopted from the design of the M19 pier foundation of the I-10 twin span bridge in Louisiana. In 2007, a static lateral load test was conducted on the M19 pier foundation, in which the eastbound and westbound piers was pulled

toward each other using high strength steel tendons and strand jacks. The M19 pier is supported by 24-battered pile group arranged in 4x6 configuration. An FE model for the M19 pile group foundation was developed in Abaqus FE package, and the results from the static load test were used to validate the FE model and material parameters. The FE model provided the capability to study the displacement, internal forces and bending moment, *p-y* curves and *p*-multipliers for each pile separately.

In the following part of the study, the verified FE model for the M19 battered pile group was modified by adjusting the pile's inclination to create FE models for two pile group configurations: vertical and mixed pile groups. The vertical pile group comprised of only vertical piles, whereas the mixed pile group comprised of two rows of battered piles and two rows of vertical piles. The FE models for the three models had similar material models, loads, boundary conditions, and interface model. The results for the three configurations were compared in terms of load-displacement response, axial reaction in the piles, lateral load distribution in the piles, soil resistance, *p-y* curves, and p-multipliers.

In the parametric study, the effect of pile spacing and clay soil type on the lateral behavior of pile groups was investigated, in which the vertical, battered, and mixed configurations considered. The pile's arrangement was chosen as 4x4 in all pile groups after the findings from the M19 case study and the pile groups comparison, which showed that the interior piles had closely similar behavior. Additionally, the effect of pile spacing was studied for small pile group comprised of 4 piles in a single row to study the effect of spacing in the two directions independently. The pile spacings considered in the study are 3D, 5D, and 7D (in reference to the pile width D), in which the spacing was taken equal in both directions. The effect of pile spacing was investigated using the properties of soft, medium, and stiff clay soil.

In the final part of the study, the lateral behavior of pile groups subjected to barge impact was investigated. The FE models for the vertical, battered, and mixed pile groups from the M19 case study were used with the addition of the pier’s superstructure components. The Jumbo Hopper barge design was used as basis for developing the barge FE model. The simulation was conducted using the explicit dynamic scheme with special considerations to the FE model boundaries and material damping behavior. The barge model was positioned to impact the pile group model at the pile cap at three different speeds, which represented low-medium barge navigation speeds.

8.2 Conclusions

The findings from this study are:

- The use of FE modeling is a viable alternative to experimental testing for studying the lateral behavior of pile groups comprehensively.

- The comparison between different pile group configurations showed that the battered pile group had the largest stiffness followed by the mixed and vertical pile groups, respectively. The lateral stiffness improvement relative to the vertical pile group was 120% for the battered pile group and 50% for the mixed pile group.

- The lateral load distribution in the pile group rows differed in each configuration. In the vertical pile group, the first (leading) row carried 30%, while it was 23.3% in each of the remaining rows. In the battered pile group, the percentage was equal in the first and fourth rows at 22%, while it was higher in the middle rows (second and third) at 28%. In the mixed pile group, the percentage was 36% in the first row at, 18% in the second and third rows, and 28% in the fourth row.

- The lateral load generated a significant axial reaction in the piles, in which the row percentage differed in each configuration. The mixed pile group generated the highest percentage of axial force followed by the battered and vertical pile groups respectively. In the vertical pile group, the average axial force ratio (relative to the lateral load) per pile was 8.5% in the first and fourth rows and 1.5% in the second and third rows. In the battered pile group, the axial force ratio was 2.5% in the first and fourth rows, whereas it was 12.5% in the second and third rows. in the mixed pile group, the first and fourth rows had axial force ratio of 9.6%, whereas the second and third rows had 5%. It was noticed that each row in the pile group coupled with its the mirror row so that the axial reaction magnitude was similar in the two rows but with opposite sign.

- The bending moment results showed that the vertical pile group generated higher bending moment at the bottom of pile cap compared to the battered and mixed pile groups under the same lateral load. In addition, the bending moment was increasing linearly with pile cap displacement in the vertical pile group. The mixed pile group had the second highest bending moment with linearly increasing trend. The battered pile group had the lowest bending moment values with fairly constant magnitude.

- Piles' damage contours gave an indication about the possible failure locations in the piles. In the vertical pile group, all piles exhibited mild-to-moderate degree of damage covering large regions at two locations; below and near the pile cap and at depth 16D below the mudline. In the battered pile group, the damage was severe in the third and fourth rows, which covered small regions near the pile cap and at depth 16D in the third row only. In the first and second rows, the damage was mild and covered small region near the pile cap. In the mixed pile group, the damage was mild in all piles near the pile cap and appeared at depth 16D in the second and fourth rows only.

- The soil resistance results showed that the shape of soil resistance profiles is closely similar for all piles in a pile group, but they differ between the pile group configurations.

- The *p*-multipliers results showed that the battered pile group had the highest *p*-multipliers followed by the mixed and vertical pile groups, respectively, which indicates a weaker influence from the group effect in the battered and mixed pile groups.
- The piles in the edge columns had a greater contribution (up to 2%) to the lateral resistance than the interior columns, which was consistently observed in the results of shear and axial forces, bending moment, and soil resistance. This translated in 0.2 raise in the *p*-multipliers for the edge columns over the interior columns.
- From the parametric study, increasing the pile spacing resulted in:
    - Decease in the axial reaction in the first and fourth rows only in all pile groups.
    - Negligible influence on the lateral load distribution between the piles.
    - Increase in the pile group efficiency in all pile groups. The largest increase in the group efficiency was observed in the vertical pile group (+38%).
    - Increase in *p*-multipliers in all piles in the pile groups, in which the p-multipliers increase 0.3-point when the spacing increased from 3D to 5D.
- The parametric study using single row/column pile groups showed that the pile row spacing had a greater influence on the *p*-multipliers than the column spacing. This was concluded after the vanishing of influence from pile column spacing at spacings greater than 5D.
- Studying the effect of clay soil type showed that the *p*-multipliers is higher in stiffer clays. In the vertical pile group, the *p*-multipliers increased 0.1-point when the clay soil type was changed from soft to medium and medium to stiff at pile spacings 3D and 5D. In the battered and mixed pile groups, a similar increase was noticed at pile spacing 3D only. Changing the clay soil at pile spacing 7D had no influence on the *p*-multipliers in all pile groups.
- The study of the pile group subjected to barge impact showed that the vertical pile group had the lowest lateral stiffness, while the battered and mixed pile groups had closely similar stiffness.
- The flexibility of the vertical pile group facilitated the increase in peak impact force magnitude when the barge speed increased.
- The battered and mixed pile groups large stiffness forced the barge bow to deform significantly so that the peak impact force magnitude remained fairly constant for all barge speeds.

- The shear force results showed that the foundation contributed up to 82% of the total lateral force. In the vertical pile group, the force distribution was 76-65% in the foundation and 24-35% in the pier columns. In the battered and mixed pile groups, the force distribution was 82% in the foundation and 18% in the pier columns.
- The lateral force distribution results showed that in the vertical pile group that the first row had slightly higher percentage (28%) compared to other rows, which had closely similar percentage (24-26%). In the battered pile group, the load percentage was evenly distributed between the rows at 25%. A large contrast in the percentage was observed in the mixed pile group. The first and fourth rows had 28% each, while the second and third rows had 22% each.
- The axial reaction results showed that only the first and fourth rows were axially active in the vertical pile group with axial force ratio of 23%. In the battered pile group, all rows were axially active with the second and third rows having 38% higher axial force ratio than the first and fourth rows. In the mixed pile group, all rows had similar axial reaction ratio at 33%.

8.3 Recommendations for future work

Some areas that are worth further investigation in the lateral behavior of pile groups are:

- The effect of the batter angle on the lateral resistance of the battered and mixed pile groups.
- The effect on pile installation (i.e. driving) on the lateral resistance of pile groups.
- The effect of pile installation sequence on the lateral resistance of pile groups.
- Incorporate the effect of foundation type (vertical, battered, mixed) on the impact force from the barge collision.
- The effect of pier height on the barge impact force.

References

Abaqus. (2011). *Abaqus Documentation*. Dassault Systèmes, Providence, RI.

Abu-Farsakh, M., Rosti, F., and Souri, A. (2015). “Evaluating pile installation and subsequent thixotropic and consolidation effects on setup by numerical simulation for full-scale pile load tests.” *Canadian Geotechnical Journal*, 52(11), 1734–1746.

Abu-Farsakh, M., Yoon, S., Ha, D., Marr, W., Zhang, Z., and Yu, X. (2011a). “Development of a substructure instrumentation system at the new I-10 twin span bridge and its use to investigate the lateral behavior of batter piles.” *Geotechnical Testing Journal*, 34(4), 332–343.

Abu-Farsakh, M., Yu, X., Pathak, B., Alshibli, K., and Zhang, Z. (2011b). “Field testing and analyses of a batter pile group foundation under lateral loading.” *Transportation Research Record: Journal of the Transportation Research Board*, 2212, 42–55.

Argyris, J., Faust, G., Szimmat, J., Warnke, E., and Willam, K. (1974). “Special issue: papers presented at the conference recent developments in the finite element analysis of prestressed concrete reactor vessels.” *Nuclear Engineering and Design*, 28(1), 42–75.

Ashour, M., and Ardalan, H. (2011). “Employment of the p-multiplier in pile-group analysis.” *Journal of Bridge Engineering*, 16(5), 612–623.

Ashour, M., and Norris, G. (2000). “Modeling lateral soil-pile response based on soil-pile interaction.” *Journal of Geotechnical and Geoenvironmental Engineering*, 126(5), 420–428.

Ashour, M., Norris, G., and Pilling, P. (1998). “Lateral loading of a pile in layered soil using the strain wedge model.” *Journal of geotechnical and geoenvironmental engineering*, 124(4), 303–315.

Ashour, M., Pilling, P., and Norris, G. (2004). “Lateral behavior of pile groups in layered soils.” *Journal of Geotechnical and Geoenvironmental Engineering*, 130(6), 580–592.

ASTM. (2012). *A416/A416M-12a. Specification for steel strand, uncoated seven-wire for prestressed concrete*. ASTM International.

Basu, D., Salgado, R., and Prezzi, M. (2009). “A continuum-based model for analysis of laterally loaded piles in layered soils.” *Géotechnique*, 59(2), 127–140.

Brown, D., Reese, L., and O’Neill, M. (1987). “Cyclic lateral loading of a large-scale pile group.” *Journal of Geotechnical Engineering*, 113(11), 1326–1343.

Brown, D., Reese, L., and O’Neill, M. (1988). “Lateral load behavior of pile group in sand.” *Journal of Geotechnical Engineering*, 114(11), 1261–1276.

Brown, D., and Shie, C. (1990). “Three dimensional finite element model of laterally loaded piles.” *Computers and Geotechnics*, 10(1), 59–79.

Chandrasekaran, S., Boominathan, A., and Dodagoudar, G. (2009). “Group interaction effects on laterally loaded piles in clay.” *Journal of geotechnical and geoenvironmental engineering*, 136(4), 573–582.

Chen, W., and Han, D. (2007). *Plasticity for Structural Engineers*. J. Ross Publishing.

Chow, Y. K. (1987). “Three-dimensional analysis of pile groups.” *Journal of Geotechnical Engineering*, 113(6), 637–651.

Chu, L., and Zhang, L. (2011). “Centrifuge modeling of ship impact loads on bridge pile foundations.” *Journal of Geotechnical and Geoenvironmental Engineering*, 137(4), 405–420.

Cicekli, U., Voyiadjis, G., and Abu Al-Rub, R. (2007). “A plasticity and anisotropic damage model for plain concrete.” *International Journal of Plasticity*, In honor of Professor Dusan Krajcinovic, 23(10–11), 1874–1900.

Comodromos, E. M., and Pitilakis, K. D. (2005). “Response evaluation for horizontally loaded fixed-head pile groups using 3-D non-linear analysis.” *International Journal for Numerical and Analytical Methods in Geomechanics*, 29(6), 597–625.

Consolazio, G., Davidson, M., and Cowan, D. (2009). “Barge Bow Force-Deformation Relationships for Barge-Bridge Collision Analysis.” *Transportation Research Record: Journal of the Transportation Research Board*, 2131, 3–14.

Consolazio, G. R., Cook, R. A., McVay, M. C., Cowan, D., Biggs, A., and Bui, L. (2006). *Barge Impact Testing of the St. George Island Causeway Bridge, Phase III: Physical Testing and Data Interpretation*. University of Florida, Gainesville, 2008, 240.

Consolazio, G. R., and Cowan, D. R. (2003). “Nonlinear analysis of barge crush behavior and its relationship to impact resistant bridge design.” *Computers & Structures*, K.J Bathe 60th Anniversary Issue, 81(8–11), 547–557.

Consolazio, G. R., McVay, M. C., Cowan, D. R., Davidson, M. T., and Getter, D. J. (2008). *Development of Improved Bridge Design Provisions for Barge Impact Loading*. University of Florida, Gainesville, 2008, 256.

Dafalias, Y. (1986). “An anisotropic critical state soil plasticity model.” *Mechanics Research Communications*, 13(6), 341–347.

Dafalias, Y., Manzari, M., and Papadimitriou, A. (2006). “SANICLAY: simple anisotropic clay plasticity model.” *International Journal for Numerical and Analytical Methods in Geomechanics*, 30(12), 1231–1257.

Das, B. M. (2011). *Geotechnical engineering handbook*. J. Ross Pub., Ft. Lauderdale, FL.

Day, R. W. (2012). *Geotechnical engineer’s portable handbook*. McGraw-Hill Professional, New York.

Diehl, T., Carroll, D., and Nagaraj, B. (1999). “Using Digital Signal Processing (DSP) to Significantly Improve the Interpretation of Abaqus/Explicit Results.” *Proceedings of ABAQUS Users’ Conference*, Chester, UK, 1–21.

Dobry, R., and Gazetas, G. (1988). “Simple method for dynamic stiffness and damping of floating pile groups.” *Geotechnique*, 38(4), 557–574.

El Naggar, M., and Bentley, K. (2000). “Dynamic analysis for laterally loaded piles and dynamic p-y curves.” *Canadian Geotechnical Journal*, 37(6), 1166–1183.

El Naggar, M., and Novak, M. (1996). “Nonlinear analysis for dynamic lateral pile response.” *Soil Dynamics and Earthquake Engineering*, 15(4), 233–244.

Elias, M. (2008). “Numerical simulation of pile installation and setup.” Ph.D dissertation, The University of Wisconsin, Milwaukee, Wisc.

Gazetas, G., and Dobry, R. (1984). “Horizontal response of piles in layered soils.” *Journal of Geotechnical Engineering*, 110(1), 20–40.

Gazetas, G., Fan, K., Kaynia, A., and Kausel, E. (1991). “Dynamic interaction factors for floating pile groups.” *Journal of Geotechnical Engineering*, 117(10), 1531–1548.

Getter, D. J., Davidson, M. T., Consolazio, G. R., and Patev, R. C. (2015). “Determination of hurricane-induced barge impact loads on floodwalls using dynamic finite element analysis.” *Engineering Structures*, 104, 95–106.

Gill, H., and Demars, K. (1970). *Displacement of laterally loaded structures in nonlinearly responsive soil*. Technical report, Naval Civil Engineering Lab, Port Hueneme, California.

Guo, W., and Lee, F. (2001). “Load transfer approach for laterally loaded piles.” *International Journal for Numerical and Analytical Methods in Geomechanics*, 25(11), 1101–1129.

Gupta, A., and Maestrini, S. (1990). “Tension-stiffness model for reinforced concrete bars.” *Journal of Structural Engineering*, 116(3), 769–790.

Hardin, B., and Drnevich, V. (1972). “Shear modulus and damping in soils: design equations and curves.” *Journal of the Soil Mechanics and Foundations Division*, 98(SM7), 667–692.

Hashash, Y., and Park, D. (2002). “Viscous damping formulation and high frequency motion propagation in non-linear site response analysis.” *Soil Dynamics and Earthquake Engineering*, 22(7), 611–624.

Hetényi, M. (1946). *Beams on elastic foundation: theory with applications in the fields of civil and mechanical engineering*. University of Michigan Press.

Huang, A.-B., Hsueh, C.-K., O’Neill, M. W., Chern, S., and Chen, C. (2001). “Effects of Construction on Laterally Loaded Pile Groups.” *Journal of Geotechnical and Geoenvironmental Engineering*, 127(5), 385–397.

Hussien, M. N., Tobita, T., Iai, S., and Rollins, K. M. (2012). “Vertical loads effect on the lateral pile group resistance in sand.” *Geomechanics and Geoengineering*, 7(4), 263–282.

Ilyas, T., Leung, C., Chow, Y., and Budi, S. (2004). “Centrifuge model study of laterally loaded pile groups in clay.” *Journal of Geotechnical and Geoenvironmental Engineering*, 130(3), 274–283.

Isenhower, W. M., Vasquez, L. G., and Wang, S.-T. (2014). “Analysis of Settlement-Induced Bending Moments in Battered Piles.” *From Soil Behavior Fundamentals to Innovations in Geotechnical Engineering*, American Society of Civil Engineers, San Antonio, TX, 497–511.

Jackson, K. M. (1979). “Fitting of Mathematical Functions to Biomechanical Data.” *IEEE Transactions on Biomedical Engineering*, BME-26(2), 122–124.

Jankowiak, T., and Lodygowski, T. (2005). “Identification of parameters of concrete damage plasticity constitutive model.” *Foundations of civil and environmental engineering*, 6(1), 53–69.

Kantrales, G. C., Consolazio, G. R., Wagner, D., and Fallaha, S. (2016). “Experimental and analytical study of high-level barge deformation for barge–bridge collision design.” *Journal of Bridge Engineering*, 21(2).

Kaynia, A., and Kausel, E. (1991). “Dynamics of piles and pile groups in layered soil media.” *Soil Dynamics and Earthquake Engineering*, 10(8), 386–401.

Larsen, O. D. (1993). *Ship collision with bridges: the interaction between vessel traffic and bridge structures*. International Association for Bridge and Structural Engineering, Zürich, Switzerland.

Lee, J., and Fenves, G. (1998). “Plastic-damage model for cyclic loading of concrete structures.” *Journal of Engineering Mechanics*, 124(8), 892–900.

Leung, C., and Chow, Y. (1987). “Response of pile groups subjected to lateral loads.” *International journal for numerical and analytical methods in geomechanics*, 11(3), 307–314.

Ling, H., Yue, D., Kaliakin, V., and Themelis, N. (2002). “Anisotropic elastoplastic bounding surface model for cohesive soils.” *Journal of Engineering Mechanics*, 128(7), 748–758.

Liu, M., and Gorman, D. G. (1995). “Formulation of Rayleigh damping and its extensions.” *Computers & Structures*, 57(2), 277–285.

Lubliner, J., Oliver, J., Oller, S., and Oñate, E. (1989). “A plastic-damage model for concrete.” *International Journal of Solids and Structures*, 25(3), 299–326.

Makris, N., and Gazetas, G. (1992). “Dynamic pile-soil-pile interaction. part ii: lateral and seismic response.” *Earthquake Engineering & Structural Dynamics*, 21(2), 145–162.

Mander, J., Priestley, M., and Park, R. (1988). “Theoretical stress-strain model for confined concrete.” *Journal of Structural Engineering*, 114(8), 1804–1826.

Matlock, H. (1970). “Correlation for design of laterally loaded piles in soft clay.” Offshore Technology Conference, Houston, TX.

Matlock, H., and Reese, L. (1960). “Generalized solutions for laterally loaded piles.” *Journal of the Soil Mechanics and Foundations Division*, 86(5), 63–94.

Matlock, H., and Ripperger, E. (1956). “Procedures and instumentation for tests on a laterally-loaded pile.” *Eighth Texas Conference on Soil Mechanics and Foundation Engineering*, Austin, TX.

McClelland, B., and Focht, J. (1956). “Soil modulus for laterally loaded piles.” *Journal of the Soil Mechanics and Foundations Division*, 82(4), 1–22.

McVay, M., Casper, R., and Shang, T. (1995). “Lateral response of three-row groups in loose to dense sands at 3D and 5D pile spacing.” *Journal of Geotechnical Engineering*, 121(5), 436–441.

McVay, M., Shang, T., and Casper, R. (1996). “Centrifuge testing of fixed-head laterally loaded battered and plumb pile groups in sand.” *Geotechnical Testing Journal*, 19(1), 41–50.

McVay, M., Zhang, L., Molnit, T., and Lai, P. (1998). “Centrifuge testing of large laterally loaded pile groups in sands.” *Journal of Geotechnical and Geoenvironmental Engineering*, 124(10), 1016–1026.

Meyerhof, G., and Yalcin, A. (1993). “Behaviour of flexible batter piles under inclined loads in layered soil.” *Canadian Geotechnical Journal*, 30(2), 247–256.

Mostafa, Y., and El Naggar, M. (2002). “Dynamic analysis of laterally loaded pile groups in sand and clay.” *Canadian Geotechnical Journal*, 39(6), 1358–1383.

Mroueh, H., and Shahrour, I. (2009). “Numerical analysis of the response of battered piles to inclined pullout loads.” *International Journal for Numerical and Analytical Methods in Geomechanics*, 33(10), 1277–1288.

Muqtadir, A., and Desai, C. (1986). “Three-dimensional analysis of a pile-group foundation.” *International Journal for Numerical and Analytical Methods in Geomechanics*, 10(1), 41–58.

Murthy, V. (1964). “Behavior of batter piles subjected to lateral loads.” Ph.D dissertation, Indian Institute of Technology, Kharagpur, India.

Mylonakis, G., and Gazetas, G. (1999). “Lateral vibration and internal forces of grouped piles in layered soil.” *Journal of Geotechnical and Geoenvironmental Engineering*, 125(1), 16–25.

Nip, D., and Ng, C. (2005). “Back-analysis of laterally loaded bored piles.” *Proceedings of the Institution of Civil Engineers - Geotechnical engineering*, 158(2), 63–73.

Nogami, T., and Konagai, K. (1988). “Time domain flexural response of dynamically loaded single piles.” *Journal of Engineering Mechanics*, 114(9), 1512–1525.

Nogami, T., and Novak, M. (1977). “Resistance of soil to a horizontally vibrating pile.” *Earthquake Engineering & Structural Dynamics*, 5(3), 249–261.

Nogami, T., Otani, J., Konagai, K., and Chen, H. (1992). “Nonlinear soil-pile interaction model for dynamic lateral motion.” *Journal of Geotechnical Engineering*, 118(1), 89–106.

Norris, G. (1986). “Theoretically based BEF laterally loaded pile analysis.” *3rd International Conference on Numerical Methods in Offshore Piling*, TECHNIP Ed., Paris, 361–386.

Novak, M. (1974). “Dynamic stiffness and damping of piles.” *Canadian Geotechnical Journal*, 11(4), 574–598.

Novak, M., and Sheta, B. (1980). “Approximate Approach to Contact Effects of Piles.” *Proceedings of Session on Dynamic Response of Pile Foundations: Analytical Aspects*, Florida.

Palmer, L., and Thompson, J. (1948). “The earth pressure and deflection along the embedded lengths of piles subjected to lateral thrust.” *Proceedings Second International Conference on Soil Mechanics and Foundation Engineering*, 156–161.

Pam, H., and Park, R. (1990). “Flexural strength and ductility analysis of spirally reinforced prestressed concrete piles.” *PCI Journal*, 35(4), 54–83.

Patra, N., and Pise, P. (2001a). “Ultimate lateral resistance of pile groups in sand.” *Journal of Geotechnical and Geoenvironmental Engineering*, 127(6), 481–487.

Patra, N. R., and Pise, P. J. (2001b). “Ultimate Lateral Resistance of Pile Groups in Sand.” *Journal of Geotechnical and Geoenvironmental Engineering*, 127(6), 481–487.

Poulos, H., and Davis, E. (1980). *Pile foundation analysis and design*. Series in geotechnical engineering, Wiley, New York.

Rajashree, S., and Sitharam, T. (2001). “Nonlinear finite-element modeling of batter piles under lateral load.” *Journal of Geotechnical and Geoenvironmental Engineering*, 127(7), 604–612.

Ranjan, G., Ramasamy, G., and Tyagi, R. (1980). “Lateral response of batter piles and pile bents in clay.” *Indian Geotechnical Journal*, 10(2), 135–142.

Rao, S. N., Ramakrishna, V. G. S. T., and Rao, M. B. (1998a). “Influence of Rigidity on Laterally Loaded Pile Groups in Marine Clay.” *Journal of Geotechnical and Geoenvironmental Engineering*, 124(6), 542–549.

Rao, S., Ramakrishna, V., and Rao, M. (1998b). “Influence of rigidity on laterally loaded pile groups in marine clay.” *Journal of Geotechnical and Geoenvironmental Engineering*, 124(6), 542–549.

Reese, L., and Cox, W. (1969). “Soil behavior from analysis of tests of uninstrumented piles under lateral loading.” *Performance of Deep Foundations*, ASTM International, West Conshohocken, PA, 160-160–17.

Reese, L., Cox, W., and Koop, F. (1974). “Analysis of laterally loaded piles in sand.” *Offshore Technology Conference*, Houston, TX.

Reese, L., Cox, W., and Koop, F. (1975). “Field testing and analysis of laterally loaded piles om stiff clay.” *Offshore Technology Conference*, Houston, TX.

Reese, L., Isenhower, W., and Wang, S. (2006). *Analysis and design of shallow and deep foundations*. John Wiley.

Reese, L., and Welch, R. (1975). “Lateral loading of deep foundations in stiff clay.” *Journal of the Geotechnical Engineering Division*, 101(7), 633–649.

Robertson, P., and Cabal, K. (2015). *Guide to cone penetration testing for geotechnical engineering*. Gregg Drilling & Testing, Inc., Signal Hill, CA.

Robertson, P., Davies, M., and Campanella, R. (1989). “Design of laterally loaded driven piles using the flat dilatometer.” *Geotechnical Testing Journal*, 12(1), 30.

Robertson, P., Hughes, J., Campanella, R., and Sy, A. (1984). “Design of laterally loaded displacement piles using a driven pressuremeter.” *Laterally Loaded Deep Foundations: Analysis and Performance*, 229-229–10.

Rollins, K., Gerber, T., Lane, J., and Ashford, S. (2005a). “Lateral resistance of a full-scale pile group in liquefied sand.” *Journal of Geotechnical and Geoenvironmental Engineering*, 131(1), 115–125.

Rollins, K., Lane, J., and Gerber, T. (2005b). “Measured and computed lateral response of a pile group in sand.” *Journal of Geotechnical and Geoenvironmental Engineering*, 131(1), 103–114.

Rollins, K., Olsen, K., Jensen, D., Garrett, B., Olsen, R., and Egbert, J. (2006). “Pile spacing effects on lateral pile group behavior: analysis.” *Journal of Geotechnical and Geoenvironmental Engineering*, 132(10), 1272–1283.

Rollins, K., Olsen, R., Egbert, J., Olsen, K., Jensen, D., and Garrett, B. (2003). *Response, analysis, and design of pile groups subjected to static and dynamic lateral loads*. Utah Department of Transportation Research Division, Salt Lake city, UT.

Rollins, K., Peterson, K., and Weaver, T. (1998). “Lateral load behavior of full-scale pile group in clay.” *Journal of Geotechnical and Geoenvironmental Engineering*, 124(6), 468–478.

Roscoe, K., and Burland, J. (1968). “On the generalized stress-strain behaviour of ‘wet’ clay.” *Engineering plasticity*, 535–609.

Ruesta, P., and Townsend, F. (1997). “Evaluation of laterally loaded pile group at roosevelt bridge.” *Journal of Geotechnical and Geoenvironmental Engineering*, 123(12), 1153–1161.

Sha, Y., and Hao, H. (2012). “Nonlinear finite element analysis of barge collision with a single bridge pier.” *Engineering Structures*, 41, 63–76.

Sha, Y., and Hao, H. (2013). “Laboratory tests and numerical simulations of barge impact on circular reinforced concrete piers.” *Engineering Structures*, 46, 593–605.

Souri, A., Abu-Farsakh, M., and Voyiadjis, G. (2015). “Study of static lateral behavior of battered pile group foundation at I-10 Twin Span Bridge using three-dimensional finite element modeling.” *Canadian Geotechnical Journal*, 53(6), 962–973.

Sun, K. (1994). “Laterally loaded piles in elastic media.” *Journal of Geotechnical Engineering*, 120(8), 1324–1344.

Terzaghi, K. (1955). “Evalution of conefficients of subgrade reaction.” *Géotechnique*, 5(4), 297–326.

Trochanis, A., Bielak, J., and Christiano, P. (1991). “Three-dimensional nonlinear study of piles.” *Journal of Geotechnical Engineering*, 117(3), 429–447.

Tschebotarioff, G. (1953). “The Resistance to Lateral Loading of Single Piles and of Pile Groups.” *ASTM special publication No. 154*, 38–48.

Vallabhan, C., and Das, Y. (1991). “Modified vlasov model for beams on elastic foundations.” *Journal of Geotechnical Engineering*, 117(6), 956–966.

Voyiadjis, G., and Song, C. (2000). “Finite strain, anisotropic modified cam clay model with plastic spin. I: theory.” *Journal of Engineering Mechanics*, 126(10), 1012–1019.

Wei, L. (2004). “Numerical simulation and field verification of inclined piezocone penetration test in cohesive soils.” Ph.D dissertation, Louisiana State University, Baton Rouge, LA.

Welch, R., and Reese, L. (1972). *Lateral load behavior of drilled shafts*. Research Report, Center for Highway Research, The University of Texas at Austin.

Wheeler, S. J., Näätänen, A., Karstunen, M., and Lojander, M. (2003). “An anisotropic elastoplastic model for soft clays.” *Canadian Geotechnical Journal*, 40(2), 403–418.

Wilson, D. (1998). “Soil-pile-superstructure interaction in liquefying sand and soft clay.” Center for Geotechnical Modeling, Dept. of Civil and Environmental Engineering, University of California, Davis, Davis, Calif.

Winter, D. A. (2009). *Biomechanics and motor control of human movement*. John Wiley & Sons, Inc.

Yang, Z., and Jeremić, B. (2002). “Numerical analysis of pile behaviour under lateral loads in layered elastic–plastic soils.” *International Journal for Numerical and Analytical Methods in Geomechanics*, 26(14), 1385–1406.

Yuan, P. (2005). “Modeling, simulation and analysis of multi-barge flotillas impacting bridge piers.” *University of Kentucky Doctoral Dissertations*.

Yuan, P., and Harik, I. (2010). “Equivalent barge and flotilla impact forces on bridge piers.” *Journal of Bridge Engineering*, 15(5), 523–532.

Zdravković, L., Potts, D., and Hight, D. (2002). “The effect of strength anisotropy on the behaviour of embankments on soft ground.” *Géotechnique*, 52(6), 447–457.

Zerwer, A., Cascante, G., and Hutchinson, J. (2002). “Parameter estimation in finite element simulations of rayleigh waves.” *Journal of Geotechnical and Geoenvironmental Engineering*, 128(3), 250–261.

Zhang, J., Chen, X., Liu, D., and Li, X. (2016). “Analysis of bridge response to barge collision: refined impact force models and some new insights.” *Advances in Structural Engineering*, 19(8), 1224–1244.

Zhang, L., McVay, M., Han, S., Lai, P., and Gardner, R. (2002). “Effects of dead loads on the lateral response of battered pile groups.” *Canadian Geotechnical Journal*, 39(3), 561–575.

Zhang, L., McVay, M., and Lai, P. (1999). “Centrifuge modelling of laterally loaded single battered piles in sands.” *Canadian Geotechnical Journal*, 36(6), 1074–1084.

Appendix A. Permissions

NRC RESEARCH PRESS LICENSE
TERMS AND CONDITIONS

Oct 30, 2017

This Agreement between Ahmad Souri ("You") and NRC Research Press ("NRC Research Press") consists of your license details and the terms and conditions provided by NRC Research Press and Copyright Clearance Center.

License Number	4218911347316
License date	Oct 30, 2017
Licensed Content Publisher	NRC Research Press
Licensed Content Publication	Canadian Geotechnical Journal
Licensed Content Title	Study of static lateral behavior of battered pile group foundation at I-10 Twin Span Bridge using three-dimensional finite element modeling
Licensed Content Author	Ahmad Souri, Murad Abu-Farsakh, George Voyiadjis
Licensed Content Date	Jun 1, 2016
Licensed Content Volume	53
Licensed Content Issue	6
Type of Use	Thesis/Dissertation
Requestor type	Author (original work)
Format	Electronic
Portion	Full article
Order reference number	
Title of your thesis / dissertation	NUMERICAL EVALUATION OF THE LATERAL BEHAVIOR OF VERTICAL AND BATTERED PILE GROUP FOUNDATIONS USING 3-D FINITE ELEMENT MODELING
Expected completion date	Dec 2017
Estimated size(pages)	160
Requestor Location	Ahmad Souri 4101 Gourrier Ave. BATON ROUGE, LA 70820 United States

Appendix B. Soil Resistance Profiles Used in the Parametric Study

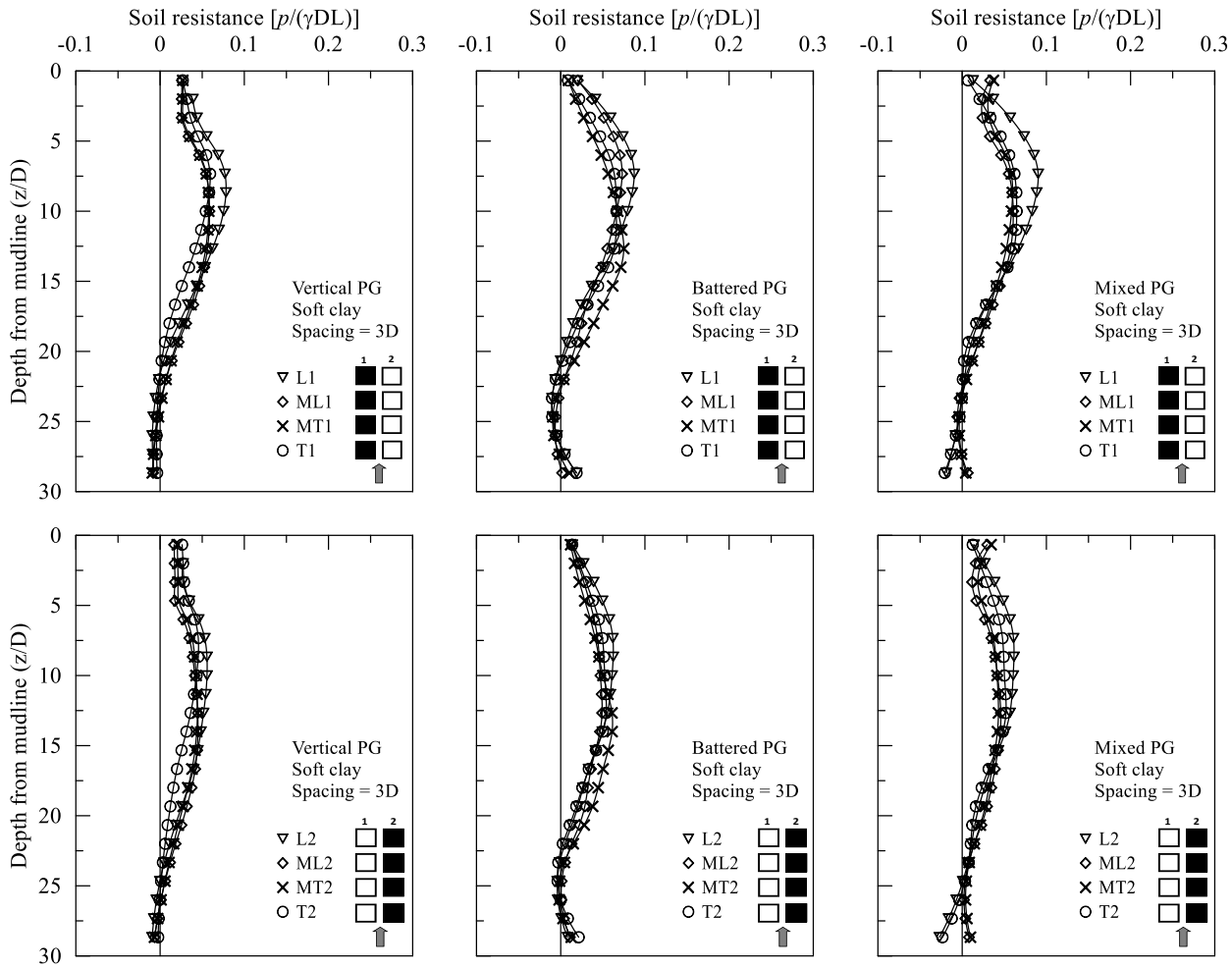

Figure B. 1. Soil resistance profiles for the pile groups in soft clay at pile spacing = 3D

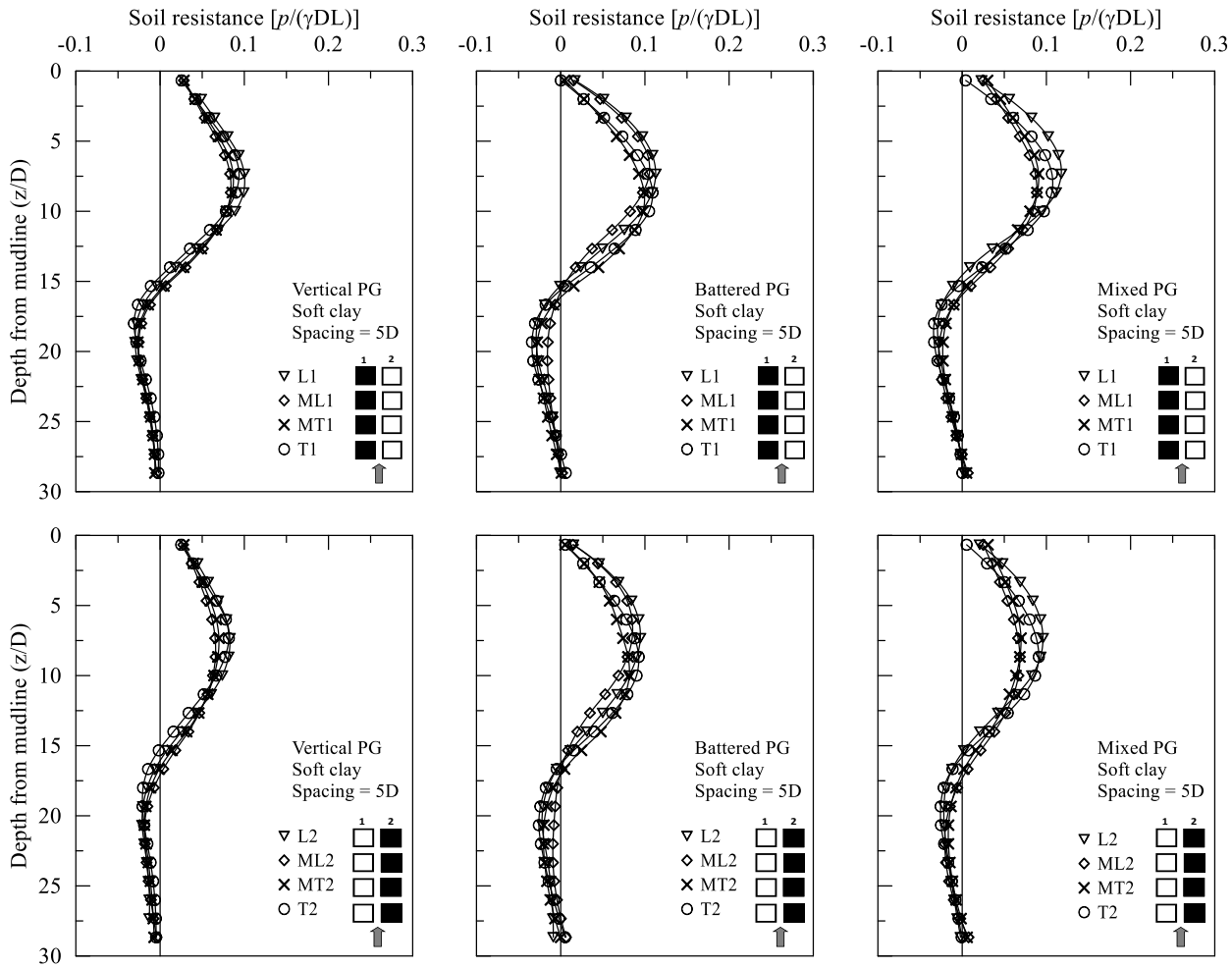

Figure B. 2. Soil resistance profiles for the pile groups in soft clay at pile spacing = 5D

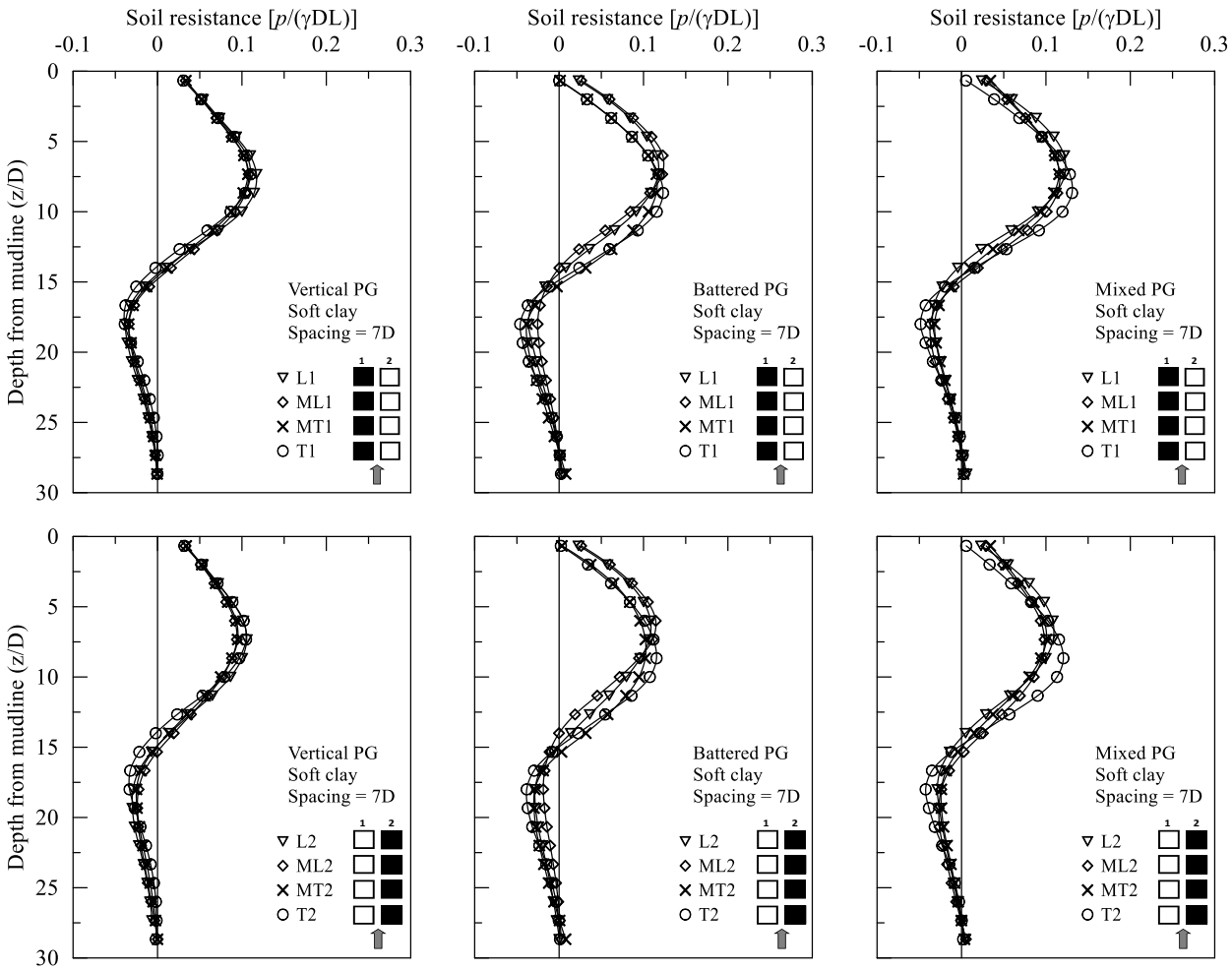

Figure B. 3. Soil resistance profiles for the pile groups in soft clay at pile spacing = 7D

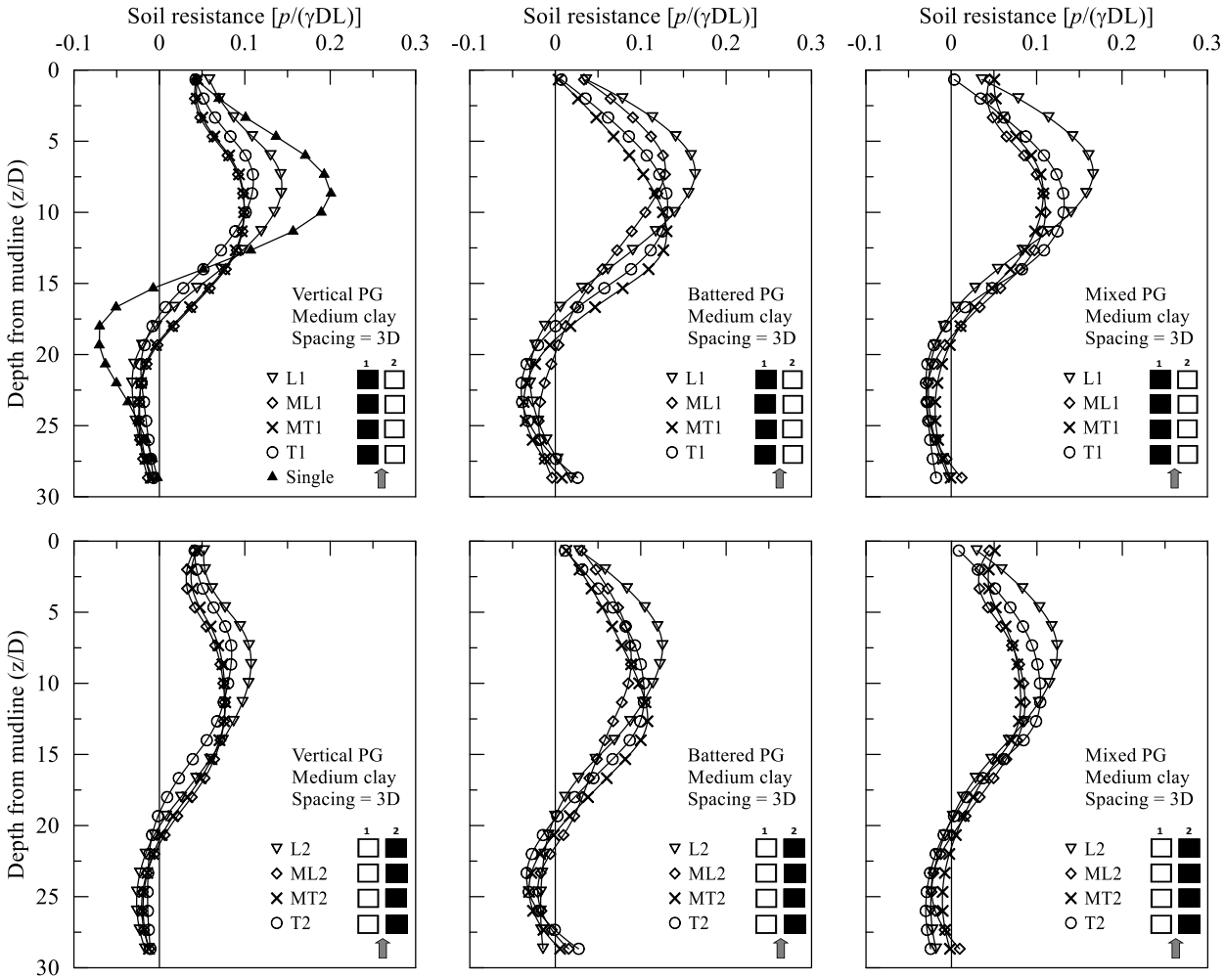

Figure B. 4. Soil resistance profiles for the pile groups in medium clay at pile spacing = 3D

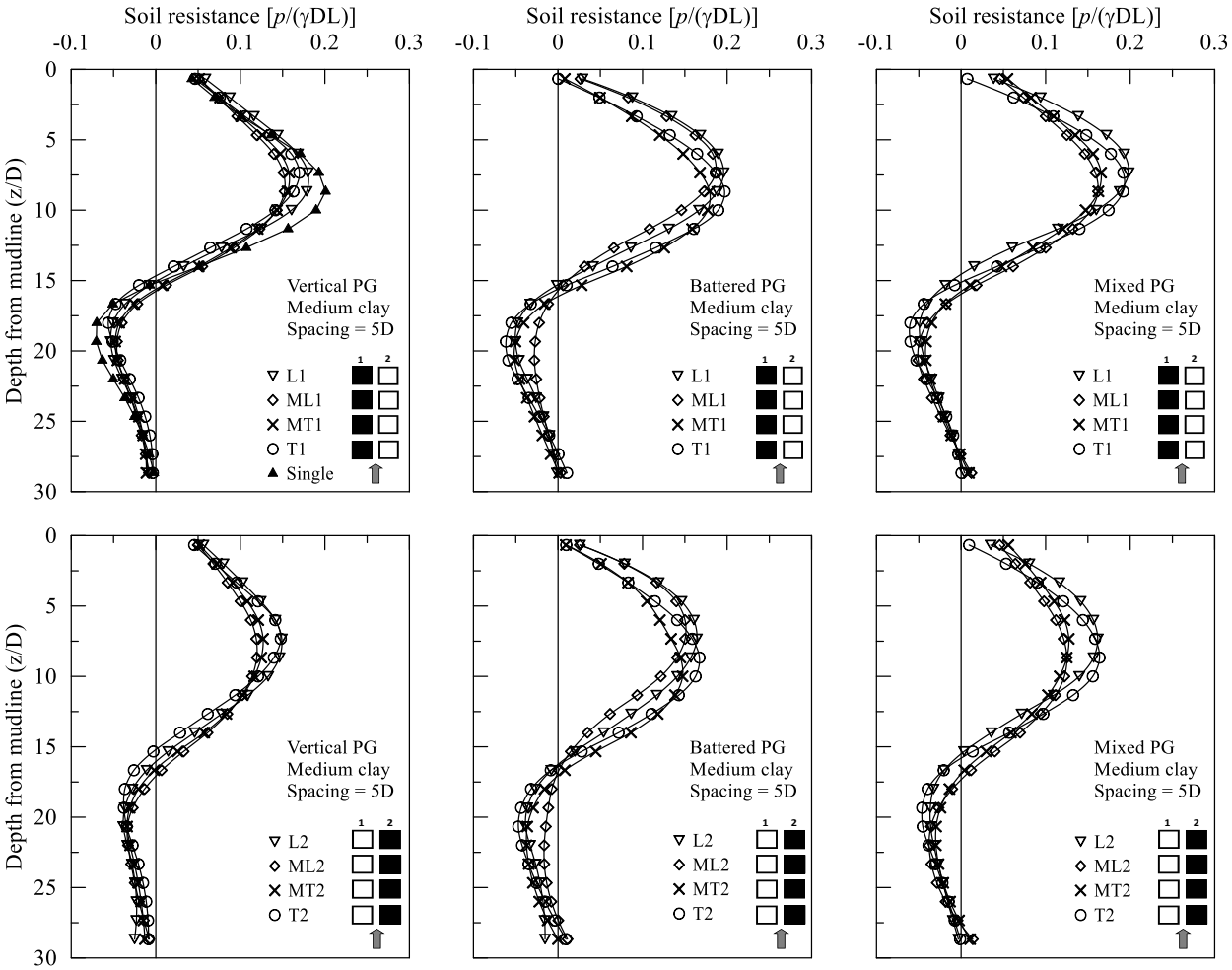

Figure B. 5. Soil resistance profiles for the pile groups in medium clay at pile spacing = 5D

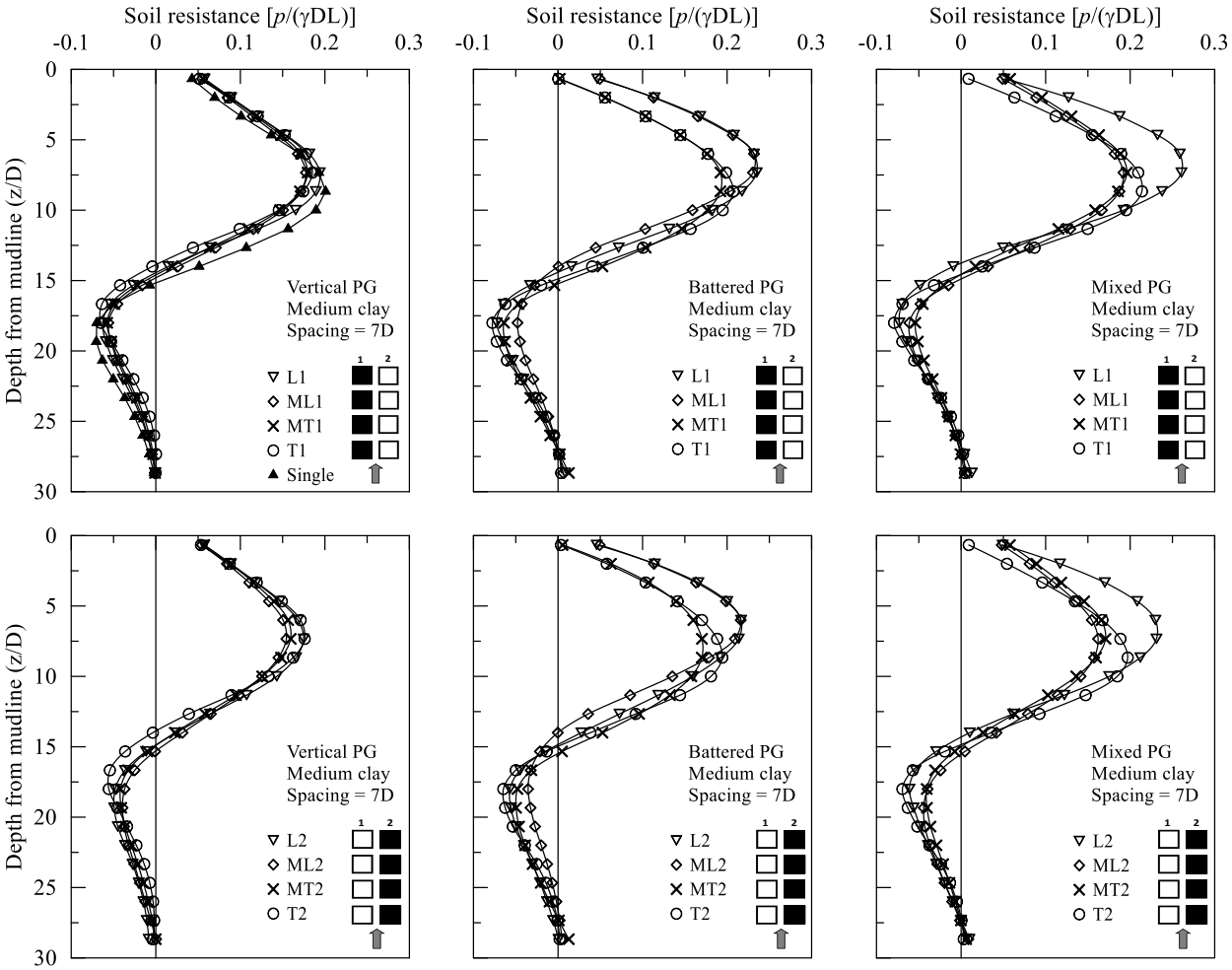

Figure B. 6. Soil resistance profiles for the pile groups in medium clay at pile spacing = 7D

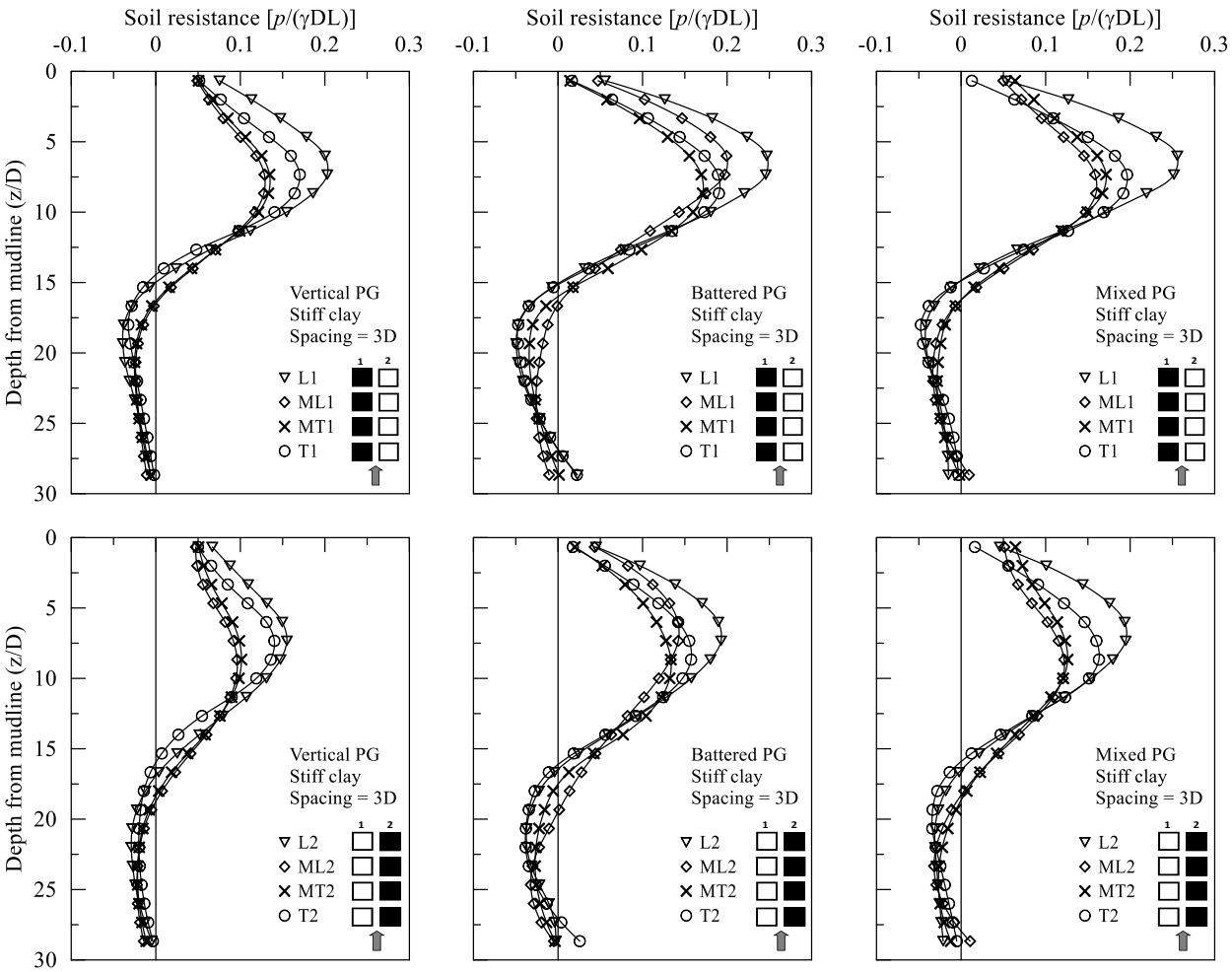

Figure B. 7. Soil resistance profiles for the pile groups in stiff clay at pile spacing = 3D

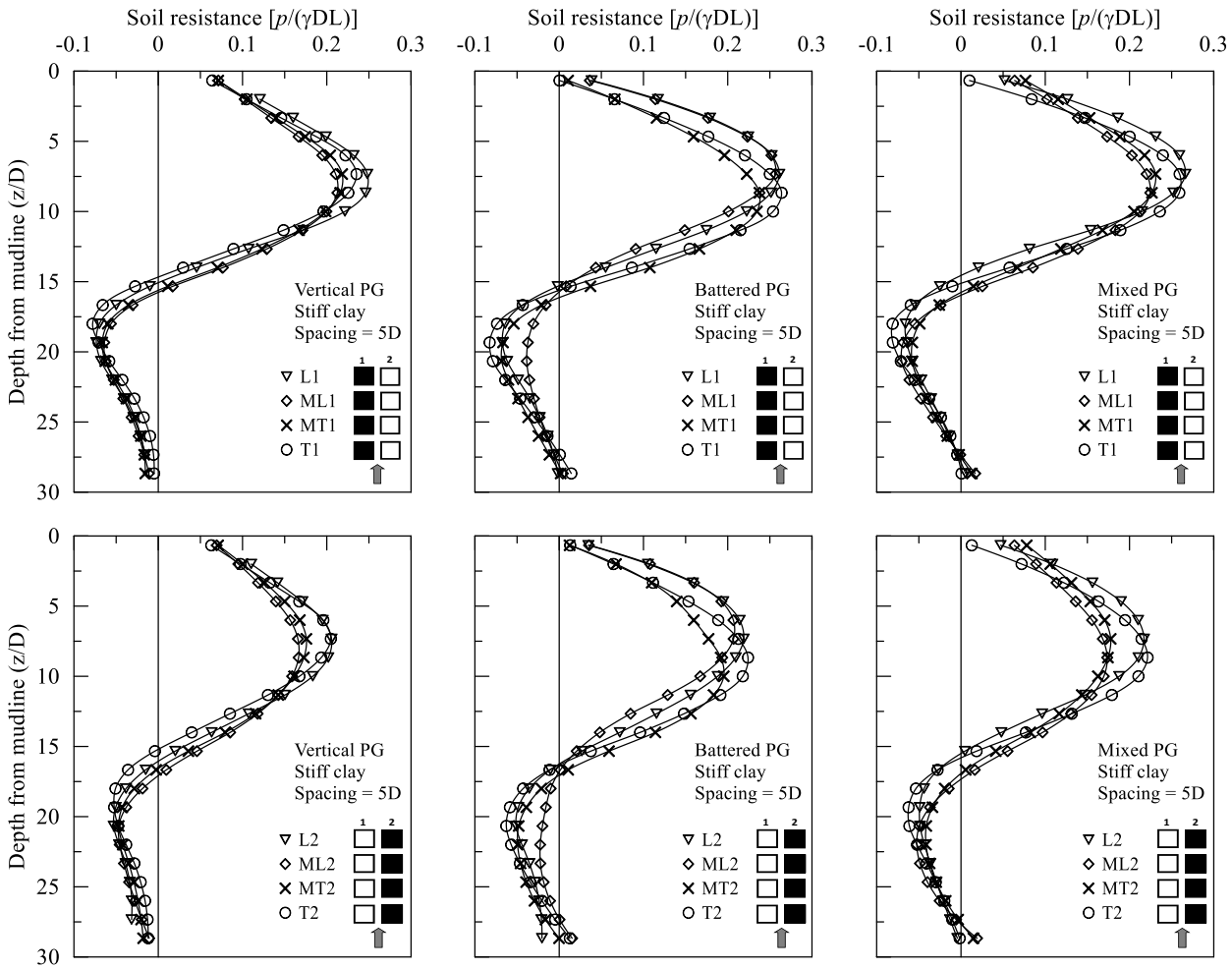

Figure B. 8. Soil resistance profiles for the pile groups in stiff clay at pile spacing = 5D

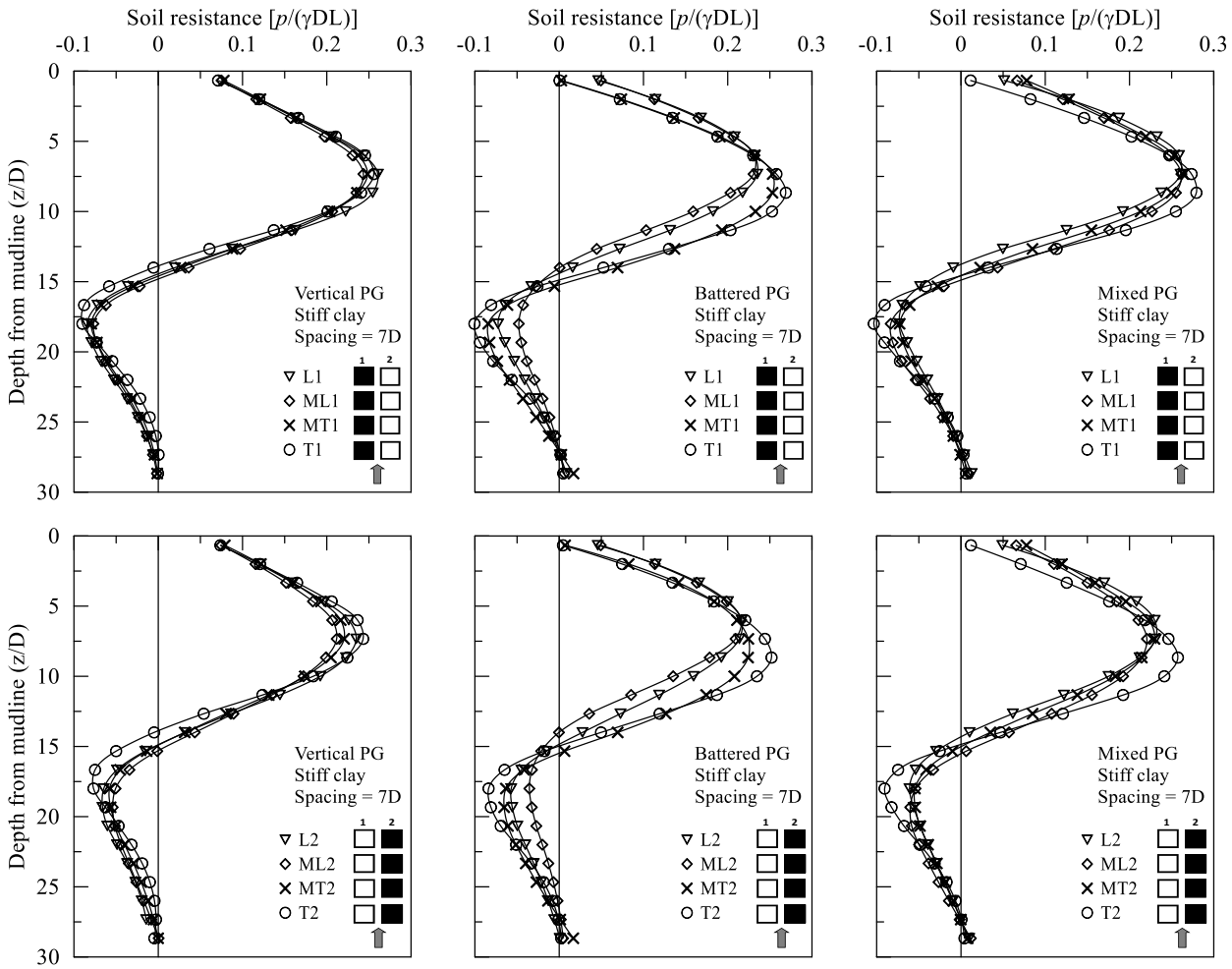

Figure B. 9. Soil resistance profiles for the pile groups in stiff clay at pile spacing = 7D

Vita

Ahmad Souri was born in Jordan in 1985. He attended the school of engineering and technology at the University of Jordan to study Civil engineering and obtained his bachelor's degree in 2007. He worked at Al-Jaber Transport & General Contracting company in UAE between 2008 and 2009. He moved to USA in 2010 to start his graduate studies. In June 2012, he obtained his master's degree in Civil engineering from Ohio University. He joined the doctoral program at Louisiana State University in September 2012.